Understanding the Relationship between Microstructure and Mechanical Properties in HIPped Ti-5Al-5Mo-5V-3Cr

by

Jianshu Gao

A thesis submitted to

University of Birmingham

for the degree of

Doctor of Philosophy

School of Metallurgy and Materials

College of Engineering and Physical Sciences

University of Birmingham

February 2018

Abstract

Beta titanium alloys have attracted a lot of attention in the past few decades in many fields due to advantages such as good corrosion resistance, good bio-compatibility and high strength-to-weight ratio.

Ti-5Al-5Mo-5V-3Cr (Ti-5553) , a relatively new generation beta titanium alloy has the advantage of high strength. It is a current generation alloy used in landing gear. Currently, landing gear components are large scale and processed through forging, followed by complex heat treatments. Many studies on this alloy were based on forging processes. As a conventional process, forging can provide required properties, but a large amounts of raw materials are wasted during this process. Therefore, HIPping (hot isostatic pressing) is an alternative way to process this alloy. In this project, work was carried out on investigating microstructures and mechanical properties (i.e. strength and fracture toughness) of HIPped Ti-5553 alloy. During comparisons on fracture toughness of different types of specimens, specimens are first heat treated to a similar strength level. And fracture toughness values are calculated at the same strength level circumstance.

Various microstructures are obtained through different heat treatments. Different microstructures (for example different grain size and different morphology of grain boundary alpha), can be achieved through specified treated temperature/ time and quenching methods. Results show that larger grain size and coarser intergranular lath-like grain boundary alpha can improve the fracture toughness.

A step quenching method can be used to form a coarse shell-like microstructure along the grain boundaries. One shell-like microstructure is obtained through different heat treatment conditions. Mechanical test was carried out on this kind of microstructure and compared to normal beta annealed microstructures. An improvement in fracture toughness is obtained.

To investigate the influence of microstructure on fracture toughness, techniques including optical microscope (OM), scanning electron microscope (SEM), and confocal laser scanning microscope have been used.

Acknowledgements

First and foremost, I would like to express my sincere gratitude to my supervisors, Prof. Paul Bowen, Dr. Hangyue Li and Dr. Xinjiang Hao, for their supervision, encouragement and support in research area.

Secondly, I want to thank the School of Metallurgy and Materials for its financial support on tuition fee.

Thanks to the other members of our group for their constructive remarks throughout my research. I would like to express my gratitude for their helpful discussions. Also thanks to Dr. T. Doel for his help with mechanical testing and my English. I would also like to thank my friends for their company and support.

Finally, I have to thank my parents for their giving me life and constant support. Last but not least, I would like to appreciate my girlfriend for her coming to my life, staying behind me for this time.

Table of Contents

Abstract 2

Acknowledgements 4

Table of Contents 5

Introduction 1

1 Literature Review 3

1.1 Titanium and its history 3

1.2 Titanium alloy classification 3

1.2.1 **α** alloys 4

1.2.2 **α + β** alloys 5

1.2.3 **β** alloys 5

1.3 Advantages and use of Ti alloys in the aerospace industry 6

1.3.1 Materials required for the aerospace industry 6

1.3.2 The use of beta titanium alloys 8

1.4 Phases in titanium alloys 10

1.4.1 Alpha phase in titanium alloys 10

1.4.2 Beta phase in titanium alloys 11

1.4.3 Metastable **ω** phase in titanium alloys 13

1.5 Ti-5553 and VT22 13

1.5.1 Applications and Advantages 13

1.5.2 Heat treatment routes 14

1.5.3 Shell-like microstructures 17

1.6 Processing methods 18

1.6.1 Conventional Methods 18

1.6.2 Powder Metallurgy 19

1.6.3 HIPping process applied to titanium alloys 20

1.7 Variant microstructure selection during heat treatment 22

1.7.1 The influence of heat treatment condition on beta phase 23

1.7.2 The influence of heat treatment condition on alpha phase 24

1.7.3 The influence of chemical composition on microstructures. 26

1.8 Mechanical Properties 26

1.8.1 Tensile strength 27

1.8.2 Factors which influence fracture toughness 28

1.9 Objectives and outline of the project 32

2 Experimental Methods 33

2.1 Materials 33

2.2 Heat-Treatment Process Overview 34

2.3 Microstructural observation 35

2.3.1 Optical microscopy 35

2.3.2 Scanning electron microscopy 36

2.4 Image processing methods 36

2.5 Mechanical properties 36

2.5.1 Vickers hardness testing 36

2.5.2 Tensile behaviour 37

2.5.3 Fracture toughness testing 38

2.5.4 Confocal scanning laser microscope 40

3 Effects of beta grain size on the mechanical properties of Ti-5553 41

3.1 Experimental methods 41

3.1.1 Material 41

3.1.2 Heat treatment processes 41

3.1.3 Microstructure observation 42

3.1.4 Image processing methods 42

3.1.5 Tensile testing 42

3.1.6 Fracture toughness testing 43

3.2 Results and discussion 43

3.2.1 Microstructures of As-HIPped alloys 43

3.2.2 Microstructures of Heat-treated alloys 43

3.2.3 Tensile testing 45

3.2.4 Fracture toughness testing 47

3.3 Summary 54

4 Effects of grain boundary α via STA heat treatment route on mechanical properties of Ti-5553 alloy 55

4.1 Experimental methods 55

4.1.1 Material 55

4.1.2 Heat treatment processes 56

4.1.3 Microstructure Observation 57

4.1.4 Mechanical Properties 57

4.2 Results and Discussion 58

4.2.1 Microstructures 58

4.2.2 Hardness testing 61

4.2.3 Tensile testing 62

4.2.4 Fracture toughness testing 63

4.3 Summary 70

5 Effects of shell-like microstructure via SQA heat treatment route on mechanical properties of Ti-5553 alloy 71

5.1 Experimental methods 72

5.1.1 Material 72

5.1.2 Heat treatment processes 72

5.1.3 Microstructure observation 73

5.1.4 Hardness testing 74

5.1.5 Image processing methods 75

5.1.6 Tensile testing 75

5.1.7 Fracture toughness testing 76

5.1.8 Fracture surface analysis 76

5.2 Results and discussion 76

5.2.1 Microstructures 76

5.2.2 Hardness testing 80

5.2.3 Tensile testing 82

5.2.4 Fracture toughness 82

5.3 Summary 86

6 The influence of microstructures obtained via beta annealed with subsequent slow cooling and ageing (BASCA) heat treatment route 88

6.1 Experimental methods 89

6.1.1 Heat treatment processes 89

6.1.2 Microstructure Observation 90

6.1.3 Mechanical Properties 91

6.2 Results and Discussion 91

6.2.1 Hardness testing 91

6.2.2 Microstructure observation 92

6.2.3 Tensile Testing 93

6.2.4 Fracture toughness testing 94

6.3 Summary 96

7 Discussion 97

8 Conclusions and future work 100

8.1 Conclusions 100

8.2 Future work 101

9 References 103

List of Tables 111

List of Figures 127

Introduction

This project investigates the relationship between microstructure and fracture toughness in HIPped Ti-5553 alloy. Based on previous studies, it is known that microstructure can be tailored by using different heat treatment conditions and that microstructure can affect fracture toughness. Therefore, controlled variable method is used to study this relationship. Based on these results, a microstructure which is beneficial to fracture toughness is designed and tested.

Chapter 1 presents a literature review which covers the microstructure and applications of beta titanium and beta alloys. Previous studies of how heat treatment parameters affect microstructure are reviewed. How microstructure influences mechanical properties are also described.

Chapter 2 describes the experimental methods used in this project. Techniques such as optical microscopy (OM), scanning electron microscopy (SEM), and confocal laser scanning microscopy are introduced. Sample preparation and mechanical tests including hardness, strength, and fracture toughness are presented. Some useful software such as ImageJ and Photoshop are also introduced.

The investigation of the influence of grain size, grain boundary alpha, shell-like microstructure, via different heat treatment routes, on fracture toughness are presented in Chapters 3 to 5. Each chapter focuses on one influencing factor.

Chapter 6 is about an industries heat treatment route. Microstructure obtained via beta anneal, slow cooling and ageing (BASCA) heat treatment condition are compared to previous results.

Chapter 7 discusses on the effects on mechanical properties and how do they influence the properties of PREP Ti-5553 alloy based on previous experiment results.

Chapter 8 summaries the results and conclusions. It also proposes some work that could be done in the future which can achieve more standing in this project.

1 Literature Review

1.1 Titanium and its history

Titanium is the world's 4th most abundant metallic element and is used for a variety of applications. Because of its outstanding strength-to-weight ratio and good corrosion resistance, titanium is very attractive to the aerospace industry, and is used for chemical processing equipment and biomedical devices [1]. Titanium was first discovered in 1790, but its uses were limited until the 1940's and 1950's [2]. The delay in the application of titanium was due to the difficulty in mining of titanium ores and the extraction from those ores. The Kroll's process (in 1950) developed the extraction method into a commercial scale [2]. For a long time, the use of titanium in aerospace and marine was limited although the weight savings and good corrosion resistance could cover some initial investment [3].

The aerospace industry is one of the largest uses of titanium alloys because of the superior structural efficiency of Ti alloys. The density of titanium is 4.5g/cm^3 which is 40% lower than that of steel. On the other hand, it has a high yield stress level of 1000 MPa. Beyond that, it has elevated temperature capabilities. With the development of new generation of aircrafts, the use of Ti alloys in two applications (airframes and aero-engines) increased gradually.

1.2 Titanium alloy classification

The α/β transus temperature of pure Ti is 882 ℃. The high temperature body centred cubic (bcc) crystal structure (β phase) transforms to the low temperature hexagonal close packed (hcp) crystal structure (α phase) at this temperature. The addition of alloying elements are used to alter the

stability of the two phases (α and β), and then modify the phase transformation temperature as shown in Fig. 1. These additional alloying elements can affect the α/β transus temperature depending on which crystal structure they stabilize. Elements (O, Al, N and C) which stabilize the α phase can increase the allotropic transformation temperature. Elements stabilising the β phase are classified into two groups (β isomorphous elements and β eutectoid forming elements) depending on its influence on the details of the binary phase diagrams. Common isomorphous stabilising elements are Mo, V, Nb and Ta, all of which have a bcc crystal structure. The addition of these stabilise the bcc structure and make it exist at a low temperature. If the content of eutectoid forming elements (Fe, Mn, Cr, Ni, Cu, Si and H) exceeds a certain concentration, intermetallic compounds will form. In addition, some elements (Zr, Hf and Sn) have more or less no effect on the α/β transus temperature and are named as neutral alloying elements [3].

Commercial titanium alloys are divided into different categories: α alloys, α+β alloys, metastable β alloys and stable β alloys depending on the two phases in the microstructure as shown in the pseudo binary phase diagram in Fig. 2.

1.2.1 α alloys

The classification of alloys called α alloys are defined by the microstructure containing only small amounts or none of the β phase at room temperature as shown in Fig. 2. A bcc crystal structure transforms to a hexagonal structure when temperature drops through the transus temperature. These alloys are commonly strengthened by interstitial α stabilising elements such as O. Additional small amounts of β phase can help to control the grain size during the recrystallization process and eliminate hydrogen embrittlement. α alloys offer good weldability, good corrosion resistance, but

have low tensile strength. They are good for use in cryogenic applications because they do not have a ductile to brittle transition. Table 1 shows some alloys in this group.

1.2.2 α + β alloys

The α + β alloys are located in a range between $\alpha/\alpha+\beta$ phase boundary and the martensitic transformation line (M_s) at room temperature. The combination of α and β phases gives a wide range to design microstructures which can be tailored by varying solution treatment, ageing and cooling rates. The most widely used α + β alloy is Ti-6Al-4V. This alloy provides an attractive balance of mechanical properties, including strength, ductility, fatigue and fracture toughness, due to the increased volume fraction of β phase. The applied temperature of α + β alloys is restricted to 400℃, i.e. fan discs and blades [4]. Some commercial α + β alloys are listed in Table 2.

1.2.3 β alloys

β alloys can be divided into metastable β alloys and stable β alloys. Stable β alloys which stand in the single β phase area are not used as commercial materials. All alloys in this classification shown in Table 3 are metastable β alloys because they are located in the α + β phase region of the phase diagram (Fig. 2).

β Ti alloys can be separated into two groups, so-called “high strength” β alloys and “heavily stabilized” β alloys. The first group, such as Ti-6246, Ti-17, β-CEZ and Ti-10-2-3, are located close to the $\beta/\alpha+\beta$ boundary (see Fig. 2). These alloys contain a high volume fraction of α phase and therefore can achieve high strength because of precipitation strengthening. The other group

(including Beta 21S and Ti-15-3) are located more to the right in the pseudo-binary phase diagram as shown in Fig. 2. These contain less α phase and have a lower maximum strength.

The β phase can be retained by fast cooling (quenching). These alloys can be heat treated to obtain a very high level of strength by microstructure optimisation. Precipitation hardening is the most effective way to harden commercial β alloys. The alloy is heated above the α/β transus temperature to obtain single β phase. After a quench, the alloy is aged at a lower temperature. The distribution of the precipitation of fine α acts as dislocation barriers and results in higher strength [5]. As shown in Fig. 2, with increasing of the amount of β stabilising elements, the α/β transus temperature declines. It allows a lower processing temperature of metastable β alloys than that of $\alpha + \beta$ alloys, i.e. Ti-10-2-3 is processed at 800℃, with a similar strength required for Ti-6-4 which is processed at 950 ℃ [6]. Also, the high content of additional β stabilisers can inhibit the $\beta - \alpha$ phase transformation which makes industries heat treatments much easier [7]. These alloys have good workability, together with deep hardenability and corrosion resistance. All advantages mentioned above makes β alloys attractive for large section applications in the aerospace industry [8].

1.3 Advantages and use of Ti alloys in the aerospace industry

1.3.1 Materials required for the aerospace industry

Requirements for materials used in the aerospace industry should be:

- Weight savings

It is clear that the high strength-to-weight ratio of titanium and its lower density, which is 40% lower than that of steel, indicate that it can act as a steel replacement although its slightly lower strength. Parts of landing gear are fabricated from Ti-10-2-3 in replacement of high strength steel 4340 M of B777 aircraft. This substitution offered a weight savings of about 580 Kg [9].

- Corrosion resistance

The good corrosion resistance of titanium alloys can cut down costs of both corrosion protective coatings and maintenance. For example, the utilisation of titanium alloys as the floor support structure under the galleys and lavatories which are in a very corrosive environment [4].

- Space limitations

The example is given of materials used in the landing gear beam. This component running between the envelopes of the wings, carries high loads. Using an Al alloy (7075) can satisfy the required loads, but would require a large volume which would not fit. Steel is also considered, but it would be much heavier owing to its high density. Ti alloys meet all the requirements [4, 9].

- Operating temperature

The components in the engine and exhaust area are operated at high temperature. The engine parts including plug and nozzle are applied at about 600℃. Beyond that, Ti alloys can be applied at cryogenic temperatures, i.e. impellors for rocket engines [9].

- Composites Compatibility

With increasing application of polymer matrix composite, the polymeric composites compatibility becomes a big issue. Al alloys and steels contacting with carbon fibre would cause corrosion problems. In order to solve this problem, titanium alloys are used because they have good compatibility with the graphite fibres in the polymeric composites. Another reason is that the coefficient of thermal expansion of titanium is between that of graphite and that of aluminium. The attachment of a composite structure and a titanium structure do not lead to high loading.

1.3.2 The use of beta titanium alloys

The main advantages of titanium alloys is their good strength-to-density ratio and high corrosion resistance. One can decrease the weight of aircraft. The other can allow titanium alloy to be applied in extreme conditions. Therefore, even though the cost is higher, they are replacing aluminium alloys and high strength steels.

β alloys mentioned in Table 3 have been widely applied in the aerospace industry.

The first use of β Ti alloys was in 1960s in the SR-71 "Blackbird" aircraft [2, 10]. Ti-13V-11Cr-3Mo (B120VCA) was introduced to the frames of aeroplanes at first. Then B120VCA was used to produce springs. Although only a very small volume was used, it started the history of Ti applications.

During the next two decades, the benefits of using β Ti alloys drew more attention. Ti-15V-3Cr-3Al-3Sn was applied into over 250 parts such as nacelles and sine-wave spars due to its good formability and high strength, replacing Ti-6Al-4V. The next important timing point came when the volume fraction of β Ti alloys exceeded that of Ti-6-4 in the Boeing 777 aircraft [3]. Ti-10V-

2Fe-3Al alloy was used to replace high-strength low-alloy steel in parts of the landing gear structure, which resulted in a weight saving of over 580Kg [9]. This savings in weight also attracted Airbus to use it in their planes in similar applications [11]. In the Boeing 777, Ti-15V-3Cr-3Al-3Sn and Ti-3Al-8V-6Cr-4Mo-4Zr were used at strength levels between 1034 MPa and 1240 MPa for a series of springs and support structures. The last mentioned beta alloy is Ti-14.7Mo-2.7Nb-3Al-0.27Si (β-21S) used at high temperature conditions, because of its good oxidation resistance and creep properties. As well as in landing gears components in Boeing and Airbus, Ti-10V-2Fe-3Al also was used in rotor systems after lowering its strength level to improve its fatigue properties [12]. High strength β titanium alloys Ti-17 and Ti-6246 are used in aero-engines (compressor disks) [3].

Another use of β Ti alloy (Ti-15-3) is in nut clips in aircraft because it is more corrosion resistant than cadmium-plated steel. Heavily stabilised β Ti alloys are used widely for springs in aeroplanes. Ti-15-3 and Beta C have a very low modulus of elasticity and they do not require painting to prevent corrosion, as well as low density [3, 9].

The next generation β titanium alloy, Ti-5Al-5Mo-5V-3Cr, is the research target in this project. The applications of Ti-5553 are introduced in following section.

Although Ti and Ti alloys have these advantages mentioned above, there are still some factors limiting their extensive use. High energy and stringent production condition are required during the whole manufacturing processes. In addition, machining is very high cost, much slower than that of aluminium alloys, and most of raw material will turn into scraps. About only 10% material can be machined out to a useful part [9, 13].

1.4 Phases in titanium alloys

Phase, this term, is used to describe a homogeneous state of matter in a region, having almost the same chemical composition with the same crystal structure and uniform properties. In metallurgy, phase is used to describe a homogeneous state of material with a certain chemical composition and a distinct crystal structure [14]. Adding other elements into titanium, it exhibits two equilibrium phases at low and high temperature, called α phase and β phase. These equilibrium phases are obtained when specimens are given long enough time for phase transformation to occur until a stable state is reached. If the thermal treatment processed is rapid giving short time for achieving equilibrium phases, non-equilibrium phases may be formed, which have higher free energy than equilibrium phases. And higher energy state would transform to lower energy state given sufficient time [15, 16].

1.4.1 Alpha phase in titanium alloys

At lower temperatures, titanium exhibits a hexagonal close-packed structure (HCP). The c/a ratio of pure α phase is 1.587, which is smaller than the ideal ratio (1.633). The modulus of elasticity E of α titanium is between 145 GPa (along the c-axis <0001>) and 100 GPa (perpendicular to the c-axis <11-20>. Because of the smaller than ideal c/a ratio, the main slip system is on the prism plane [3] along the <11-20> direction as shown in Fig. 3 [17].

In beta titanium alloys, there is only a small volume fraction of α phase precipitating from the β matrix. In order to distinguish the α phase observed under microscopy, they are named as intergranular α, intragranular α and grain boundary α, according to their various nucleation sites. Intergranular α is referred to α phase which precipitates at grain boundaries or from grain boundary α layer and grows into the interior of β grains. Intragranular α precipitates within beta grains, nucleating at defects or metastable phases (ω or β'). Grain boundary α is also known as allotropic alpha, precipitating and growing along grain boundaries [3].

There is another classification method for α phase is according to its morphology. Alpha phase can be classified into basketwave α, colony α, lath α and globular α. Different morphology of α phase can be obtained through different heat treatment conditions which will be discussed in the following sections [3, 18].

In addition, α phase can be divided into primary α (α_p) and secondary α (α_s) depending on its precipitation sequence. Primary α mostly forms early at heat treatment steps, such as during solution treatment or the cooling period from the solution treatment temperature. Secondary α mainly forms during ageing. The primary α can influence the precipitation of secondary alpha as acting as nucleation sites [19].

1.4.2 Beta phase in titanium alloys

Beta phase has a body centered cubic (BCC) structure. The unit cell is shown in Fig. 4. The BCC structure of β phase is more open, where atoms would vibrate more heavily. This is the reason that

β phase is stable at high temperature region. The unit cell of β phase, it has six close packed planes {110} and four closet packed directions <111> [3, 18].

For pure titanium, β phase is obtained through heating α phase above 883 ℃ (β transus temperature). Only adding β stabilizing elements (i.e. Mo, V, Cr Fe, Nb, Ta, W, Cu, Pt and Au) can lower the β transus temperature and even retain β phase at room temperature [3]. Two classifications of β stabilizing elements isomorphous stabilizing elements and eutectoid forming elements have been introduced in Chapter 1.2 as shown in Fig. 1.

The E-values of β phase is impossible to measure at room temperature due to its instability. It can be roughly estimated by using E-values of α phase at transus temperature and Ti-V alloys in the water quenched conditions. Beta stabilizing elements lower the modulus to between 55 GPa and 115 GPa. Many applications such as springs and fasteners have similar E modulus [20-22].

In order to understand the influence of β phase stabilizing elements quantitatively, the Mo equivalency is used [15].

$[Mo]_{eq}$ =[Mo]+0.2 [Ta]+0.28 [Nb]+0.4 [W]+0.67 [V]+1.25 [Cr]+1.25 [Ni]+1.7 [Mn]+1.7 [Co]+2.5 [Fe]

1.4.3 Metastable ω phase in titanium alloys

The ω phase was first found by Frost et al. [23]. The ω phase is found in metastable β Ti alloys. The first type, called athermal ω phase, formed during quenching method from the β solution temperature to room temperature, by a diffusion less transformation. This process has been found in Ti-5553 alloy [3, 24]. The athermal ω phase distributes uniformly as very fine particles with a size of 2-4 nm.

The other type, isothermal ω phase is formed through low temperature ageing in the ω + β phase region. The chemical composition of isothermal ω phase is solute lean compared to β phase [3]. The isothermal ω particle is observed in ellipsoidal or cuboidal shape depending on misfit strain [25]. This phase can play a role as nucleation sites, contributing to a uniform distribution of α phase, which is good for the strength of material. Therefore, some research is focusing on controlling the dispersion of isothermal ω phase in β alloy.

1.5 Ti-5553 and VT22

1.5.1 Applications and Advantages

Ti-5553 is a new generation metastable β alloy which is modified from the Russian alloy VT-22 (Ti-5Al-5V-5Mo-1Cr-1Fe) [10, 26]. It was introduced firstly by Titanium Metals Corporation [27]. Compared with VT22, Ti-5553 (Ti-5Al-5Mo-5V-3Cr) has a lower Fe content and higher Cr content. This alloy was produced for large components such as landing gear and other airframe structure components in new generation aircrafts because of its high strength and corresponding not too low

ductility. The Ti-5553 alloy developed from VT-22 provides a good balance of strength, ductility and toughness. The tensile strength can be heat treated up to 1517 MPa, because of the precipitation of fine α phase [28]. It can provide a tensile strength of 1309 MPa with about 10% elongation [27].

Compared with the previous generation alloys, Ti-10-2-3, used for landing gear, Ti-5553 provides a wider processing window at high-strength level [29, 30]. To achieve an acceptable balance among strength, ductility and toughness, Ti-10-2-3 goes through a complex processed route, while processing route for Ti-5553 is much simpler. Ti-5553 is less sensitive to heat treatment variables and suffer only a slightly loss in mechanical properties by air cooling which gives a thicker section size (150 mm) [10]. This makes an easier production route possible for Ti-5553 alloy. Initially, this alloy was developed to replace high-strength steel and Ti-10-2-3 at the strength of 1241 MPa.

This alloy was developed by Boeing and the world's largest titanium manufacture, VSMPO, aiming to improve the hardenability of VT22 and durability as well. The outstanding hardenability of Ti-5553 alloy makes it reach high strength levels up to 1517 MPa. Also, good damage-tolerance is obtained by adjusting processing routes [10]. A similar alloy, Ti-5Al-5Mo-5V-3Cr-1Zr is used by Airbus at a lower strength level (1100 MPa) [31]. Considering the high cost of titanium, it is only used in areas which are difficult to inspect or maintain.

1.5.2 Heat treatment routes

Heat treatments methods for VT22 alloy have been studied. Specimens were solutionized and aged with two types of cooling methods between these two steps; air cooling to room temperature and furnace cooling to the ageing temperature. It was found that solution temperature affected the grain

size. The grain growth occurred at higher solution temperature, resulting in a loss of strength. The strength of this alloy was found to improve with fast cooling rate [32, 33]. The increase of ageing temperature also brought down the strength of material.

There is a wide of possible microstructures of Ti-5553 alloys based on its phases controlled by separate variations in the heat treatments.

It was observed that either bimodal or lamellar microstructures can be achieved in this alloy [34]. The final microstructure depends on the solution temperature in the single β phase or α+β phase regions. Also in Harper's work, the formation of athermal ω phase was observed after an oil quench and isothermal ω phase acted as nucleation sites for α precipitation during the following age [8]. Another study found that only when quenched-specimens heated below 400℃, the coarsening process of ω phase occurred accompanied with α precipitation at its interfaces. As the athermal ω is dispersed uniformly, the coarsening isothermal ω, playing the nucleation sites led to homogeneous distribution of α precipitations [8].

Study of microstructural control in this alloy found that intragranular alpha only formed at an ageing temperature below 700℃. Ageing treatment carried out above that temperature only obtained relatively low strength as the α phase becomes very coarse. Results also suggested that lower ageing temperature under 600℃ would decrease the ductility due to the formation of ω phase [35].

Like other β-Ti alloys, solution temperature influences beta grain size. A higher temperature over the beta transus temperature will form larger beta grains [3, 36]. An important parameter is cooling

rate from the solution temperature which controls the precipitation of continuous GB α layers [3]. Some researchers found that higher cooling rates from the annealing temperature produce thinner α plates, which is good for tensile strength in Ti-5553 alloy [37]. Generally, ageing is the last step in the processing route. It is necessary because it produces an optimum balance between strength and ductility and fracture toughness. Ageing temperature and time determines the size and volume fraction of precipitation of α phase [3]. Some studies carried out on the effect of quench method reveal that a step quench (SQ) followed by a holding time affect the morphology (thickness, length and Vol%) of precipitation of grain boundary alpha and intragranular alpha [38-40]. Samples were solutionized at a temperature above beta transus and then step quenched to a temperature below the beta transus and held for a period of time before they are quenched to room temperature.

One of the common heat treatment methods used for Ti-5553 alloy is the beta-annealed, slow cooled and aged (BASCA) process which was designed by Boeing Company [41]. The BASCA heat treatment process can provide higher toughness with a relatively high level of strength. Samples are solutionized at a temperature above the beta transus for a period of time and then slow cooled to the ageing temperature, holding for some time as shown in Fig. 5.

The other common process is called solution treated and aged (STA) which is applied to improve strength. Solution treatment is done just below the beta transus for 2 h and then cooled to room temperature. Samples are aged at 593 ℃ for 8 h before air cooling (Fig. 5). Material treated in this condition has been used for the truck beam forgings of large components (i.e. landing gears) on aircraft [10]. This STA heat treatments route also being expected for high strength parts like fasteners [42].

1.5.3 Shell-like microstructures

Another heat treatment condition named as step quenched and aged was carried out for Ti-5553 alloy by Nag et al. [38, 39]. A series of experiments based on different solution and ageing temperature were conducted. The amount of α_p precipitation was observed from a sample which was step-quenched from 1000℃ to 800℃ and then held for 4 hours. The α_p preferred to form at the β grain boundaries where the density of α laths was higher than that of precipitates within β grains. Similar results were found in Harper's work [39], slow cooling from one ageing condition to another led to the α phase only forming at some grain boundary areas. Furthermore, the size of these grain boundary α precipitates was larger than intragranular α laths.

This phenomenon is further investigated and its influence on mechanical properties is studied in the present work. A heat treatment route was designed for obtaining shell like microstructure and how it influenced on properties was studied.

As Ti-5553 alloy is a potential material for use in landing gear, its design should meet some requirements. The landing gear is a very heavy part of aircraft, since it provides a suspension system during taxi, take-off and landing. Therefore, the selected material should have a high strength-to-density ratio providing a low weight and requiring small storage volume. As far as safety is concerned, it should also have high toughness which means the ability to absorb more energy during rising and landing and reduce the impacting to the airframe. Also, it would be better to have a low maintenance fee and long life cycle [43].

1.6 Processing methods

As discussed in last Chapter 1.3, it has been pointed out that the main restriction for Ti alloys wide use is its high cost in production. Large amounts of raw material are wasted. In order to save cost, researchers have considered processing methods. In this section, conventional methods and powder metallurgy will be introduced and compared.

1.6.1 Conventional Methods

One of the reasons which restricts the use of titanium alloys is high cost during the manufacture process [10]. The traditional processes for titanium alloy manufacture are casting or forging. The use of casting has increased when casting is more economic. With some Ti alloys such as Ti-6-4, mechanical properties are comparable to those processed by forging. Also, net shape casting solves the shaping difficulty in some brittle alloys by forging and machining. For metastable β alloys, Beta C and Ti-15-3, are most attractive to the foundry. They are more castable and can be heat treated up to 1170 MPa strength [2]. Nonetheless, for some special applications, porosity and other defects which occur during casting need subsequent repair which increases the cost. Besides, microstructures obtained by casting have large grains and dendrites harming mechanical properties [44]. Therefore, casting is not the first choice for high strength β titanium alloys.

Forging as a shaping method has been widely used for titanium alloys components. Forging technology for titanium alloys has developed dramatically during the last two decades. It produces most titanium alloy products each year. Selection of optimal forging and thermal processes can obtain shapes close to the designed. Microstructures are controllable to meet different required

properties. To achieve these advantages, the cost of forging always needs to be considered. Expensive tooling (excessive die wear) is needed. Besides, the cost of raw Ti alloys material is very high. For example, only 10% as-forged plates can be machined out into components, the rest is turned into chips. As titanium is very expensive, it is important to develop a technique which leads to a reduction of fly-to-buy ratio and decreases the cost during the processes [2, 4]. Powder metallurgy came into sight as a near or net-shape processing method [45, 46].

1.6.2 Powder Metallurgy

Titanium powder metallurgy (PM) offers the possibility of producing net or near net-shape components with less raw material costs. And final products do not require complex machining. It is more efficient and more economical than the conventional methods. Generally, there are two categories of PM techniques:

- Blended elemental PM, in which a blend of elemental powders (alloy additions), along with master alloy or other desired additions as a binder, is cold compacted into a green shape and then vacuum sintered to higher density and uniform chemistry.
- Pre-alloyed PM, in which pre-alloyed powder is consolidated by cold pressing and sintering or HIP.

Recently, hot isostatic pressing (HIPping) has drawn attention to replacing forging to produce near net shape bulk. In this work, pre-alloyed (Ti-5553) powder was processed using HIPping.

Ti-5553 powders can be produced by two different techniques: plasma rotating electrode process (PREP) and gas atomisation (GA). They are both common commercial methods. In the plasma

rotating electrode process, a machined bar of a desired chemical composition is rotated at high speed inside an atmosphere chamber. The localized melting is caused by a plasma torch in a vacuum furnace. Molten droplets are flung off the bar surface by the centrifugal force, cooling and are collected from the collection port [2]. A diagram of PREP is shown in Fig. 6.

Gas atomisation is a non-centrifugal process and used to produce superalloy, titanium alloys and high alloy steels and other powders [47]. A diagram of vertical gas atomisation unit is shown in Fig. 7. Molten metal is poured into a pouring box with a nozzle which is used to control the size and shape of the metal stream. High speed inert gas breaks up the stream into droplets. Those particles solidify during the flight and become powders [2].

Most research has used forging to produce samples [48-51]. The relationship between mechanical properties and microstructures of HIPped Ti-5553 alloy has been rarely studied.

1.6.3 HIPping process applied to titanium alloys

HIPping is an advanced processing technology in the fabrication of titanium alloys through powder metallurgy since the 1970s [52]. Comparing with conventional methods, hot isostatic pressing can save materials, reduce machining and form near-net-shape components, which can result in more efficient material utilization. It also archives 100% theoretical density and more homogeneous microstructure and improving mechanical properties [53]. J. CHEN et. al. reported that HIPping can eliminate the shrinkage and porosity in Ti-6246 and increase UTS and elongation as 9.2% and 6.32% respectively [54]. Yield strength improved by HIPping also was confirmed by M. XIANG et. al., yield strength increasing from 833 MPa (cast process HIP process) to 765 MPa (cast process) [55]. They also pointed that fast heating rate during HIP can produce coarse equiaxed alpha phase

which is beneficial to plasticity. A typical condition for Ti-64 under HIP is at 950℃, 100 MPa for 4 h [56]. Tensile properties for Ti-64 produced by different techniques are listed in Table 4. The result shows that HIPping can bring competitive strength and ductility to the product.

To achieve such improved properties, several steps are included in a typical HIPping process, as shown in Fig. 8 [57] [58]. The first step is to fabricate can according to the components design. Then the can will be filled with metal powder and the can will be evacuated, degassed and sealed so that no impurities will remain in the final product. The next step will be the core part of this technique, hot isostatic pressing (HIP). During this step, the component is subjected to both elevated temperature and isostatic gas pressure in a high-pressure containment vessel. The actual temperature and pressure depend on the type of material to be fabricated. The pressurizing gas used in this step is normally argon or other inert gas so that the material does not chemically react. The pressure to be applied to the can is applied by heating up the chamber which causes the pressure inside the vessel to increase. Associated gas pumping is also adopted in many systems to achieve the necessary pressure level. Because the pressure is applied through the pressured gas, so that the pressure is applied to the material in the can evenly from all directions and hence named as "isostatic". Note that the temperature chosen for HIP is normally below 0.8 x T solidus. The purpose is to avoid liquid phase forming. After HIP, the container can will be removed (step 4) by machining, acid pickling or slipping-off techniques. Thereafter, the consolidated component is acquired and shall be heat treated to get the desired microstructure.

1.7 Variant microstructure selection during heat treatment

After the first-step of material processing, to obtain desired properties, material still needs to undergo proper heat treatment. Titanium alloys can have various microstructures based on different phases. Before understanding microstructural influence on tensile properties and fracture toughness, those various microstructures need to be obtained.

Choosing different heat treatment routes is a useful method to achieve a range of strength levels for titanium alloys. Basically, solution treatment and ageing treatment are the key points. Different parameters used in these two steps affect the morphology of microstructures like shape, volume fraction and size. As shown in Fig. 9, line AC is the beta transus temperature. At points above this line like point D means specimens are solution heat treated. When the temperature drops from the β regime into the α+β area (point E), microstructures includes primary alpha phase and retained beta phase. At point F temperature, where specimens are aged secondary alpha will transform from retained beta phase. Microstructures may contain primary alpha, secondary alpha and retained beta phases.

In this section, the relationship between heat treatment parameters and microstructure will be discussed. This will be helpful to choose a proper heat treatment condition for design purposes.

1.7.1 The influence of heat treatment condition on beta phase

Ti-5553 alloy is a metastable β titanium alloy. It mainly contains alpha (α), beta (β) and omega (ω) phases. Each phase has its own stable temperature range and beta phase is stable at high temperatures. For Ti-5553 alloy, the α/β transus temperature is 850℃. Single β phase is stable above this temperature [59].

The purpose of heat treatment is to tailor microstructure of material which can affect the mechanical properties, by using different solution treatment and ageing treatment conditions. In this work, the required mechanical properties are high strength and high fracture toughness.

The relationship between heat-treated microstructure and heat treatment condition has been widely studied.

As mentioned above, beta solid solution forms above the alpha/beta transus temperature. As temperature drops below 850℃, entering the alpha+beta two phases region, the precipitation of alpha phase begins [59-61]. Beta titanium alloys, unlike alpha+beta Ti alloys, can achieve metastable beta phase at room temperature upon quenching.

Typical heat treatment routes are shown in Fig. 5. Solution treatment is carried out as the first step to obtain single beta phase. Solution treated temperature and time are important in beta solution treatment, because they influence the final beta grain size. For Ti-10V-2Fe-3Al, researchers used 900℃, 1100℃ and 1200℃ as solution treated temperature, which are all above beta transus temperature (830℃) of Ti-10V-2Fe-3Al. Experimental results showed that at the same solution treated time, higher temperature produced larger grain size in this alloy [62]. And in another study,

it was pointed that longer solution treatment time lead to the larger grain size of beta phase [63]. For a given alloy, higher heat treatment temperature can achieve larger grains in shorter time. Also, long holding time at the solution treated temperature can bring larger grains. It has also been noticed that, grain size has an influence on mechanical properties, which will be discussed in this thesis.

In beta titanium alloys, the typical microstructure is a beta annealed microstructure. It can be obtained through an easy heat treatment route as shown in Fig. 10. As for beta annealed microstructure, the key characteristic is the formation of continuous alpha layers which are located at GB （grain boundary）area. To obtain the beta annealed microstructure, the processing route must contain two steps, recrystallization (also could be called solution treatment) in the single beta phase area and ageing in the alpha+beta phase area [3].

Another processing routes for β Ti alloys is shown schematically in Fig. 11 resulting in a β processed microstructures. It can be seen that there is no recrystallization step compared to the β annealed route. Finally, an unrecrystallized structure with highly deformed β grains can be achieved [3].

1.7.2 The influence of heat treatment condition on alpha phase

Besides beta phase, the morphology of α phase will vary depending on the different heat treatment conditions applied.

At temperatures below the alpha/beta transus, α phase begins to nucleate from β phase. Different cooling methods and the various ageing temperatures would result in different morphology, size, thickness, volume fraction and distribution. For instance, the cooling rate from solution treatment

is important to the morphology of α_p [3, 64]. And sometimes, a step-quenching method will result in special microstructures [38, 39].

The precipitation of α phase is preferred to occur at β grain boundary areas. For all β-Ti alloys, a continuous α layer forms at GBs. During the cooling period, coarse primary α phase precipitates along grain boundaries and grows into the β matrix. Those α phases with the same and multiple crystallographic variants are called colony α and basketweave α microstructures. It has been observed in other research that the thickness of this primary α phase is determined by the cooling rate from the solution treatment temperature. Slower cooling rates allow specimens to soak at high temperatures for long times which could promote elemental diffusion, resulting in thicker α plates. Meanwhile, the size (length) of α phase is influenced by cooling rate in a similar way [3, 65-68].

The other type of α phase, so-called secondary α phase (α_s) forms during ageing in the $\alpha + \beta$ phase region. For β-Ti alloys, it has been confirmed that metastable phases such as isothermal ω (ω_{iso}) or the orthorhombic α'' can form during ageing [69-72]. These precursor metastable phases act as nucleation site of the α platelets, helping to obtain a uniform distribution of α_s. Heating rate from room temperature dominates the phase transformation sequence. Higher heating rate leads to direct transformation into $\alpha + \beta$ phase [51]. Heating rate influences the final distribution of α platelets [3]. In similar β-Ti alloys, the effect of ageing temperature and time has been studied [73-75]. Compared to ageing time, ageing temperature plays a more important role, which can affect microstructural features including size, volume fraction and distribution of α platelets [3]. Increasing ageing temperature, lowering volume fraction of α at equilibrium, can lower the yield stress and shorten the time to reach maximum state due to faster diffusion. On the other hand,

longer ageing time gives enough time for fine α_s to grow into coarse α_s. The cooling rate after ageing treatment also influences the morphology of α_s platelets. Slowing cooling rate gives longer time for α_s growth into large scale [3].

1.7.3 The influence of chemical composition on microstructures.

Apart from these physical methods tailoring final microstructures, chemical composition by adding elements such as carbon can influence α precipitation. Small amount of carbon addition can refine and homogenize the α precipitation during ageing β-solutionized Ti-5553 alloy. Bedsides, the tendency of α_p precipitating along grain boundary is reduced as well [76].

1.8 Mechanical Properties

After processing, alloys still need to be heat treated to achieve the final mechanical properties. During the heat treatment routes, parameters in heat treatment are selected according to correlation between conditions and microstructures. Understanding the relationship between microstructure and mechanical properties (tensile strength and fracture toughness) will help choose proper heat treatment conditions.

1.8.1 Tensile strength

1.8.1.1 Effect of beta grain size.

It has been pointed out that the formation of a continuous layer of α phase can not be eliminated, which is detrimental to tensile properties. This is because of dislocations pile-up at grain boundary triple points, which leads to local stress concentrations [77]. The crack nucleation forms easily at these triple points. And the slip length can be seen as equal to the grain boundary length. In β-Ti alloys, smaller grain size gives smaller grain boundary length, and higher tensile strength. Therefore, it is believed that in most of Ti-alloys smaller grain size is beneficial to tensile properties [3, 37, 62, 78-80]. In other research, unexpected results were found in beta Ti-15-3 alloy, where tensile strength increased with β grain size within a certain range of grain size. Researchers regarded this phenomenon as different precipitation of α phase occurring in large-size and small-size grains [81].

1.8.1.2 Effect of alpha precipitation

In order to achieve a higher strength level of β-Ti alloys, the most efficient method is precipitation hardening. Small α platelets attribute to higher strength levels than large α platelets. This is because small α platelets are more difficulty to deform than large α platelets. In a fully aged condition, the volume fraction of α phase is constant. More small size α platelets precipitation means less large α platelets precipitation, resulting in increasing the dislocation density, also hardening the material. Therefore, according to Orowan relationship, the yield stress is proportional to d^{-1}, where d is the inter-particle distance. This is also called dislocation hardening. Similar results have also been found in Ti-6Cr-5Mo-5V-4Al and β-CEZ alloy [82, 83]. A combined theory

between precipitation hardening and dislocation hardening can be used to illustrate higher volume fraction α phase brings higher yield stress in Ti-5553 alloy [84]. It is confirmed that higher volume fraction of finer α_s contributes to tensile strength [37].

Also, the distribution of α phase forming during ageing treatment also affects the tensile strength. Obtaining a more homogeneous distribution of α platelets is good to tensile for properties[60].

1.8.2 Factors which influence fracture toughness

Fracture toughness is used to describe the ability of a material tolerating a crack before it fractures. It can express the resistance of a material to final fracture occurring in the presence of a crack in a quantitative way [85]. It is one of the most important properties in all materials for many applications. Many investigations have been carried out on fracture toughness. A large amount of work has been on focusing on microstructural features like beta grain size, volume fraction of alpha, thickness of different alpha phases and alpha-morphology affecting fracture toughness [74, 80, 81, 86-94].

1.8.2.1 Contributions to fracture toughness

Generally speaking, there are two contributions to fracture toughness. One is the intrinsic resistance of a material, the other is crack front roughness also called crack geometry. The intrinsic resistance about the strength difference between the matrix and the soft zones, at which the cracking occurs. A large difference, meaning high strength level, lead to easier crack starting between them. That's why fracture toughness decreases with increasing strength for most of alloys. Only in individual cases does the correlation between strength and fracture toughness shows a reverse tendency.

Unexpected results were found by Breslauer and Rosen. For Ti-15-3 alloy, when the grain size was in a certain range, both tensile strength and fracture toughness increased at the same time indicating a positive correlation. It was explained by the researchers that the morphology of the α phase precipitation is different within large grains and fine grains, which influenced the mechanical properties [81].

The other contribution, crack front roughness, is independent of strength level. A rougher crack path is good for fracture toughness. It can absorb more energy during crack propagation, forming a rougher fracture surface.

Taking both of two contributions into consideration can be used to analyse the relationship between strength and fracture toughness [3].

1.8.2.2 The effect of beta phase

It has been found that larger α colony size can affect the fracture toughness in Ti-6Al-4V. For a coarse structure, it has a higher K_{Ic}-values than that for the fine structure [3]. In β-Ti alloys such as β-CEZ and Ti-10V-4.5Fe-3Al, the β grain size plays a similar role as α colony size in α + β alloys. A fine grain size microstructure has a relatively lower fracture toughness value than a coarse grain size microstructure. It also exhibits a smoother fracture surface topography. This phenomenon that large grain size benefits fracture toughness in β Ti alloy can be explained as the larger grain size is, the rougher crack front profile will be. Roughening the crack front profile makes it difficult for a crack to propagate. In these alloys, the contribution of rough crack geometry (crack

profile) dominates the contribution from formation of crack within soft zone along continuous grain boundary α layer [3, 62, 81, 95-97].

1.8.2.3 Effect of alpha phase

In all microstructural conditions, the fracture toughness is reduced with increasing in yield stress.

1.8.2.3.1 Effect of the α_p

In some research on Ti-10-2-3, it has been found that elongated α_p has a higher fracture toughness than that of globular α_p. The explanation was made by fractographic observation. Under SEM microscopy, it was observed that more crack deviation occurred by elongated α_p phase and crack propagation went along the α_p/β matrix interfaces. While, for globular α_p, crack path is mainly through β matrix and grain boundary α layers. This difference between the two morphologies of α_p leads to various roughness in fracture surface [98].

In addition to morphology (elongated or globular) of α_p, the volume fraction is also pointed out to influence the fracture toughness. A higher volume fraction leads to a lower fracture toughness. This is because higher volume fraction of α_p, lead to a smaller interspace between α_p, at which the voids prefers to nucleate leading to higher void density. Compared to lower volume fraction of α_p specimen, higher α_p volume fraction specimen has a much flatter fracture surface [98].

In addition to those two parameters, the sub-grain boundary α film has an effect on fracture toughness. These α phase precipitate at sub-grain boundaries forming a thick, continuous layer,

which provides a lower energy path for crack propagation. It is believed crack path along the sub-grain boundary α layer is easier than the path through β matrix [98].

All three factors mentioned before are schematically illustrated in Fig. 12.

Work done by Fan, et al. [48] indicates that the coarse grain boundary α and intragranular α is good for fracture toughness. If these phases are coarser and longer, this can lead to a more tortuous crack path meaning higher fracture toughness.

1.8.2.3.2 Effect of secondary alpha phase ($\boldsymbol{\alpha_s}$)

In this section, the effect of α_s will be reviewed. In experiments carried out by Lutjering and Peters [82], β-CEZ specimens were heat treated through different conditions and achieved three types of microstructure. The first one contained very fine α_s. The second one only had coarse α_s. The third microstructure included both fine and coarse α_s structures. Results show the structure with coarse α_s has the best fracture toughness. The second high fracture toughness values belongs to mixed structure. It is believed that large size α_s has a function of retarding crack growth, improving the fracture toughness. At the same time, large α_s causes more local crack reflection. The small α_s has very least significant influence on fracture toughness [3].

Understanding the relationship among heat treatment conditions, microstructures and mechanical properties is necessary in this project. It will help to design the experimental methods for Ti-5553 alloy.

1.9 Objectives and outline of the project

The application of Ti-5553 alloy has increased rapidly. HIPping is an alternative process and lacks studies on the influence of microstructures on mechanical properties. It is necessary to do some research on this.

Also, high fracture toughness for Ti-5553 alloy is a requirement in some applications like landing gear. Understanding how microstructures like grain size, grain boundary alpha affecting the fracture toughness and how they are obtained through different heat treatment conditions are useful to improve fracture toughness. In this work a shell-like microstructure is designed and investigated on its combination between strength and fracture toughness.

2 Experimental Methods

2.1 Materials

Specimens used in this project were prepared from pre-alloy Ti-5553 alloy powder which was produced by the plasma rotating electrode process (PREP). Two kinds of powders with different chemical composition were used. One has a small addition of carbon (0.08 wt%) . The other one is undoped PREP Ti-5553 alloy. The size range of powder is 125~1000 μm. Different materials were chosen to investigate various influence factors on mechanical properties. More details will be given in the following chapters.

The alloy powder was HIPped in steel cans with a diameter of 42 mm and height of 220mm. Before filling, the cans were tested for leaks. The cans were then filled with alloy powder. The cans were then outgassed at a pressure of 10^{-5} mbar for 24 h and then crimp-closed. The powder filled cans were then HIPped at 900℃ and 150MPa for 2 h in the EPSI Lab HIP facility as shown in Fig. 13. The required blanks were then machined from the HIPped can with electric-discharge-machining (EDM).

2.2 Heat-Treatment Process Overview

During the come of this work, many different heat treatments were conducted, depending on the required microstructure and properties. It is more appropriate to give details of the different heat treatment condition in the results Chapter 3-6. For every heat treatment the testpieces were wrapped in Fe foil to restrict the effects of oxidation.

In Chapter 3, in order to investigate the effects of grain size of mechanical properties. Specimens were heat treated into different grain size. PREP 0.08% C Ti-5553 were solutionized at 900℃, 1000℃, and 1050℃ for 1 h and 4 h. And then, selected samples were aged at 650℃ for 6 h.

In Chapter 4, PREP NC Ti-5553 samples were solutionized at 900℃ for 1 h. And then, solutionized samples were aged at two conditions, 600℃ 6 h and 650℃ 6 h to achieve designed strength level.

In Chapter 5, step quenching and aged process was applied. A series of heat treatment schedule combined different solutionizing condition (900℃ 1h and 1000℃ 1 h), holding condition (650℃ 40 min and 680℃ 1 h) and final ageing condition (600-660℃, 4 or 5 h) together to achieve designed microstructures.

In Chapter 6, beta annealed with subsequent slow cooling and ageing process was applied. Solution treatment condition was selected at 1000℃ for 1 h. And then specimens were slow cooled to 600℃ 5 h and 640℃ 5 h repectively.

2.3 Microstructural observation

After each heat treatment, metallographic investigation was required. Specimens were cut from heat treated samples using electro discharge machine (EDM) and cut into small pieces by disk cutting machine. Small-size specimens were mounted in conductive bakelite. Mounted specimens were ground on a piano 220 disc at a speed of 250 rpm until the surface was flat. The following polishing procedure had two stages. In the first stage, specimens were polished using MD-Largo/ 9 μm at rotational speed of 150 rpm for up to 10 min. Then, they were polished by finer MD-Chem/ 0.05 μm at the same rotational speed for 6 min as described in Table 5. All polishing procedure are conducted with corresponding polishing liquid.

After the final polishing stage, some specimens were chemically etched with 2%vol hydrofluoric acid and 98%vol water for about 15 s for microstructural exanimation.

2.3.1 Optical microscopy

Optical microscopy (OM) was used to observe microstructure such as grain size under low magnification. It is also used in hardness testing for measuring dimensions of pattern formed by indenter. Optical microscopy was also used to examine fracture surface and measure crack length after fracture toughness testing.

2.3.2 Scanning electron microscopy

Scanning electron microscopy (SEM) JEOL 7000 was used to observe microstructural features under high magnification. Different phases and fracture surface are all observed and analysed using SEM equipment. SEM was also used to exam fracture surface.

2.4 Image processing methods

Image analysis was conducted using ImageJ software whose operation panel as shown in Fig. 14 is used to process images obtained by a SEM or OM.

The other software used is Adobe Photoshop. Numbers of high magnification images on adjacent areas were spliced together putting much more features together in one picture.

2.5 Mechanical properties

2.5.1 Vickers hardness testing

Hardness is a basic mechanical property widely used to estimate mechanical properties of metals and their alloys quickly. Vickers hardness test is a simple way to estimate yield strength (in MPa) of metal materials [99, 100]. There is a formula that states the relationship between Vickers hardness and yield strength approximately. This formula is expressed by,

$$\sigma=\frac{HV}{0.33}$$

where, σ is tensile strength in MPa and HV is Vickers hardness in HV.

In this project, Vickers hardness was measured on a MH-5L micro hardness tester (automatic hardness machine). Loading force was to 300g and dwelling time followed default value(10s). Two perpendicular diagonals formed by diamond indenter were measured for Vickers Hardness calculation. The calculation formula is given below [101].

$$HV=\frac{1.8544F}{d^2}$$

where, F is the loading force in kg and d is the average length of the diagonal in mm.

Each valid hardness value is the average of 20 test points. The specimen preparation were the same as that for microstructural observation listed in Table 4.

2.5.2 Tensile behaviour

To reach the aims of investigation on the influence of microstructures on mechanical properties i.e. strength and fracture toughness, tensile testing is necessary. Heat-treated samples were cut into 10 mmØ cylindrical blanks using EDM as shown in Fig. 16. These were machined into final testpiece as shown in Fig. 17 [102]. The diameter of testpiece is 4 mm and the gauge length is 20 mm. Tensile tests were carried out on a Zwick machine as shown in Fig. 15 at a strain rate of 0.5%/ min at room temperature. An extensometer was used for precise strain control. The fracture surfaces of failed specimens were observed using a JEOL 7000 SEM.

2.5.3 Fracture toughness testing

Fracture toughness testing of Ti-5553 alloy was carried out on compact tension (CT)-specimen referring to the British Standard 7448 [103]. CT-specimens were cut from heat-treated bars and then sent out for machining into the final shape as shown in Fig. 18. Pre-cracking of specimens was prepared on an Amsler Vibrophore testing machine at room temperature. Pre-cracks were produced via fatigue with a stress ratio of 0.1 and a frequency range between 70 and 80 Hz. The maximum loading force was set as 3.6 kN and reduced to 2 kN according to the British Standard. The final testing was done on a Zwick machine at room temperature in air. The crosshead speed was 0.5 mm/min. A clip gauge was put between the knife edges across the notch of the specimen to record the crack opening displacement (COD) obtaining loading force-COD curves. K_{Ic}/K_Q-values were calculated from these recording data from the equation as followed [103]:

Where

$$K_Q = \frac{F_Q}{BW^{0.5}} \times f'(\frac{a_0}{W})$$

$$f'\left(\frac{a_0}{W}\right) = \frac{(2+\frac{a_0}{W}) \times (0.886 + 4.64\frac{a_0}{W} - 13.32\frac{{a_0}^2}{W^2} + 14.72\frac{{a_0}^3}{W^3} - 5.6\frac{{a_0}^4}{W^4}}{(1-\frac{a_0}{W})^{1.5}}$$

K_Q is the provisional value of plane strain fracture toughness K_{Ic}; F_Q is the particular value of applied loading force on specimen; W is the width of specimen; B is the thickness of specimen; a_0 is the average original crack length of specimen.

If the K_Q satisfies all criteria in standard as listed below, it is valid and can be reported as K_{Ic}.

$$2.5(\frac{K_Q}{\sigma_{YS}})^2 < a_0, \text{ B and } (W-a_0)$$

Where

σ_{YS} is yield strength of specimen.

Three types of fundamental fracture mode were classified by Irwin [104], which are shown in Fig. 19.

1. Mode I (Opening Mode): The crack opening only suffers a stress perpendicular to the xz-plane.
2. Mode II (Sliding Mode): The two crack surfaces slide along the crack front under the influence of a shear stress perpendicular to the yz-plane.
3. Mode III (Sliding Mode): The two crack surfaces slide along z-axis under the influence of a shear stress parallel to the xy-plane.

Stress intensity factors can be defined corresponding to each type and named as K_I, K_{II} and K_{III}, respectively. For most of structural materials $K_{Ic} < K_{IIc} \leq K_{IIIc}$ and most fracture toughness date refers to mode I loading. In this investigation, all loading modes are mode I.

The fracture surfaces of failed specimens were observed using OM and SEM. Some testpieces were section through the fracture surface metallographically prepared so that the crack propagation path could be seen.

The crack propagation paths of fracture specimens were analysed after polishing and etching. 3D images of fracture surface were obtained using a confocal scanning laser microscope (LEXT).

2.5.4 Confocal scanning laser microscope

Fracture surfaces were also examined using a confocal scanning laser microscope. This allows a 3D profile of a fracture surface to be created. During each scan, an appropriate area was firstly selected. Then upper and lower Z-positions were identified. The upper Z-position is determined by the highest point on the surface and the lower Z-position is the lowest position. Another parameter, the Z-step size which is the appropriate slice thickness, need to be selected at 1μm. After sequential scanning, all scanning data is stacked and converted into 3D models. After smoothing and spike removal functions, final 3D models were obtained.

In the 3D images, different colours are used to represent Z-values. Based on these colours, the fluctuation of the surface can be indicated. The roughness values (R_a) were also calculated automatically.

3 Effects of beta grain size on the mechanical properties of Ti-5553

This chapter studies the influence of beta grain size on mechanical properties of Ti-5553 alloy. It is mentioned in the literature review section that solutionized temperature can affect beta grain size. Various solution treatment conditions were applied to samples to obtain different beta grain sizes. After measuring beta grain sizes, three grain sizes (46, 100 and 168 μm) specimens were chosen to do the following mechanical testing.

3.1 Experimental methods

3.1.1 Material

PREP Ti-5553 alloy with the additional of 0.08 wt% carbon was chosen to study the influence of beta grain size on mechanical properties especially fracture toughness.

3.1.2 Heat treatment processes

Before heat treatment, samples were wrapped in Fe-foil to avoid contact with oxygen in air. Box furnace was used to do heat treatment. The beta transus temperature of Ti-5553 is about 850℃. Various solution temperatures above the beta transus listed in Table 6 were selected for tries to get different beta grain sizes. Samples were solutionized treated at 900℃ for 1 h, 1000℃ for 1 h, 1050℃ for 1 h and 1050℃ for 4 h. Then, they were water quenched to room temperature for microstructural observation. 4 Selected samples were then given an ageing at the same temperature

at 650℃ holding for 6 h as shown in Fig. 20 and Table 7. The mechanical properties were conducted as described in Chapter 2.

3.1.3 Microstructure observation

In this section, the aim is to study the influence of grain size on fracture toughness in PREP 0.08% Ti-5553 alloy.

All four groups of PREP 0.08% C Ti-5553 samples were prepared well including grinding/polishing and etching for microstructure observation using OM and SEM. Images were taken by optical microscope and then grain size were measured by software ImageJ.

Besides, the volume fraction of secondary alpha phase was also calculated.

Details on sample preparation for OM and SEM observation are illustrated in previous section 2.

3.1.4 Image processing methods

Software ImageJ was used to measure some features of different phases for quantitative analysis.

3.1.5 Tensile testing

During the experiments, all specimens with different grain sizes were designed to be heat treated to the same strength level awaiting for fracture toughness comparison.

In this part, the accurate tensile strength values were obtained.

All experiment operation was introduced in previous section.

3.1.6 Fracture toughness testing

Fracture toughness tests were conducted following British Standard [103].

Analysis on fracture surface was done using OM, SEM and Confocal techniques.

3.2 Results and discussion

3.2.1 Microstructures of As-HIPped alloys

Material powders were HIPped at 900℃ and 150MPa for 2 h and then metallographic samples prepared for microstructural observation. Microstructures of as-HIPped alloys were observed under SEM on the both low and high magnification. Fig. 21 (a) and (b) are from PREP NC Ti-5553 samples; (c) and (d) are from PREP 0.08% C Ti-5553. The grain size) in PREP 0.08% Ti-5553 sample was measured to be ~150 μm which is much larger than that in PREP NC (~ 50 μm). The formation of continuous α layer at the grain boundaries of PREP NC Ti-5553 samples and very fine α precipitating in the interior of the grain were found. While, in the as-HIPped PREP 0.08%C Ti-5553, coarse α laths were found on both the grain boundary and inside the grain.

3.2.2 Microstructures of Heat-treated alloys

Fig. 22 shows optical images of 3 groups of samples showing that only beta phase were retained after solution treatment followed by water quench. This is because that the beta transus temperature of Ti-5553 alloy is about 850℃ and all selected solutionizing temperatures (900℃, 1000℃ and 1050℃) were above this. Group 1 samples which were solution treated at 900 ℃ for 1 h have an

average grain size of 46 μm. With increasing the solutionizing temperature up to 1000℃, the average grain size of samples increased to 100μm. For group 3 samples (solutionized at 1050℃ 1 h) and group 4 samples (solutionized at 1050℃ for 4h), the average grain size was 141 μm and 168μm respectively. In order to obtain a larger range of grain size, group 3 sample was not chosen for further testing. Three groups (1, 2 and 4) with average grain sizes of 46 μm, 100 μm and 168 μm are shown in Fig. 22 and Table 8.

After measuring grain size, these three groups' samples were aged at 6 h (see Table 7). After polishing and etching, SEM images of these 3 groups were taken to study microstructural features of PREP 0.08% C Ti-5553 alloy. Images in Fig. 23 shows microstructures at grain boundary areas of samples with grain size of 46 μm, 100 μm and 168 μm. A continuous grain boundary α layer formed in all three groups of samples. The formation of α_s phases during ageing are very similar. This is a result of the same ageing condition (650℃ for 6 h). This basketweave structure α_s phase was distributed uniformly along grain boundaries as illustrated in Fig. 23. In Fig. 23 (c), carbides indicated by white arrows were discovered at the grain boundaries. Carbides exist also in the other two samples, but are not shown in Fig. 23 (a) and (b). Higher solution temperature and longer time results in the growth of beta grains. These carbides act as pinning sites at grain boundaries restricting grain growth. As grain boundaries grew to reach these carbides, it would be difficult for beta grains to grow more due to carbides' pinning function. Carbides also caused the discontinuity of grain boundaries as shown in Fig. 23 (c). More intragranular α phase precipitation appearance are displayed in Fig. 24. The similarity in basketweave appearance characteristic of α_s because of same ageing treatment is easily observed.

In order to understand the influence of different solution treatment conditions on the final microstructure, the volume fraction of α phase of the three groups of samples were measured. These images in Fig. 24 were transferred into black/white pictures and black areas were counted using ImageJ software threshold function. The results of volume fraction of alpha phase are listed at Table 7. The result shows that there is 29.4%, 29.5% and 28.0% alpha phase formed in the 3 groups' samples respectively during ageing treatment. In addition, the morphology and size of α precipitates are quite similar. It confirms that different solution treatment conditions did not cause any changes in the volume fraction, morphology and size of α precipitates. This indicates that solution treatment conditions only affect the beta grain size. The only variable in these groups which would influence mechanical properties is grain size.

3.2.3 Tensile testing

Three tensile tests from each group were performed. Tensile tests of PREP 0.08% C Ti-5553 samples with different grain sizes (46, 100 and 168 μm) were performed as described in Chapter 2. The data and results are given in Fig. 26 and Table 10 respectively. From each group, only one tensile curve indicating the relationship between strength and elongation is shown in Fig. 26,while average results are shown in Table 10. Results show that the three groups' had similar average values of ultimate tensile strength (UTS) around 1350 MPa. Similarly, values of $\sigma_{0.2\%}$ (YS) are all about 1333MPa. This is because the same ageing treatment condition results in the almost the same microstructural features of α phase precipitation within equiaxed β grains. For β Ti alloys, this fine internal precipitation of α phase plays a significant role in influencing the strength of the alloy [3]. It has been found that for β-CEZ increasing the size of α_s caused the strength to drop. Furthermore,

same ageing condition can heat treat specimens into similar strength level. It has also been found that grain size has no effect on strength from the present testing results. This phenomenon was also found in β-CEZ by Peters et al. And it could be illustrated that β-Ti alloys were hardened by incoherent particles (e.g. α_s in Ti-5553 alloy) rather than grains [97].

However, the values of ductility show a different trend. Samples with the smallest grain size of 46 μm had a higher ductility (about 6.7% elongation) compared to the other two groups samples with larger grain size. As grain size increases to 100 μm, the average value of ductility drops slightly to 6.3%. When the grain size increases up to 168 μm, the average value of elongation decreased to 1.9% (Table 10). This phenomenon is because of larger grain size meaning longer grain boundary length (longer slip length) which can result in losing ductility (from 6.7% dropping to 1.9%).

These results show that for PREP 0.08% C Ti-5553 alloy, the grain size has limited effect on strength when the grain size range is between 46 μm~168 μm. But larger grain size can impact on ductility. It is possible to tailor microstructure to obtain alloy having both good strength and ductility. In high strength β-Ti alloys, dislocation pile-ups occurring at grain boundary triple points causes local stress concentration. Crack nucleation starts from the triple point at grain boundary. The slip length can be seen as the distance between two triple points. Some studies have found that the relationship between ductility and grain boundary length D (grain size) can be illustrated as true fracture strain $\varepsilon_F \sim D^{-1}$. It further explains why samples with 46 μm grain size has a higher ductility.

3.2.4 Fracture toughness testing

3.2.4.1 Experimental results

Fracture toughness tests were carried out at room temperature. Each group had 3 specimens to be tested. Firstly, fatigue-precracking was done using an Amsler Vibrophore fatigue testing machine. Secondly, the displacement of opening mouth of the specimen is caused by a loading force resulting in crack extension.

The loading force and crack opening displacement are recorded for further data analysis determining F_Q (particular value of F) as shown in Fig. 27. These three curves are selected from each group specimens (46 μm, 100 μm and 168 μm). All curves show a linear relationship between force and displacement at the loading stage. Then the curves become non-linearity during the plastic deformation and stable crack extension regime. Before the determination of K_Q, particular force F_Q needs to be defined. Firstly, a line fitted to the curve in the elastic deformation part and noted as OA. Thereafter a line, noted as OF_d with a slope 5% less than line OA is drawn in the same graph (see Fig. 27). A force F_d is determined by the interaction between curve and OF_d. All tests curve in this project are confirmed to type III record referring to British Standard [103]. Therefore, F_Q is equal to F_d. As F_{max}/F_Q is less than 1.10, the K_Q calculation is accorded to equation in chapter 2.5.3.Values of K_Q which is a provisional value of K_{Ic} (plane strain fracture toughness) was calculated firstly. And these K_Q-values need to be verified before regarding as K_{Ic}.

The results of the fracture toughness as a function of grain size are given in Table 9 and Fig. 28. With increasing grain size from 46 μm to 100 μm, a very slightly increase in fracture toughness occurred from 33.6 MPa $\cdot m^{0.5}$ to 33.9 Pa $\cdot m^{0.5}$ which is unlikely to be significant. When grain

size was treated to a larger level (168 μm), K_{Ic}-value increased up to 37.2 MPa $\cdot m^{0.5}$. As in microstructural observation section, the only difference among these specimens is the grain size, which is the only variable can influence the fracture toughness.

3.2.4.2 Fractographic observation and analysis

3.2.4.2.1 Fracture surface under OM

Fig. 29 shows fractographs of three groups' specimens under OM. The bright area is pre-cracking area which is smooth and reflects more lights. The dark area was formed by fracture toughness testing which has a rougher surface. From (a) to (c), under the same magnification, it is clear that grain size is increasing because larger facets can be seen in (c).

3.2.4.2.2 Fracture surface under SEM

Fig. 26 shows fractographs of PREP 0.08% samples with different grain size. (a), (b) and (c) are low magnification images of the transition area between the fatigue pre-crack and stable crack extension presenting different morphology among these samples. Fig. 26 (e), (f) and (g) are high magnification images on selected areas of (a), (b) and (c). Both intergranular and transgranular fracture are found in Fig. 26 (a), (b) and (c). As the crack grew from the fatigue pre-crack into stable extension, most fracture was transgranular. The crack propagation routes are through grains. These cracks propagates further until reaching grain boundaries. Some of them then choose soft grain boundary areas to propagate as indicated by black circles on the figures. In high magnification images, it can be seen that facets formed by intergranular crack growth are smooth while transgranular facets are rough. Fig. 26 (c) shows a larger transgranular area. This is because this

specimen has the largest grain size and therefore the crack has to go through a larger area or a longer distance to encounter contiguous grains compared to other two groups specimens.

Fractographs of stable crack extension areas of these samples are shown in Fig. 31. From Fig. 31 (a) to (c), fracture surfaces of the three groups of samples with different grain sizes are displayed. From these images, it can be seen that the grain size has little impact on fracture path. They all show mixed fracture including both intergranular and transgranular fracture. It appears that intergranular fracture results in more smooth facet than transgranular fracture, which can be used for to identify crack path method.

To give more proof to identify the crack propagation path, some observations have been carried out. Cross sections of specimens with different grain size were prepared for microstructure observation. Samples were cut following line A-A in Fig. 32 for cross section observation. Samples were mounted, polished and etched well as described in Chapter 2. SEM images were taken to investigate crack propagation paths. These cross-sectional images were merged into one image which could cover a large area. Merged images are shown in Fig. 33, covering the stable extension regions.

In each image the position where the fatigue pre-crack ends is indicated and the crack growth direction is from left to right. Fig. 33 (a) shows the cross section of a sample with a 46 μm grain size. It can be seen that most of the crack path is transgranular, passing through β matrix grains, leaving quite a smooth path. Very little of the crack path is intergranular fracture as marked by the white circle. During the whole process, the crack path stayed close to the mode I direction with very little deviation.

An interpretation of crack propagation through beta grains is shown in Fig. 34. During the ageing step, large amounts of α_s precipitated inside β grains which become obstacles in front of the crack tip. The length scale of these α_s platelets is about a fraction of one micro metre, which means they are too small to deform plastically or fracture. As the crack enters the grain, it easily breaks up the β matrix rather than the α_s. It is difficult to deform fine α_s, therefore, the crack passes around the fine α_s and continues to propagate within the grain. Fig. 38 illustrates how a crack can propagate between adjacent grains. The crack has two options, one is passing through the β matrix, the other is going along the grain boundary. Most crack paths select the first option in a sample with 46 μm grain size. This phenomenon is shown in Fig. 35 (a). Regions of transgranular fracture are marked by blue arrows and intergranular fracture paths are marked by white arrows. As a whole, the crack propagating direction is parallel to the precracking direction. Even though a small deflection occurred because of the fine α_s during the progress, it returns back to the overall direction.

The cross-sectional images of samples which have grain size of 100 μm and 168 μm are shown in Fig. 33 (b) and (c). Compared to the sample with a grain size of the 46 μm, 100 μm sample has a more fluctuating crack path, which has more intergranular fracture. Because of the increase in grain size, the crack has a longer propagation length and have a rougher fracture surface. Some of crack front began to go along low-angle grain boundaries indicating intergranular fracture, as shown in high magnification image (Fig. 35 (b)), where mixture fracture paths are marked.

It has to be mentioned that one carbide was found at a grain boundary marked by white circle in Fig. 23. A similar precipitated carbide is also observed in Fig. 36 (a). The volume fraction of

carbides is much larger than that of α_s, but is a similar effect on the crack. Crack tip can not break the carbide, therefore it passes around it and regarding it as a larger α_s precipitate.

Fig. 33 (c) is a cross-sectional image of a sample with 168 μm grain size which has the highest K_{Ic}-values. Fig. 35 (c) is a higher magnification image of rectangular area C in Fig. 33 (c). It is located in the stable extension region but very close to the left side pre-cracking area. The transgranular crack shows a very strong trend of intergranular fracture as it encounters the first grain boundary. Due to the high angle path, it failed to grow further along the grain boundary leaving behind a small crack and back to the intragranular path.

Fig. 33 (b) and (c) shows similar cross-sectional features indicating a mixed fracture path. Therefore, 3D confocal microscopy was used to determine any differences between these two kinds of samples as shown in Fig. 40 (b) and (c). Unlike the 2D images in Fig. 33 (b) and (c), Fig. 40 (b) and (c) taken by 3D confocal microscopy, give more details globally. After comparing their fracture morphology, the 168 μm grain size sample has more fluctuation during crack propagation. It has a more concave-convex fracture surface.

Fig. 36 shows higher magnification images at Fig. 33 (c), showing transgranular and intergranular regions of the sample with 168 μm grain size. Fig. 36 (a) is a transgranular area, where the crack cut into the next adjacent grain and passed through it. In this region the crack passed precipitated carbide particles as indicated by white circles. They do not appear to have any effect on the transgranular propagation. The mechanism of transgranular fracture is illustrated in Fig. 37. Fig. 36 (b) shows a region of intergranular fracture path as indicated by white arrows. Under high magnification, the breaking-up of grain boundary is clearly seen. As the crack coming from the left

side reaches point A, it takes a low angle path relating to the main crack direction (from left to right) and then goes along the next grain boundary. After reaching point B, intergranular fracture becomes transgranular fracture. The mechanism of crack growth in the material with a grain size of 168 μm can be explained in Fig. 38. Both intergranular and transgranular cracking occur during crack propagation. In the range of grain size between 46 μm and 100 μm, the crack went through the first grain as transgranular fracture. As the crack front encountered grain boundary of next grain, the crack deflected into going along a grain boundary. Compared to other samples with smaller grain size, more transgranular fracture occurred in larger grain size samples. This observation is also confirmed by low magnification cross-sectional images Fig. 33 (c).

Fracture surfaces (see Fig. 39) observed under SEM, give more details at the mechanism. At high magnification, it can be seen that fracture occurred by microvoid coalescence (Fig. 39). Fine dimples are clearly seen in all three SEM images. Fracture mechanisms of all three types of specimen show ductile fracture. The scale of dimples of the three different samples are very similar. Besides, some particles are pointed within dimples. These particles are believed to fine α_s-phase whose strength is higher than contiguous matrix. Therefore, when the crack encounters high strength α_s as it propagates through grains, microvoids may initiate between α_s-phase and β matrix. The interpretation of crack propagation when it encounters a strong α_s-phase is shown in Fig. 34.

3.2.4.2.3 Confocal analysis

Aiming to investigate the fracture surface of samples quantitatively, 3-D scanning confocal microscopy has been used. Using the feature, only seeing images at one depth level each time, it

can provide surface profiles of fracture surfaces. Combining with previous results, more accurate analysis can be done. 3D images (1280 μm × 960 μm) of fracture surface of PREP 0.08 % C samples with different grain sizes (46 μm, 100 μm and 168μm) are displayed in Fig. 40. These three selected areas are all from the stable extension area which dominates the fracture toughness and the direction of each crack propagation is indicated by white arrow.

The software allows the fracture surface to be presented using various colours. One plane is marked as zero or the base plane. Planes above and below it are represented by depth of white and green colour. The fluctuation of topography can be displayed well by this technology.

Simply comparing these three images Fig. 40 (a), (b) and (c) together, Fig. 40 (a) belonging to 46 μm grain size sample has the smoothest fracture surface. As grain size increases, the fracture surface becomes rougher as shown in Fig. 40 (b) and (c). Most fracture in the 46 μm grain size sample propagated through grains. The small amount of intergranular crack path did not cause much crack deflection because of its small scale of grain size. As a result, all these parameters finally indicate a relatively smooth fracture surface. Using 3D confocal, it can be clearly seen that the increase in grain size result of in different fluctuant fracture surfaces. For the 100 μm grain size sample, intergranular cracking began to show a different fracture morphology. Some deep hollows appear on the surface. At a grain size of 100 μm, within this region, the crack has a rougher propagation path. There is more intergranular fracture going along grain boundaries and crack propagating planes are farther away from the base plane than those in the sample with a grain size of 46 μm. The largest grain size among these three groups is shown in Fig. 40 (c). It can be seen that more area shows up as intergranular fracture. Restricting fracture is the result of crack going

along grain boundaries. It can be seen as grains taken off leaving 'holes' behind. Therefore, large-scale of 'holes' represent that intergranular fracture occurred here.

3.3 Summary

Combined with fracture results, it is clear that the largest grain size sample has the highest K_{Ic}-value. But the effect of grain size on fracture toughness depends on the grain size range. As the grain size between 46 μm and 100 μm, this effect is not very clear. But as grain size goes up to 168 μm, it began play an important role in influencing fracture roughness. For smaller grain sizes, the intergranular fracture is not the dominant mode. The geometrical contribution is not the most important influence. When larger grain size obtained, the influence of grain size begins to become more important.

It also indicates that intergranular fracture is good to fracture toughness in this chapter. More intergranular cracking occurred in specimens with a larger grain size which have higher fracture toughness values.

4 Effects of grain boundary α via STA heat treatment route on mechanical properties of Ti-5553 alloy

It has been pointed that crack tip blunting effects occurring at grain boundaries could benefit fracture toughness, K_{Ic}-value. That suggest that appropriate morphology of grain boundary α (by tailoring the microstructure) could offer a good balance between strength and fracture toughness. Therefore, in this chapter, the aim is to investigate the influence of grain boundary α in Ti-5553 alloy on fracture toughness.

4.1 Experimental methods

4.1.1 Material

In this part, two kinds of material were used. One was PREP NC (non-carbon additional) Ti-5553 alloy, the other was PREP C Ti-5553 with addition of 0.08% C (PREP C).

These two kinds of material were chosen because small addition of carbon would result in less coarse α phase forming at grain boundaries which was found in a previous study [76]. For undoped PREP Ti-5553 alloy (PREP NC), there was coarse α precipitating along grain boundaries, which shows quite a different morphology.

As discussed in Chapter 1, fracture toughness can be influenced by several factors including an intrinsic contribution and a geometrical contribution. The geometrical contribution is about the crack front profile affecting the crack propagation path.

The other contribution is the intrinsic contribution which is about difference in strength between the matrix and the precipitated α phase. In this chapter, doped and undoped Ti-5553 alloy are heat treated to the same strength level eliminating the intrinsic contribution.

Under the same strength condition, only the morphology of grain boundary alpha is likely to play a key role of affecting crack propagation, and therefore influence fracture toughness.

4.1.2 Heat treatment processes

Before heat treatment the specimens were wrapped in Fe-foil to prevent oxidation, as described in detail in Chapter 2. In chapter 3, the influence of grain size was investigated and found that as grain size was increased above a certain size, fracture toughness (K_{Ic} values) was improved. Therefore, the test pieces must be heat treated such that the grain size was the same throughout. In Chapter 3, the effect of grain size on mechanical properties for PREP C Ti-5553 alloy and heat treatment conditions corresponding to different grain size have been recorded. For PREP NC Ti-5553 samples, it was necessary to find the effect of heat treatment on grain size. The processing schedule for Ti-5553 alloy is briefly shown in Fig. 41. Samples were solutionized at T1 temperature which is above the beta transus. Different solution treatment temperature T1 and time can tailor beta grain size.

Heat treatments of PREP C Ti-5553 alloy detailed in Chapter 2 are shown in Table 7. Solution heat treatment used for PREP NC Ti-5553 alloy is shown in Table 12. PREP C specimen has a grain size of 168 μm and PREP NC specimen has a grain size of 169 μm were selected to do the

mechanical tests. After obtaining the required grain size the next target is to determine the appropriate ageing conditions. Two kinds of specimens need to be aged to same strength level to meet design requirement. Details in ageing treatment conditions are shown in Table 13 and Table 14. Ageing heat treatment was conducted at 600 and 650℃ for 6 h.

4.1.3 Microstructure Observation

Details were introduced in Chapter 2.

4.1.4 Mechanical Properties

Aiming to studying the influence of grain boundary alpha on mechanical properties, a series of mechanical testing would be carried out. It includes hardness, tensile and fracture toughness tests.

4.1.4.1 Hardness Testing

After the same grain size was obtained through adjusting solution treatment, the same strength was tried to get using different ageing conditions. Hardness testing was used in experiments, as it was used to estimate the strength level of specimens. After ageing treatment, hardness values were measured. Hardness can be used to predict the strength. Various heat treatment routes lead to different strength levels and specimens with required strength were selected for further investigation.

4.1.4.2 Tensile Testing

After gaining hardness results, those conditions which matched the design strength were used for tensile testing. Tensile testing was done following the British standard. YS and UTS values of specimens can provide useful information for investigating the influence of grain boundary morphology on fracture toughness.

4.1.4.3 Fracture Toughness Testing

Fracture toughness testing is the most important part in this project. PREP C and PREP NC Ti-5553 specimens were tested separately according to British standard. Comparing K_{Ic}-values to study the influence of grain boundary morphology on fracture toughness is the key.

Observation on fracture surfaces is helpful to understand the mechanism of fracture. Fracture mode and crack propagation path are useful to understand the effect of grain boundary morphology on fracture toughness. Qualitative and quantitative comparisons were conducted.

4.2 Results and Discussion

4.2.1 Microstructures

In order to achieve the purpose of this chapter, the effect of grain size on mechanical properties need to be removed. Hence the same grain size of both PREP C and NC Ti-5553 was obtained through a series of tries.

Based on results in chapter 3, specimens following different heat treatment conditions, as shown in Table 10, obtain various grain size such as 46， 100, 142 and 168 μm. In the beginning, PREP NC was heat treated at 900℃ for 1h followed by WQ. Grain size measurement was conducted using imageJ software.

OM images of two kinds of specimens are displayed in Fig. 42 and Fig. 43. Fig. 42 shows microstructure of PREP C Ti-5553 sample which was solution treated at 1050℃ for 4 h. This specimen has a grain size of 168 μm. Fig. 43 show the microstructure of PREP NC Ti-5553 sample which has a grain size of 169 μm. These two grain size samples (168 μm PREP C sample and 169 μm PREP NC sample) match experimental design quite well. Therefore, these two heat treatment condition were selected for further tests.

During the solution treatment, samples were held above the β/α transus for long enough period and followed by water quenched to room temperature. This means that β phase was retained after quenching as shown in their OM images.

Besides pictures taken by optical microscopy, SEM images can provide more information on how microstructure affects fracture toughness. Attention is focused on samples after ageing treatment. Fig. 44 shows different grain boundary microstructural morphology of PREP C Ti-5553 specimen after solution and ageing treatment. The ageing treatment was chosen depending on hardness results. PREP C specimen was aged at 650℃ for 6h and PREP NC specimen was aged at 600 ℃ for 6h. Three types of grain boundaries were observed under SEM microscopy. The first type is displayed as a continuous alpha layer in Fig. 44 (a). Secondly, discontinuous alpha layer is shown in Fig. 44 (b). Thirdly, a carbide pinning at grain boundary alpha layer junction was found in Fig.

44 (c). These grain boundary alpha with different morphology has no effect on precipitation of α_s. Either intergranular α_s and intragranular α_s has the same microstructure and morphology.

PREP NC presents two kinds of grain boundary. One is covered with continuous alpha layer shown in Fig. 45 (a), the other is not as shown in Fig. 45 (b). Compared to PREP C, precipitation of α phase along grain boundary shows different morphological features. Very fine and tiny scale α forms adjacent to grain boundaries, in contrast to the intragranular α phase precipitating within prior β grains. In interior of β grains far away from the grain boundary, α_s phase is present as a triangle shape basket-weave microstructure which is much coarser.

Fig. 46 shows the microstructure in the interior of both PREP C and NC samples. Both two materials have similar internal grain microstructures. Small scale precipitation of α phase distributes uniformly. In order to describe the difference quantitatively, ImageJ software was used to measure the length and width of α phase of PREP C and NC samples. Attention was paid to the length of α phase. The distribution of α phase is displayed in histograms in Fig. 47 and Fig. 49. In PREP C Ti-5553 samples, most α length distributes between 0.2 μm and 0.8 μm accounting for 87.5%. The remaining 12.5% α phase length-size is a bit larger. For PREP NC Ti-5553 samples, the largest amount (61.4%) of intragranular α has a length located between 0.5 μm and 1.0 μm. The second largest group (27.7%) has length between 1.0 μm and 1.5 μm. Other small groups are at the left or right side in the histogram as shown in Fig. 49.

In terms of width, histograms are shown in Fig. 48 and Fig. 50. In PREP C Ti-5553 alloy, the largest group has width distributed between 0.10 μm and 0.20 μm taking over 84.3%. Other α phase with width smaller than 0.10 μm or larger than 0.20 μm in total occupy 15.7%. For PREP

NC samples, most α phase (about 65.3%) has width between 0.075 μm and 0.125 μm. About 23.2% α phase has width is larger than 0.15 μm. Small-width-size alpha taking over 11.6% has size smaller than 0.075 μm.

Considering both width and length of intragranular α phase, PREP NC Ti-5553 has larger α phase. In general, the length and thickness of α_s phase would influence the strength. But strength is affected by several features. A proper balance can obtain the desired strength level.

According to previous chapter, it is noted that geometrical contribution plays an important role on influencing fracture toughness in Ti-5553 alloy.

How these differences affected fracture toughness will be discussed below.

4.2.2 Hardness testing

It is known that hardness testing is a simple method to estimate strength of a material. It provides a material-saving method which is necessary in this project. A very small piece of sample can be used this estimation. During the tries process, approximately estimating was finished. After ageing process confirmed, investigation moved to next stage.

In my previous work, the relationship between yield stress and Vickers hardness of Ti-5553 alloy has been found. It shows a linear relationship which can be expressed by the equation:

$$\sigma_{0.2}=5.367x-984.1608$$

Where $\sigma_{0.2}$ is the value of yield stress; x is the value of Vickers hardness [105]. Considering the difference of material and testing equipment, there might be some errors in this equation. But it still has some significance.

The first tries started with PREP C sample. The sample was solution treated at 1050℃ for 4 h and was aged at 650℃ for 6 h. As shown in

Table 13, it has a Vickers hardness value of 411.6 HV. Using the above equation, the tensile strength should be around 1300 MPa.1300MPa was selected as the target yield stress for PREP NC. Solution treated samples were aged at 600 and 650℃ for 6 h achieving hardness values of 413.1 and 379.1 HV respectively. The sample heat treated at 900℃ 1h, WQ, and aged at 600℃ 6h processed the closest hardness value (413.1 HV) to that of PREP C Ti-5553 sample (411.6 HV) (see Table 13). Therefore, bulk specimens of these two materials were heat treated using these selected processes for further testing and observation.

4.2.3 Tensile testing

The tensile test results are shown in Table 14. Each group had 3 specimens to be tested. Two materials, PREP C Ti-5553 and PREP NC Ti-5553, both have very similar grain size. As mentioned in hardness tries, they were intended to be processed to the same hardness level which means their strength values were expected to be similar. Tensile testing results show that quite similar values were obtained. For PREP C Ti-5553 sample, the YS was 1337±1.4 MPa and the UTS was 1348±3.5 MPa. The YS and UTS of PREP NC Ti-5553 alloy are 1302±0.7 and 1349±1.4

repectively. Although they have similar strength values, the elongation values are different (1.9±0.3% and 3.1±0.2%). PREP NC Ti-5553 has better elongation. Stress-strain curves for PREP C and PREP NC Ti-5553 samples are shown in Fig. 51 and Fig. 52.

4.2.4 Fracture toughness testing

4.2.4.1 Experimental results

The main purpose of this chapter is to investigate the influence of grain boundary alpha on fracture toughness. Up to now, samples of PREP C and PREP NC Ti-5553 with almost the same grain size and tensile strength have been produced after many heat treatment tries. Fracture toughness testing was carried out at room temperature. Each group had 4 specimens to be tested. Fracture toughness results are listed in Table 15. PREP C Ti-5553 sample has a K_{Ic}-value of 37.2±1.69 MPa· $m^{\frac{1}{2}}$ which is 13.7% lower than that of PREP NC Ti-5553 sample whose K_{Ic}-value reached 42.3±1.32 MPa· $m^{\frac{1}{2}}$. As the materials have the same grain size and almost same UTS around 1350MPa, this improvement of fracture toughness must be on account of microstructural features.

4.2.4.2 Fractographic observation and analysis

Observation started from the transition area where a distinguishing line between the pre-crack area and crack stable extension was. Fig. 53 and Fig. 54 give details of the stable extension areas near the transition line in PREP 0.08% C and PREP NC Ti-5553 alloys repectively. To comparing these two pictures, the proportion of transgranular and intergranular modes as the crack entered into crack stable extension specimen was calculated.

As shown in Fig. 53, it is noted that in PREP C Ti-5553 specimen almost all the area across the transition zone indicates transgranular fracture mode. Transgranular fracture occurred starting from the pre-crack into stable crack extension occupying 72.3% area in this picture.

In PREP NC Ti-5553 specimen (Fig. 54), as the crack propagated into the specimen from the transition line, it transferred from transgranular to intergranular fracture very quickly. As the crack propagation process continued, most of cracks were intergranular. The smooth facets in Fig. 54 indicates that the crack follows breaking grain boundaries. Some of those smooth intergranular fracture have been circled. It can be seen that intergranular fracture takes up most of area in this picture. By quantitative analysis, only 28.9% of the area was formed by transgranular fracture. Compared to PREP C Ti-5553 alloy having an almost 100% transgranular area (Fig. 61), this confirms that the morphology of α phase forming at grain boundaries really affects the fracture path of Ti-5553 alloy.

In Fig. 55, a higher magnification image showing more details of the fracture surface of PREP C Ti-5553. It can be seen that the crack breaks into the specimen as transgranular fracture. Those transgranular fracture facets were marked with black polygons. The formation process of flat facets is illustrated in Fig. 34. As the crack starts to propagate, it grows into the β matrix going along its direction rather than along the grain boundary. When crack propagates in the interior of β grains, small scaled intragranular α_s (~1 μm) can't reroute the crack path. These small fluctuations do not dominate the propagation direction. Overall, flat transgranular facets are left behind on the fracture surface.

The rest of the crack in Fig. 55, went along breaking-up grain boundary. This phenomenon can be explained as some grain boundary area being softer than the β matrix, making the energy required to split adjacent grains lowering than that required split β matrix. Therefore, the crack propagation path is shown schematically in Fig. 56. The crack comes from the left, encounters the first grain boundary, prefers a less tortuous crack path with less angled deflection. A full intergranular crack propagation path is shown in Fig. 56.

Fractographic images in Fig. 53 and magnified selected-area image in Fig. 55 in PREP C Ti-5553 specimen shows a mixed fracture path indicating both inter- and transgranular path, but transgranular fracture dominates.

In order to understand the fracture mechanism of PREP C Ti-5553 alloy, more high magnification images are needed. As shown in Fig. 57, large-scaled dimples are observed in the circled area and small particles are left inside the dimples indicated by white arrows. These features are formed due to tiny α_s phase distributed in the β matrix. Small and tiny α_s is unlikely to fracture. The crack must go around the α_s as illustrated in Fig. 58. The blue ellipses represents α_s phase. As crack approaches the particles there is interfacial failure between the α_s and the surrounding β matrix. Those microvoids grow and coalesce until adjacent microvoids linking together. This process is illustrated in Fig. 58.

The area outside of the white circle in Fig. 57 requires a higher magnification to show a clearer image. Fig. 59 is taken under this requirement and indicates more detail of the transgranular fracture surface. A mixture of large scale and small scale microvoids is distributed on the surface. The large

microvoids are deep and some contains small particles inside. While small microvoids is much shallower.

Fig. 60 shows a high magnification image of PREP NC Ti-5553 specimen at the precrack to stable extension transition area where the transition line can be clearly seen. Both intergranular and transgranular fracture occurred in this area. As discussed with Fig. 54 above intergranular fracture played a dominant role in PREP NC Ti-5553 specimen. It is seen that transgranular went into grains within a short distance and transferred into intergranular fracture. Fig. 60 shows a lot of differences compared to Fig. 55. In PREP NC Ti-5553, fracture is more intergranular than transgranular.

Fig. 62 shows a large area of stable crack extension on the fracture surface indicating more features in PREP NC Ti-5553 specimen. This stable extension surface consists of intergranular and transgranular fracture. Smooth facets show intergranular fracture occurred. Other rough areas indicate transgranular fracture. A few secondary crack can also be seen as shown in Fig. 63. Under low magnification, it appears that there is nothing on the intergranular facets. Using high magnification, shallow dimples are found on the facets (Fig. 64).

4.2.4.3 Comparing fracture features

It has been confirmed that transgranular fracture occurred in both types of specimens. To investigate the fracture mechanism, higher magnification observation is required. Transgranular fracture surfaces are shown in Fig. 65 comparing fracture mechanism. Fig. 65 (a) is a transgranular facet in PREP C Ti-5553 alloy. It shows microvoids coalescence. It consists of coarse microvoids and they are surrounded by fine microvoids. It is noticed that some large microvoids embodying globular particles inside.

In Fig. 65 (b) a transgranular area in PREP NC Ti-5553 alloy is shown. It displays a very similar fracture morphology to PREP C Ti-5553 specimen. It shows microvoid coalescence mode as well. Difference size dimples are distributed on the transgranular fracture surface.

After comparing Fig. 65 (a) and (b), it indicates that PREP C and NC specimens have very similar dimple size.

The other fracture mode, intergranular fracture, is shown in Fig. 66. Fig. 66 (a) is a selected area under high magnification in PREP C Ti-5553 specimen and (b) is from PREP NC Ti-5553 alloy. On these intergranular facets, unlike transgranular facets, only shallow dimples are observed. Therefore, compared to transgranular facets, intergranular facets are much smoother. The differences between these two fracture modes resulting in different fracture surface features are illustrated in Fig. 34 and Fig. 56. The rough transgranular fracture facets were formed as the crack went through β matrix and bypassed hard α_s which are difficult to break up. Cracks formed at the interfaces and failure occurred by microvoids coalescence. Microvoids nucleating at interfaces between β matrix and α_s grew and finally broke up specimens.

PREP C Ti-5553 alloy has a very sharply delineated grain boundary microstructure along either continuous or discontinuous α layers as shown in Fig. 44. There is no prominent different microstructural α phase at grain boundary areas. PREP NC Ti-5553 specimen has a quite different morphology of α-laths at grain boundary as shown in Fig. 45. Coarse and large α-laths from grain boundaries into the grains. Taking all intergranular fracture into consideration, intergranular fracture occurred at weak grain boundaries as shown in Fig. 56. Adjacent grains are spilt separately leaving smooth facets.

Fracture features on both kinds of PREP Ti-5553 alloys are similar including shallow dimples. But the area between adjacent facets where grain boundary layers broke up appears different. These areas are marked as A and B in Fig. 66 (a) and (b). Area A in PREP C Ti-5553 alloy contains shallow dimples where microvoids initiated at the interface between grain boundary α layer and surrounding β matrix resulting in specimen rupture. The dimples size and morphology is same as those on intergranular facets. In Fig. 66 (b), area B in PREP NC Ti-5553 contains coarser and larger dimples which is different to the shallow dimples on adjacent facets. This phenomenon could be explained by the precipitation of α-laths at grain boundaries. These large-scale α phase ruptured leaving microvoids behind.

4.2.4.4 Crack path observation

Fig. 67 illustrates cross-sectional images of two kinds of PREP C and NC Ti-5553 samples. More details on crack propagation can be observed from these images. The direction of crack propagation is from left to right. Generally speaking, from these two images, they both indicate a mixed fracture path including transgranular and intergranular fracture. Two blue lines mark the upper and lower position of the crack path. The height intercept in Fig. 67 (a) is 368.6 μm and (b) has a height intercept value of 571.4 μm. In some degree, a larger height intercept could indicate how tortuous the crack path is. Combining with fracture toughness data, PREP NC Ti-5553 specimen having a higher K_{Ic}-value (42.3±1.32 MPa· $m^{\frac{1}{2}}$) than PREP C Ti-5553 specimen (37.2±1.69 MPa· $m^{\frac{1}{2}}$). As the cross-sectional image is from one of the infinite slices on fracture surface, it can only provide some reference meaning. It can be seen that a mixture of transgranular and intergranular fracture occurred on both side-face images. Combined with fracture surface images (Fig. 61 and Fig. 62),

it provides more evidence on this results. It is also seen that there is more transgranular fracture than intergranular in PREP C Ti-5553 specimen. The result in PREP NC Ti-5553 alloy is the reverse of this. In some respect, intergranular fracture plays a dominant role in benefiting fracture toughness.

4.2.4.5 Confocal analysis

Advanced technology confocal microscopy was used to obtain 3D fracture surface images giving more details on crack fluctuation. Experimental result images are shown in Fig. 68. Fig. 68 (a) is fracture surface in PREP C Ti-5553 specimen. The colour depth of white and green represents the facet Z-axial position. Fig. 68 (b) shows the fracture surface of PREP NC Ti-5553 alloy. In this image, green colour indicating the position is near Z=0 plane. Blue colour means that area is above the Z=0 plane. Red colour means that area is below than green colour plane. The deeper colour means much more fluctuation.

Results from analysis software show the Z-axial range of Fig. 68 (a) and (b) are 240 μm and 446 μm due to different amplification factor, x5 in (a) and x10 in (b).

From Fig. 68 (a), it can be seen that both intergranular and transgranular fracture facets existing on this fracture surface. The large green and white areas indicate transgranular area. The interfaces between white and green areas result from intergranular fracture. In totally, transgranular areas are flat facets. This phenomenon is shown in Fig. 69. For instance, the crack went along grain boundary at the first grain and cut through the next few grains, then went along the last grain boundary.

In Fig. 68 (b), multi-colours appear on the fracture surface. A mixed fracture including transgranular and intergranular is found. Blue and red colour distributed on the fracture surface indicate many fluctuations occurring. Compared to large transgranular facets in PREP C Ti-5553 specimen, many more fluctuations represent small-scale facets. More fluctuations requires more energy during crack propagation bringing a better fracture toughness of specimens. The mechanism of crack growth in PREP NC Ti-5553 alloy is explained in Fig. 70. As seen in this figure, the crack encountered a grain boundary and went along grain boundaries between adjacent grains, marked as region A and C in Fig. 70. While in region B, transgranular cracking occurred. Combined A, B and C together, it gives the whole fracture surface morphology.

4.3 Summary

The morphology of grain boundary alpha precipitates was found to be different in PREP 0.08% C and PREP NC Ti-5553 have different precipitating morphology of grain boundary alpha. There is no alpha lath precipitating at grain boundary in PREP 0.08% C Ti-5553 specimen. In contrast, alpha lath growing from grain boundary into interior grains was observed in PREP NC Ti-5553 specimen.

Fracture toughness tests revealed that PREP NC Ti-5553 specimens has a higher K_{Ic} value (42.3 MPa· $m^{\frac{1}{2}}$) comparing to PREP 0.08% C specimen (37.2 MPa· $m^{\frac{1}{2}}$) which has the same grain size and the same strength level. Difference was found in the fracture mechanisms in these two microstructures, as more intergranular fracture was found in PREP NC Ti-5553 sample compared to PREP 0.08% C sample. This suggests that intergranular fracture mode is beneficial to toughness property in this alloy.

5 Effects of shell-like microstructure via SQA heat treatment route on mechanical properties of Ti-5553 alloy

Even though HIP processing brings benefits such as homogeneous microstructure and low material wastage, the existing boundaries between prior beta grains which are regarded as not good for mechanical properties such as fracture toughness. It has been found that intergranular fracture is good to fracture toughness. In this project, the aim is to produce more intergranular occurred and actions were taken into heat treatment process. Manipulating temperature and time in each step of heat treatment can obtain an optimized microstructure. Designing a shell-like microstructure which is like a solid ball having a hard core covered by soft shell. Soft shell would be preferred by crack propagation presenting as more intergranular fracture and lead to distortion of crack growth which could improve fracture toughness.

A shell like microstructure was produced by step quenching and ageing (SQA) by Nag et al [38, 39]. In this chapter, the aim is to control the precipitation of α_p producing a shell like microstructure along grain boundary regions. To achieve this goal, a lot of heat treatments were conducted as tries. Samples heat treated using selected conditions were used for following mechanical properties testing and compared to a solution treatment and aged (STA) condition. How the shell-like microstructure (α_p laths) influences the mechanical properties will be investigated.

5.1 Experimental methods

5.1.1 Material

Undoped PREP Ti-5553 alloy was used to study the shell-like microstructure (α_p) obtained by SQA processing on mechanical properties.

5.1.2 Heat treatment processes

There are two types of heat treatment processes used in this chapter. They are SQA and STA processes. The furnace used in heat treatment has been introduced in chapter 2. Similarly, Fe-foil covering samples aims to preventing oxygen contamination.

5.1.2.1 Step quenching and aged (SQA) processing schedule

The SQA processing schedule is shown in Fig. 71. Unlike the STA processing schedule as shown in Fig. 72, a T_Q temperature is added between T_1 and T_2. Samples were solution treated at T_1 for a period of time, step quenched to T_Q and held for a short time. Then, samples were water quenched to room temperature and aged at T_2. Holding samples at T_Q can lead to the formation of α_p at grain boundaries in preference to intragranular α_p. To accomplish the SQ procedure, samples were moved from a furnace at T_1 into a second furnace at T_Q directly. PREP samples were heat treated by various conditions used to obtain a desired shell-like microstructure. Some of them are listed in Table 16.

After tries on these SQ conditions, SQ1 and SQ5 were selected to do further study. Because they got the more intergranular and coarser α_p. Samples were aged at 600℃ to 640 ℃ with an interval of 20℃ for 4 or 5 h respectively. Details on SQA processes are tabulated in Table 18.

Vickers hardness testing was used for each heat treatment tries. Samples with Vickers hardness reaching the required values were used for further mechanical properties testing.

5.1.2.2 Solution treating and aged (STA) processing schedules.

Aiming to study the influence of the shell-like microstructure, a microstructure without soft α_p along β grain boundaries, was used as a reference. Samples were heat treated using STA processing routes as shown in Fig. 72 and Table 19. Compared to SQA processing schedule, the process of STA is quite simple. Inter-holding temperature (T_Q) is removed during the process. Undoped PREP Ti-5553 samples are solution treated at T_1 temperature above the beta transus and water quenched. Then, samples are aged at T_2 and water quenched to obtain the final microstructure.

5.1.3 Microstructure observation

Microstructure observation plays a very important role in this chapter. The purpose of this chapter is to study the effect of shell-microstructure on mechanical properties and design a microstructure which can benefit fracture toughness. For instance, samples with specific microstructures (through SQ processes) will be selected depending on its microstructure observed under SEM. Moreover,

fractographic observation including intergranular α_p and intergranular α_p is also conducted under SEM. Besides, orientation of grains along crack growth path is analysed using EBSD.

In other ways, hardness indentation patterns are seen under OM which is used to analyse the effect of shell-like microstructure on hardness/ strength.

5.1.4 Hardness testing

In experiments, a series of tries were done to get good strength and the desired microstructures. It is unwise to machine each for tensile testing. Vickers hardness was used to estimate tensile strength.

As mentioned in chapter 2 experimental methods, tensile strength can be easily estimated by the division of HV by 0.33. This equation helps to pick out samples processed by both STA and SQA which were heat treated to designed strength range quickly. Precise values of YS and UTS would be measured in further investigation.

In this chapter, hardness values of samples heat treated by different conditions were measured to compare their tensile strength easily and choose samples to do further investigation.

Besides, comparing hardness values between intergranular α_p-laths (grain boundaries regions) and intragranular α_s inside β grains is a useful method to study the effect of shell-like microstructure on strength.

5.1.5 Image processing methods

In this chapter, software ImageJ and Adobe Photoshop are widely used. ImageJ provides a number of functions such as length, perimeter and area which are used to measure features of α and β phases. Another major application of ImageJ is to measure volume fraction of precipitation of α phase.

Adobe Photoshop is a powerful image processing tool, but it is only used to adjust brightness/ contrast and combine images together.

More details on this two software were introduced in previous chapter.

5.1.6 Tensile testing

Strength of samples were designed according to hardness value using 3 times relationship [101]. They can be used for selection of proper heat treatment methods. Therefore, tensile test is applied to obtain specific values of samples.

To reduce test error from experimental equipment and parameters, all specimens were machined into the same dimensions according the standard and all tests were conducted using the same machine. Parameters of the experiment were set the same values. More details are referred to Chapter 2 experimental methods.

5.1.7 Fracture toughness testing

Experimental procedures were introduced in Chapter 2.

5.1.8 Fracture surface analysis

Fracture surface analysis is conducted using a Confocal Laser Scanning Microscope OLS 3000. Using this microscope it is possible to colour 3D observations and some values revealing fracture surface features such as roughness. Calculation of roughness is useful to study the influence of different microstructures leading to various fracture surface on mechanical properties (fracture toughness).

5.2 Results and discussion

5.2.1 Microstructures

5.2.1.1 Different shell-like microstructures obtained by various SQ processes

Aiming to get samples with the desired shell-like microstructures, various heat treatment conditions were applied to undoped Ti-5553 samples. Fig. 73 shows an SEM image of a step-quenched sample which was solution treated at 900℃ for 1 h, step quenched and held at 650℃ for 40 min. From the image, it can be seen that both intergranular and intragranular α_p precipitated during this processing. In other previous work [38, 39], it has been pointed that the temperature range of step-quenching can influence the precipitation of alpha phase especially in the aspect of distribution. Therefore, in the next experiments, the holding temperature was adjusted to 680℃ and same

holding time. Microstructure is shown in Fig. 74. Using the same solution treatment conditions, SQ sample held at 680℃ condition leads to more α_p forming at grain boundary areas. Compared with the sample held at 650℃ shown in Fig. 73, the sample held at 680℃ (Fig. 74) has more α_p precipitating along grain boundaries. In order to form more and larger intergranular α_p, the holding time was extended to 1 h. Fig. 75 shows the precipitation of α_p along grain boundaries grew larger as expected. Meanwhile, the α_p forming with beta grains also grew into large scale. Attentions were moved to solution treatment temperature. A higher temperature of 1000℃ was selected to do further tries. A samples solution treated at 1000℃ for 1h, step quenched to 680℃ and held for 40 min is shown in Fig. 76. It is clearly found that very little precipitation of intragranular α_p occurred. Most α_p prefers to form at grain boundaries areas. To obtain larger α laths around grain boundaries, a longer holding time was given. Finally, the desired shell-like microstructure is shown in Fig. 77. Through these tries, two heat treated conditions, 900℃ 1h, SQ, 650℃ 40 min, WQ (Fig. 73) and 1000℃ 1h, SQ, 680℃ 1h (Fig. 77) were chosen for further investigation.

5.2.1.2 Comparisons of two selected shell-like microstructures obtained via different SQA processes.

Heat-treated samples step quenched from 900℃ 1h to 650℃ 40 min were then aged at 600℃ for 4 h. Using SEM microscopy, as shown in Fig. 78, the resulting structure mainly consists of coarse α_p-laths along β grain boundaries and fine basketweave α_s in β grains. Fig. 78 (a) is a low magnification image of this sample. Higher magnification images in Fig. 78 (b) and (c) show

different morphology of alpha phases in β grain boundaries areas. In Fig. 78 (b) and (c), some finer α_s precipitating adjacent to α_p phase is marked by white arrows. It also has been found that α_p-laths forming at discontinuous grain boundary alpha layer grow into β grains, marked by red arrows, as shown in Fig. 78 (b). There is no precipitation on the continuous grain boundary alpha layer, marked by blue arrows, as shown in Fig. 78 (c). Fig. 78 (d) is a higher magnification image of the sample showing fine α_s precipitating in the β grains.

Undoped Ti-5553 alloy samples were step quenched from 1000℃ 1 h to 680℃ for 1 h and then aged at 640℃ for 5h. A typical microstructure is shown in Fig. 79 and Fig. 80. Similar to the microstructures shown in Fig. 78, most coarse α_p-laths preferred to precipitate at grain boundaries. A higher magnification image (Fig. 80 (a)) shows that these lath-like alpha phases could only form at discontinuous β grain boundaries. Using this step quenched condition leads to more α_p forming as intergranular type. At the same time, only few intragranular α_p appears in β grains, marked by white arrows. α_s forming during ageing treatment is finer in length and thickness than those α_p at grain boundaries area as shown in Fig. 79 and Fig. 80.

It has been observed that the step quenching method can result in much coarser α_p forming shell-like microstructures along β grain boundaries. The dimensions of these α_p-laths are measured using image analysis ImageJ software. Table 20 contains measurement results of two SQA samples (900℃ 1h, SQ, 650℃ 40 min, WQ, 600℃ 4h and 1000℃ 1h, SQ, 680℃ 1h, WQ, 640℃ 5h). As shown in this table, the length of intergranular α_p is 7.24$\pm$1.50 μm longer than that of intragranular

α_s (2.06$\pm$1.02 μm) in the sample heat treated via SQA1 process. The intergranular α_p is thicker than intragranular α_s (0.30 $\pm$0.06 μm vs. 0.09$\pm$0.03 μm). The same phenomenon has also been observed in sample heat treated via SQA4. SQA4, step-quenching from 1000℃ to 680℃ leads to a larger length difference between intergranular α_p and intragranular α_s (16.6$\pm$6.78 μm vs. 2.18$\pm$0.99 μm). In terms of thickness, either intergranular α_p or intragranular α_s grew, but it did not increase as large as length did.

5.2.1.3 Beta annealed microstructures obtained via STA process

Fig. 81 shows undoped Ti-5553 with solution treatment at 900℃ for 1h and water quenching.

Fig. 81 shows that only beta is observed. The morphology of the grain boundaries is quite different from samples treated through SQ processing. There is no α phase forming along grain boundaries. These is only continuous α layer existing on the beta grain boundary.

The second step for STA processing is ageing quenched specimens at different selected ageing temperatures 600℃ and 650℃. Specimens were held at the ageing temperature for 6 h and then water quenched to room temperature. Unlike SQA specimens, there are no intergranular α laths at grain boundaries. SEM images are shown in Fig. 82 and Fig. 83. In these SEM images, (a) is at low magnification of x4000 showing areas both at grain boundaries and the interior of grains and (b) is at high magnification of x10000 showing grain boundary area. Compared to Fig. 79, it is clear that specimens treated using STA processing have cleaner grain boundaries. Fine α_s precipitation distributed uniformly inside the β grains. These α phases were all forming in the

ageing step. Because, the solution treatment was followed by water quenching no coarse α phases formed.

In addition, different ageing temperature also influences the length/size of α phase. After quantitatively measurement, the results are listed in Table 20. The results indicates that higher ageing temperature results in larger size of α. α phase in STA2 specimen has an average length of 1.21±0.49 μm which is larger than that in STA1 specimen (0.73±0.30 μm).

5.2.2 Hardness testing

5.2.2.1 Selection of samples heat treated by STA for further investigation

Samples processed by STA are designed as a reference. Two different heat treatment processes were applied to undoped Ti-5553 alloy as listed in Table 19. After that, hardness and strength were measured respectively. The value of Vickers hardness of sample STA1 is 413.1±3.75 HV which is higher than that of sample STA2 (379.1±4.80 HV). The estimated tensile strength values of samples, STA1 and STA2, is around 1150 MPa to 1200 MPa. Values of UTS of sample STA1 and STA2 are in accordance with designed UTS. These two samples were selected to do further study.

5.2.2.2 Selection of samples heat treated by SQA for further investigation

As mentioned before, samples processed by SQA need to be heat treated to a similar strength level around 1200 MPa or Vickers hardness level about 410 HV.

Conducting various tries on heat treatments based on experiences adjusting temperature and time leads to different hardness values as shown in Table 22 and Fig. 84. Sample SQA1 (900°C 1 h, SQ,

650℃ 40 min, WQ, and 600℃ 4 h, WQ) with a hardness value of 410 has an estimated tensile strength of around 1230 MPa. Another sample SQA6 (1000℃ 1 h, SQ, 680℃ 1h, WQ, and 640℃ 5 h, WQ) with a hardness value of 367.4 has an estimated strength of about 1100 MPa. Comparing these specimens with STA specimens with similar strength would give out details on the effect of the shell-like microstructure on fracture toughness. Hence these two samples are chosen to study the influence of shell-like microstructure on fracture toughness in the strength range between 1100 MPa and 1230 MPa.

It also has been found that Vickers hardness/ tensile strength of samples are predominately affected by ageing conditions rather than holding conditions during step quench process. The trend between ageing temperature and hardness is clear that increasing ageing temperature from 600℃ to 660℃ decreases values of Vickers hardness from 401.5 HV to 352.5 HV. This phenomenon is consistent with that occurring in samples processed by STA.

5.2.2.3 Comparison of different strength at grain boundary area and interior area of shell-like microstructure in SQA samples

Any difference between mechanical properties at the grain boundary region and the interior of the grain is considered in this section with micro hardness. The indenter was positioned at a grain boundary area and inside β grains. Examples are given in Fig. 85. In Fig. 85 (a) an indentation is left on the α_p-laths and (b) the indentation is on the finer α_s. Valid results are obtained as listed in Table 23. These results are the average of 20 tests. The average Vickers hardness on intergranular α_p at grain boundary areas is 378 ± 15 HV which is lower than that (413 ± 11) on intragranular α_s within β grains. This means that shell-like microstructure creates a soft region along grain

boundaries. In the other words, the core of the grains is harder. This feature is expected to affect the crack propagation path which can absorb more energy during fracture toughness testing.

5.2.3 Tensile testing

Tensile tests were carried out at room temperature to assess tensile strength accurately of undoped Ti-5553 alloy specimens treated using different heat treatment routes (STA1, STA2, SQA1 and SQA6). Each group has 3 specimens to be tested. The yield stress, tensile strength and elongation are listed in Table 24 and Fig. 86. Even though, different quenching methods used for two types of heat treatment processes (SQA and STA), the tensile properties are mainly associated with ageing conditions. Similar strength results were obtained by similar ageing conditions.

These results meet expectations. The yield stress of these four groups of specimens are located at around 1150 MPa and 1200 MPa. And the corresponding UTS values are around 1200 MPa and 1270 MPa.

5.2.4 Fracture toughness

5.2.4.1 Experimental results

Fracture toughness of specimens (STA1, STA2, SQA1 and SQA6) were tested at room temperature. Results are shown in Table 26. At first, K_Q values were calculated. The value of factor $2.5\times(K_Q/\mathrm{YS})^2$ was obtained and compared to validity criteria. The results meet all requirements and K_Q were recorded as K_{Ic}.

As mentioned in experiments design, specimens treated through STA and SQA were expected to be heat treated into two groups with similar strength level. Yield stress and K_Q values are put into one scatter diagram in Fig. 87.

It can be seen in Fig. 87, data points locate at both ends. At a relatively lower strength level, the specimens processed via STA have a lower fracture toughness values than those processed via SQA process. While, at higher strength level, the right side of the cross point (1145, 59), the SQA produces brings a better fracture toughness. Based on this diagram, as the yield stress increases, the difference in fracture becomes larger. The yield stress is around 1145 MPa with a rough K_{Ic} value of 59 MPa· $m^{\frac{1}{2}}$. In the literature review, some research has pointed that the fracture toughness values should decrease with increasing strength. However, SQA1 specimen with a higher YS and also has a better fracture toughness compared to STA1 specimen.

5.2.4.2 Fractographic observation and analysis

In terms of the improvement in fracture toughness by SQA route, investigation on its influence on fracture mechanism were carried out in this chapter. Attentions were paid on those specimens at relatively higher strength level. Comparison was executed between SQA1 and STA1 on fracture surface.

5.2.4.2.1 Fracture surface under OM

OM images from SQA1 and STA1 specimens are displayed in Fig. 88 and Fig. 89. The lighter region in the upper part of the image is the pre-cracking area and dark lower region is the crack extension area. Under the optical microscope, it is no apparent difference between these two specimens.

5.2.4.2.2 Fracture surface under SEM

In Fig. 90, two specimens' fracture surface image taken by SEM at low magnification are displayed. Fig. 90 (a) shows specimen processed through the STA route and (b) is processed through the SQA route. The dark area on left side of end image is pre-cracking area and the light area is the crack extension area. On the whole, they both show a mixture of fracture modes including intergranular and transgranular. But intergranular fracture dominates, and the whole fractography of crack extension area is rough.

Fig. 91 (a) is selected area on fracture surface from STA1 specimen, showing the morphology. These smooth facets are intergranular areas. The other relatively rough areas are transgranular. The intergranular fracture occurred at grain boundaries, splitting the adjacent grains. The microstructure of STA specimens has been shown in Fig. 82. Like other β titanium alloys, a continuous α layer precipitates at grain boundaries forming a soft area adjacent to it. These soft grain boundaries form an easy path way for crack propagation. Fig. 91 (b) show a higher magnification image focusing on intergranular facets, which are very flat and smooth. The morphology of a transgranular area is

displayed in Fig. 92. Unlike the intergranular area, it failed by microvoids coalescence (MVC). These really fine voids can be seen clearly in the image.

SEM observation of SQA specimens are shown in Fig. 93. As intergranular fracture occurred, the profile of the grains can be seen. In SQA specimens, two types of morphology of intergranular facets were found. As shown in Fig. 93 (a) and (b), lath-like patterns were found on the facet surfaces. But on some other facets, there are no patterns as shown in Fig. 93 (c).

Combined with microstructure of SQA specimens (see Fig. 77), this phenomenon can be explained. Thanks to the SQA heat treatment route, the morphology of α precipitation at grain boundaries area shows distinguishing features. One type of boundary is covered with coarse α_p, and the other type of grain boundary has no precipitation at all as shown in Fig. 78. As the crack grows inside the specimen, adjacent grains were broken up along boundaries forming these patterns, which absorbed more energy compared to smooth facets in STA specimens, improving the fracture toughness.

Fig. 94 shows the details of the morphology of transgranular area. The morphology of this area is similar for both specimens via SQA and STA, showing very fine microvoids and some coarse dimples. Transgranular fracture occurred when the crack cut through a β grain matrix. The initiation of the crack is at the α_s/β interfaces. Due to similar ageing conditions, the size and volume fractions of α_s are almost same.

5.2.4.2.3 Crack path observation

Fig. 95 shows cross sectional regions of specimens treated via STA and SQA routes. Fig. 95 provides more evidence that proves the fracture in these two types of specimens are a mixture of

intergranular and transgranular. The percentage of intergranular cracking is very similar in these two specimens. The next two images in Fig. 96 and Fig. 97 were taken at higher magnification. For the STA1 specimen (Fig. 96), the intergranular crack path is very smooth along the grain boundary. However for SQA1 specimen (Fig. 97), the crack deviated at the interface of coarse α/β matrix, indicating a different morphology. This can be used to explain, why specimens via SQA routes have better fracture toughness. More energy was consumed as the intergranular path propagates presenting a more tortuous pathway.

5.2.4.2.4 Confocal analysis

The last technique used to investigate these two types of heat treatment routes is confocal scanning laser microscope. In Fig. 99, fracture surfaces of these two specimens very similar. Roughness values were calculated by software giving a comparison quantitatively. The average roughness value of STA1 specimen is 28.7 μm and that value of SQA1 specimen is 32.5 μm. This provides more evidence that SQA routes can result in a rougher fracture surface.

5.3 Summary

By investigating the relationship between microstructure and mechanical properties in STA and SQA specimens, it has been found that specimens treated via SQA had higher K_{Ic} values than those of specimens treated via STA (45.2 to 42.3 MPa· $m^{\frac{1}{2}}$ and 60 to 56.7 MPa· $m^{\frac{1}{2}}$) at the same stress levels.

The shell-like microstructure formed by SQA heat treatment routes is beneficial to fracture toughness, due to the rougher crack pathway.

In this shell-like microstructures, the micro hardness results show that grain boundary areas having a hardness value of 378 HV are softer than that of the interior grain areas (413 HV). Therefore, crack propagation preferred to go along grain boundaries.

6 The influence of microstructures obtained via beta annealed with subsequent slow cooling and ageing (BASCA) heat treatment route

In the previous chapters, different microstructures of PREP NC Ti-5553 alloy have been produced due to various heat treatment methods. A very common heat treatment method used in industry is a beta annealed with subsequent slow cooling and ageing (BASCA) heat treatment. This involves a solution treatment above the beta transus temperature for a period to obtain single β phase, and furnace cooling (FC) to the required ageing temperature and holding for ageing. In a previous study, this beta annealed with subsequent slow cooling and ageing process is believed to optimize fracture toughness [106]. These two heat-treatment routes are shown in Fig. 100 and Fig. 101 respectively. The aim of this chapter is to design a BASCA process that produces a microstructure which can be compared with the SQA treated samples. The effect of microstructure on mechanical properties (especially fracture toughness) is considered.

The design plan is heat treating specimen using different methods into similar strength level and then doing fracture toughness testing. Therefore, only PREP NC Ti-5553 alloy was selected to do the experiments. Using only one kind material could reduce the impact factors from raw materials.

6.1 Experimental methods

6.1.1 Heat treatment processes

In this chapter, aiming to comparing the influence of two kinds of heat treatment methods, SQA and BASCA, on fracture toughness. Heat treatment processes similar to previous chapters, oxidation prevention procedure is necessary during heat treatment. How to do oxidation prevention has been described in previous chapters.

In this part, two heat treatment furnaces are required. One is used for solution treatment and furnace cooling (FC) to the required ageing temperature. After this, the specimen was transferred solutionized specimen into an ageing furnace and held for a period. This complex procedure is used to achieve Processing schedule applied in this process is shown in Fig. 101.

A treatment schedule is required to obtain a similar strength level in PREP NC Ti-5553 alloy as that achieved in PREP NC Ti-5553 alloy by SQA6. As shown in chapter 3, the grain size within a certain range affects fracture toughness. In order to eliminate the influence of this factor, the same solution treatment process as that used in the SQA process, 1000 ℃ for 1hr was chosen. Temperature T2 then had to be selected to give the required strength.

The heat treatments used in these tries are given in Table 26. In total, four groups of specimens were heat treated. Specimens BASCA1 and BASCA2 were solution treated at 1000℃ for 1 h and then FC to 600℃ and 640℃ respectively followed by immediate WQ to observe the solution treated microstructure. BASCA3 and BASCA4 were aged at 600, 640℃ repectively for 5 h aiming to obtain the required strength.

The influence of several factors (i.e. grain size, grain boundary alpha, interior alpha and shell-like microstructure) on fracture toughness have been investigated in previous chapters and reviewed. Based on current results, the designed shell-like microstructure obtained via SQA route is the most beneficial to fracture toughness. The influence of either STA or SQA has been studied. The last route, BASCA, will be tested in this chapter and used to compare with specimens treated via the SQA route.

In order to compare the different influences of BASCA and SQA6 heat treatment methods, reference specimens group using SQA6 heat treatment method was tabulated in Table 27 and Fig. 100. All experimental results including microstructure and mechanical properties have been obtained in previous chapter. Along with SQA schedule (Fig. 100), specimen was solutionized at 1000℃ for 1 h, and transferred into 680℃ furnace holding for 1 h, then water quenched. The ageing condition is 640℃ 5 h. The only difference between BASCA and SQA6 is the intermediate-holding process between solution treatment and ageing treatment in the SQA6 process.

The temperature vs. time data during furnace cooling process from 1000℃ to 600℃ was recorded and is shown in Fig. 102. It shows an approximately linear relationship between temperature and time. The slope is -1.96 and intercept is 947. The cooling rate is about 117.6℃/min.

6.1.2 Microstructure Observation

Details on operating steps of these equipment have been introduced in chapter experimental methods.

6.1.3 Mechanical Properties

6.1.3.1 Hardness Testing

As in previous chapters, hardness testing was the first step during mechanical property tests. As the hardness values of reference group SQA6 specimen is about 370 HV, the target hardness-value of BASCA processed specimens is around this value 370 HV.

6.1.3.2 Tensile Testing

After the heat treatment procedure had been chosen, tensile tests were performed. Each group had 3 specimens to be tested.

6.1.3.3 Fracture toughness

Through fracture toughness results, how this BASCA process influence the fracture toughness can be explained. The detailed process of fracture toughness testing has been introduced referred to chapter experimental methods.

Each group had four specimens to be tested.

6.2 Results and Discussion

6.2.1 Hardness testing

The required Vickers harness value is around 370 HV equivalent to a tensile strength of roughly 1200 MPa strength. Therefore, the aiming hardness value of BASCA processed specimen is 370 HV. The hardness results are tabulated in Table 30. BASCA3 produces a hardness value of 382 ± 19

which is close to targeted hardness value. For the BASCA4 specimen, the hardness value is lower than the expected level. Hence, the heat treatment condition of BASCA3 specimen was selected for further testing.

During the hardness testing process, optical images were taken of indentation patterns by OM of BASCA3 and BASCA4 specimens, shown in Fig. 103. Dimensions of indentation pattern left on the specimen surface were measured and recorded as Diagonal 1 and 2. Combined with loading force (300 g in both testing), the Vickers hardness values could be obtained.

6.2.2 Microstructure observation

In section 6.2.1, based on hardness results it was decided that BASCA3 was the heat treatment that would be used for mechanical property testing. Therefore, microstructures of BASCA3 were observed under SEM.

A specimen was FC to 600℃ and then water quenched to room temperature in order to obtain the microstructure formed through the first step. Fig. 104 shows the microstructure from this heat treatment route. The microstructures consists of a dark β matrix and bright α precipitation. Three types of α phases can be seen, grain boundary α, intergranular α and intragranular α. Fig. 105 shows a higher magnification image of grain boundary areas in Fig. 104. Fig. 105 (a) and (b) indicate different morphology of intergranular α. One type is coarse intergranular α growing from the grain boundary into the interior of the grains, arraying uniformly. The other is intergranular α scattered along the grain boundary.

The size of these two types of α_p (i.e. Fig. 105) was measured. They will be referred to as large inter-α_p (Fig. 105 a) and small inter-α_p (Fig. 105 b) respectively. Results are recorded in Table 28. Large- and small-α_p have lengths of 12.91$\pm$2.70 μm and 2.73$\pm$1.13 μm respectively.

Ageing according to treatment BASCA3 (600℃ 5hr, see Table 26) resulted in the microstructure shown in Fig. 106. Fine basketweave α_s precipitated in the β matrix. The size and thickness scales are smaller than those of α_p.

6.2.3 Tensile Testing

Results of tensile test are shown in Table 30. The strain/stress curve are drawn in Fig. 107 and Fig. 108. The BASCA3 specimen has a UTS value of 1133.5 MPa with elongation of 7.5%. The UTS value of SQA6 specimen is 1202 MPa with elongation of 6.2%. As mentioned above, the target strength is around 1200 MPa. So far, this attempt was completed. It confirms the heat treatment processes are proper. It has to be mentioned that the final strength level of BASCA3 specimen is lower than that of SQA6, even though their hardness results showed the reverse trend. But considering these are average results, it was accepted. The reason why BASCA3 specimen has lower strength is likely to be the longer cooling time and slower cooling range from 1000℃ to 600℃, which precipitated a greater volume fraction of α_p. Hence less α_s could be precipitated to contribute to strength.

Stress/strain curves in Fig. 107 and Fig. 108 give more details of the tensile testing. It can be seen that three BASCA specimens show three different values of elongation. While the strength of

SQA6 specimens are unitive. This is also likely to be related to heterogeneous precipitation of α phase.

6.2.4 Fracture toughness testing

6.2.4.1 Experimental results

After testing, all results were found to be valid to be recorded as K_{Ic}. Results are listed in Table 31. The four specimens tested had K_{Ic}-values of 65.2 MPa· $m^{\frac{1}{2}}$, 63.7 MPa· $m^{\frac{1}{2}}$, 60.3 MPa· $m^{\frac{1}{2}}$ and 65.8 MPa· $m^{\frac{1}{2}}$. The average value is 63.8$\pm$2.47 MPa· $m^{\frac{1}{2}}$.

In order to compare the BASCA route and SQ route affecting on fracture toughness, related results were put into a scatter diagram in Fig. 110. The BASCA3 condition appears to have a slightly higher toughness than the SQA6 condition, 63.8 vs. 60.05 MPa· $m^{\frac{1}{2}}$. However, if the trend of fracture toughness with yield stress found for SQA material, shown in Fig. 109, is considered, the toughness of BASCA3 condition might be lower than expected.

6.2.4.2 Fractographic observation and analysis

6.2.4.2.1 Fracture surface under OM

The fracture surface of a BASCA3 specimen was observed under OM and is shown in Fig. 110. The surface is very similar to the SQA specimens, compared with Fig. 89.

6.2.4.2.2 Fracture surface under SEM

A low magnification SEM image of the fracture surface from a BASCA3 specimen is shown in Fig. 111. The fracture process consists of both intergranular and transgranular fracture.

Some intergranular facets have lath-like patterns, while others do not. This phenomenon was also found in SQA specimens. It is because of their similar shell-like microstructure. However for SQA specimens as shown in Fig. 77 in Chapter 5, there are two types of grain boundaries, one is decorated the other is not. In BASCA3 specimens (Fig. 104), almost every boundary is decorated with alpha phase. The difference is the amount of precipitation. As in selected area in Fig. 111 shown in Fig. 112, this facet is all covered with lath-like pattern. Others may only be covered with parts of patterns.

6.2.4.2.3 Crack path observation

In Fig. 113, the crack propagation path is displayed. The direction of crack propagation is from left to right. The features of a mixture of intergranular and transgranular fracture can be clearly seen. Intergranular fracture dominates the crack growth.

In order to see how the crack pathway changes, higher magnification images were taken as shown in Fig. 114. In Fig. 114 (a), the crack path stage A is zigzag, propagating along the coarse α_p. At stage B, the crack path is smooth, growing along the grain boundary. This difference is because of the uneven distribution of these coarse α_p, which has been pointed out in Fig. 104. Fig. 114 (b) and (c) are another two examples.

6.2.4.2.4 Confocal analysis

Fig. 115 is an image taken by confocal scanning laser microscopy. The different colour represent different heights on the fracture surface. The fluctuation of this specimen is large. Its corresponding roughness value is about 65.2 μm. This image provides more evidence of the intergranular fracture that occurred in the BASCA3 specimen.

6.3 Summary

The BASCA3 specimen has the highest fracture toughness value (63.8 MPa· $m^{\frac{1}{2}}$) during this whole investigation. This result shows that the BASCA heat treatment route could lead to a relatively rough surface mainly via intergranular fracture mode.

The morphology on the intergranular fracture facets vary depending on how the grain boundary is decorated by coarse α_p which was precipitated during the furnace cooling stage. This type of decoration on grain boundaries leads to a more tortuous crack path, and a rougher fracture surface. As the crack propagates, these coarse alpha phase play act as obstacles. The crack has to bypass these coarse phases. This bypass action results in rough facets formed by intergranular fracture.

7 Discussion

The effect of grain size on the toughness properties and fracture behaviour of the PREP Ti-5553 alloy has been demonstrated at the same strength range around 1350 MPa. The results in section 3.1.6 suggest larger grain size can increase K_{Ic} value. But such as an influence is only pronounced in a certain range of grain size. Result indicate that grain size reaching 168 μm brings 10% improve on fracture toughness property. All three specimens were heat treated at the same ageing condition and have very similar morphology of α_s. Only difference is grain size, which can affect the fracture toughness. This phenomenon coincides with research mentioned in section 1.8.2.2. But it is lacking in more tests to identify the exactly range of grain size which can affect fracture toughness.

Fractographs of the fractured specimens have in specimens has shown that all fracture contains both transgranular and intergranular. While, the alloy with a larger grain size (168 μm) has more intergranular fracture mode and thus more crack reflection. It has been pointed out that crack reflection can absorb more energy during crack propagation [3]. This explains why intergranular fracture benefits the high fracture toughness value. Also, confocal 3D fractographic image shows that specimen with the larger grain size (168 μm) has a rougher fracture surface than the other two (46 μm and 100μm), due to more intergranular fracture mode than flat transgranular fracture. This should be the reason for higher fracture toughness values measured in microstructures with larger grain sizes.

The different alpha morphologies of grain boundary in the alloys with same grain size specimens (PREP 0.08% C and PREP NC Ti-5553 alloys) also showed different K_{Ic} values as listed in

Table 16. K_{Ic} value of PREP NC Ti-5553 is 13.7% higher than that of PREP 0.08% C Ti-5553 specimen. The effect of grain size and strength in this investigation has been eliminated. The microstructural observation indicates that the different morphology and size of alpha phases at grain boundary area could result in such difference. This influence is still on the fracture mechanism as shown in SEM fractographic images (Fig. 53 and Fig. 54) that more transgranular fracture occurred (72.3%) in PREP 0.08% Ti-5553 specimen than that (28.9%) in PREP NC Ti-5553 specimen. It is suggested that larger inter-alpha phase can result in more intergranular fracture occurred and is good to toughness property. Crack path observation (Fig. 67) and confocal 3D images (Fig. 68) can confirm this speculation. PREP NC Ti-5553 specimen has more fluctuation during crack propagation and its fracture surface is rougher than the other's. Besides, the existence of alpha phase forming at grain boundaries can lead to more intergranular fracture.

Based on these results, chapter 5 aimed to design a shell-like microstructure through SQA heat treatment route. This SQA procedure produced a microstructure with coarse inter-alpha phase around grain boundary and fine intra-alpha laths in the interior of beta grains. The following fracture toughness results (as shown in Fig. 86 and Fig. 87) shows that this shell-like microstructure has positive influence on fracture toughness. Especially in high strength condition, this shell-like microstructure can bring better toughness property. Hardness testing results indicate that the

intergranular alpha phase has a lower hardness value of 378±15 HV than that (413±11 HV) of intragranular alpha lath. This means hard core (inside grain) is covered by soft shell and the strength at grain boundary is lower than that inside grain. In addition, high magnification cross-sectional image (Fig. 97) shows that crack grows along these large and coarse inter-alpha phase at the grain boundary which causes more crack deflections in the SQA1 specimen. On the other hand, crack grows smoothly along the grain boundary in the STA1 specimen (Fig. 96). The interpretation of crack propagation in SQA specimen is shown in Fig. 98. Because of the influence of coarse alpha plates at grain boundary, crack path has more chances to bypass them rather than directly along straight grain boundary.

Results show that BASCA3 specimen has a K_{Ic} value of 63.8 MPa· $m^{\frac{1}{2}}$ with and a strength of 1056 MPa. Because strength of SQA specimen is higher than 1138 MPa, they cannot be compared together directly. Fig. 109 shows that SQA specimens may have a better toughness at the same strength level according to the extrapolation to the strength of 1060 MPa. Further tests in BASCA with different strength is needed to confirm such a speculation. Microstructural observation between BASCA and SQA specimens indicates that the different decoration at grain boundary affects the toughness properties. Either coarse or fine alpha plates forms at grain boundary area as shown in Fig. 105. It is different to the microstructure in SQA specimen in Fig. 79, the precipitation of coarser alpha plates. This difference leads to crack path with both bypass alpha plates and along grain boundary. During the crack growth, BASCA specimens have less reflection and tortuous path than SQA specimens.

8 Conclusions and future work

8.1 Conclusions

1. Results show that higher temperature and longer holding times can increase beta grain size in PREP C Ti-5553. After solution treatment at 900℃ 1h, 1000℃ 1h, 1050℃ 1h and 1050℃ 4h and followed by water quenching, the grain sizes of specimens are 46, 100, 142 and 168 μm. Using the same ageing condition, specimens treated through different solution treatment can achieve the same strength level. The effect of grain size on fracture toughness is depending on the grain size range. When the grain size grows from 46 to 100 μm, it has no obvious effect on fracture toughness. As it goes up to 168 μm, there is an increase in K_{Ic} of 10.7% from 33.6 to 37.2 MPa· $m^{\frac{1}{2}}$. Larger grain size produces more intergranular cracking, resulting better fracture toughness.
2. As PREP C and PREP NC Ti-5553 specimens having the same grain size were treated into the same strength level, PREP NC specimens have a higher fracture toughness value compared to that of PREP C specimen (42.3 vs. 37.2 MPa· $m^{\frac{1}{2}}$). The grain boundaries of PREP NC specimen are decorated with α-laths phases, which makes more intergranular fracture occurred during crack propagation and PREP C specimen do not have. Hence, more intergranular cracking was observed on the fracture surface in PREP NC specimen. This proves that intergranular cracking can improve fracture toughness.

3. It suggests that the shell-like microstructure at grain boundaries is good to fracture toughness. Using SQA heat treatment route, coarse α_p preferably precipitates at grain boundary area. This microstructure can increase fracture toughness values (60 vs. 56.7 MPa· $m^{\frac{1}{2}}$ and 45.2 to 42.3 MPa · $m^{\frac{1}{2}}$), compared to specimens without shell-like microstructure. The best shell-like microstructure was obtained through a SQA route of 1000℃ 1h, SQ, 680℃ 1h, WQ, 640℃ 5h. From fractographic observation, SQA specimens have a rougher fracture surface than the STA specimens, which is believed to be the key to improving fracture toughness. The dimension of intergranular α is 0.57×16.6 μm (width×length) which is larger and intragranular α of 0.24 × 2.18 (width×length). Micro hardness testing results indicate that strength at grain boundary areas is lower than that at the interior of grains.
4. Using a BASCA heat treatment, its fracture toughness property is not so good as SQA specimens. And the size and distribution of α_p via the BASCA route does not form a complete shell-like structures around grains.

8.2 Future work

1. In the whole project, the strength range considered was between 1040 MPa to 1240 MPa, which is a very narrow range. Trends of different specimens fitted by two points is not enough to express the whole properties of different specimens. Because of limits of material, experiments haven't been done enough. More specimens with different strength level should be tested. Based a large mass of results, the trend can be more convincing. Especially for BASCA

specimens, there is only one dot on scatter diagram. More fracture toughness results from BASCA specimens with higher strength should be tested.

2. Different heat treatment process combinations were used to tailor the microstructures. Theoretically, it has infinite combinations. It is worth to spend more time trying more heat treatment parameters, finding a better combination. For grain size, most specimens have a quite large size of 168 μm which may be harmful to properties. A higher solution treated temperature and shorter holding time are recommended for future work.
3. For the shell-like microstructure, those precipitates of coarse α_p were observed at one-side of grain boundaries. It needs to explain the mechanism of this type of precipitation. Furthermore, areas between coarse α_p are not clearly seen under SEM. Whether other phases formed at that areas also need be investigated. TEM is recommend for future work.

9 References

1. Moll, J.H. and C.F. Yolton, *Production of titanium powder*, in *Metals Handbook, Vol 7, Powder Metal Technologies and Applications*. 1998, ASM. p. 381.

2. Boyer, R., G. Welsch, and E.W. Collings, *Materials Properties Handbook: Titanium Alloys*. 1994, USA: ASM International. Materials Park.

3. Lütjering, G. and J.C. Williams, *Titanium*. 2003, New York: Berlin Heidelberg.

4. Boyer, R.R., *An overview on the use of titanium in the aerospace industry.* Materials Science and Engineering: A, 1996. **213**(1–2): p. 103-114.

5. Kuroda, D., et al., *Design and mechanical properties of new β type titanium alloys for implant materials.* Materials Science and Engineering: A, 1998. **243**(1–2): p. 244-249.

6. Jackson, M., *Microstructural Evolution of Titanium Alloys During Isothermal Subtransus Forging*, in *The Department of Materials*. 2002, Imperial College London.

7. Flower, H.M., *Microstructural development in relation to hot working of titanium alloys.* Materials Science and Technology, 1990. **6**(11): p. 1082-1092.

8. Harper, M.L., *A study of the microstructural and phase evolutions in TIMETAL 555*. 2004, The Ohio State University.

9. Boyer, R.R., *Attributes, characteristics, and applications of titanium and its alloys.* JOM, 2010. **62**(5): p. 21-24.

10. Boyer, R.R. and R.D. Briggs, *The use of β titanium alloys in the aerospace industry.* Journal of Materials Engineering and Performance, 2005. **14**(6): p. 681-685.

11. Rendigs, K.H. *Titanium Products Used at AIRBUS*. in *Ti-2003 science and technology : proceedings of the 10th world conference on titanium*. 2004. CCH-Congress Center, Hamburg, Germany: Wiley VCH.

12. Antoine, G., J. Panter, and M.H. Campagnac. *Application of Ti-10-2-3 in Rotor Hub Parts of EUROCOPTER*. in *Beta Titanium Alloys in the 00's Symposium*. 2005. San Francisco, CA: Annual Meeting of The Materials Society.

13. Froes, F.H. and A.M. Imam, *Cost Affordable Developments in Titanium Technology and Applications*, in *Cost Affordable Titanium III*. 2010. p. 1-11.

14. Porter, D. and K. Easterling, *Phase transformations in metals and alloys, third edition*. 2009: CRC Press.

15. Boyer, R., E.W. Collings, and G. Welsch, *Materials Properties Handbook: Titanium Alloys*. 1994: ASM International.

16. Collings, E.W., *The physical metallurgy of titanium alloys*. 1984, Metals Park, OH: American Society for Metals.

17. *9 - Titanium alloys for aerospace structures and engines*, in *Introduction to Aerospace Materials*, A.P. Mouritz, Editor. 2012, Woodhead Publishing. p. 202-223.

18. Banerjee, S. and P. Mukhopadhyay, *Phase Transformations Examples from Titanium and Zirconium Alloys*. 2007: Elsevier.

19. Aaronson, H.I., et al., *Sympathetic nucleation: an overview.* Materials Science and Engineering: B, 1995. **32**(3): p. 107-123.

20. Fedotov, S.G., *Peculiarities of Changes in Elastic Properties of Titanium Martensite*, in *Titanium Science and Technology*, R.I. Jaffe and H.M. Burte, Editors. 1973, Plenum Press: New York. p. 871-880.

21. Ferrero, J.G., *Candidate materials for high-strength fastener applications in both the aerospace and automotive industries.* Journal of Materials Engineering and Performance, 2005. **14**(6): p. 691-696.

22. Long, M. and H.J. Rack, *Titanium alloys in total joint replacement—a materials science perspective.* Biomaterials, 1998. **19**(18): p. 1621-1639.

23. Frost, F.D., et al., *Isothermal Transformations of Titanium-Chromium Alloys.* Transactions of the American Society for Metals, 1954. **46**.

24. Nag, S., et al., *ω-Assisted nucleation and growth of α precipitates in the Ti–5Al–5Mo–5V–3Cr–0.5Fe β titanium alloy.* Acta Materialia, 2009. **57**(7): p. 2136-2147.

25. Froes, F.H. and T.D. Association, *Titanium Technology: Present Status and Future Trends ; Based on a Collection of Articles ... from the Journal of Metals*. 1985.

26. Tetyukhin, V.V. *Current State of Russian Titanium Industry and VSMPO: Development of New High Strength Alloys for Aircraft and Civil Engineering*. in *Proceedings of 13th Annual Titanium Conference*. 1997. Proceedings of 13th Annual Titanium Conference: ITA.

27. Zeng, L., *High-Strength Titanium Fasteners.* Advanced Materials & Processes, 2006. **164**(12): p. 34.

28. Nyakana, S.L., J.C. Fanning, and R.R. Boyer, *Quick reference guide for β titanium alloys in the 00s.* Journal of Materials Engineering and Performance, 2005. **14**(6): p. 799-811.

29. Jones, N.G., et al., *Thermomechanical processing of Ti–5Al–5Mo–5V–3Cr.* Materials Science and Engineering: A, 2008. **490**(1–2): p. 369-377.

30. Boyer, R.R. and G.W. Kuhlman, *Processing properties relationships of Ti-10V-2Fe-3Al.* Metallurgical Transactions A, 1987. **18**(12): p. 2095-2103.

31. Panter, J., et al. *Influence of Thermo-Mechanical Treatments on Micrstructure and Mechanical Properties of NEar Beta Titanium Alloy VST 55531*. in *Beta Titanium Alloys in the 00's Symposium*. 2005. San Francisco, CA: Annual Meeting of The Materials Society.

32. Orlova, L.M., et al., *Metallographic study of β-solid solution decomposition for titanium alloy VT22.* Metal Science and Heat Treatment, 1986. **28**(1): p. 73-77.

33. Moiseev, V.N., et al., *Heat Treatment of Titanium Alloy VT22.* Metallovedenie i Termicheskaya Obrabotka Metallov, 1990. **3**: p. 46-49.

34. Harper, M.e.a. in *Ti-2003: Science and Technology, Processing. 10th World Conference on Titanium*. 2004. Hamburg, Germany: Wiley-VCH Verlag GmbH & Co. KGaA.

35. Clément, N., A. Lenain, and P.J. Jacques, *Mechanical property optimization via microstructural control of new metastable beta titanium alloys.* JOM, 2007. **59**(1): p. 50-53.

36. Kar, S.K., et al., *Quantitative microstructural characterization of a near beta Ti alloy, Ti-5553 under different processing conditions.* Materials Characterization, 2013. **81**: p. 37-48.

37. Ghosh, A., et al., *Microstructure–fracture toughness correlation in an aircraft structural component alloy Ti–5Al–5V–5Mo–3Cr.* Materials Science and Engineering: A, 2013. **568**(0): p. 61-67.

38. Nag, S., *Influence of Beta Instabilities on the Early Stages of Nucleation and Growth of Alpha in Beta Titanium Alloys*. 2008, The Ohio State University.

39. Nag, S., et al., *Non-classical homogeneous precipitation mediated by compositional fluctuations in titanium alloys.* Acta Materialia, 2012. **60**(18): p. 6247-6256.

40. Kar, S.K., et al., *Quantitative microstructural characterization of a near beta Ti alloy, Ti-5553 under different processing conditions.* Materials Characterization, 2013. **81**(0): p. 37-48.

41. Specification, B.M., *Titanium 5Al-5V-5Mo-3Cr Die Forgings and Bars*. 28 August 2006.

42. Fanning, J., et al., *Heat Treatment, Microstructure and Properties of TIMETAL 555*, in *Ti-2007, Science and Technology: Proceedings of the 11th World Conference on Titanium*, M. Ninomi, et al., Editors. 2007, JIMIC5: Kyoto, Japan. p. 499-502.

43. Divakaran, V.N., G.V.V. Ravi Kumar, and P. Srinivasa Rao. *Landing gear design and development-how advanced technology is helping meet challenges*. 2015 [cited 2015; Available from: http://www.infosys.com/engineering-services/white-papers/Documents/landing-gear-design-and-development.pdf.

44. Kuhn, H.A. and F.R. Dax, *Powder-Metallurgy Product and Process-Development at Concurrent Technologies Corporation.* International journal of powder metallurgy 1996. **32**(3): p. 229.

45. Wu, X. and J. Mei, *Near net shape manufacturing of components using direct laser fabrication technology.* Journal of Material Processing Technology, 2003. **135**: p. 266-270.

46. Jovanović, M.T., et al., *The effect of annealing temperatures and cooling rates on microstructure and mechanical properties of investment cast Ti–6Al–4V alloy.* Materials & Design, 2006. **27**(3): p. 192-199.

47. Rabin, B.H., G.R. Smolik, and G.E. Korth, *Characterization of entrapped gases in rapidly solidified powders.* Materials Science and Engineering, 1990. **A124**: p. 1-7.

48. Fan, J.K., et al., *The interrelationship of fracture toughness and microstructure in a new near β titanium alloy Ti–7Mo–3Nb–3Cr–3Al.* Materials Characterization, 2014. **96**(0): p. 93-99.

49. Kar, S.K., et al., *Processing-microstructure-yield strength correlation in a near β Ti alloy, Ti–5Al–5Mo–5V–3Cr.* Materials Science and Engineering: A, 2014. **610**(0): p. 171-180.

50. Qin, D., et al., *Tensile deformation and fracture of Ti–5Al–5V–5Mo–3Cr–1.5Zr–0.5Fe alloy at room temperature.* Materials Science and Engineering: A, 2013. **587**(0): p. 100-109.

51. Settefrati, A., et al. *Precipitation sequences in beta metastable phase of Ti-5553 alloy during ageing*. in *Proceeding of the 12th World Conference on Titanium (Ti-2011)*. 2012. Beijing: CNCC.

52. WANG, L. and H. SHI, *Powder Metallurgy Technology for High Performance Titanium Alloy.* Aerospace Materials & Technology, 2003. **33**(3): p. 42-44.

53. Duszczyk, J., L.Z. Zhuang, and L. Buekenhout, *Densification of a rapidly solidified nickel aluminide powder-I application of hot-isostatic pressing diagrams.* Journal of Materials Science, 1998. **33**(11): p. 2735-2743.

54. CHEN, J., et al., *Effect of hot isostatic pressing on microstructure and tensile properties of Ti6242 alloy casting.* Heat Treatment of Metals, 2016. **41**(2): p. 94-97.

55. XIANG, M., et al., *Effect of Hot Isostatic Press Process on Microstructure and Properties of PM Ti-6Al-4V Alloy Part.* Titanium Industry Progress, 2017. **34**(4): p. 30-31.

56. Penrice, T.W., *Metals Handbook, Vol 7, Powder Metallurgy, 9th ed.* 1984: American Society for Metals.

57. Meiner, K.E. and J.C. McCall, Metal Powder Report, 1981. **36**: p. 437.

58. Cahn, R.W., P. Haasen, and E.J. Kramer, *Materials Science and Technology*. Processing of Metals and Alloys. Vol. 15. 1991, Weinheim, Germany: VCH Verlagsgesellschaft. 143.

59. Cotton, J.D., et al. *Phase Transformations in Ti-5Al-5Mo-5V-3Cr-0.5Fe*. in *World conference on titanium; Ti-2007 science and technology*. 2007. Sendai, Japan: Japan Institute of Metals.

60. Bania, P. *Beta Titanium Alloys in the 1990's*. in *The Minerals, Metals and Materials Society*. 1993. Warrendale, USA.

61. Jones, N.G., et al., *β Phase decomposition in Ti–5Al–5Mo–5V–3Cr.* Acta Materialia, 2009. **57**(13): p. 3830-3839.

62. Bhattacharjee, A., et al., *Influence of β grain size on tensile behavior and ductile fracture toughness of titanium alloy Ti-10V-2Fe-3Al.* Metallurgical and Materials Transactions A, 2006. **37**(5): p. 1423-1433.

63. Fan, J., et al., *Influence of solution treatment on microstructure and mechanical properties of a near β titanium alloy Ti-7333.* Materials & Design, 2015. **83**: p. 499-507.

64. Kar, S.K., et al., *Processing-microstructure-yield strength correlation in a near β Ti alloy, Ti–5Al–5Mo–5V–3Cr.* Materials Science and Engineering: A, 2014. **610**: p. 171-180.

65. Foltz, J., et al., *Formation of Grain Boundary α in β Ti Alloys: Its Role in Deformation and Fracture Behavior of These Alloys.* Metallurgical and Materials Transactions A, 2011. **42**(3): p. 645-650.

66. Gil, F.J., et al., *Formation of alpha-Widmanstatten structure: effects of grain size and cooling rate on the Widmanstatten morphologies and on the mechanical propertiesin Ti6Al4V alloy.* Journal of Alloys and Compounds, 2001. **329**(1-2): p. 142-152.

67. Ohmori, Y., H. Natsui, and K. Nakai, *Crystallographic Analysis of α Phase Formation in a Metastable β Ti Alloy.* Materials Transactions, JIM, 1998. **39**(1): p. 49-56.

68. van Bohemen, S.M.C., et al., *Nucleation and variant selection of secondary α plates in a β Ti alloy.* Acta Materialia, 2008. **56**(20): p. 5907-5914.

69. Ivasishin, O.M., et al., *Precipitation and recrystallization behavior of beta titanium alloys during continuous heat treatment.* Metallurgical and Materials Transactions A, 2003. **34**(1): p. 147-158.

70. Bruneseaux, F., et al. *In Situ Characterization of the Transformation Sequences of Ti17 Alloy by High Energy X-ray Diffraction: Influence of the Thermal Path*. in *World conference on titanium; Ti-2007 science and technology*. 2007. Sendai, Japan: Japan Institute of Metals.

71. Sanguinetti, R., et al., *Decomposition of β-metastable phase in β-Cez alloy during continuous heating.* Journal de Physique IV, 1993. **03**: p. 517-531.

72. Ohmori, Y., et al., *Effects of ω-phase precipitation on β→α, α'' transformations in a metastable β titanium alloy.* Materials Science and Engineering: A, 2001. **312**(1–2): p. 182-188.

73. Srinivasu, G., et al., *Tensile and fracture toughness of high strength β Titanium alloy, Ti–10V–2Fe–3Al, as a function of rolling and solution treatment temperatures.* Materials & Design, 2013. **47**(0): p. 323-330.

74. Du, Z., et al., *Effect of heat treatment on microstructure and mechanical properties of a new β high strength titanium alloy.* Materials & Design, 2014. **55**: p. 183-190.

75. Jia, W., W. Zeng, and H. Yu, *Effect of aging on the tensile properties and microstructures of a near-alpha titanium alloy.* Materials & Design, 2014. **58**: p. 108-115.

76. Wain, N., et al., *The influence of carbon on precipitation of α in Ti–5Al–5Mo–5V–3Cr.* Materials Science and Engineering: A, 2010. **527**(29–30): p. 7673-7683.

77. Peters, M., G. Lütjering, and G. Ziegler, Z. Metallkd, 1976. **67**: p. 811.

78. Bhattacharjee, A., et al., *Effect of grain size on the tensile behaviour and fracture toughness of Ti-10V-4.5Fe-3Al beta titanium alloy.* Transactions of the Indian Institute of Metals, 2008. **61**(5): p. 399-405.

79. Tamirisakandala, S., et al., *Processing, microstructure, and properties of β titanium alloys modified with boron.* Journal of Materials Engineering and Performance, 2005. **14**(6): p. 741-746.

80. Terlinde, G.T., T.W. Duerig, and J.C. Williams, *Microstructure, tensile deformation, and fracture in aged ti 10V-2Fe-3Al.* Metallurgical Transactions A, 1983. **14**(10): p. 2101-2115.

81. Breslauer, E. and A. Rosen, *Relationship between microstructure and mechanical properties in metastable β titanium 15-3 alloy.* Materials Science and Technology, 2013. **7**(5): p. 441-446.

82. Peters, J.O. and G. Lutjering, Z. Metallkde, 1998. **89**: p. 464.

83. Li, C.-L., et al., *A study on the microstructures and tensile properties of new beta high strength titanium alloy.* Journal of Alloys and Compounds, 2013. **550**(0): p. 23-30.

84. Welk, B.A., *Microstructural and Property Relationships in -Titanium Alloy Ti-5553*, in *Materials Science and Engineering*. 2010, The Ohio State University.

85. Hertzberg, R.W., R.P. Vinci, and J.L. Hertzberg, *Deformation and Fracture Mechanics of Engineering Materials*. 5th edition ed. 2012: John Wiley & Sons.

86. Feng, X., et al. *Influence of Microstructure on Fatigue Crack Propagation and Fracture Toughness of Large Ti-6Al-4V Cast Structure* in *13th International Conference on Fracture* 2013. Beijing, China: International Congress on Fracture.

87. Richards, N.L., *Quantitative evaluation of fracture toughness - microstructural relationships in alpha-beta titanium alloys* JMEPEG, 2004. **13**: p. 218-225.

88. Richards, N.L., *Prediction of crack deflection in titanium alloys with a platelet microstructure.* Journal of Materials Engineering and Performance, 2005. **14**(1): p. 91-98.

89. Richards, N.L. and J.T. Barnby, *The relationship between fracture toughness and microstructure in alpha-beta titanium alloys.* Materials Science and Engineering, 1976. **26**(2): p. 221-229.

90. Filip, R., et al., *The effect of microstructure on the mechanical properties of two-phase titanium alloys.* Journal of Materials Processing Technology, 2003. **133**(1–2): p. 84-89.

91. Bao, R.Q., X. Huang, and C.X. Cao, *Optimisation of hot die forging processes of Ti-10V-2Fe-3Al alloy.* Materials Science and Technology 2013. **21**(4): p. 451-458.

92. Wang, X., et al., *Effect of primary and secondary alpha phase on tensile property and fracture toughness of Ti-1023 titanium alloy.* Acta Metall Sin, 2007. **43**(11): p. 1129-1137.

93. Agarwal, N., et al., *Heat Treatment, Microstructure And Mechanical Properties Of A Metastable β Titanium Alloy Timetal®21s.* Transactions of the Indian Institute of Metals, 2008. **61**(5): p. 419-425.

94. Williams, D., *Overview: Microstructure and Properies of Beta-Titanium*, in *Beta-Titanium Alloys in the 1980's*, R.R. Boyer and H.W. Rosenberg, Editors. 1984. p. 19-69.

95. Albrecht, J. and G. Lütjering. *Titanium'99: Science and Technology, CRISM "Prometey"*. 2000. St. Petersburg, Russia.

96. Lütjering, G., *Property optimization through microstructural control in titanium and aluminum alloys.* Materials Science and Engineering: A, 1999. **263**(2): p. 117-126.

97. Peters, J.O., et al. *Synthesis, Processing and Modelling of Advanced Materials*. in *THird ASM international Conference*. 1997. USA: ASM

98. Terlinde, G., H.J. Rathjen, and K.H. Schwalbe, *Microstructure and fracture toughness of the aged ,β-Ti Alloy Ti-10V-2Fe-M.* Metallurgical Transactions A, 1988. **19**(4): p. 1037-1049.

99. *ASM HANDBOOK*. 10th ed. Vol. 02. 1990, Materials Park, Ohio, USA: ASM International.

100. Askeland, D.R. and P.P. Phulke, *The Science and Engineering of Materials*. 5th ed. 2005, USA: Thompson Publishers.

101. International, A., *ASTM E384-10e2*, in *Standard Test Method for Knoop and Vickers Hardness of Materials*. 2010: West Conshohocken, PA.

102. *ASTM Annual Book of Standards*, in *E8M-11 Standard Test Methods for Tension Testing of Metallic Materials*. 2011, ASTM International: West Conshohocken, United States.

103. *British Standard*, in *BS 7448-1:1991 Fracture mechanics toughness tests*. 2002, British Standards Institute: London.

104. G. R., I., *Analysis of stresses and strains near the end of a crack traversing a plate.* Journal of Applied Mechanics, 1957. **24**: p. 361-364.

105. GAO, J., *Understanding the relationship between microstructure and fracture toughness of HIPped Ti-5Al-5Mo-5V-3Cr alloy*. 2012, University of Birmingham.

106. Bartus, S.D., *Evaluation of Titanium-5Al-5Mo-5V-3Cr (Ti-5553) Alloy against Fragment and Armor-Piercing Projectiles* 2009, Army Research Laboratory: U.S.

107. Froes, F. and J. Smugersky, *Powder Metallurgy of Titanium alloys*. 1980, Warrendale, PA: American Institue of Mechanical Engineers.

108. Lenel, F.V. and G.S. Ansell, *The State of the Science and Art of Powder Metallurgy.* JOM, 1982. **34**(2): p. 17-29.

List of Tables

Table 1 A list of commercial α alloys [3].

Common Name	Alloy Composition (wt%)	T_β (℃)
Grade 1	CP-Ti (0.2Fe, 0.18O)	890
Grade 2	CP-Ti (0.3Fe, 0.25O)	915
Grade 3	CP-Ti (0.3Fe, 0.35O)	920
Grade 4	CP-Ti (0.5Fe, 0.40O)	950
Grade 7	Ti-0.2Pd	915
Grade 12	Ti-0.3Mo-0.8Ni	880
Ti-5-2.5	Ti-5Al-2.5Sn	1040
Ti-3-2.5	Ti-3Al-2.5V	935

Table 2 A list of commercial α + β alloys [3].

Common Name	Alloy Composition (wt%)	T_β (℃)
Ti-811	Ti-8Al-1V-1Mo	1040
IMI 685	Ti-6Al-5Zr-0.5Mo-0.5Si	1020
Ti-6242	Ti-6Al-2Sn-4Zr-2Mo-0.1Si	995
Ti-6-4	Ti-6Al-4V	995
Ti-662	Ti-6Al-6V-2Sn	945
IMI 550	Ti-4Al-2Sn-4Mo-0.5Si	975

Table 3 A list of commercial β alloys [3].

Common Name	Alloy Composition (wt%)	T_β (℃)
Ti-6246	Ti-6Al-2Sn-4Zr-6Mo	940
Beta-CEZ	Ti-5Al-2Sn-2Cr-4Mo-4Zr-1Fe	890
Ti-10-2-3	Ti-10V-2Fe-3Al	800
Beta 21S	Ti-15Mo-2.7Nb-3Al-0.2Si	810
Ti-LCB	Ti-4.5Fe-6.8Mo-1.5Al	810
Ti-15-3	Ti-15V-3Cr-3Al-3Sn	760
Ti-5-5-5-3	Ti-5Al-5Mo-5V-3Cr	830

Table 4 Tensile properties of Ti-64 processed by different fabrication techniques [107].

Process	Tensile strength (MPa)	Yield strength (MPa)	Elongation (%)	Reduction in area (%)
Cast	930	841	7	15
Isothermally forged	965	875	15	40
Diffusion	924	855	11	23
Blended elemental PM	917	834	11	18
Prealloyed PM HIPping	979	882	14	26

Table 5 Grinding/polishing procedures for Ti-5553 alloys.

Polishing cloths (Struers company)	Rotational speed (rpm)	Time (min)
Piano 220	250	Until flat
MD-Largo/ 9 **µm**	150	about 15
MD-Chem/ 0.05 **µm**	150	about 6

Table 6 Solution treatment processes for PREP C Ti-5553 alloy.

	T1 (℃)	t1 (h)	Quench	Grain Size (µm)
PREP 0.08%C	900	1	WQ	46
PREP 0.08%C	1000	1	WQ	100
PREP 0.08%C	1050	1	WQ	142
PREP 0.08%C	1050	4	WQ	168

Table 7 Heat treatment processes for 0.08% C Ti-5553 alloy.

Sample group	T1 (℃)	t1 (h)	Quench	T2 (℃)	t2 (h)	Quench
1	900	1	WQ	650	6	WQ
2	1000	1	WQ	650	6	WQ
3	1050	1	WQ	650	6	WQ
4	1050	4	WQ	650	6	WQ

Table 8 Grain size results for 0.08% C Ti-5553 alloy.

Sample group	T1 (℃)	t1 (h)	Quench	Grain Size (μm)
1	900	1	WQ	46
2	1000	1	WQ	100
3	1050	1	WQ	142
4	1050	4	WQ	168

Table 9 Results of volume fraction of alpha phase of three groups samples.

Sample group	1	2	4
Volume fraction of alpha phase (V_α%)	29.4	29.5	28.0

Table 10 Room temperature tensile testing of HIPped 0.08% C Ti-5553 alloy with different grain size.

	$\sigma_{0.2\%}$ (MPa)	UTS (MPa)	El. (%)
46 μm	1336±5.7	1364±5.8	6.7±2.0
100 μm	1329±0.7	1353±1.4	6.3±1.4
168 μm	1337±1.4	1347±3.5	1.9±0.3

Table 11 Fracture toughness values of PREP 0.08% C samples with three grain size.

	K_{Ic} (MPa· $m^{\frac{1}{2}}$)		Average K_{Ic} (MPa· $m^{\frac{1}{2}}$)
46 µm	33.7	33.5	33.6
100 µm	33.8	34.1	33.9
168 µm	35.9	38.3	37.2

Table 12 Solution treatment processes for PREP NC Ti-5553 alloy.

	T1 (℃)	**t1 (h)**	**Quench**	**Grain Size (µm)**
PREP NC	900	1	WQ	169

Table 13 Heat treatment process of PREP C samples and hardness result.

	T1 (℃)	**t1 (h)**	**Quench**	**T2 (℃)**	**t2 (h)**	**Quench**	**Hardness (HV)**
PREP 0.08%C	1050	4	WQ	650	6	WQ	411.6

Table 14 Heat treatment process of PREP NC samples and hardness result.

	T1 (℃)	t1 (h)	Quench	T2 (℃)	t2 (h)	Quench	Hardness (HV)
PREP NC	900	1	WQ	600	6	WQ	413.1
PREP NC	900	1	WQ	650	6	WQ	379.1

Table 15 Heat treatment conditions and tensile testing results.

	Heat treatment condition	Grain Size (μm)	YS (MPa)	UTS (MPa)	Elongation (%)
PREP C Ti-5553	1050℃ 4 h, WQ 650℃ 1 h, WQ	168	1337±1.4	1347±3.5	1.9±0.3
PREP NC Ti-5553	900℃ 1 h, WQ 600℃ 1 h, WQ	169	1302±0.7	1349±1.4	3.1±0.2

Table 16 Heat treatment conditions and fracture toughness results.

	Heat treatment condition	Grain Size (μm)	Fracture Toughness K_{Ic} (MPa· $m^{\frac{1}{2}}$)
PREP C Ti-5553	1050℃ 4 h, WQ 650℃ 6 h, WQ	168	37.2±1.69
PREP NC Ti-5553	900℃ 1 h, WQ 600℃ 6 h, WQ	169	42.3±1.32

Table 17 Different heat treatment routes for PREP NC Ti-5553 alloy samples using step quenching.

	Solutionizing temperature and time	Intermediate quenching method	Holding temperature and time	Quenching method
SQ1	900℃ 1 h	SQ	650℃ 40 min	WQ
SQ2	900℃ 1 h	SQ	680℃ 40 min	WQ
SQ3	900℃ 1 h	SQ	680℃ 1 h	WQ
SQ4	1000℃ 1h	SQ	680℃ 40min	WQ
SQ5	1000℃ 1h	SQ	680℃ 1h	WQ

Table 18 Different heat-treatment routes for selected undoped PREP Ti-5553 alloy samples which were step quenched and aged.

	Solutionizing temperature and time	Intermediate quenching method	Holding temperature and time	Quenching method	Ageing temperature and time	Quenching method
SQA1	900℃ 1 h	SQ	650℃ 40 min	WQ	600℃ 4h	WQ
SQA2	900℃ 1 h	SQ	650℃ 40 min	WQ	600℃ 5.5h	WQ
SQA3	1000℃ 1h	SQ	680℃ 1h	WQ	600℃ 4h	WQ
SQA4	1000℃ 1h	SQ	680℃ 1h	WQ	600℃ 5h	WQ
SQA5	1000℃ 1h	SQ	680℃ 1h	WQ	620℃ 5h	WQ
SQA6	1000℃ 1h	SQ	680℃ 1h	WQ	640℃ 5h	WQ
SQA7	1000℃ 1h	SQ	680℃ 1h	WQ	660℃ 5h	WQ

Table 19 STA heat-treatment route for undoped PREP Ti-5553 alloy sample.

	Solutionizing temperature and time	Intermediate quenching method	Ageing temperature and time	Quenching method
STA1	900℃ 1 h	WQ	600℃ 6h	WQ
STA2	900℃ 1 h	WQ	650℃ 6h	WQ

Table 20 Measurement results (length and thickness of α phase) of two shell-like microstructures via two SQA processes.

		Intergranular α_p		Intragranular α_s	
		Length (μm)	Thickness (μm)	Length (μm)	Thickness (μm)
SQA1	900℃ 1 h, SQ, 650℃ 40 min, WQ, 600℃ 4 h	7.24±1.50	0.30 ±0.06	2.06±1.02	0.09±0.03
SQA4	1000℃ 1 h, SQ, 680℃ 1h, WQ, 640℃ 5 h	16.6±6.78	0.57±0.09	2.18±0.99	0.24±0.16

Table 21 Measurement results (length of α phase) of two specimens via STA process.

Sample number	Heat-treatment route	Length (μm)
STA1	900℃1h, WQ, 600℃6h, WQ	0.73 ±0.30
STA2	900℃1h, WQ, 650℃6h, WQ	1.21 ±0.49

Table 22 Vickers hardness and estimating strength of undoped Ti-5553 alloy though STA processes.

Sample number	Heat-treatment route	Vickers hardness (HV)	Estimated yield stress (MPa)
STA1	900℃1h, WQ, 600℃6h, WQ	413.1±3.75	1254
STA2	900℃1h, WQ, 650℃6h, WQ	379.1±4.80	1151

Table 23 Hardness values of undoped Ti-5553 alloy samples with different SQA treatments.

	SQ conditions	Ageing temperature and time	Vickers hardness
SQA1	900℃ 1 h, SQ, 650℃ 40 min, WQ	600℃ 4 h, WQ	410±4.9
SQA2		600℃ 5.5h, WQ	386.4±3.1
SQA3	1000℃ 1 h, SQ, 680℃ 1h, WQ	600℃ 4 h, WQ	N/A
SQA4		600℃ 5 h, WQ	401.5±12.5
SQA5		620℃ 5 h, WQ	386.3±10.6
SQA6		640℃ 5 h, WQ	367.4±13.9
SQA7		660℃ 5 h, WQ	352.5±9.8

Table 24 Hardness results of undoped Ti-5553 sample which was heat treated as 1000℃ 1 h, SQ, 680℃ 1h, WQ, and 640℃ 5 h, WQ.

	On intergranular α_p	On intragranular α_s
Vickers hardness	378±15	413±11

Table 25 Tensile properties for undoped Ti-5553 alloy through different heat treatment routes.

Sample number	Heat-treatment route	Yield stress (MPa)	Fracture stress (MPa)	Elongation (%)
STA1	900℃1h, WQ, 600℃6h, WQ	1195±12.07	1263±10.70	4.9±0.42
STA2	900℃1h, WQ, 650℃6h, WQ	1152±6.07	1204±4.18	4.8±0.85
SQA1	900℃ 1 h, SQ, 650℃ 40 min, WQ, 600℃ 4 h, WQ	1229±0.52	1291±10.40	2.2±1.22
SQA6	1000℃ 1 h, SQ, 680℃ 1h, WQ, 640℃ 5 h, WQ	1138±14.6	1202±10.50	6.2±1.53

Table 26 Fracture toughness testing results and yield stress from Ti-5553 specimens via STA and SQA heat treatment processes.

Sample number	Heat-treatment route	Yield stress (MPa)	Fracture Toughness K_{Ic} (MPa· $m^{\frac{1}{2}}$)	Average K_{Ic} (MPa· $m^{\frac{1}{2}}$)
STA1	900℃1h, WQ, 600℃6h, WQ	1195	43.1/ 41.5	42.3
STA2	900℃1h, WQ, 650℃6h, WQ	1152	55.2/ 55.9/ 58.9	56.7
SQA1	900℃ 1 h, SQ, 650℃ 40 min, WQ, 600℃ 4 h, WQ	1229	45.1/ 45.3	45.2
SQA6	1000℃ 1 h, SQ, 680℃ 1h, WQ, 640℃ 5 h, WQ	1138	60.0/60.1	60.1

Table 27 Different BASCA heat treatment routes for PREP NC Ti-5553 alloy samples.

	Solutionizing temperature (T1) and time	Intermediate quenching method	Ageing temperature (T2) and time	Quenching method
BASCA1	1000℃ 1 h	FC to	600℃	WQ
BASCA2	1000℃ 1 h	FC to	640℃	WQ
BASCA3	1000℃ 1 h	FC	600℃ 5 h	WQ
BASCA4	1000℃ 1 h	FC	640℃ 5 h	WQ

Table 28 SQ6 heat treatment route for PREP NC Ti-5553 alloy samples.

	Solutionizing temperature and time	Intermediate quenching method	Holding temperature and time	Quenching method	Ageing temperature and time	Quenching method
SQA6	1000℃ 1h	SQ	680℃ 1h	WQ	640℃ 5h	WQ

Table 29 Length of large inter-α_p and small inter-α_p.

	Length (μm)
Large inter-α_p	12.91±2.70
Small inter-α_p	2.73±1.13

Table 30 Vickers hardness results of BASCA processed specimens.

	Solutionizing temperature (T1) and time	Intermediate quenching method	Ageing temperature (T2) and time	Quenching method	Vickers Hardness (HV)
BASCA3	1000℃ 1 h	FC	600℃ 5 h	WQ	382±19
BASCA4	1000℃ 1 h	FC	640℃ 5 h	WQ	341±11

Table 31 Tensile testing results of BASCA3 and SQA specimens.

	Heat treatment conditions	YS (MPa)	UTS (MPa)	Elongation (%)
BASCA3	1000℃ 1 h, SC, 600℃ 5 h	1056±2.42	1133.5±6.22	7.5±1.91
SQA6	1000℃ 1 h, SQ, 680℃ 1 h, 640℃ 5 h	1138±14.6	1202±10.50	6.2±1.53

Table 32 Fracture toughness testing results and yield stress from Ti-5553 specimens via BASCA 3 heat treatment route.

	Heat treatment route	**Yield stress (MPa)**	**Fracture Toughness K_{Ic} (MPa· $m^{\frac{1}{2}}$)**	**Average K_{Ic} (MPa· $m^{\frac{1}{2}}$)**
BASCA3	1000℃ 1 h, FC, 600℃ 5 h	1056	65.2/63.7/60.3/65.8	63.8±2.47

List of Figures

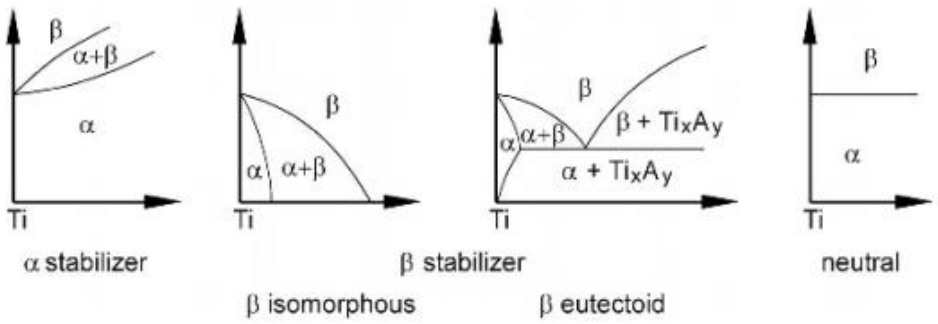

Fig. 1 Schematic diagrams showing the effect of alloying elements on the phase diagrams of titanium alloys [3].

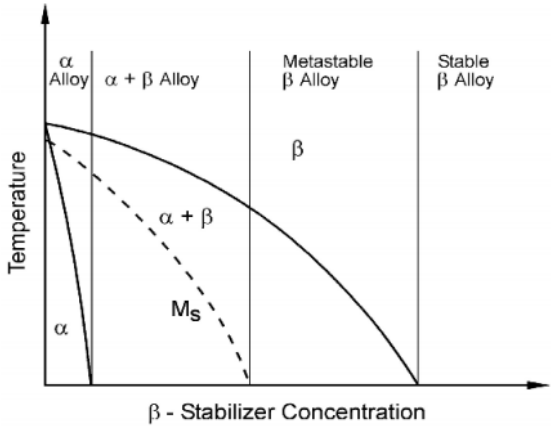

Fig. 2 Pseudo binary phase diagram of titanium alloy with the alloy categories [3].

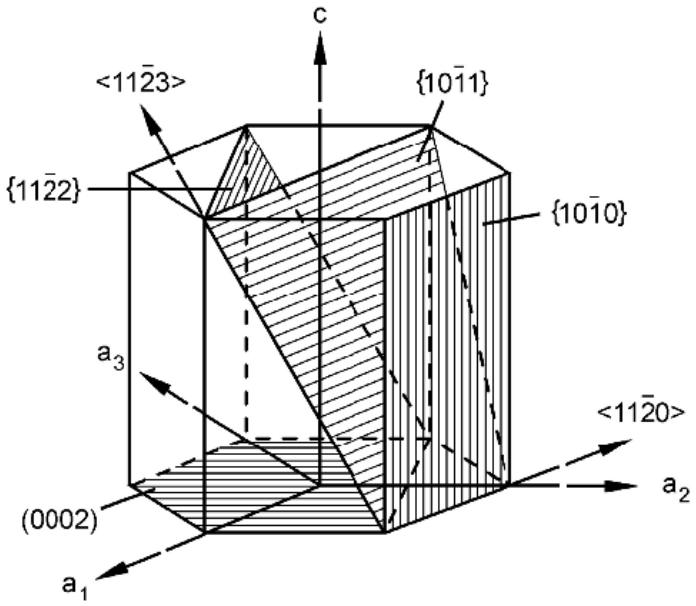

Fig. 3 Slip systems in the HCP α phase.

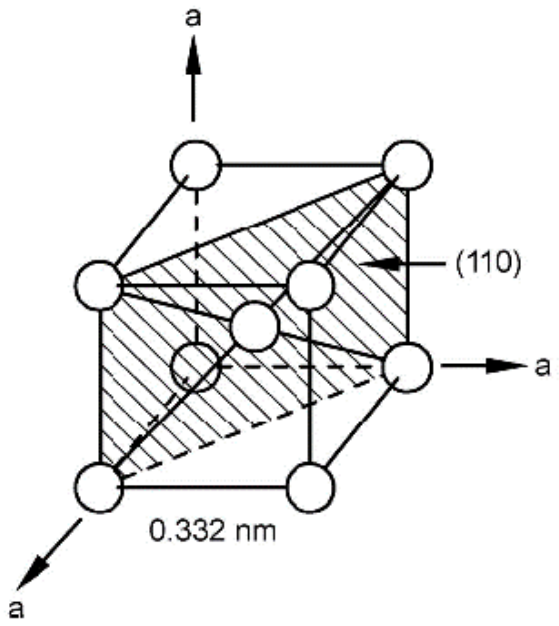

Fig. 4 The unit cell of BCC structure of beta phase.

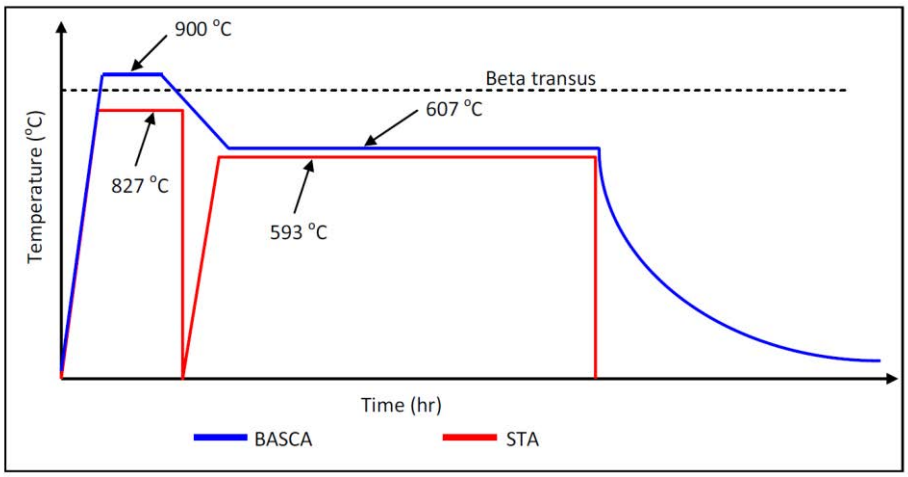

Fig. 5 The BASCA and STA heat treatment processes for the Ti-5553 alloy.

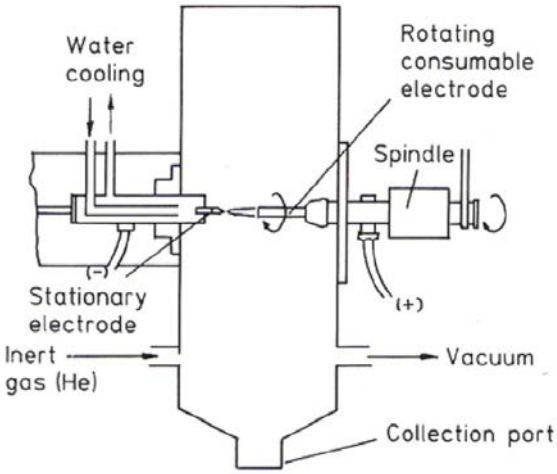

Fig. 6 Schematic diagram of plasma rotating electrode process (PREP) [108].

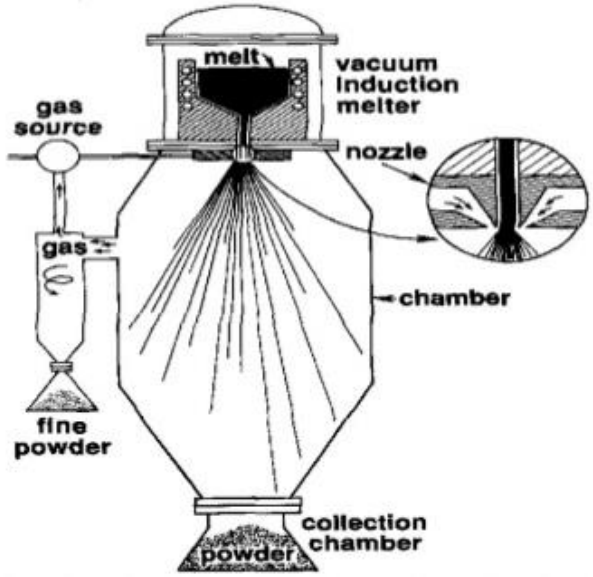

Fig. 7 A vertical gas atomiser.

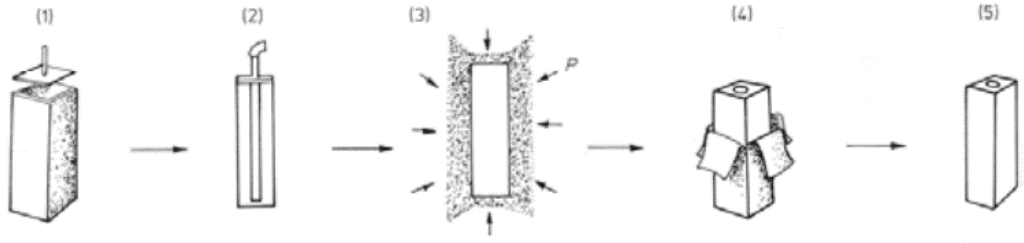

Fig. 8 Processing steps in hot isostatic pressing for powder consolidation: (1) fabricate can; (2) fill powder in can, evacuate, degas and seal; (3) HIP; (4) take out specimen; (5) consolidated powder obtained [57]

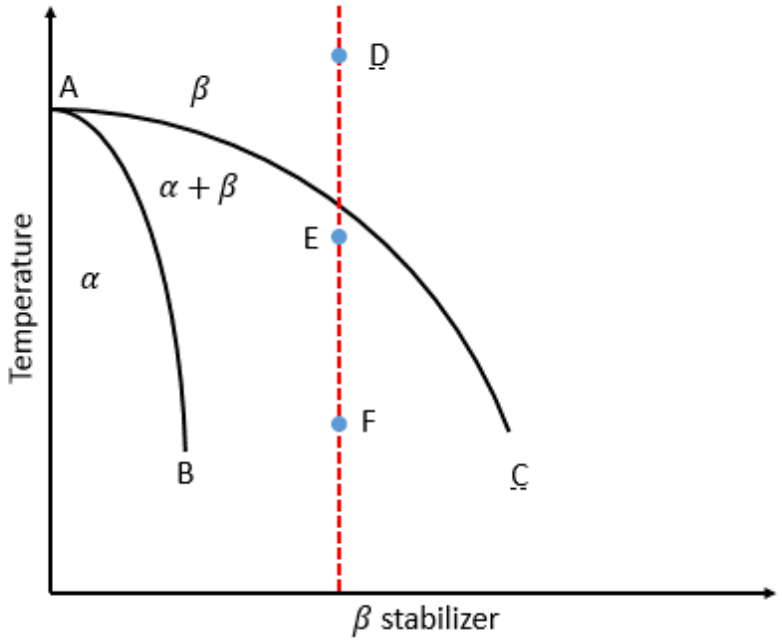

Fig. 9 Pseudo-Binary phase diagram

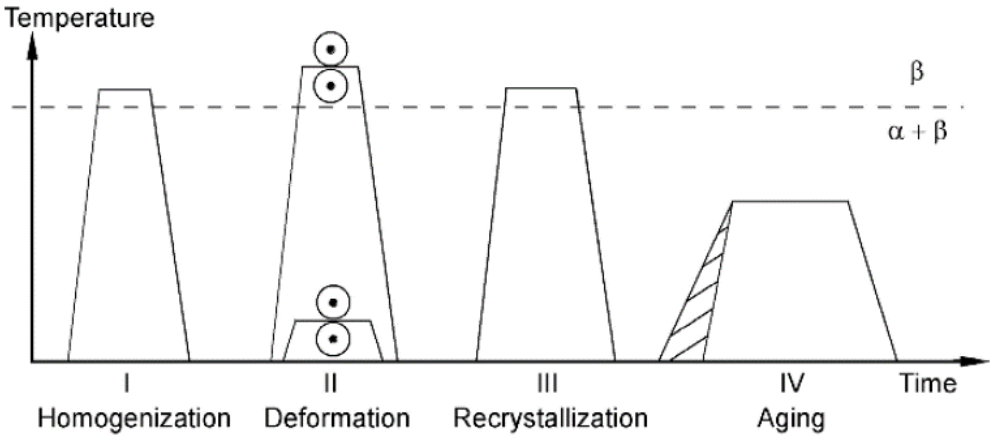

Fig. 10 Processing route for β annealed microstructures.

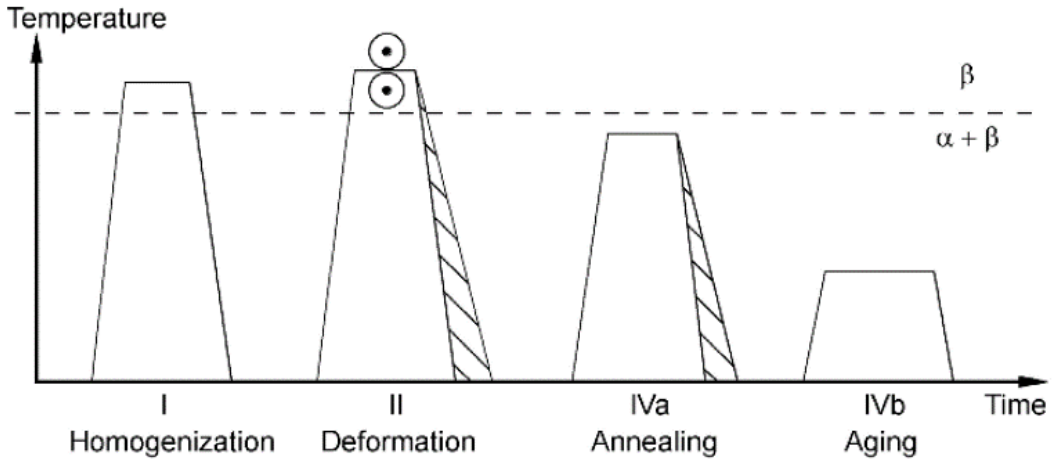

Fig. 11 Processing route for β processed microstructures.

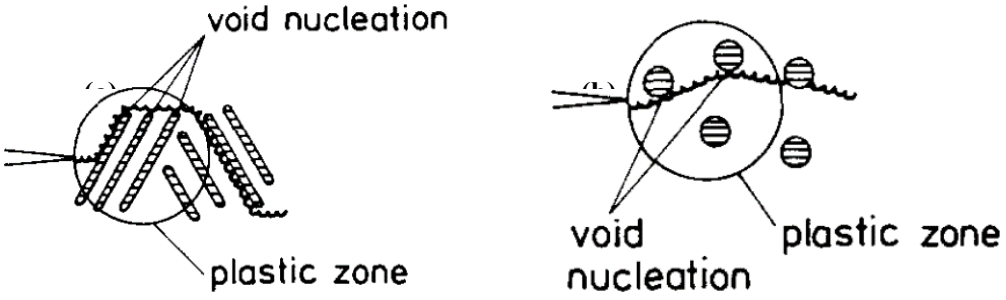

Fig. 12 Schematic illustration of crack growth. (a) Elongated α_p phase; (b) Globular α_p phase.

Fig. 13 Picture of EPSI Lab HIP facility.

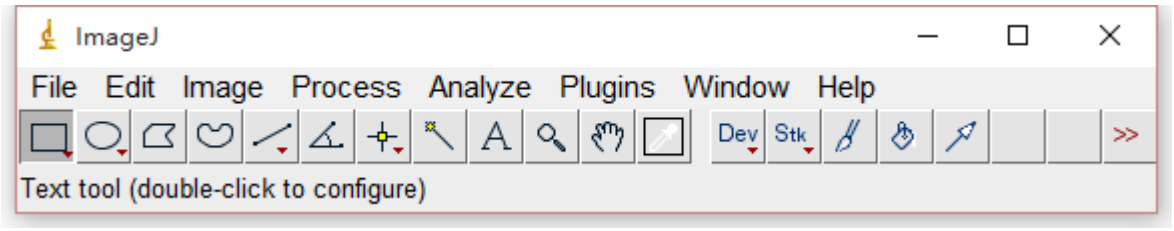

Fig. 14 Control panel of ImageJ software.

Fig. 15 Tensile testing machine.

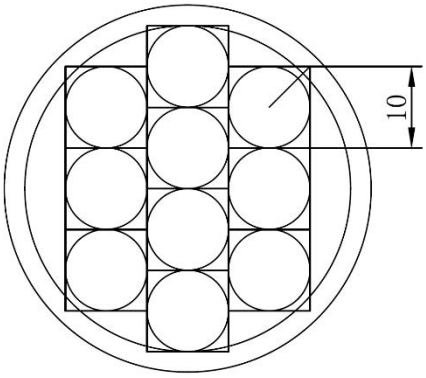

Fig. 16 10 mmØ cylinders cut from heat-treated samples.

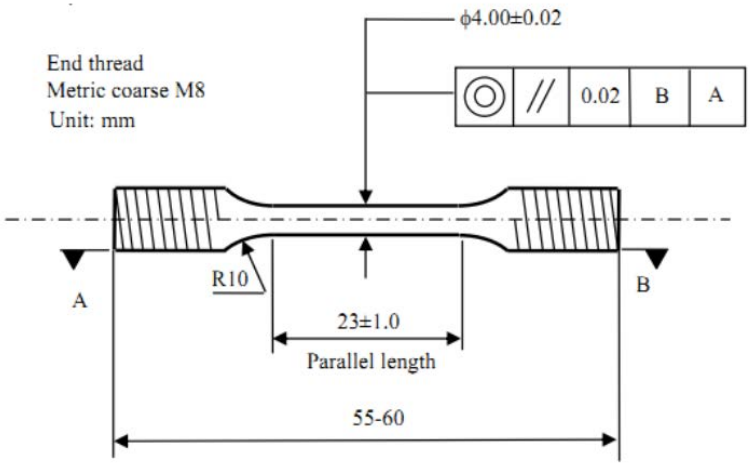

Fig. 17 Final dimensions of tensile test specimens [102].

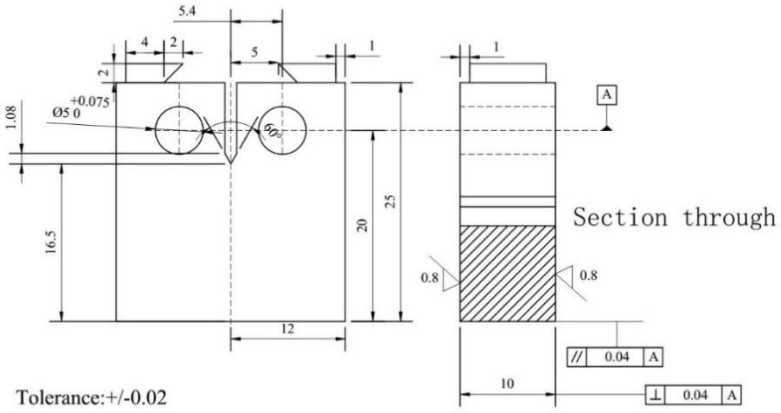

(mm)

Fig. 18 Dimensions of final shape CT-specimens for fracture toughness testing [103].

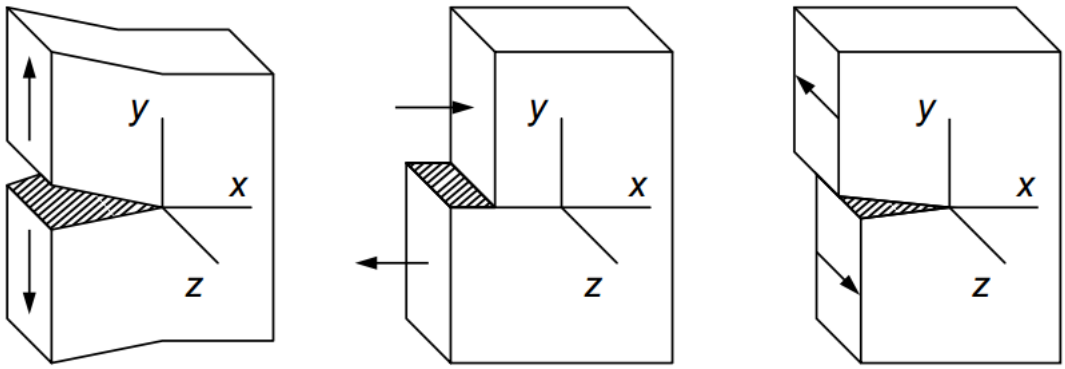

(a) (b) (c)

Fig. 19 Three fundamental fracture modes: (a) Mode I (opening), (b) Mode II (sliding), (c) Mode III (tearing).

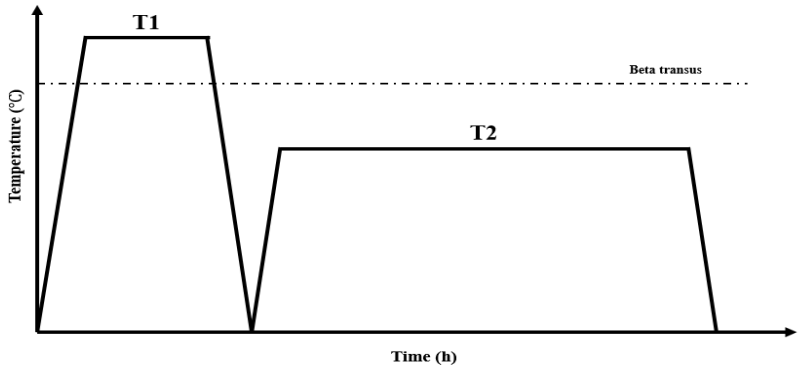

Fig. 20 Processing schedule for PREP 0.08% C Ti-5553 alloy.

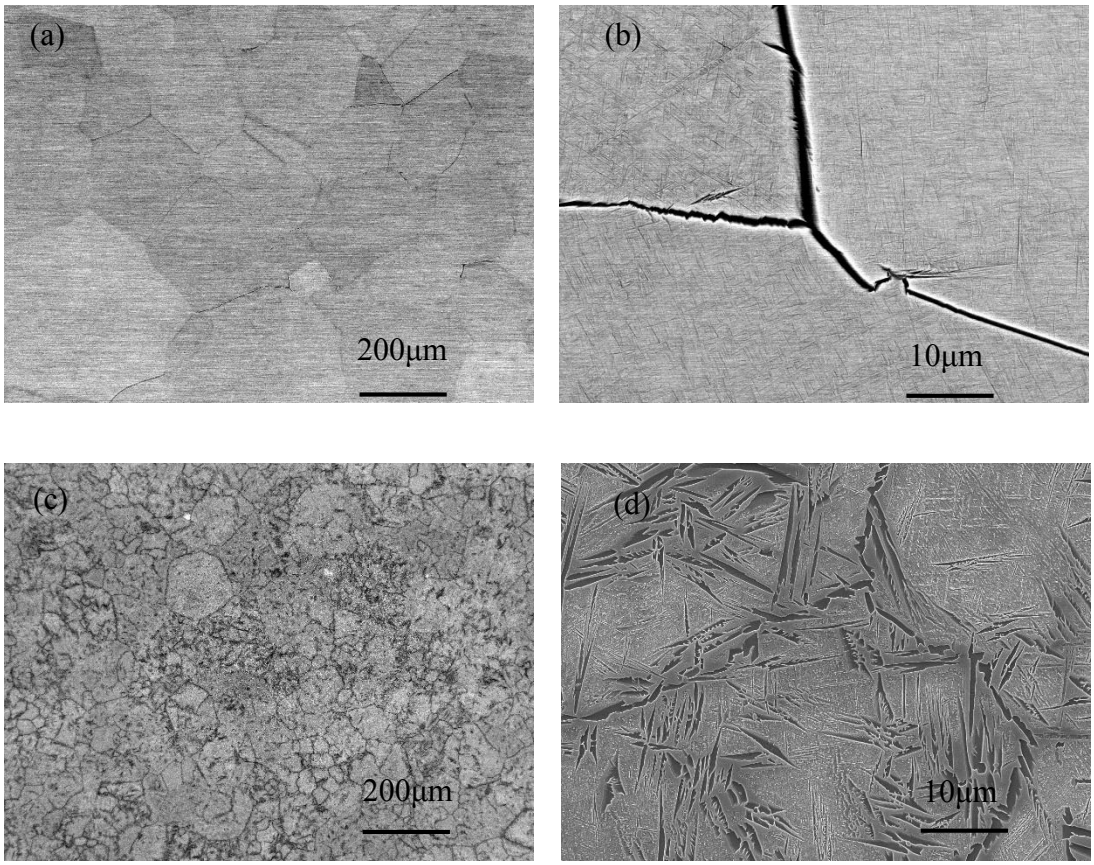

Fig. 21 Images for as-HIPped specimens, (a) PREP NC Ti-5553 alloy, × 100 (b) PREP NC Ti-5553 alloy, × 2000, (c) PREP 0.08% C Ti-5553 samples, × 100 (d) PREP 0.08% C Ti-5553 samples, × 2000.

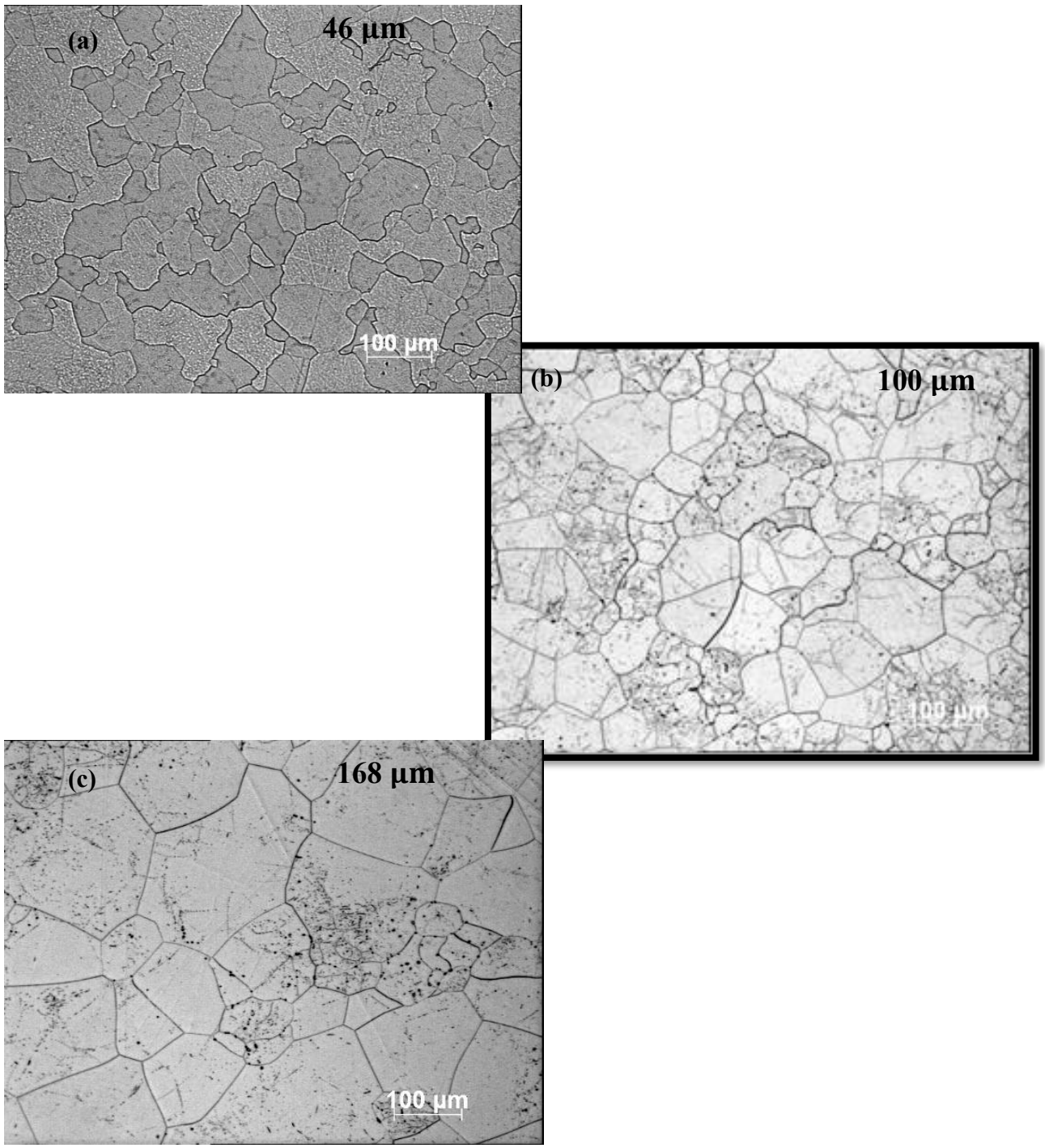

Fig. 22 Optical images of PREP 0.08% C samples at different solution treatments, (a) 900℃ 1 h; (b) 1000℃ 1 h; (c) 1050℃ 4h.

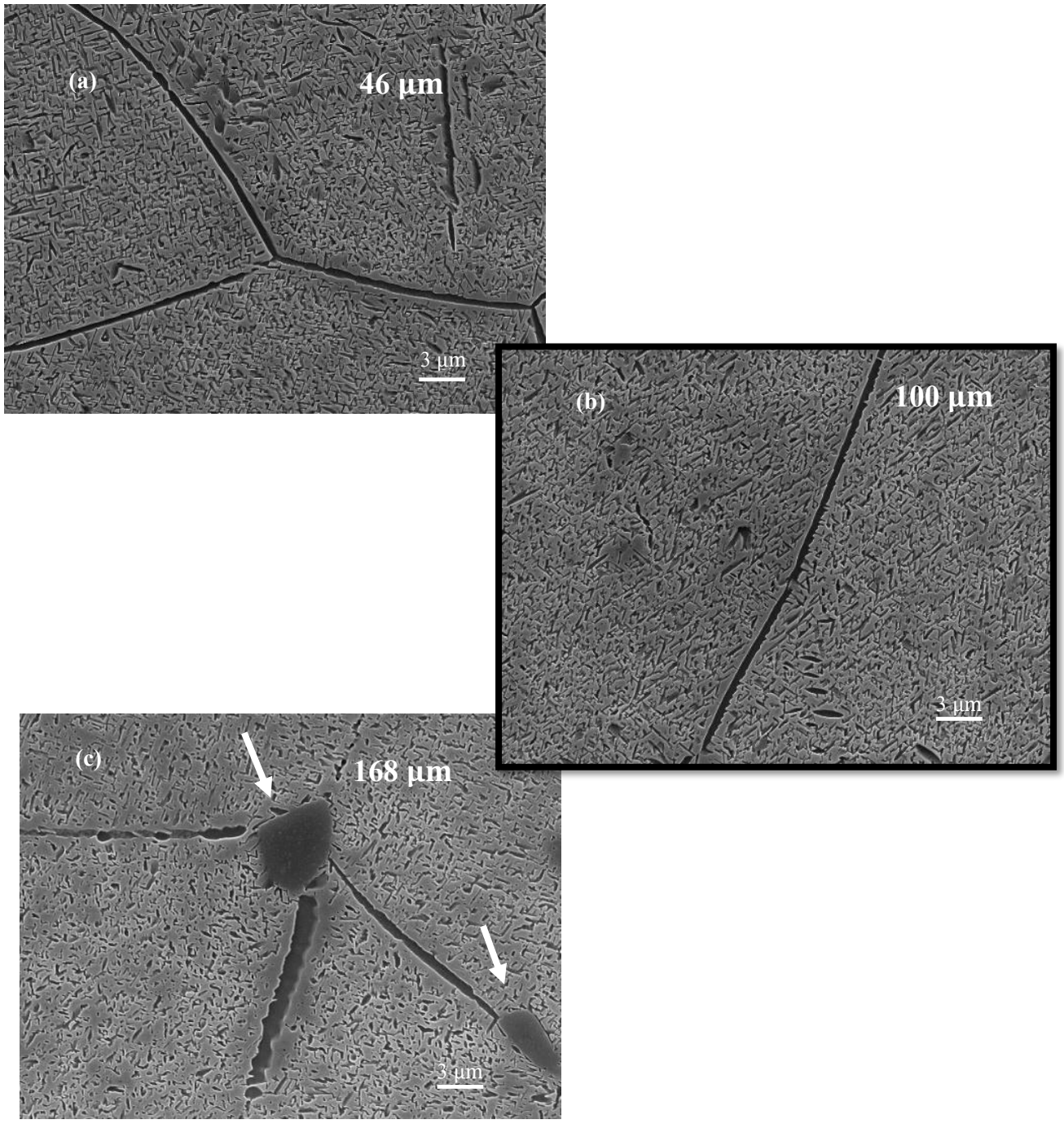

Fig. 23 SEM images at grain boundaries area of PREP 0.08% C Ti-5553 samples aged at 650℃ for 6h, (a) group 1 samples with average grain size of 46 µm; (b) group 2 samples with average grain size of 100 µm; (c) group 4 samples with average grain size of 168 µm.

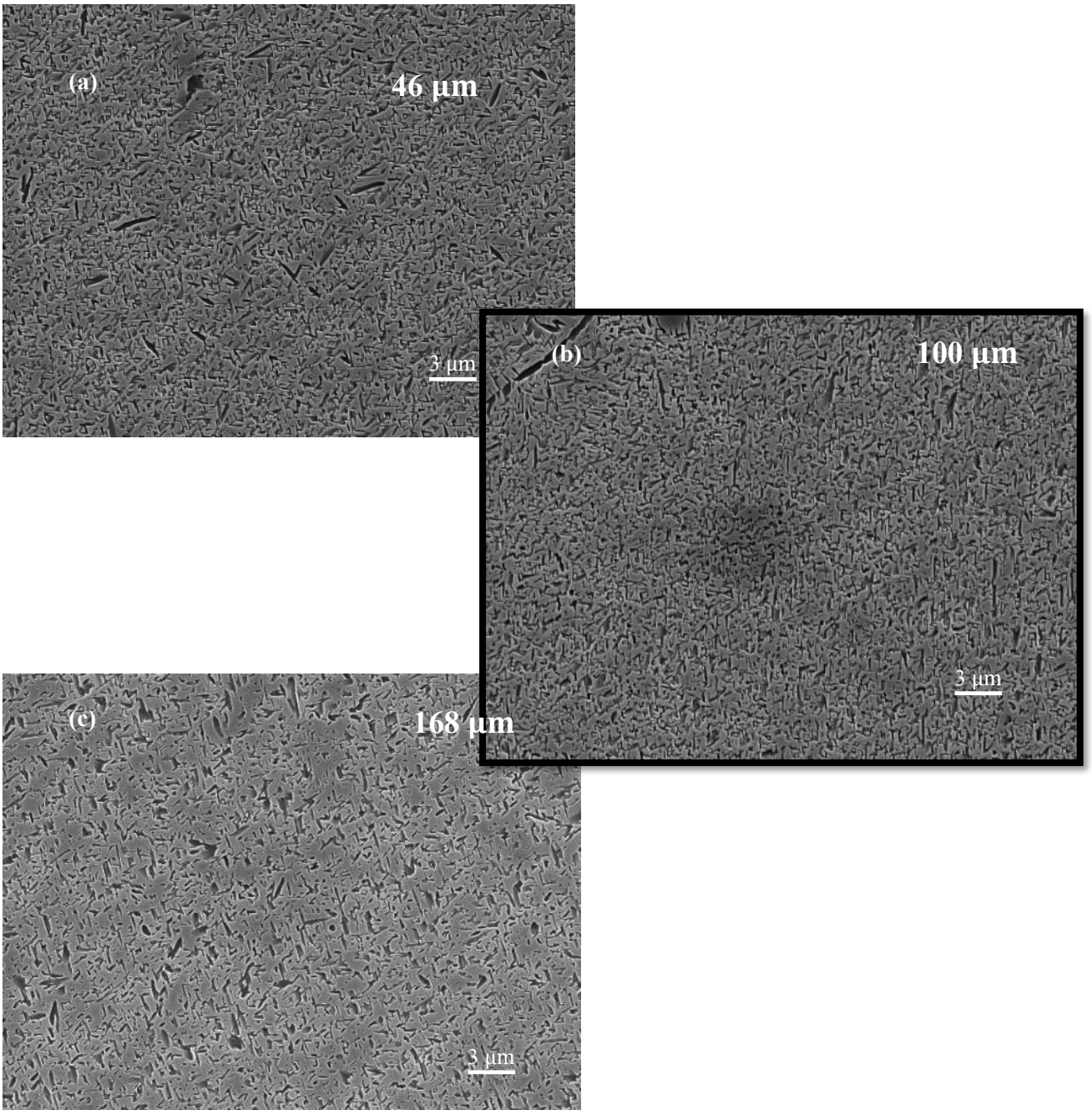

Fig. 24 SEM images within beta grains of PREP 0.08% C Ti-5553 samples aged at 650℃ for 6h, (a) group 1 samples with average grain size of 46 µm; (b) group 2 samples with average grain size of 100 µm; (c) group 4 samples with average grain size of 168 µm.

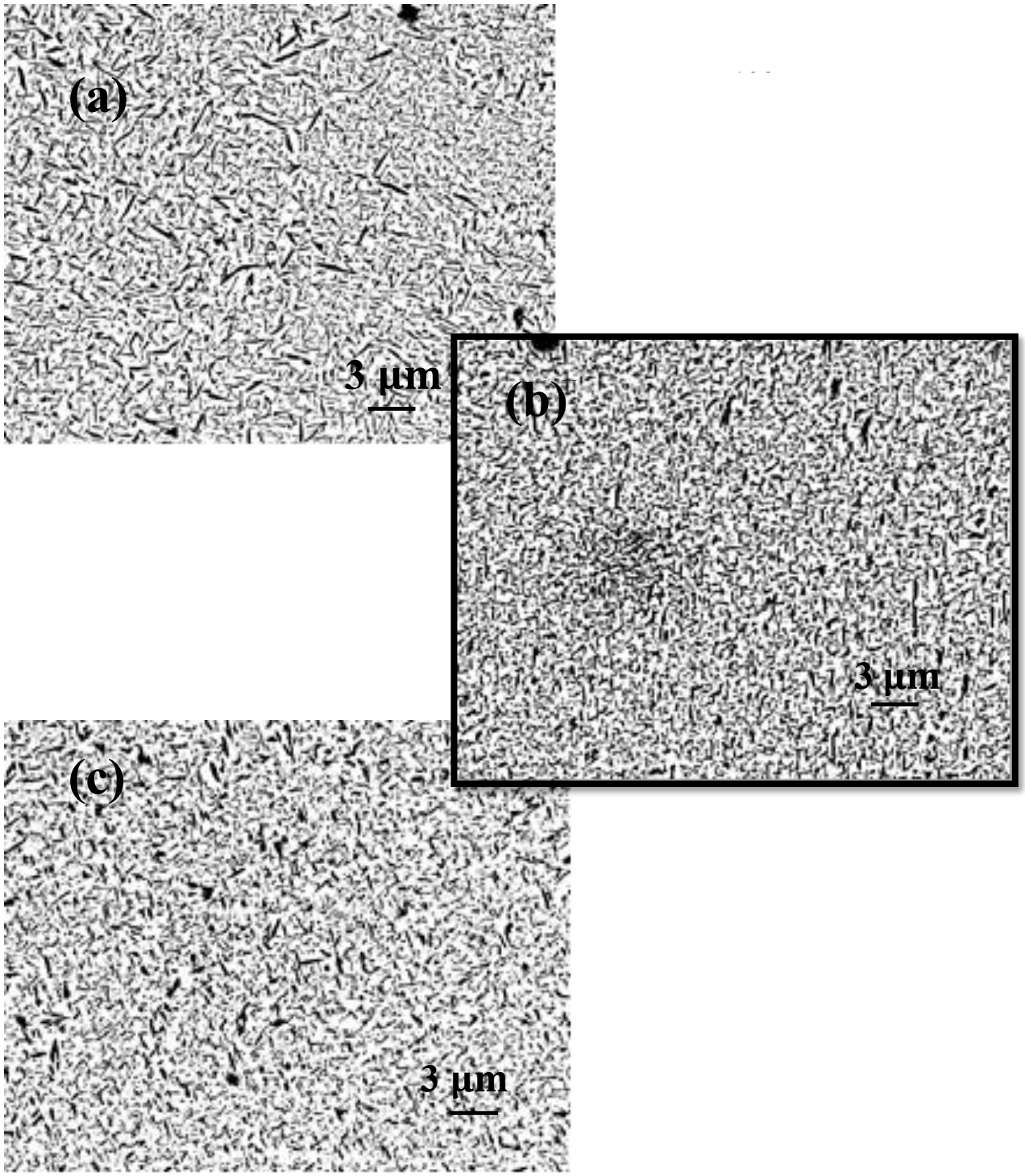

Fig. 25 SEM images in the grains of heat treated PREP 0.08% Ti-5553 samples with different grain sizes: (a) 46 μm; (b) 100 μm; (c) 168 μm.

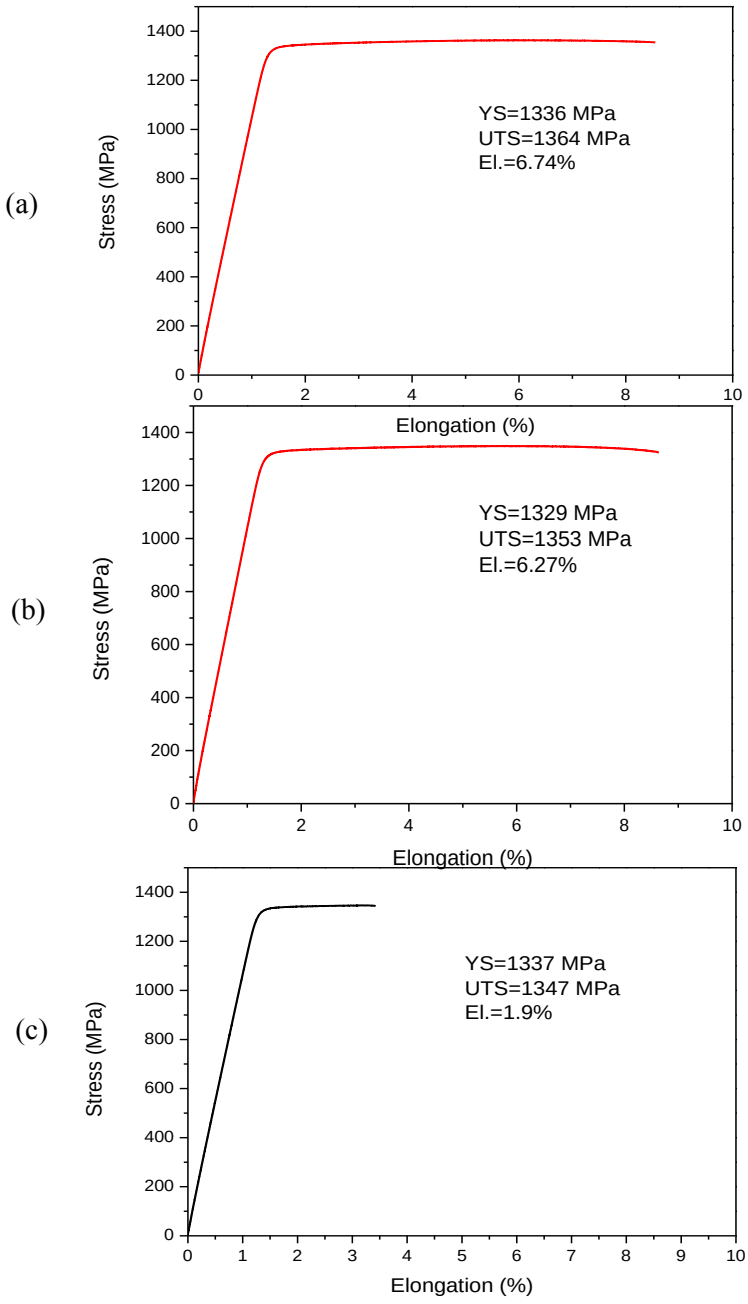

Fig. 26 Room temperature tensile testing of PREP 0.08% C Ti-5553 samples with different grain size by various heat treatment conditions: (a) 46 μm, group 1, 900℃ 1h, WQ, 650℃ 6 h, WQ; (b) 100 μm, group 2, 1000℃ 1h, WQ, 650℃ 6 h, WQ; (c) 168 μm, group 4, 1050℃ 1h, WQ, 650℃ 6 h, WQ.

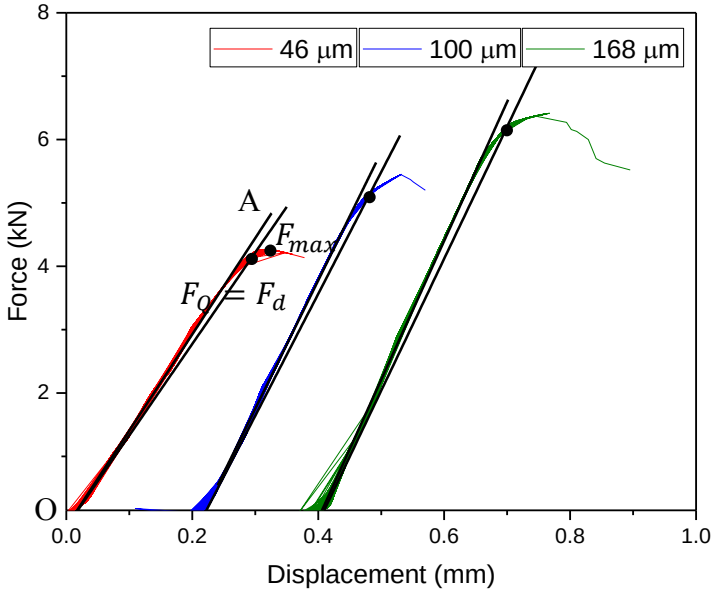

Fig. 27 Typical force vs. clip gauge displacement curve obtain from three type specimens, red curve is from 46 μm grain-size PREP 0.08% C specimen, blue curve is from 100 μm grain-size PREP 0.08% C specimen and green curve is from 168 μm grain-size PREP 0.08% C specimen.

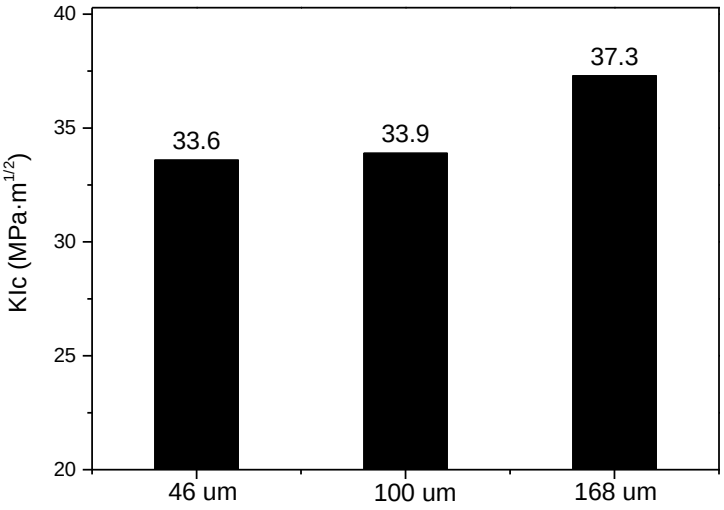

Fig. 28 Fracture toughness results of three groups' samples with different grain size (46 μm, 100 μm and 168 μm).

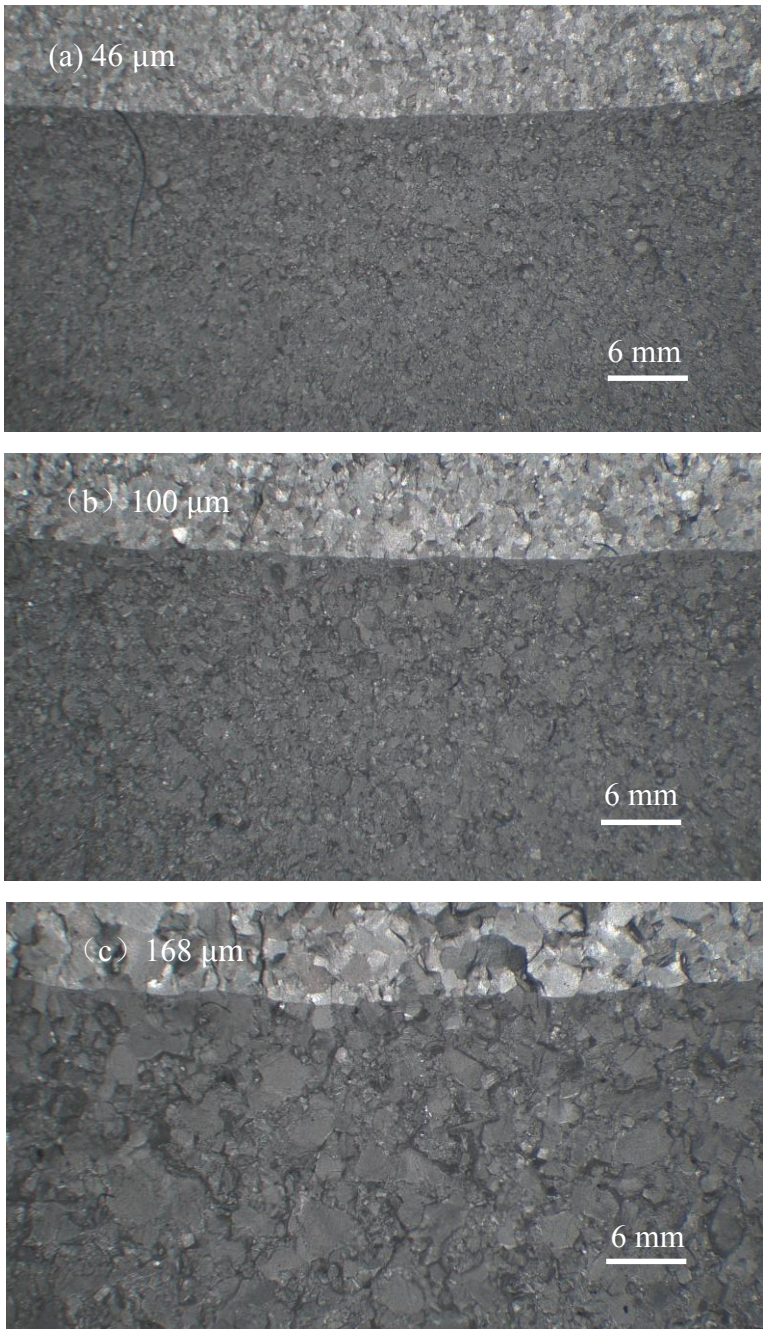

Fig. 29 Images of fracture surface of specimens with different grain size taken under OM, (a) 46 μm (b) 100 μm (c) 168 μm.

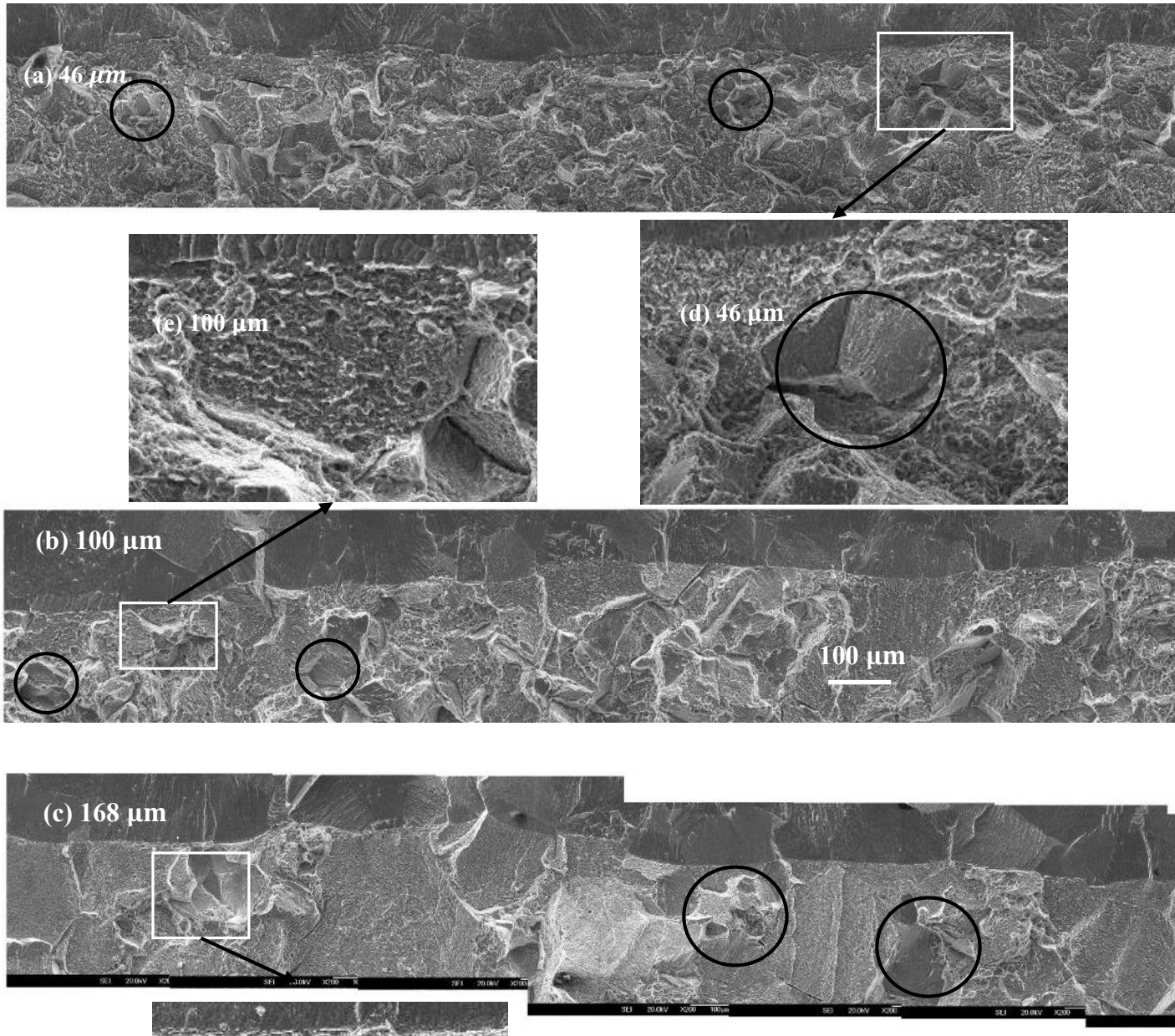

Fig. 30 Fractographs of PREP 0.08% C specimens with different grain size, (a) 46 μm, (b) 100 μm, (c) 168 μm,(d),(e) and (f) are high maginification images of (a), (b) and (c).

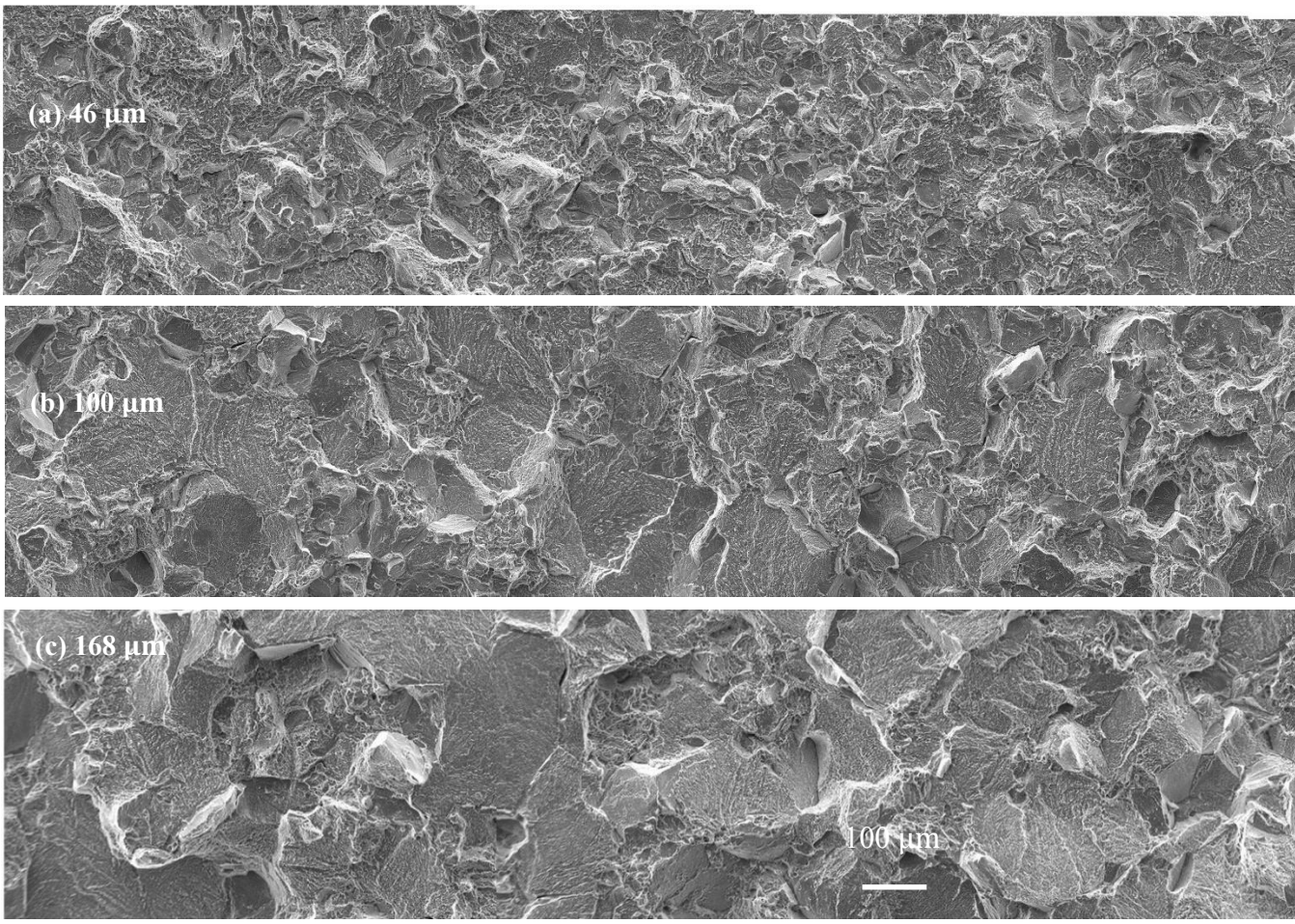

Fig. 31 Fractographs of stable extension areas of PREP 0.08% C CT testing samples with different grain size, (a) 46 µm, (b) 100 µm, (c) 168 µm.

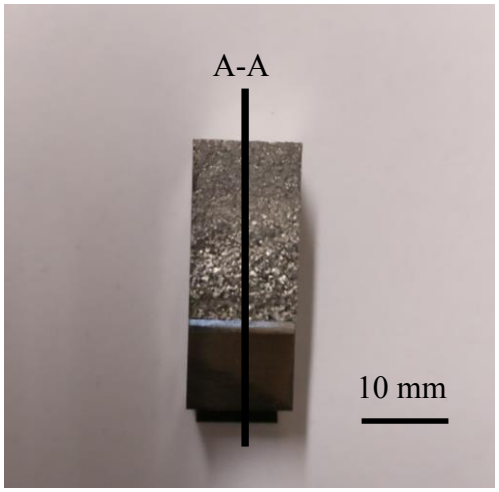

Fig. 32 Specimens were cut following A-A line.

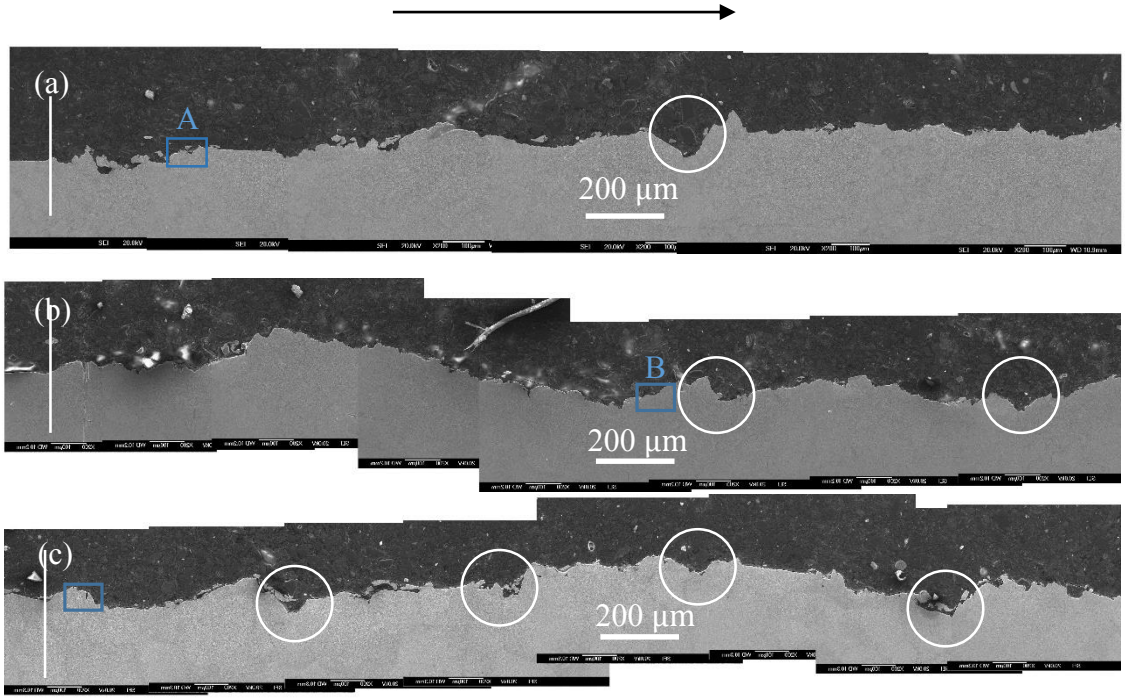

Fig. 33 Cross-sectional images of three samples with different grain size, (a) 46 µm, (b) 100 µm, (c) 168 µm, showing different crack propagation path and the crack growth direction is from left to right.

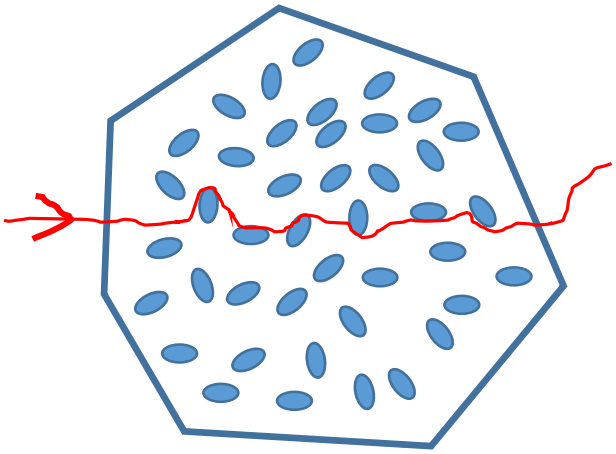

Fig. 34 An interpretation of crack propagating when it encounters a strong α_s-phase.

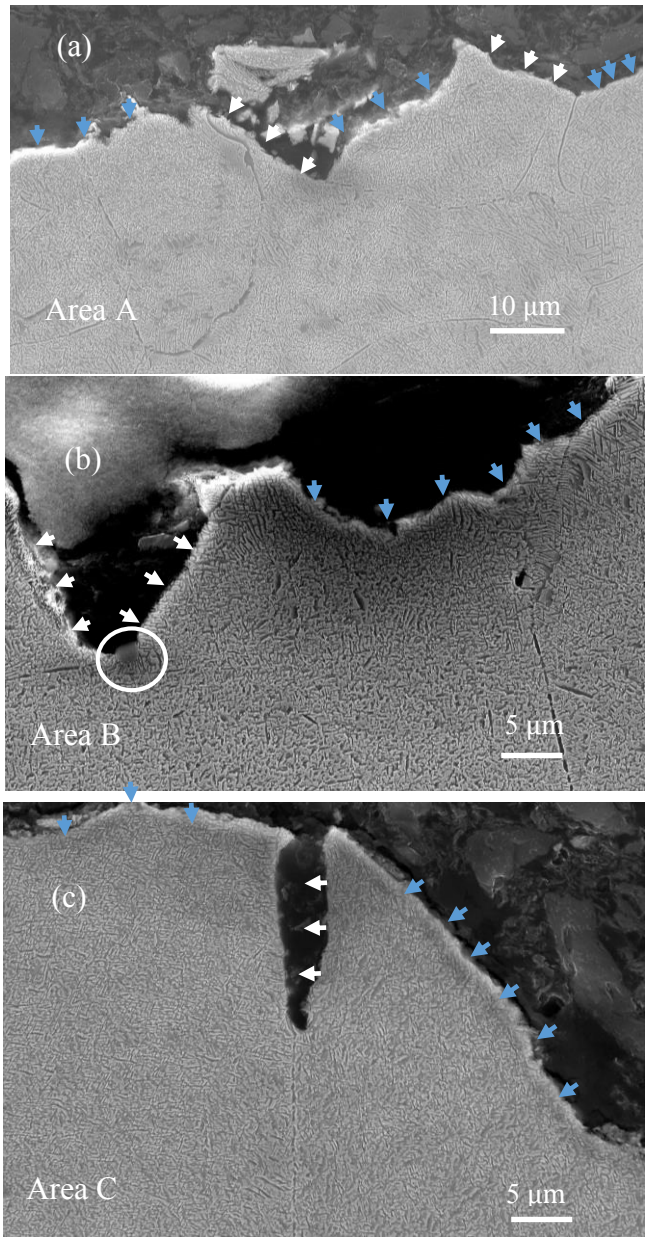

Fig. 35 High magnification image of selected area in Fig. 33, showing more crack propagation details, (a) is zooming in rectangular area A， (b) is zooming in rectangular area B. (c) is zooming in rectangular area C. While arrows indicate intergranular areas and blue arrows indicate transgranular areas.

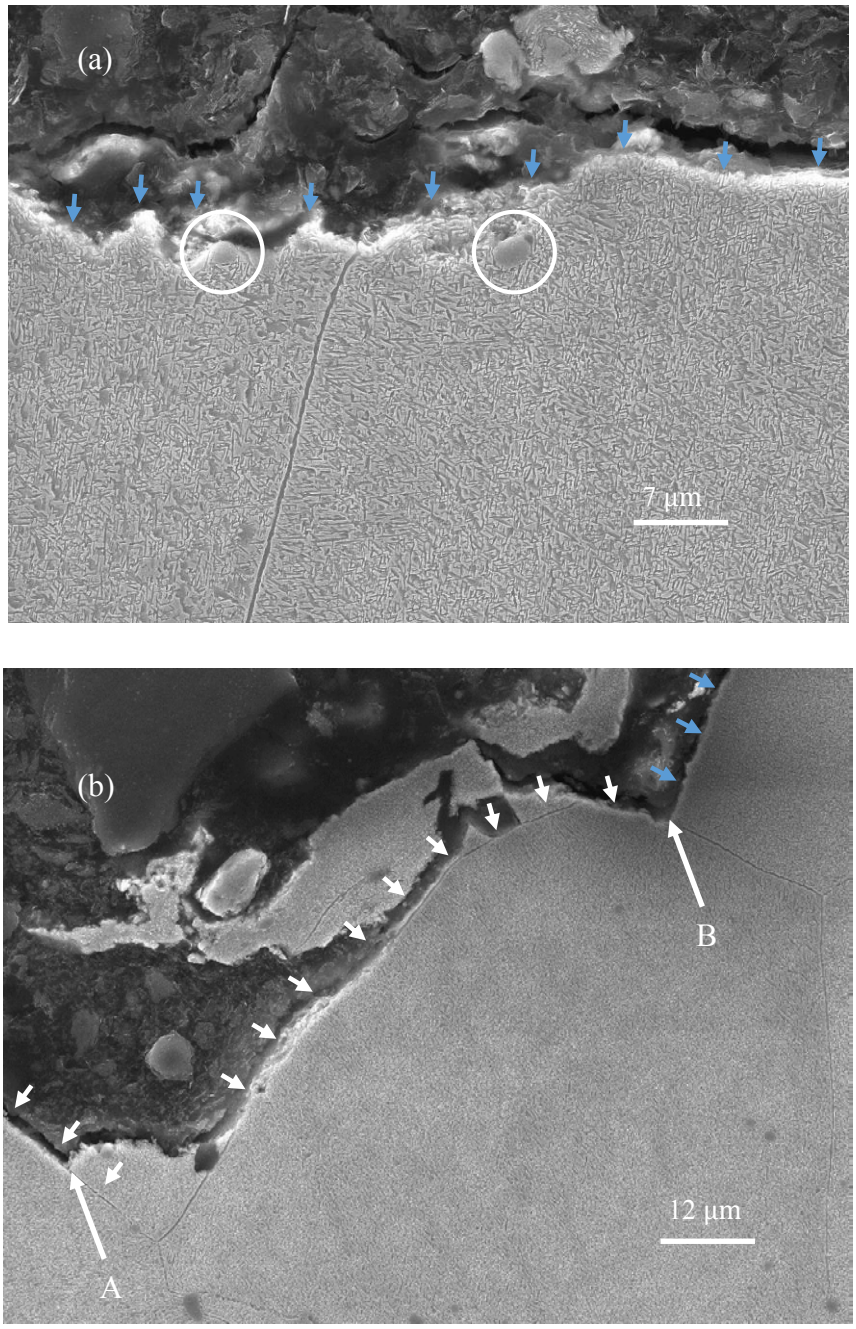

Fig. 36 High magnification image of selected area in Fig. 33 (c), showing more crack propagation details, (a) is high magnification image in intergranular region, (b) is high magnification image in transgranular region.

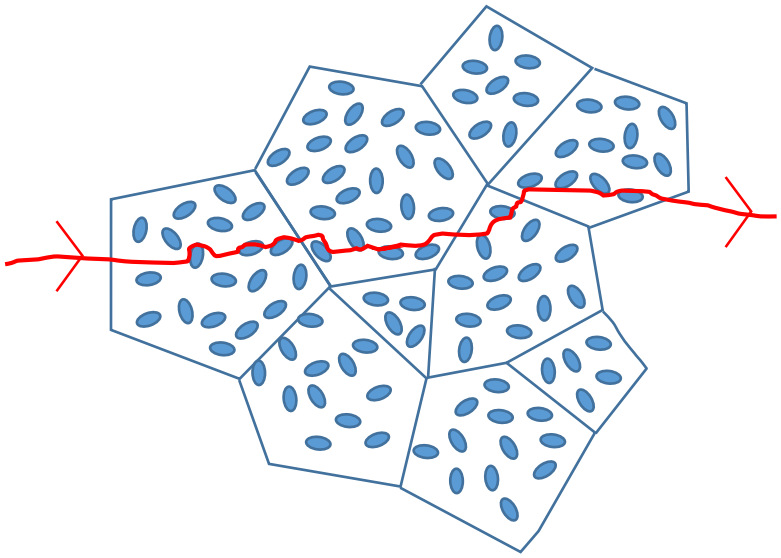

Fig. 37 An interpretation of crack propagation between adjacent grains.

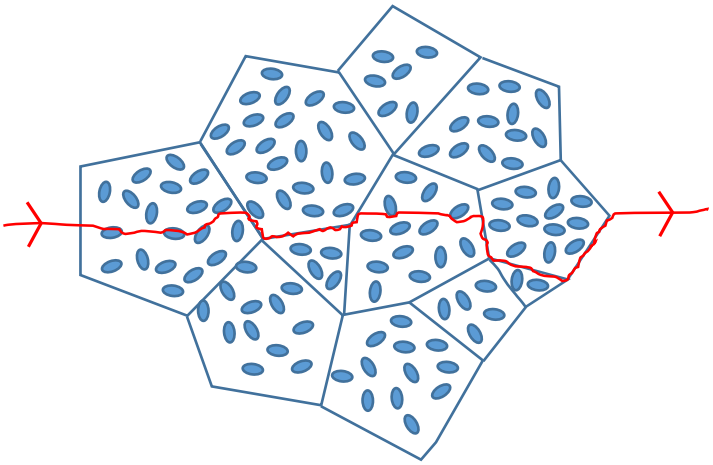

Fig. 38 An interpretation of a mixed fracture of intergranular and transgranular.

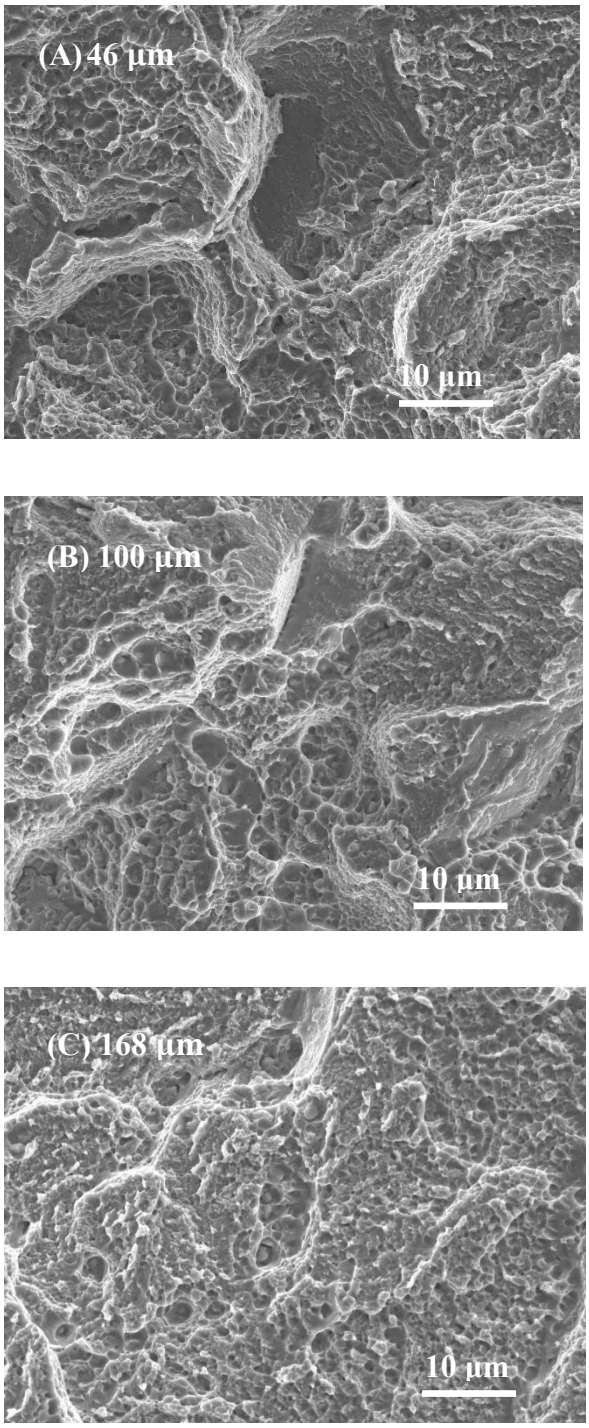

Fig. 39 Fracture surface images taken by SEM on stable extension regions of PREP 0.08% C samples with different grain size, (a) 46 µm (b) 100 µm (c) 168 µm

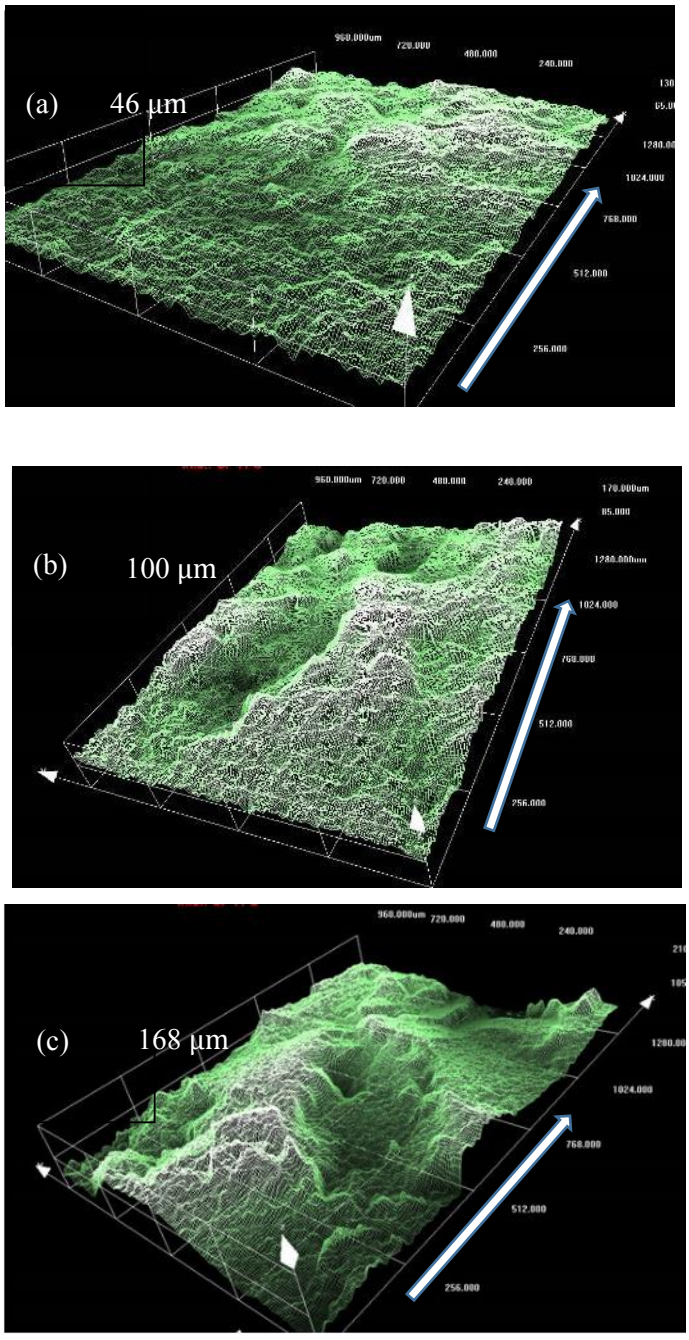

Fig. 40 Confocal images of PREP 0.08% C samples with different grain size, (a) 46 µm; (b) 100 µm; (c) 168µm.

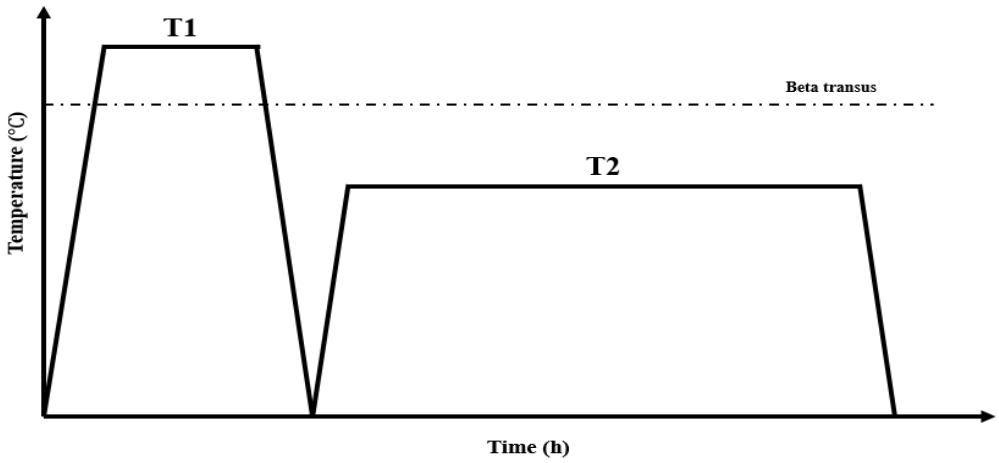

Fig. 41 Processing schedule for Ti-5553 alloy.

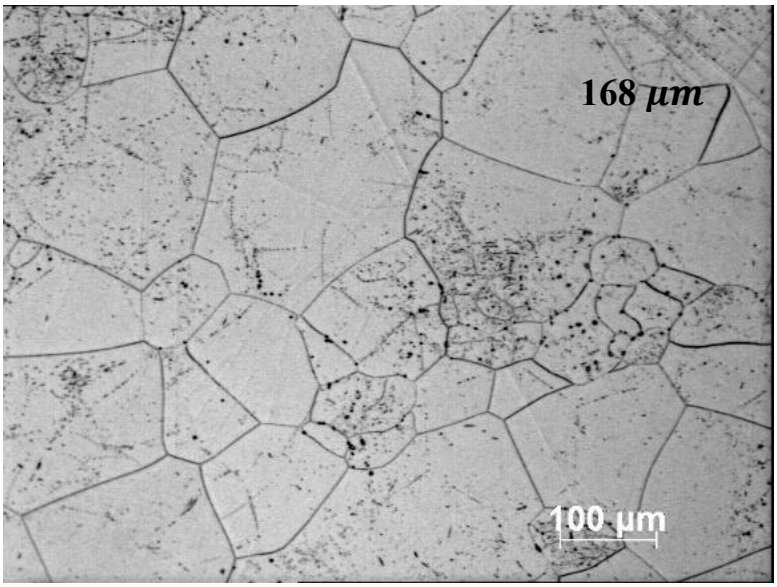

Fig. 42 OM image of PREP C Ti-5553 alloy, 1050℃ 4h, WQ

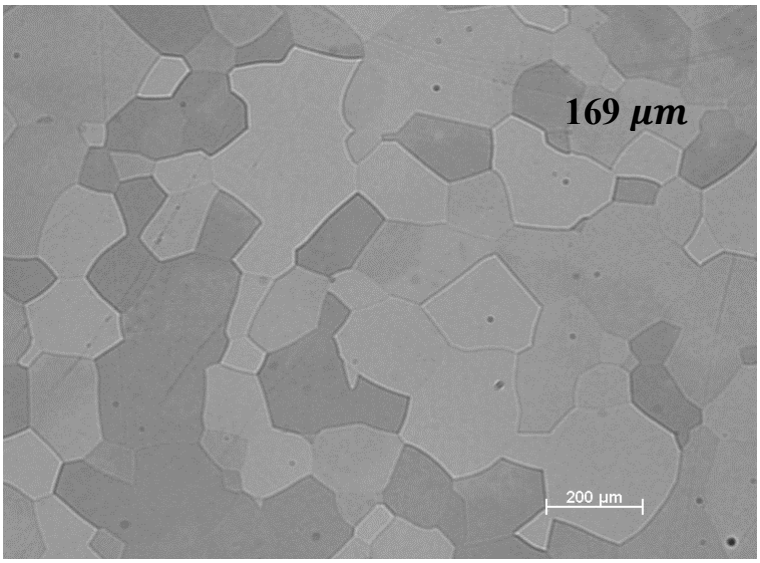

Fig. 43 OM image of PREP NC Ti-5553 alloy, 900℃ 1h.

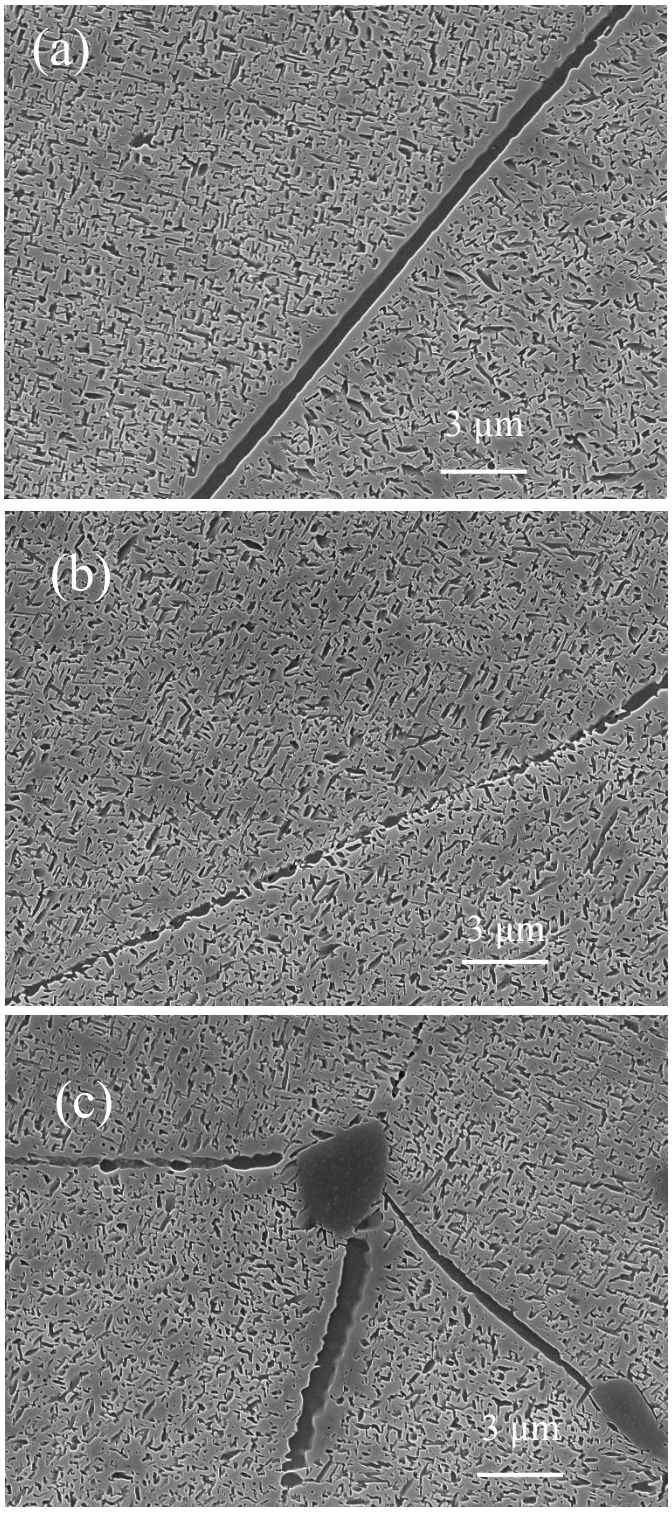

Fig. 44 SEM image of PREP C sample after ageing treatment.

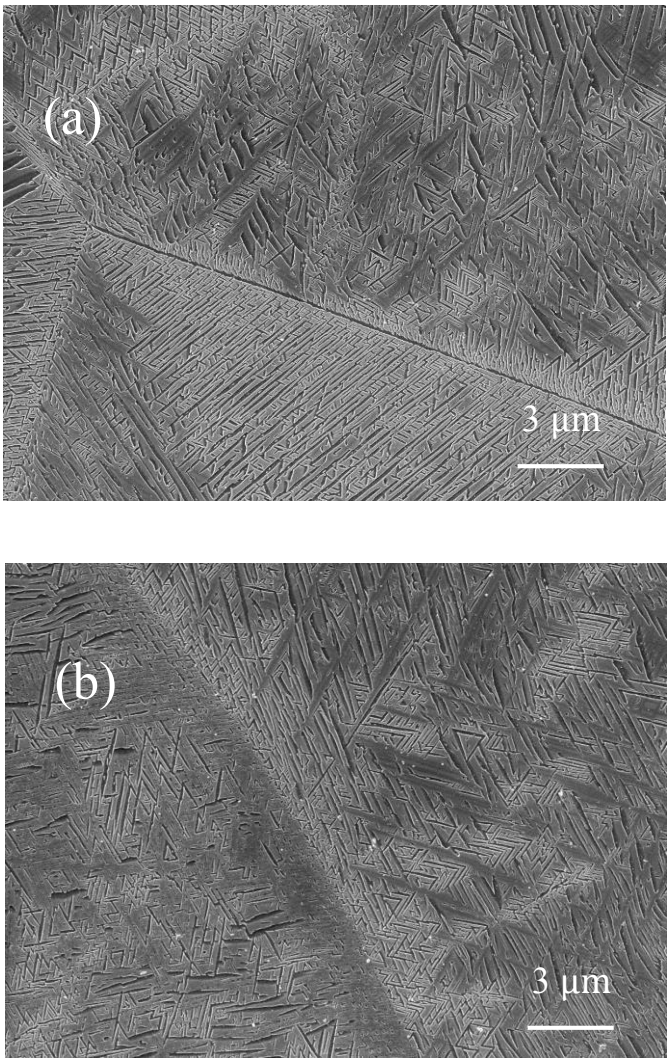

Fig. 45 SEM image of PREP NC Ti-5553 sample after ageing treatment.

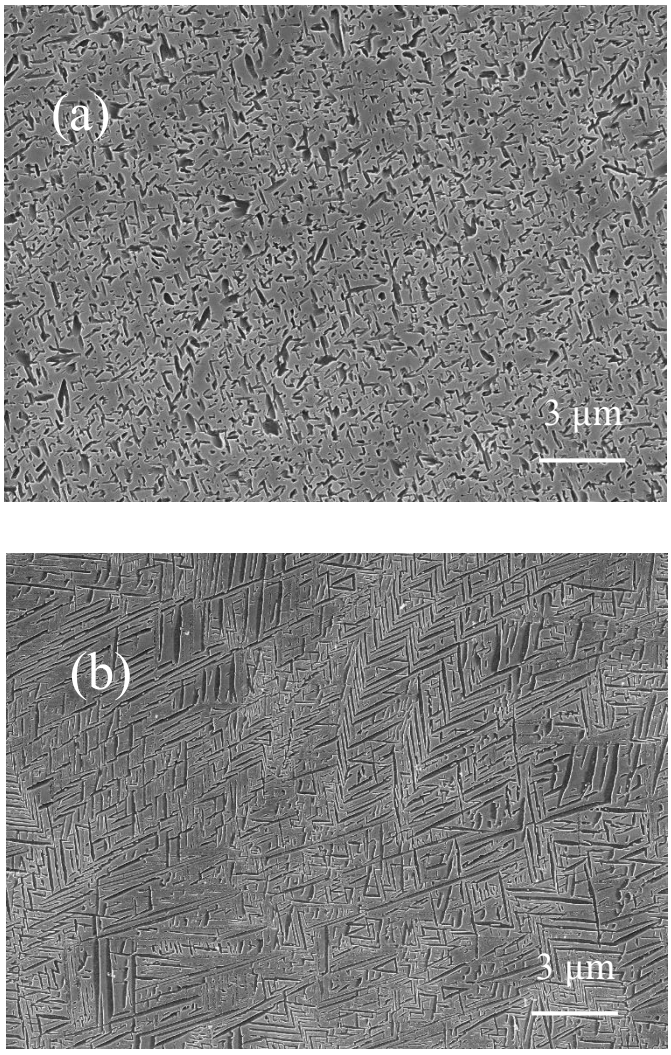

Fig. 46 The morphology of intragranlular α phase of two kinds of samples after ageing treatment, (a) is PREP C Ti-5553 samples, (b) is PREP NC Ti-5553 samples.

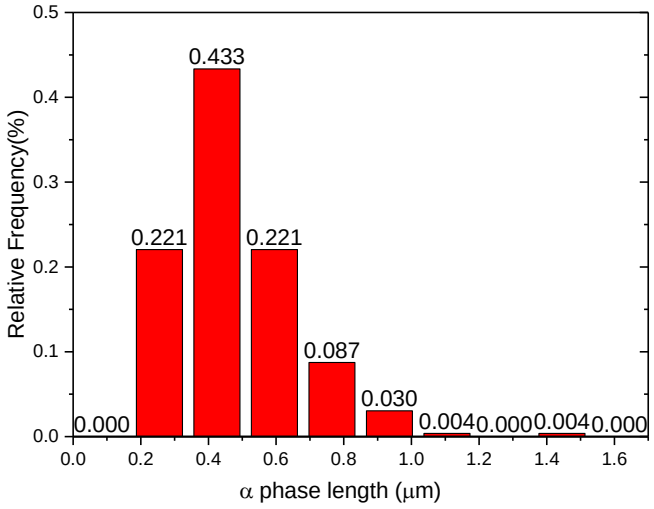

Fig. 47 Distribution of length of intragranular α phase of PREP C Ti-5553 alloy.

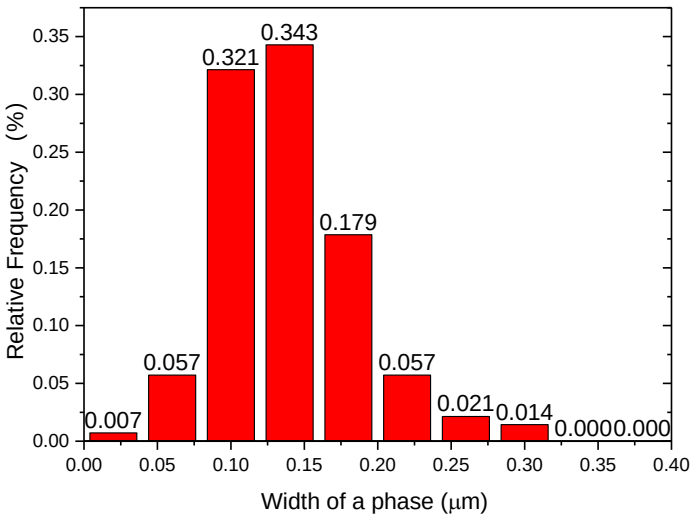

Fig. 48 Distribution of width of intragranular α phase of PREP C Ti-5553 alloy.

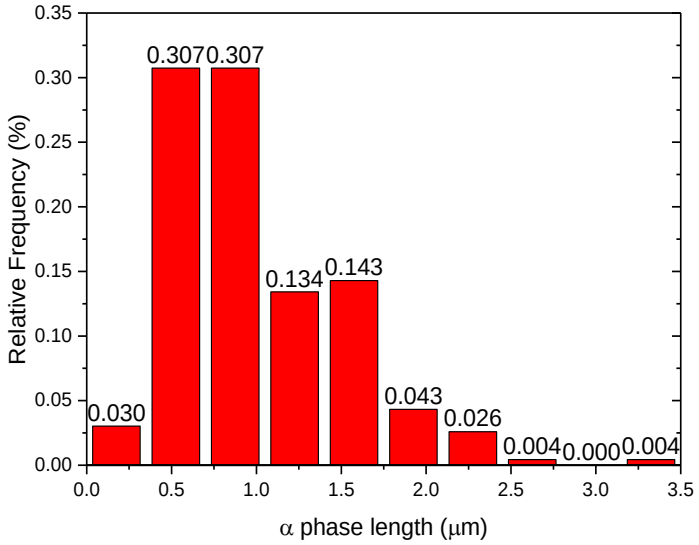

Fig. 49 Distribution of length of intragranular α phase of PREP NC Ti-5553 alloy.

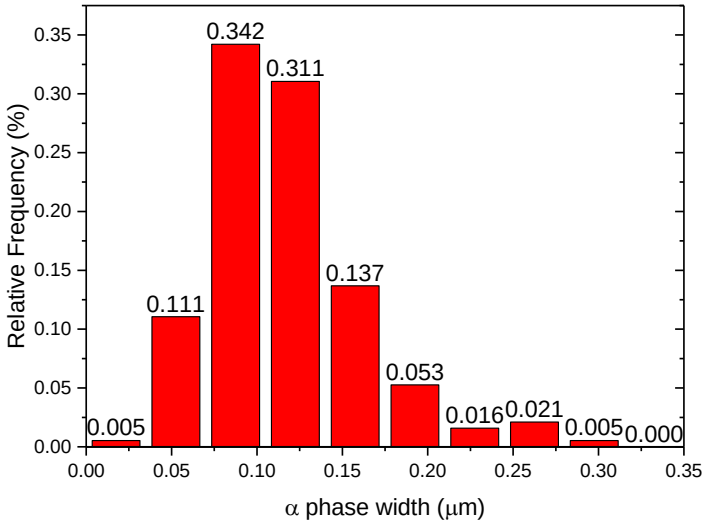

Fig. 50 Distribution of width of intragranular α phase of PREP NC Ti-5553 alloy.

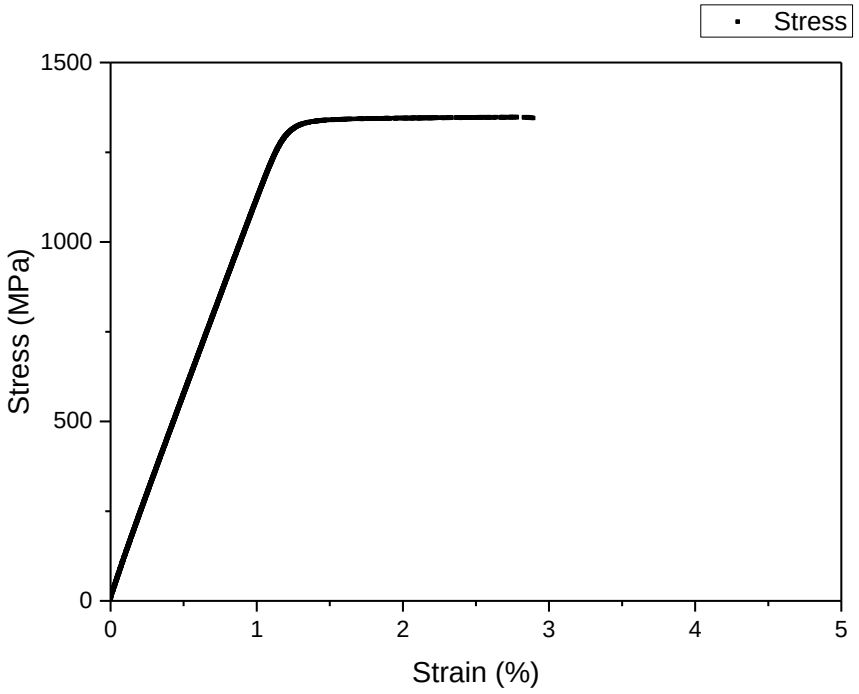

Fig. 51 Stress-Strain curve for room temperature tensile testing of PREP 0.08%C Ti-5553 samples.

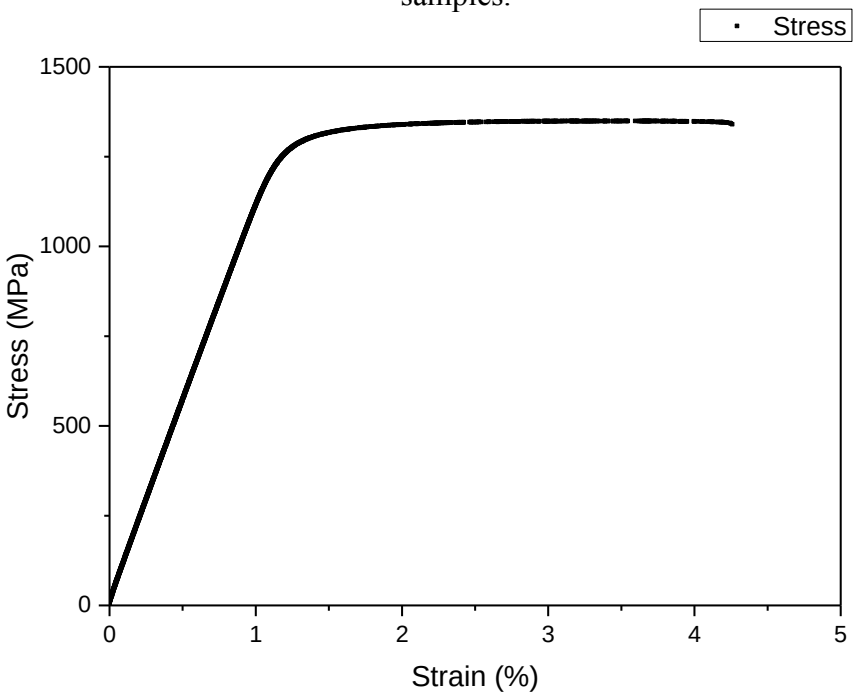

Fig. 52 Stress-Strain curve for room temperature tensile testing of PREP NC Ti-5553 samples.

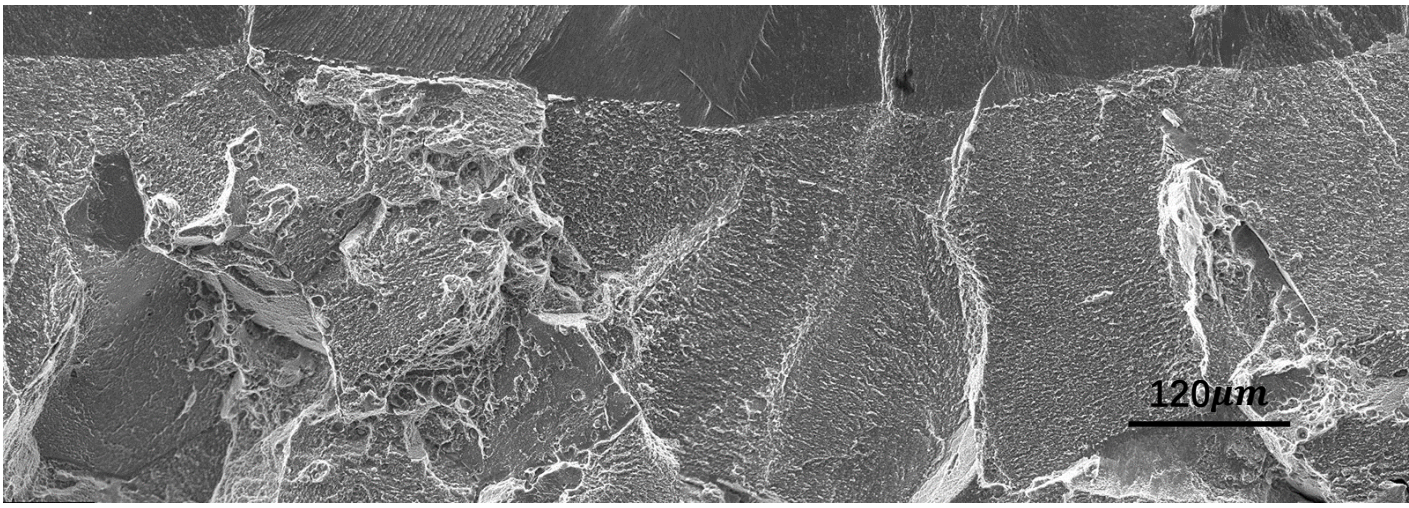

Fig. 53 SEM image of transition area between pre-crack and stable extension in PREP C Ti-5553 sample (1050℃ 4 h, WQ, 650℃ 6 h, WQ).

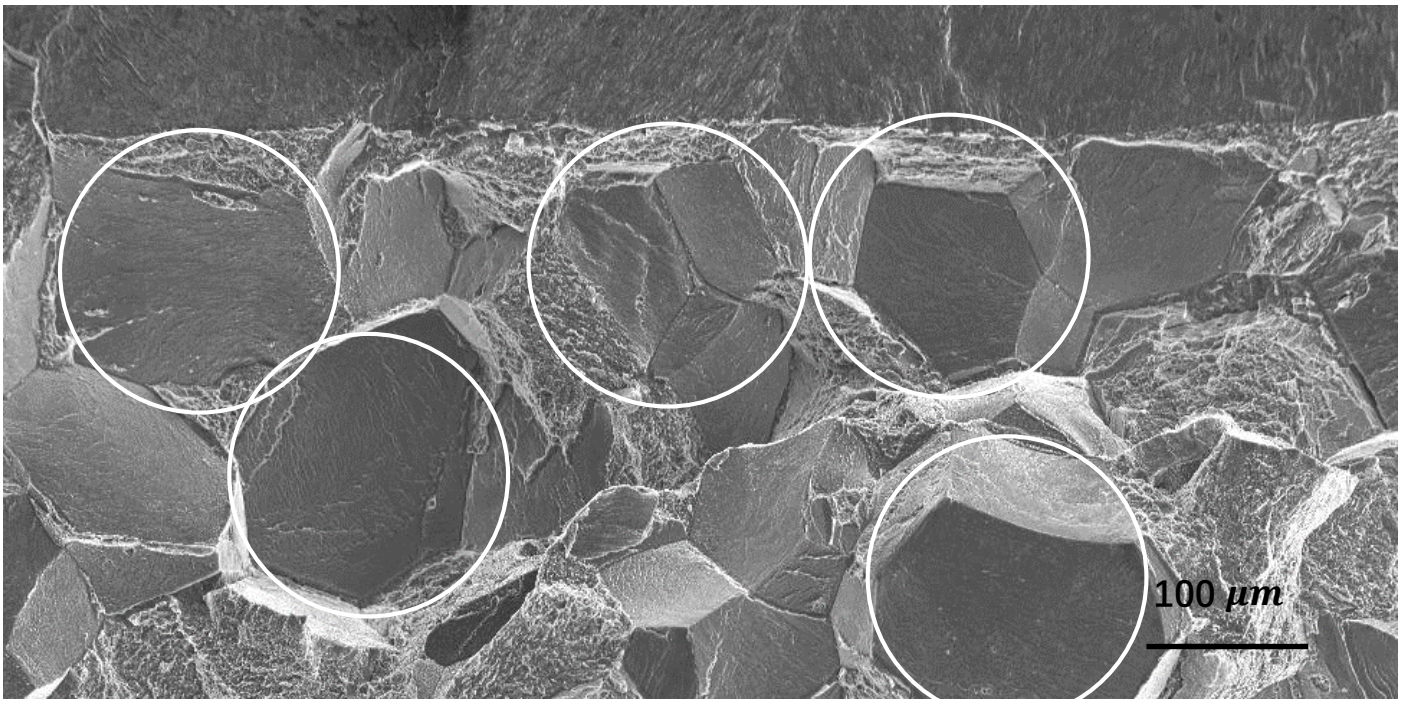

Fig. 54 SEM image of transition area between pre-crack and stable extension in PREP NC Ti-5553 sample (900℃ 1 h, WQ, 600℃ 6 h, WQ).

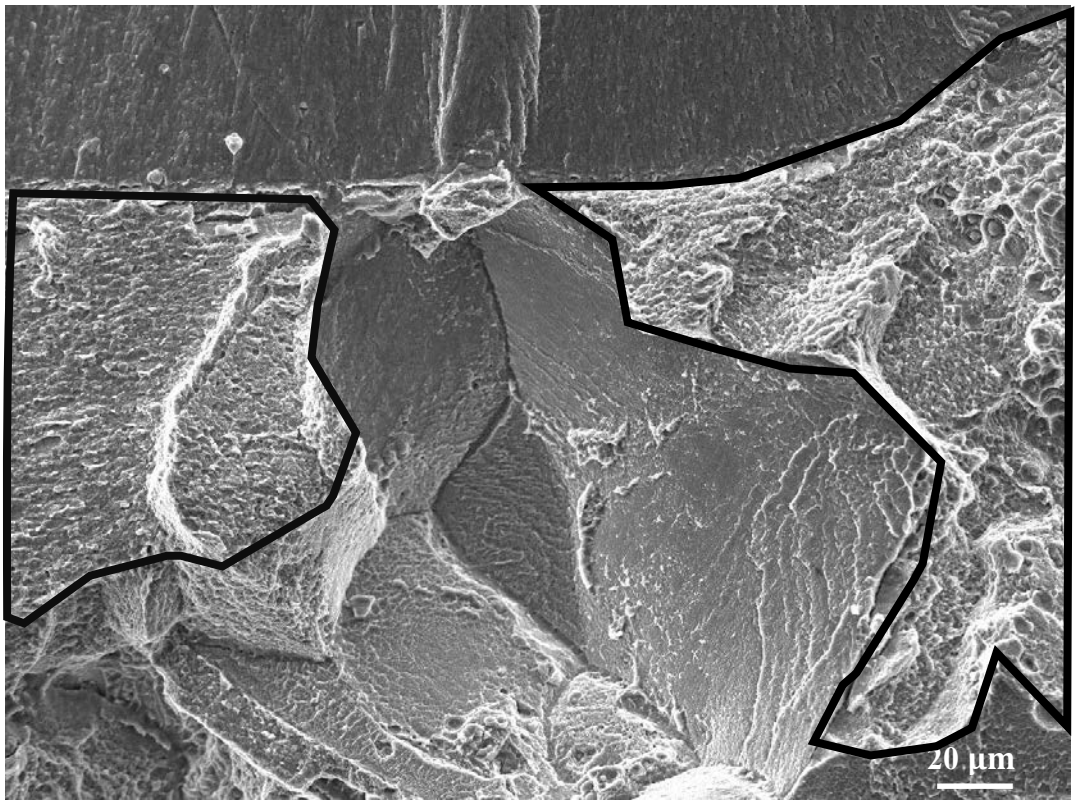

Fig. 55 High magnification image of a selected transition area including intergranular and transgranular fracture in PREP C Ti-5553 specimen.

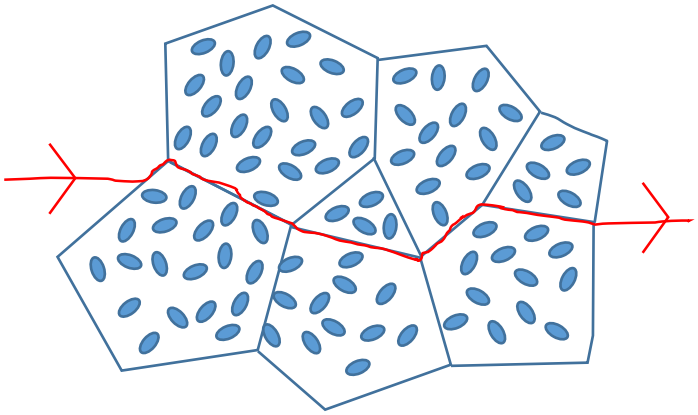

Fig. 56 The interpretation of crack propagating when it goes along weak grain boundary.

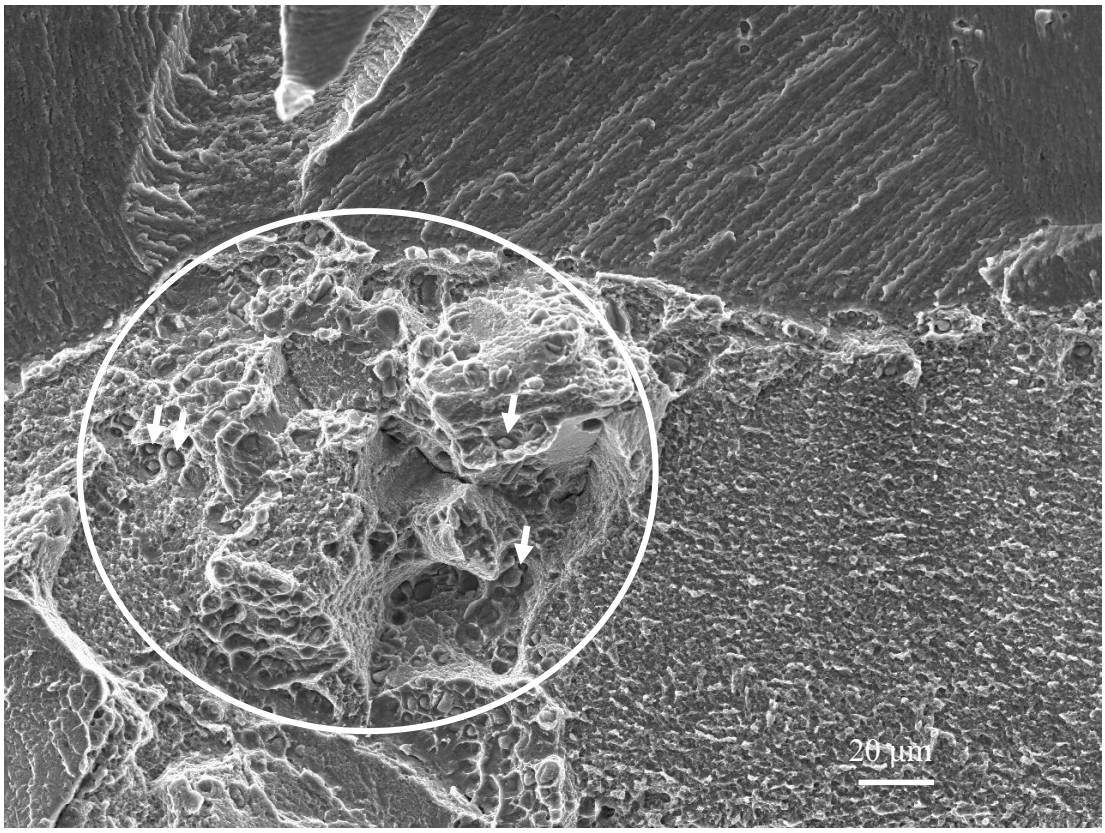

Fig. 57 High magnification image of a selected area in PREP C Ti-5553 specimen.

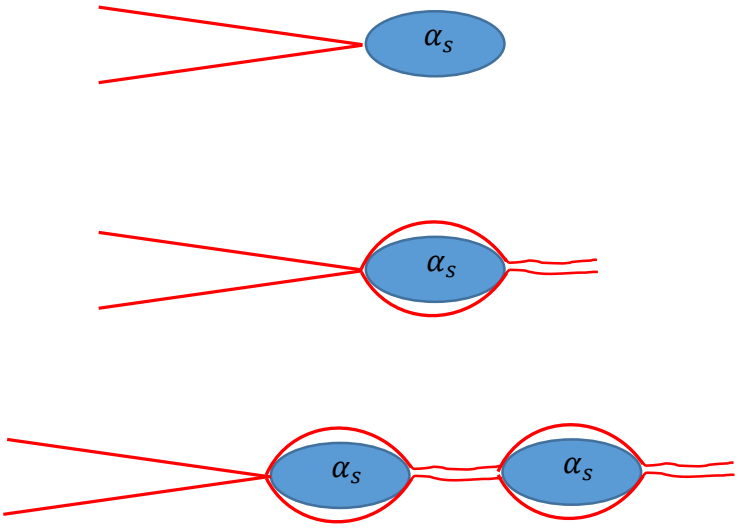

Fig. 58 Interpretation of crack encountering tiny α_s and going surround it during propagating process.

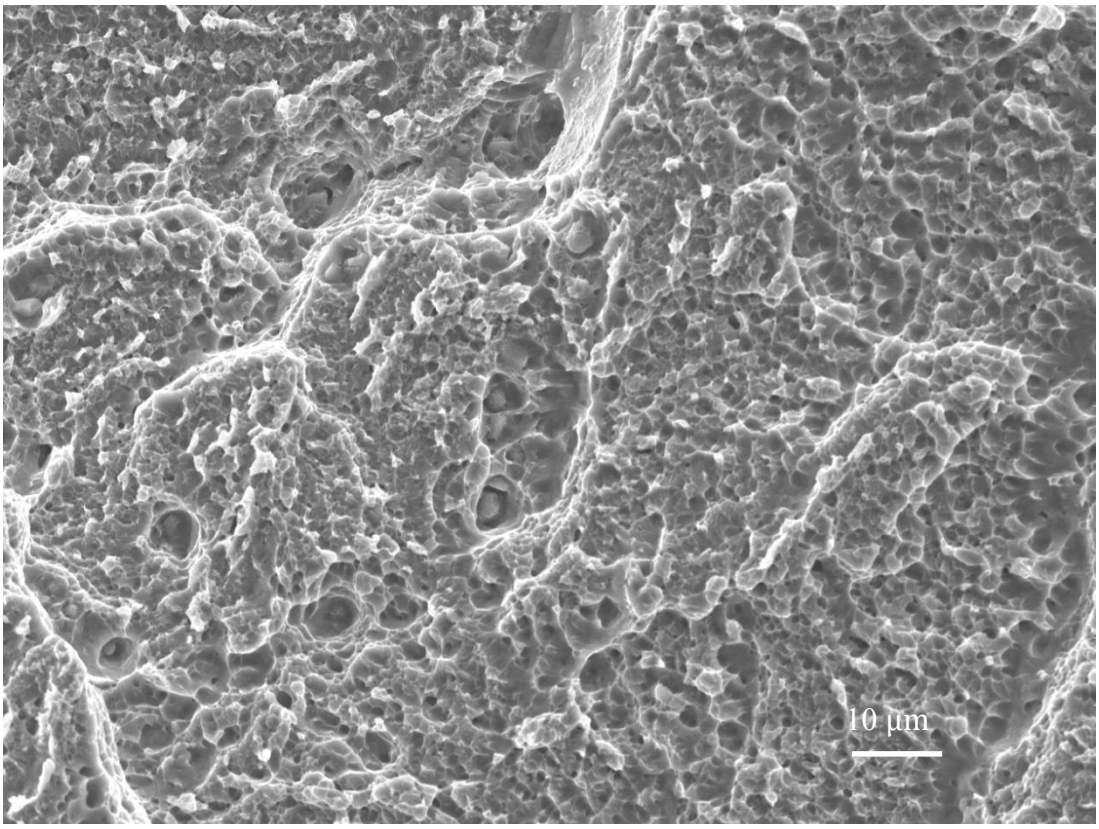

Fig. 59 High magnification SEM image at transgranular area in PREP C Ti-5553 specimen.

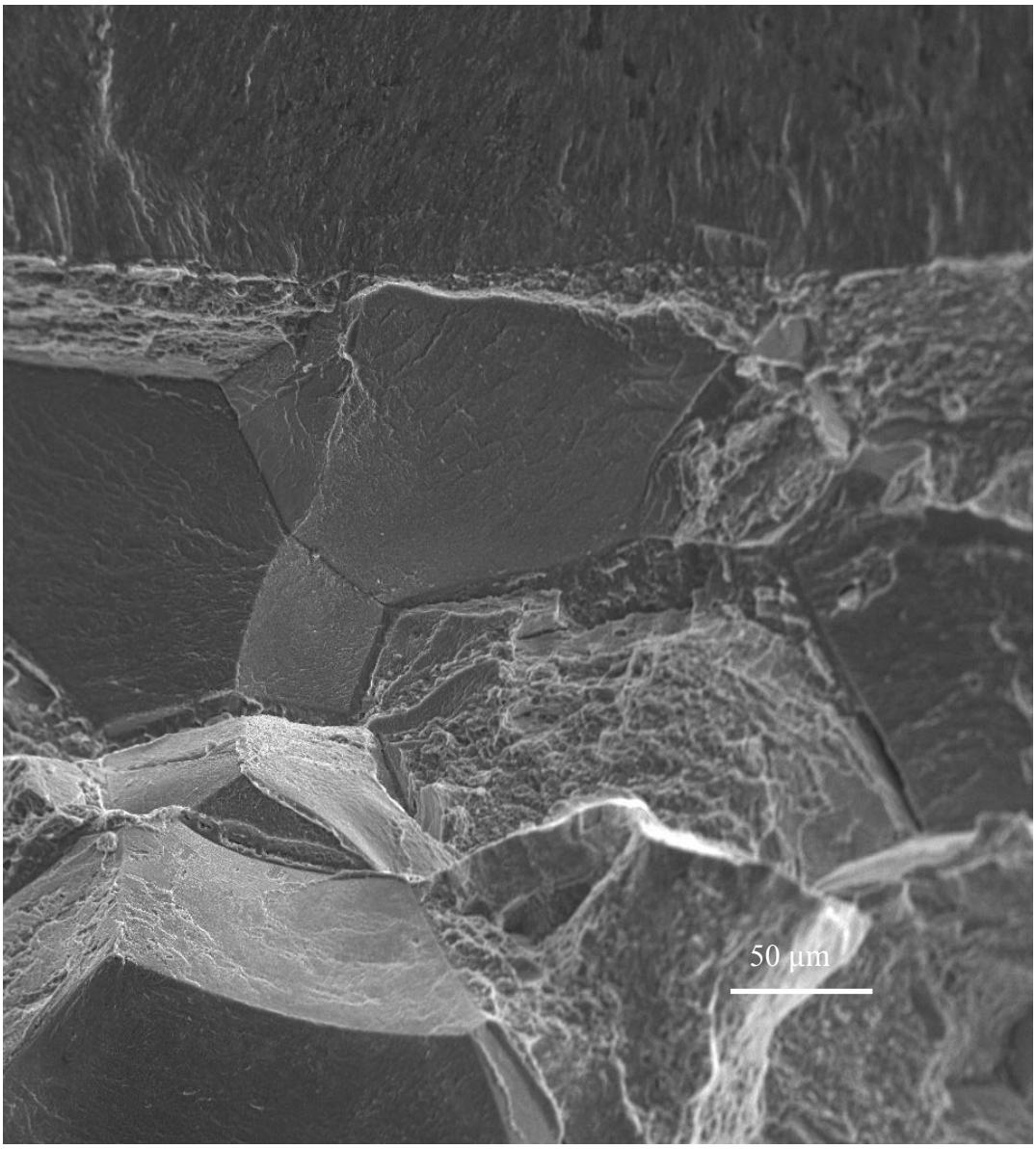

Fig. 60 High magnification image of a selected transition area including intergranular and transgranular fracture in PREP NC Ti-5553 specimen.

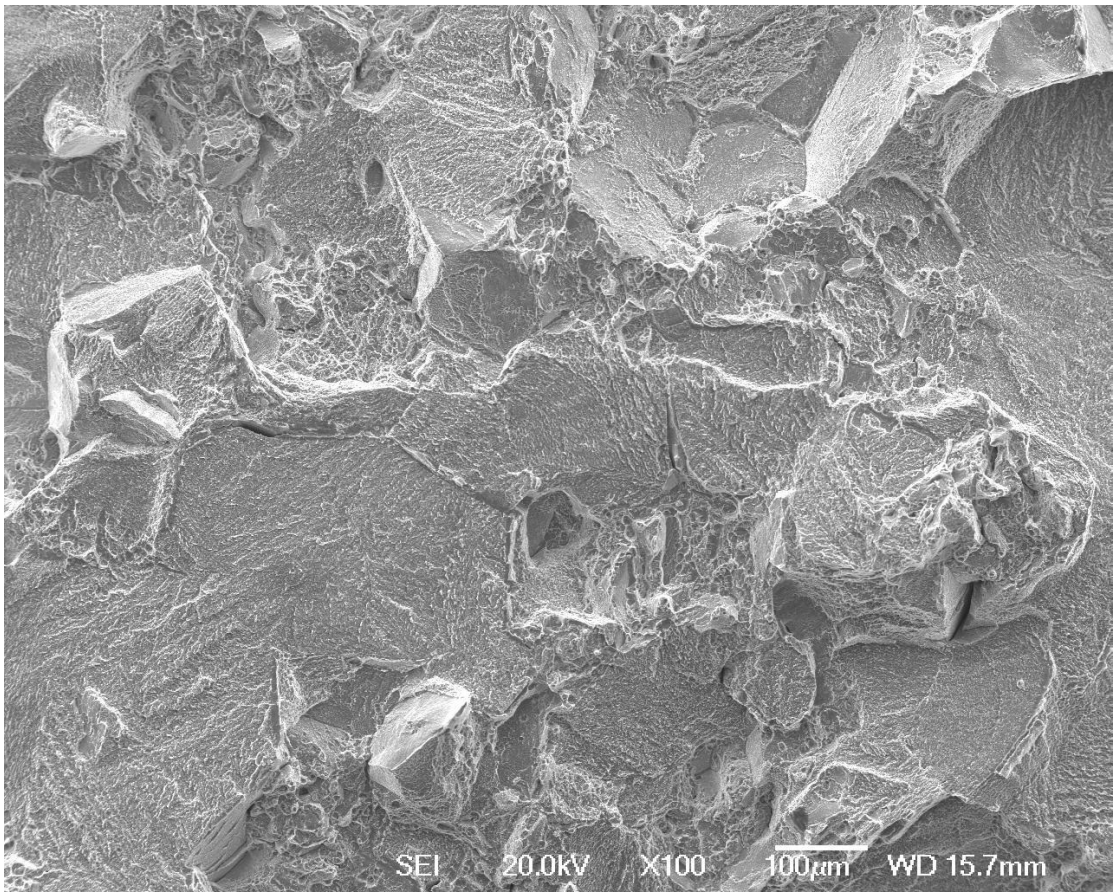

Fig. 61 Low magnification fractography of PREP C Ti-5553 specimen.

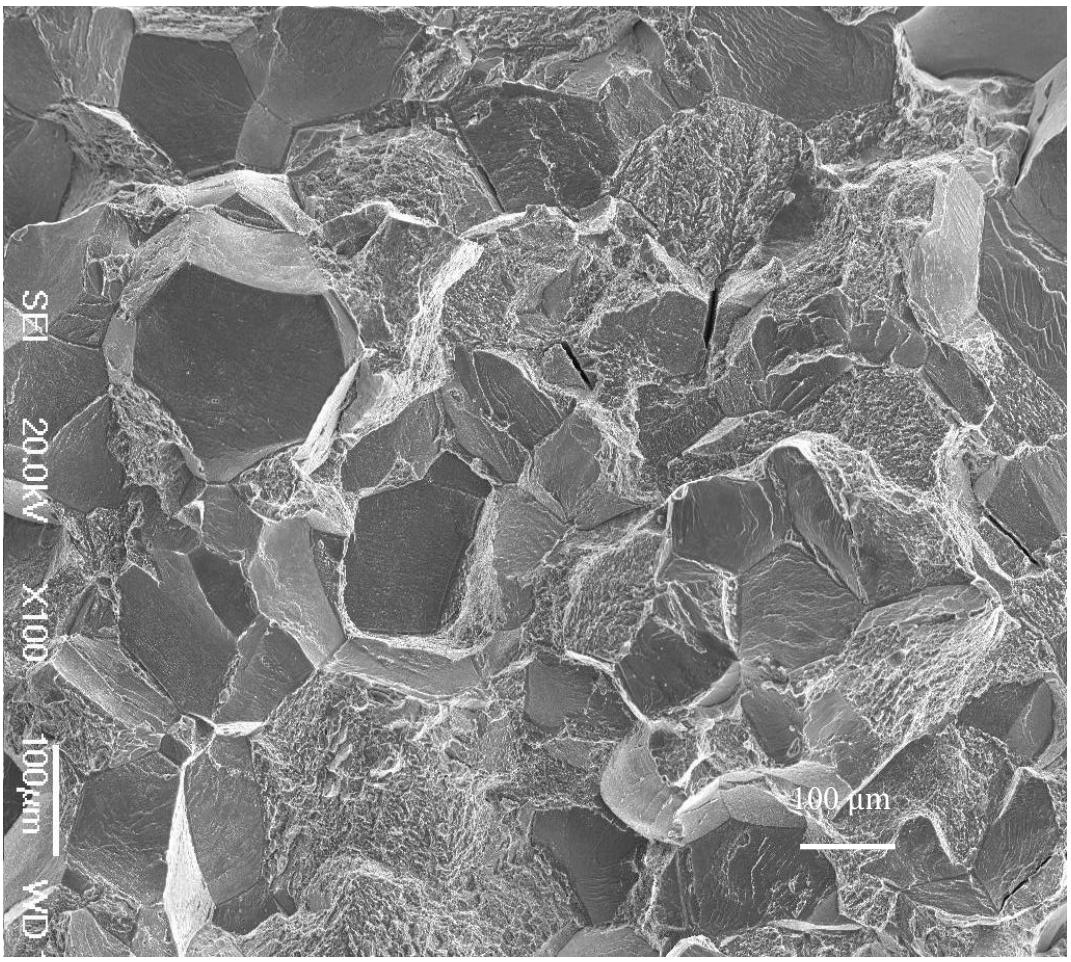

Fig. 62 Low magnification fractography of PREP NC Ti-5553 specimen.

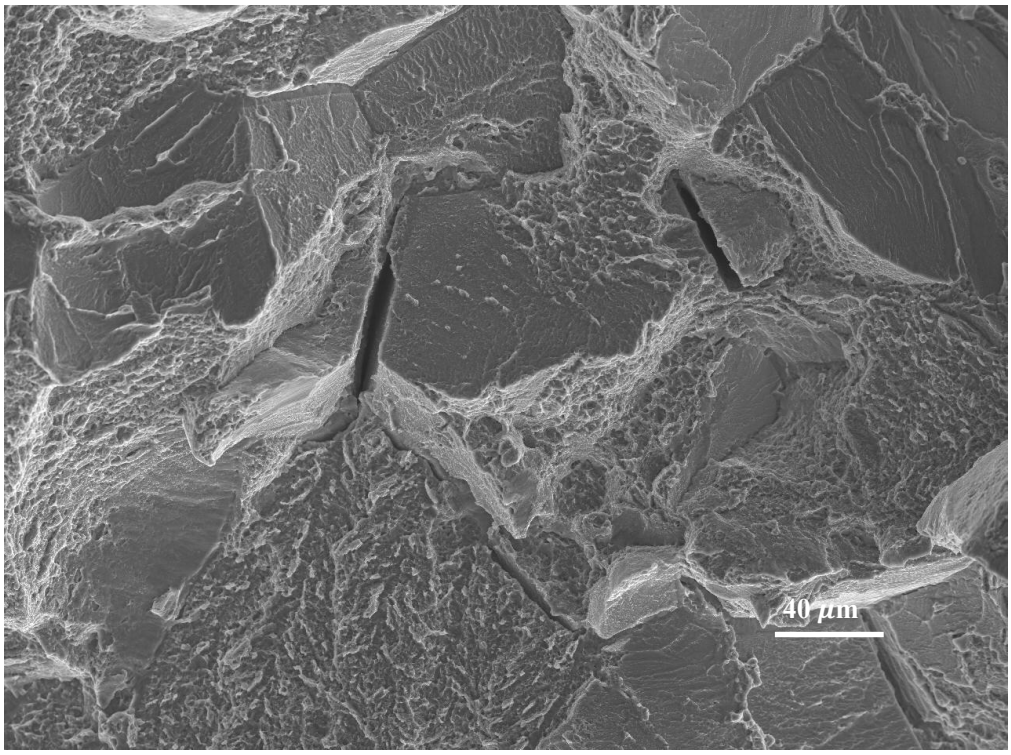

Fig. 63 High magnification image on selected area in PREP NC Ti-5553 alloy.

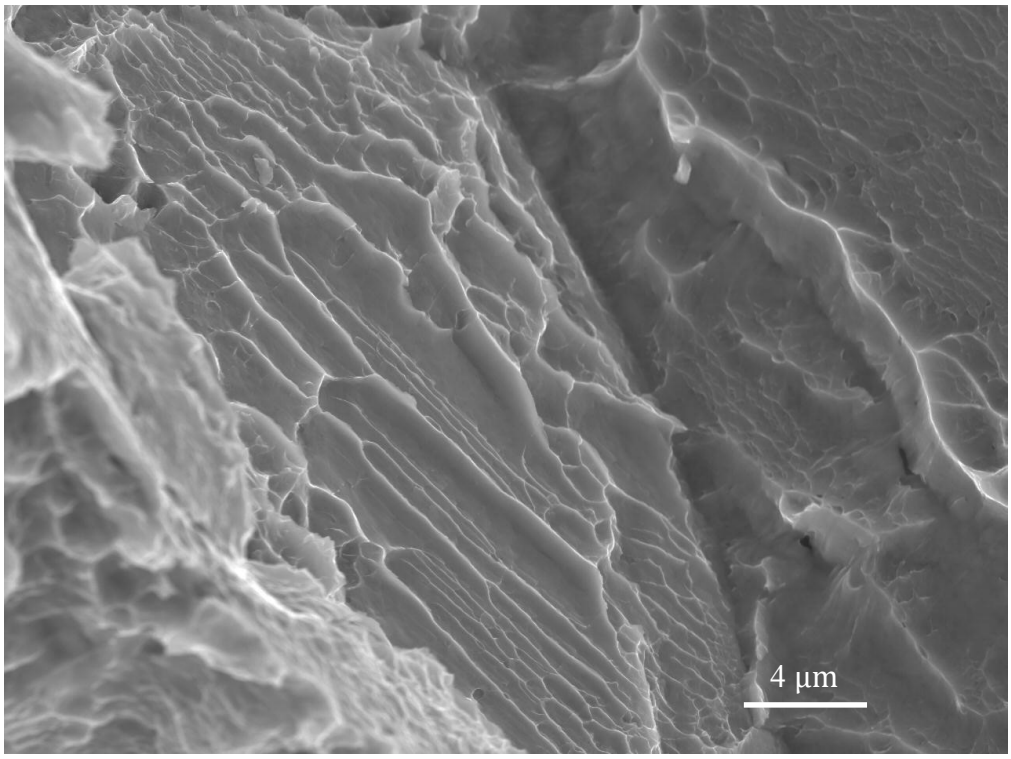

Fig. 64 High magnification image focusing on intergranular fracture facets in PREP NC Ti-5553 alloy.

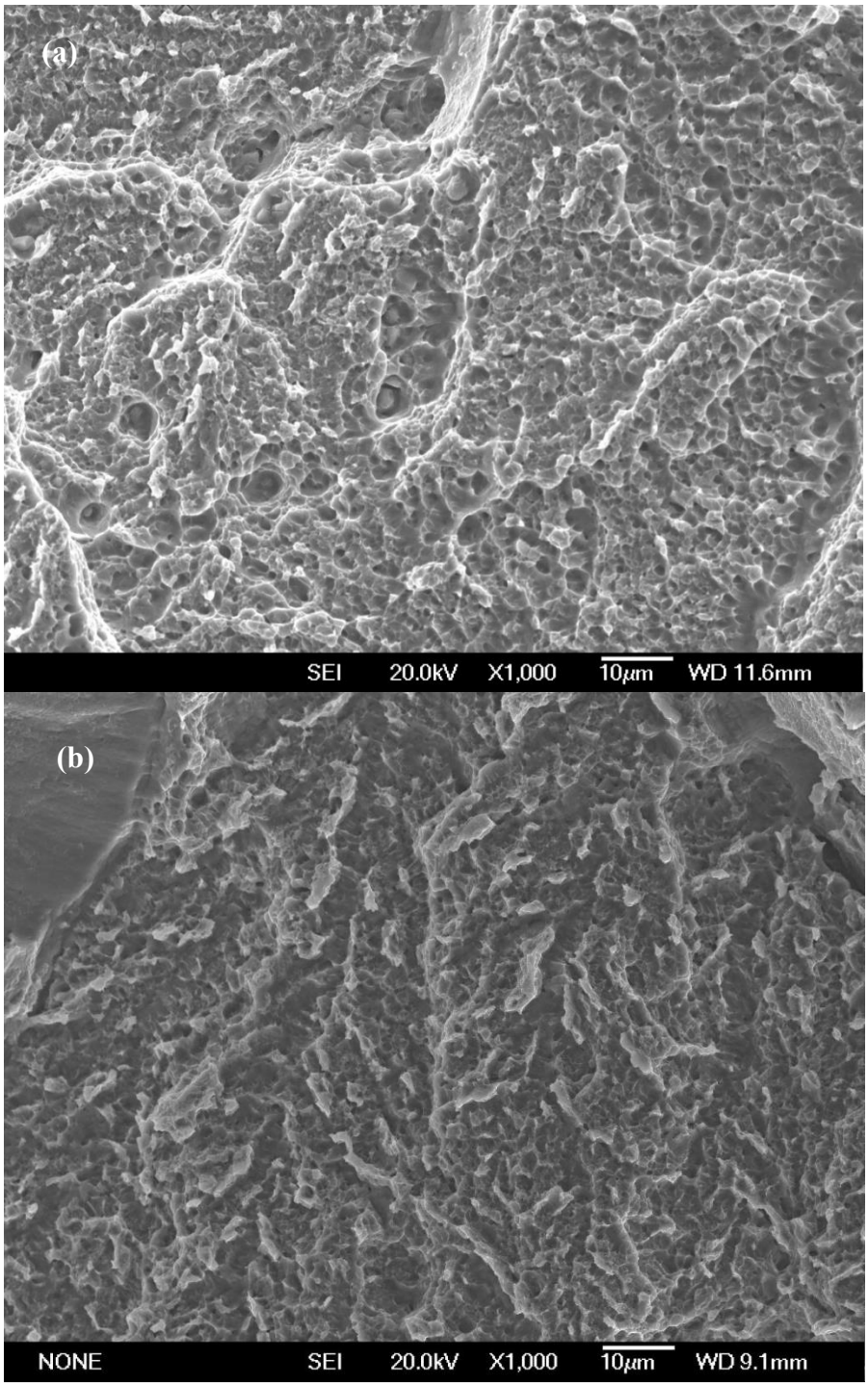

Fig. 65 1000x magnification image at transgranular fracture area of Ti-5553 specimens, (a) is in PREP C, (b) is in PREP NC.

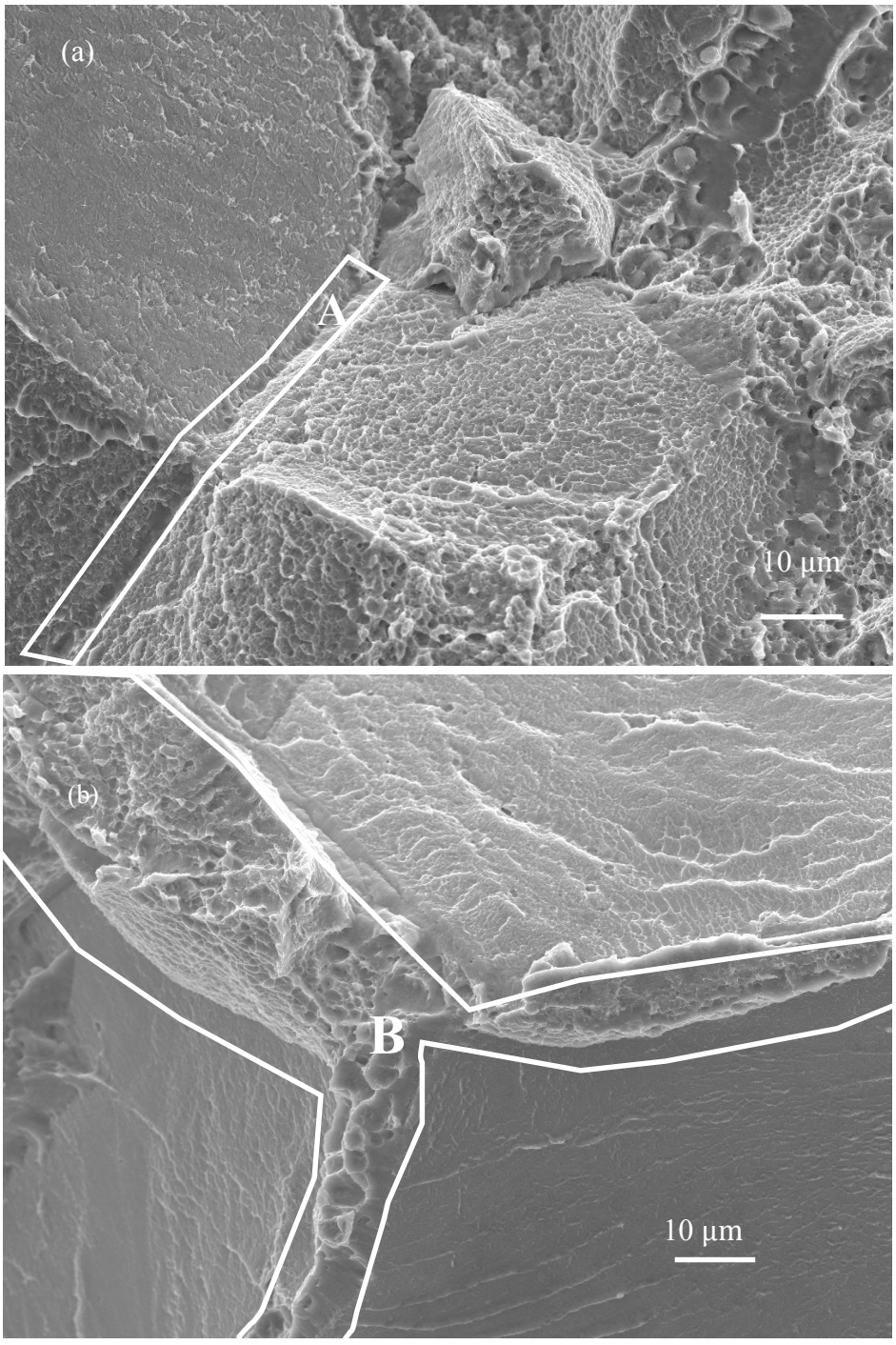

Fig. 66 1000x magnification images of intergranular fracture area of Ti-5553 specimens, (a) is in PREP C Ti-5553 specimen, (b) is PREP NC Ti-5553 specimen.

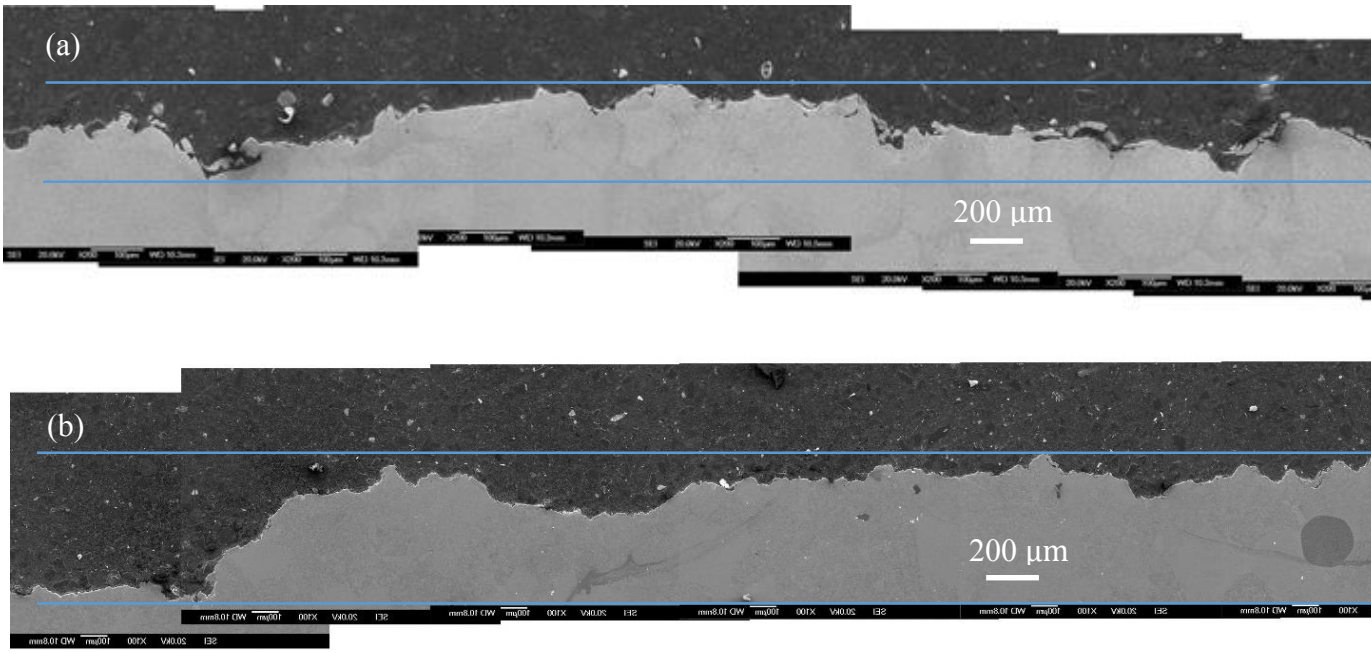

Fig. 67 Cross-sectional images of two kinds of PREP Ti-5553 alloy, (a) PREP C Ti-5553 sample, (b) PREP NC Ti-5553 sample, indicating different crack propagation path.

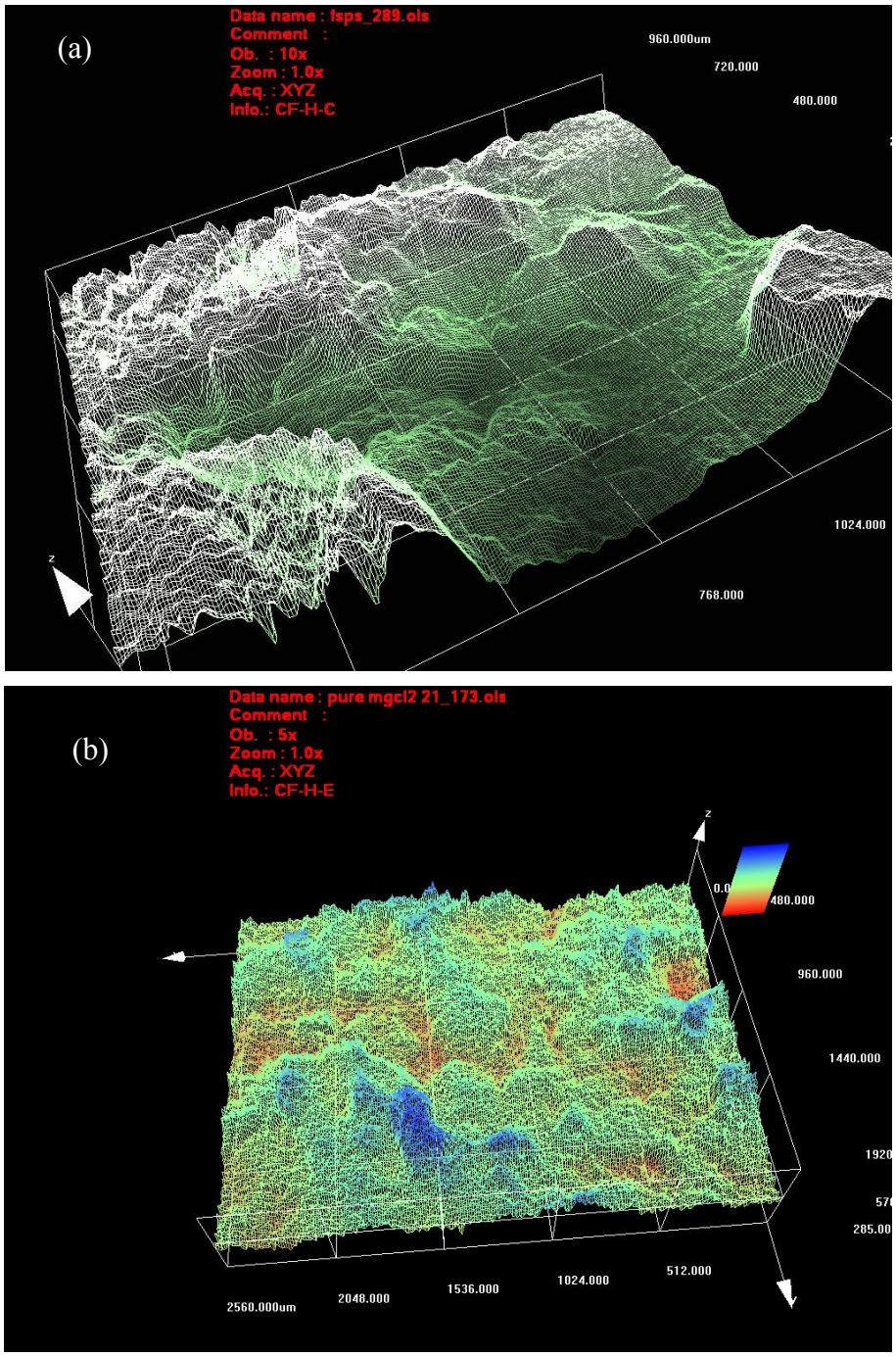

Fig. 68 Confocal images of two kinds of Ti-5553 alloy, (a) PREP C Ti-5553, (b) PREP NC Ti-5553.

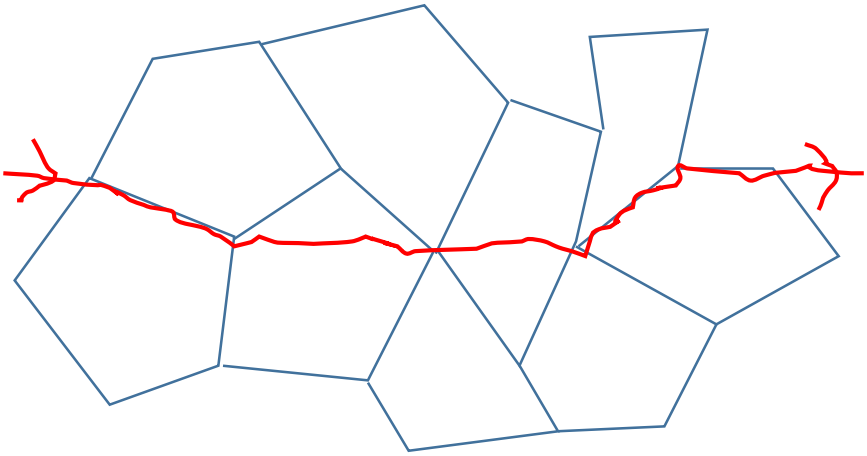

Fig. 69 An interpretation of mixed fracture occurred in PREP C Ti-5553 alloy.

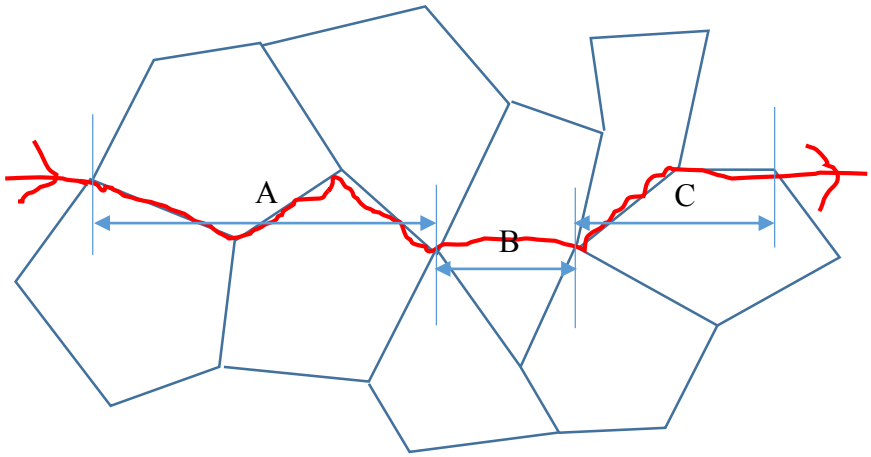

Fig. 70 An interpretation of mixed fracture occurred in PREP NC Ti-5553 alloy.

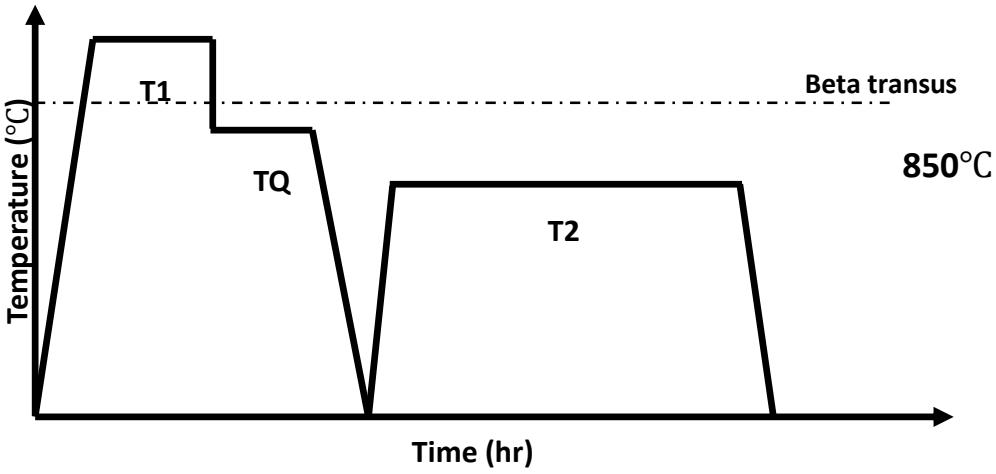

Fig. 71 SQA processing schedule for undoped PREP Ti-5553 alloy.

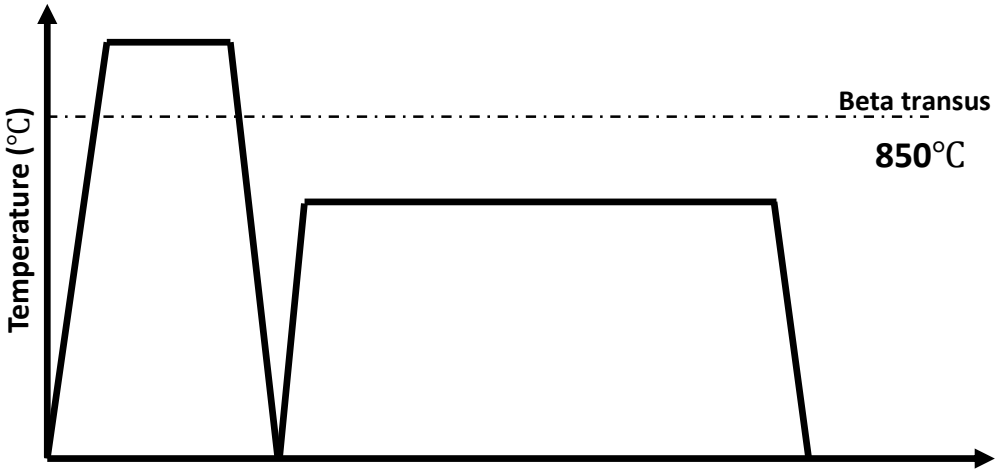

Fig. 72 STA processing schedule for undoped PREP Ti-5553 alloy.

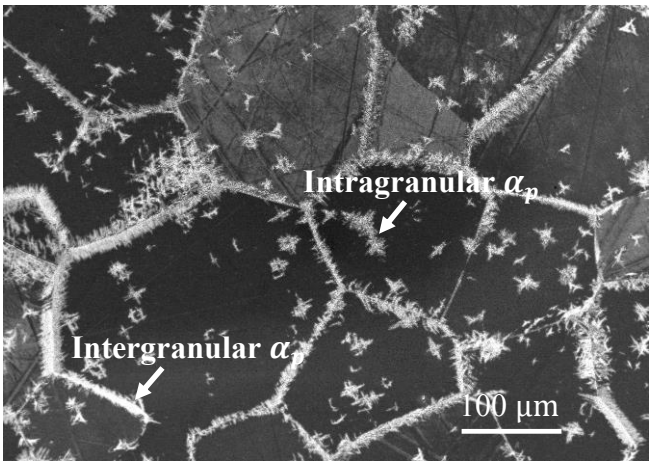

Fig. 73 SEM image of undoped PREP Ti-5553 sample which were solutionized at 900℃ for 1 h, step quenched and held at 650℃ for 40 min followed by water quenching.

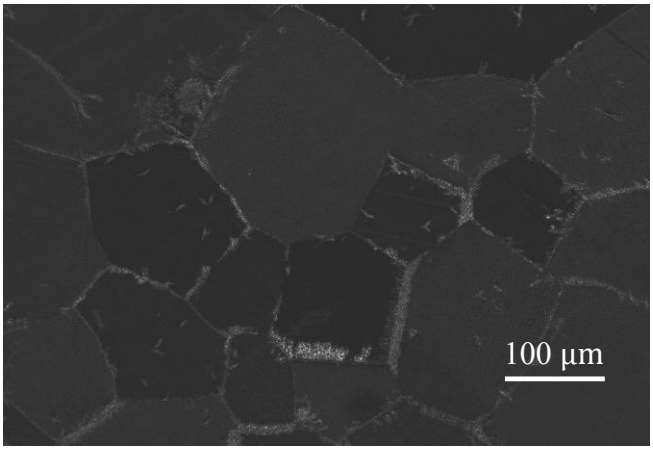

Fig. 74 SEM image of undoped PREP Ti-5553 sample which were solutionized at 900℃ for 1 h, step quenched and held at 680℃ for 40 min followed by water quenching.

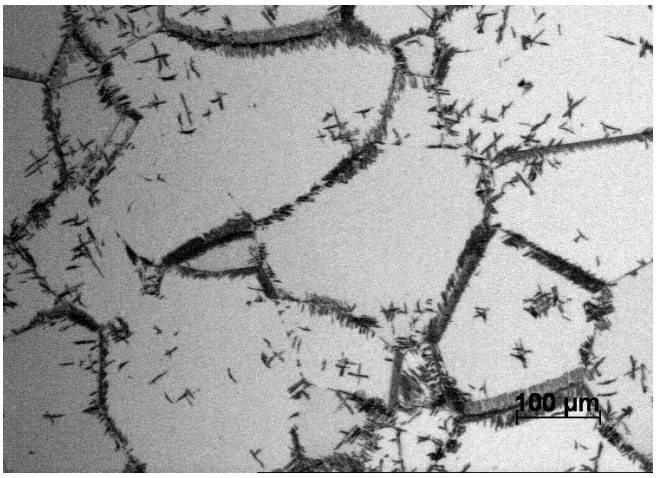

Fig. 75 OM image of undoped PREP Ti-5553 sample which were solutionized at 900℃ for 1 h, step quenched and held at 680℃ for 1h followed by water quenching.

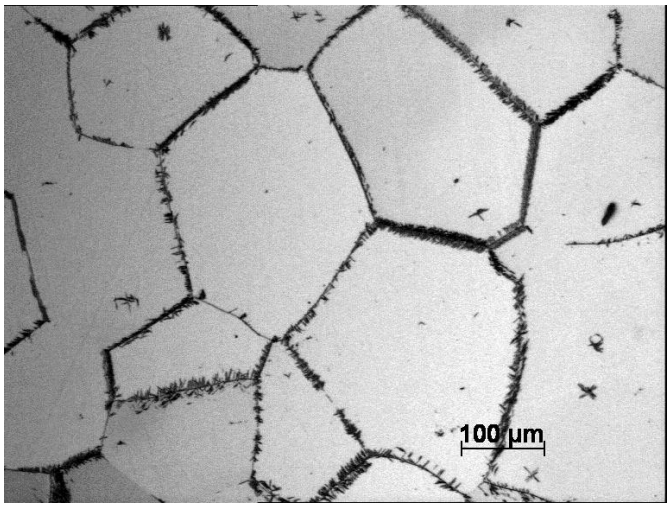

Fig. 76 OM image of undoped PREP Ti-5553 sample which were solutionized at 1000℃ for 1 h, step quenched and held at 680℃ for 40 min followed by water quenching.

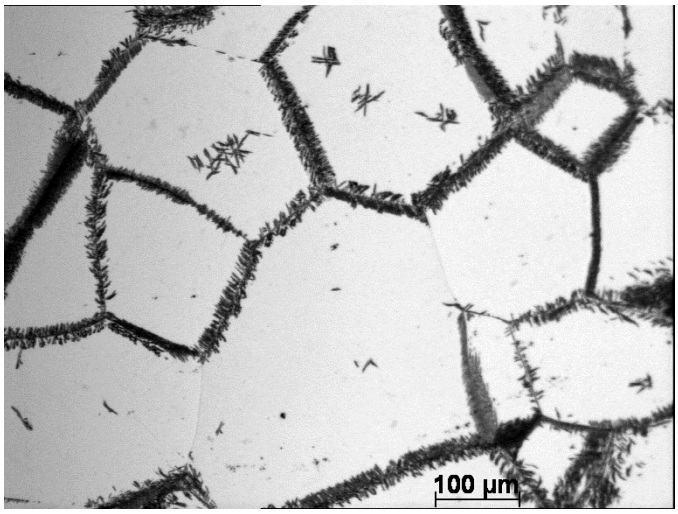

Fig. 77 OM image of undoped PREP Ti-5553 sample which were solutionized at 1000℃ for 1 h, step quenched and held at 680℃ for 1 h followed by water quenching.

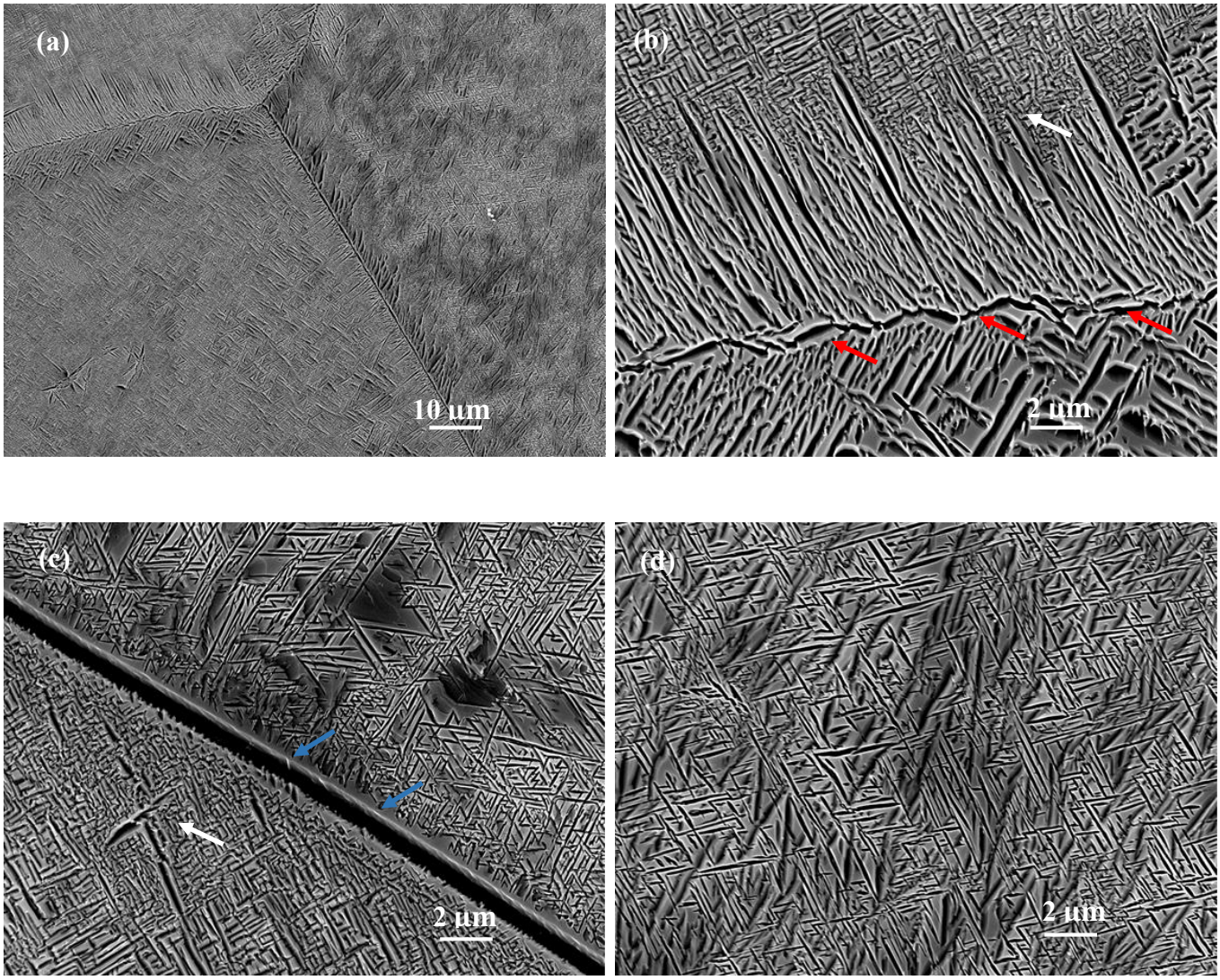

Fig. 78 SEM images of undoped Ti-5553 samples which were solution treated at 900℃ for 1 h, step quenched and held at 650℃ for 40 min, and aged at 600℃ for 4 h.

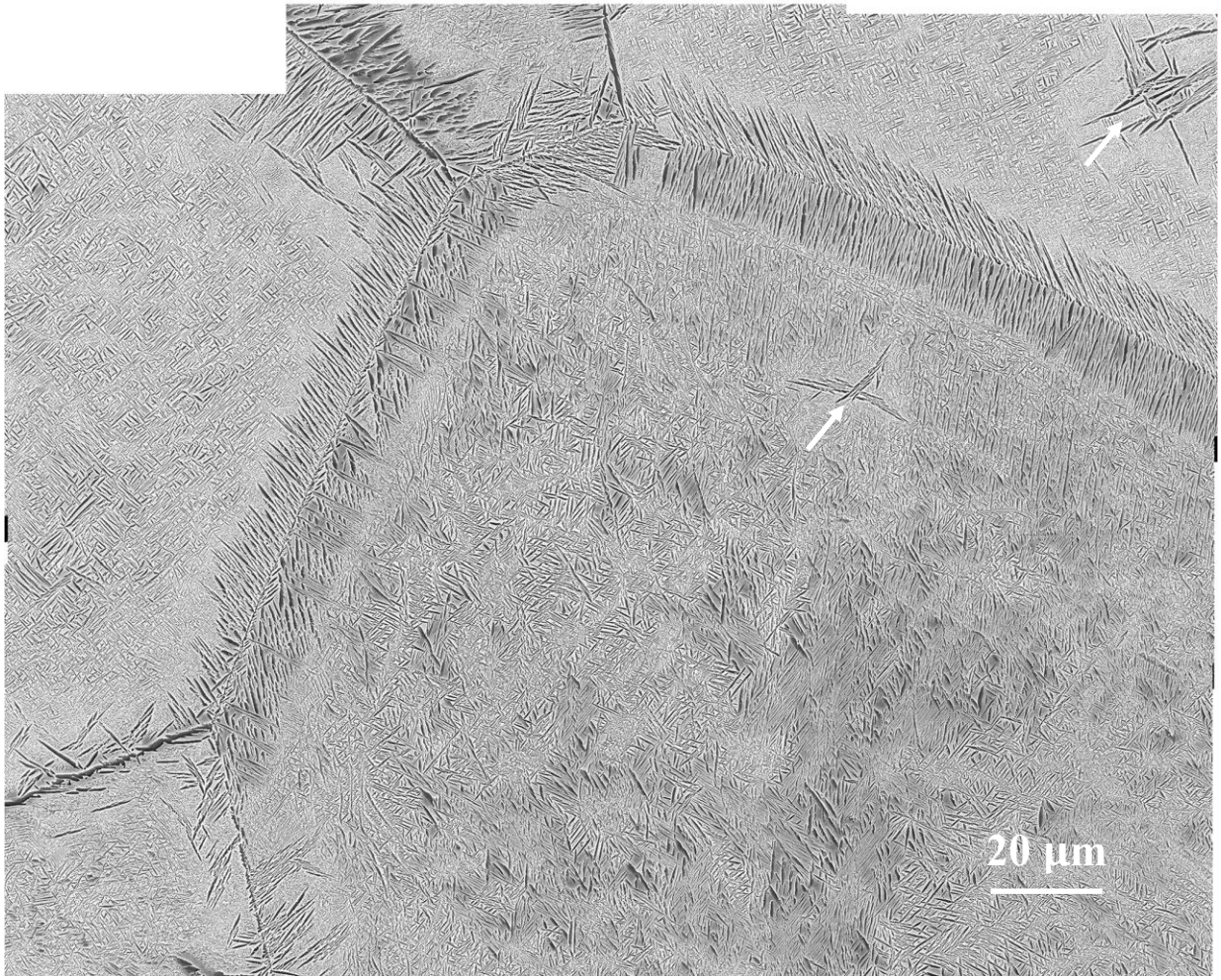

Fig. 79 Low magnification SEM image (composed by a few pictures) of undoped Ti-5553 samples which were solutionized at 1000℃ for 1 h, step quenched and held at 680℃ for 1 h, and aged at 640℃ for 5 h.

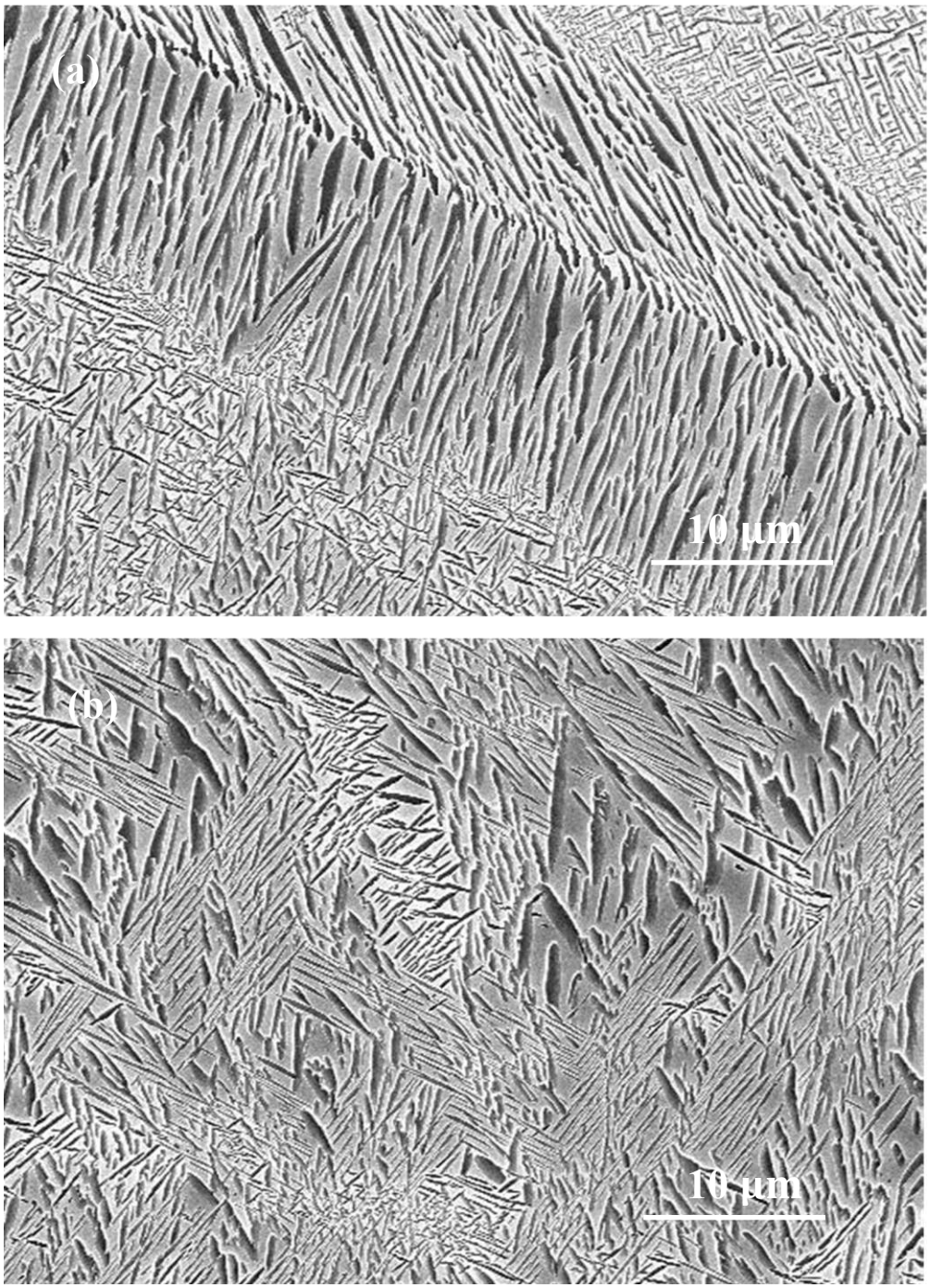

Fig. 80 Enlargement of two areas in Fig. 79, (a) showing precipitation of α_p at grain boundaries area, (b) showing precipitation of α_s within β grains.

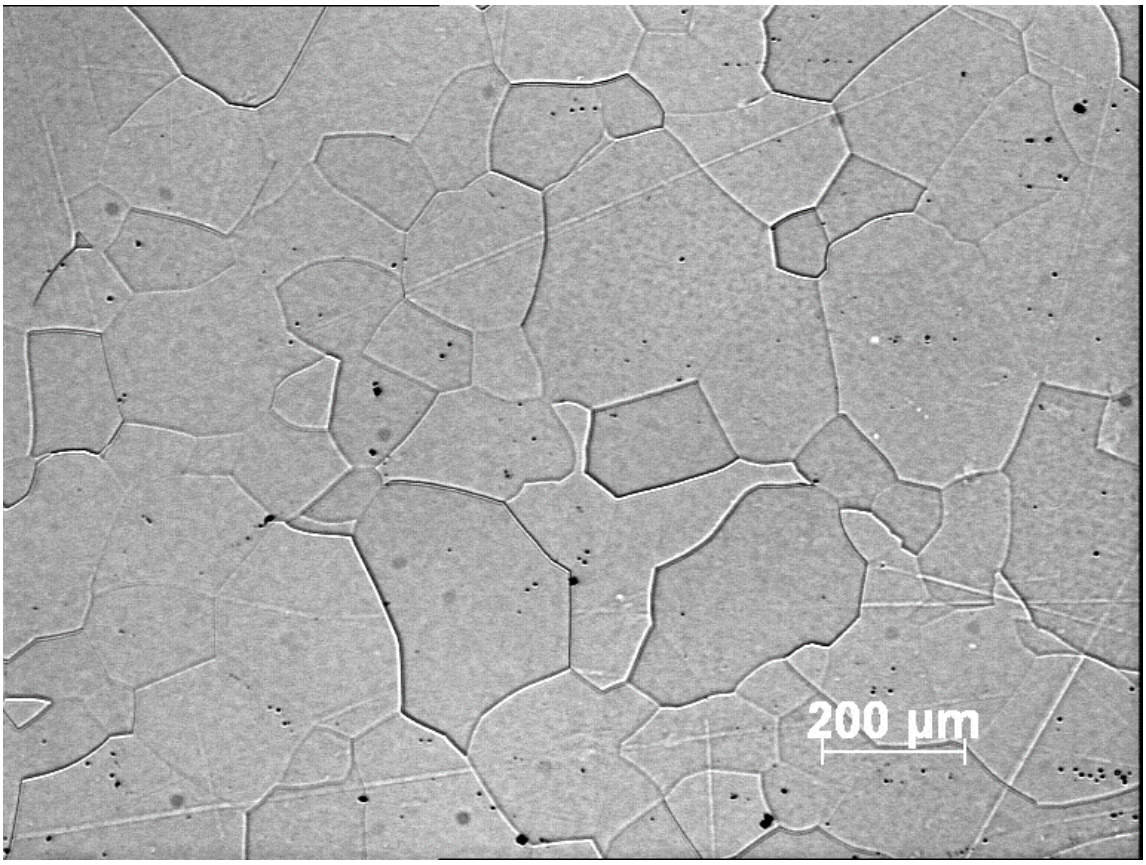

Fig. 81 OM image of undoped PREP Ti-5553 sample which were solutionized at 900℃, 1h and water quenched to room temperature.

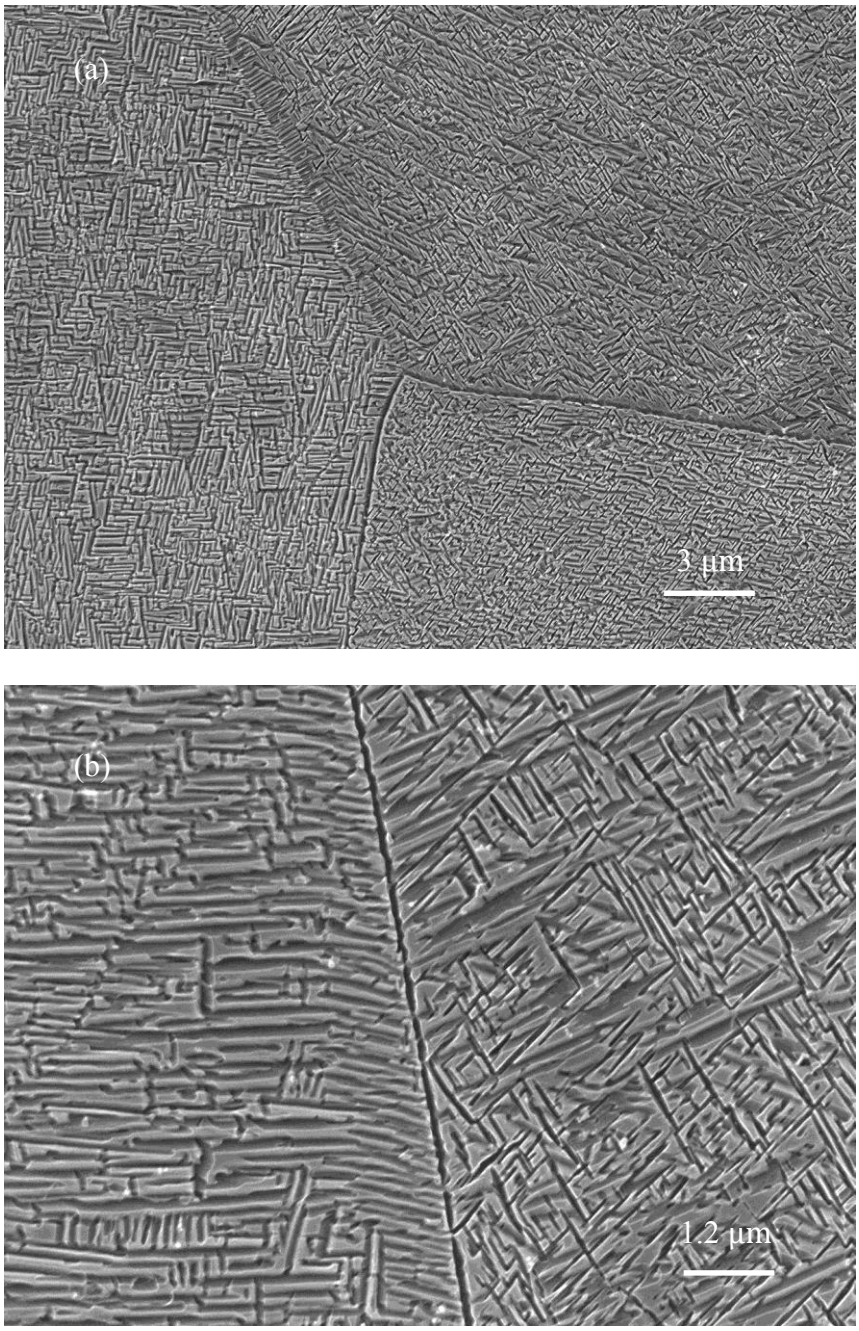

Fig. 82 SEM images for PREP Ti-5553 specimen (STA 1), 900℃ 1h, WQ, 600℃ 6h, WQ, (a) x4000, (b) x10000

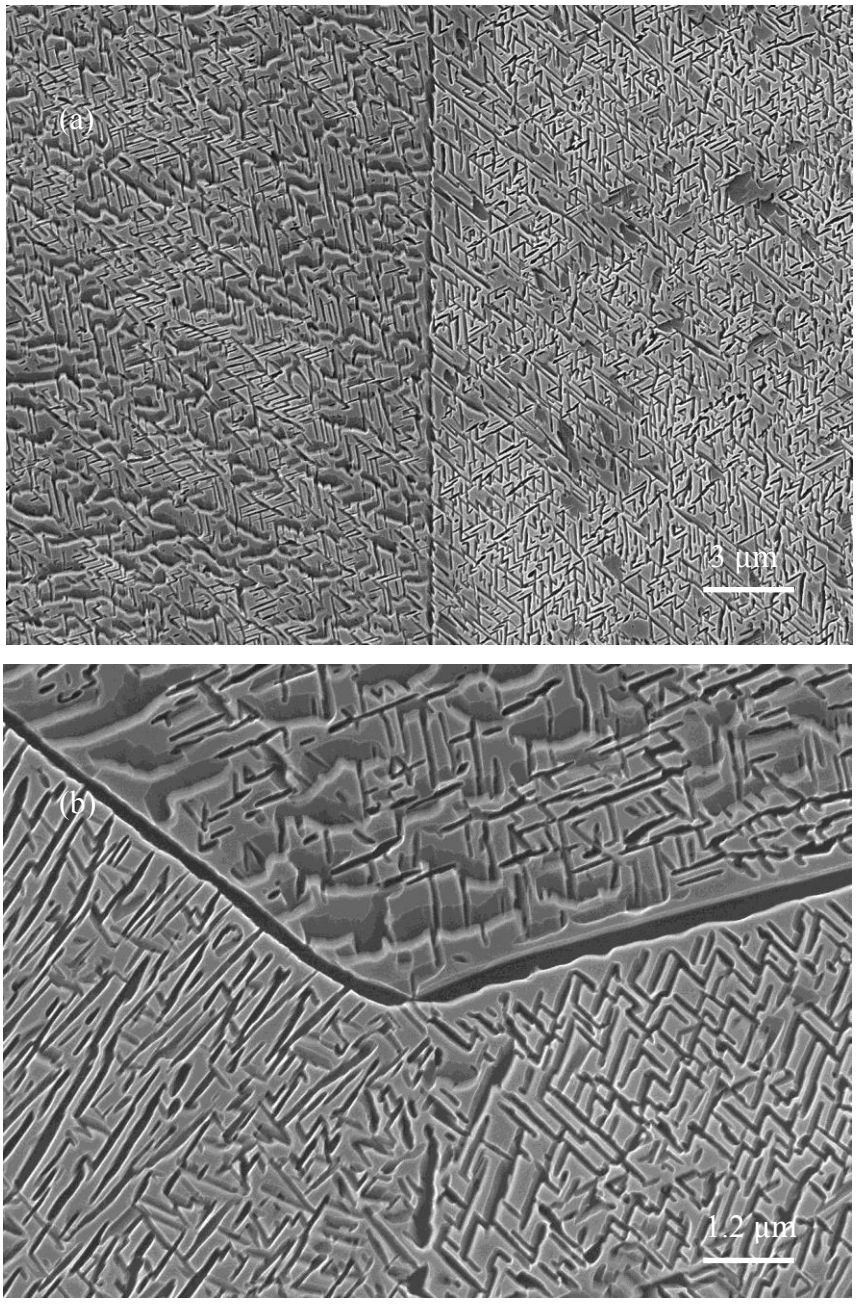

Fig. 83 SEM images for PREP Ti-5553 specimen (STA 2), 900℃ 1h, WQ, 650℃ 6h, WQ, (a) x4000, (b) x10000

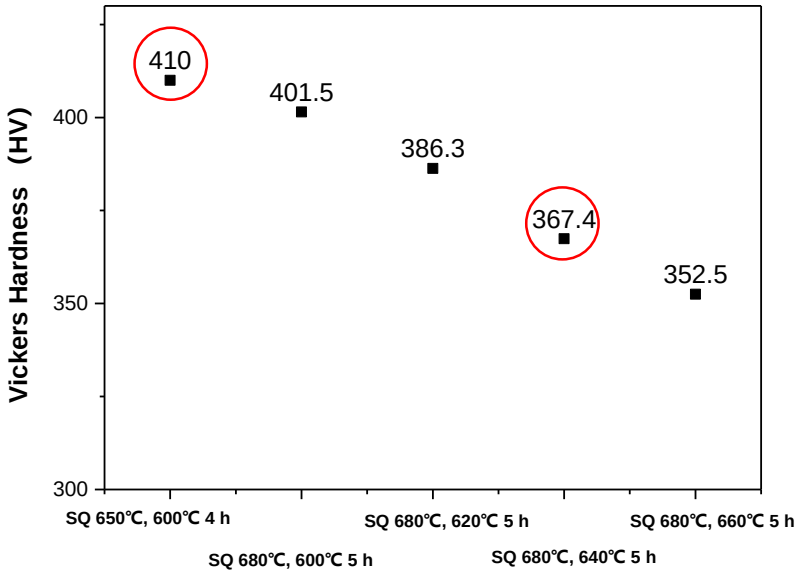

Fig. 84 Vickers hardness testing results of different SQ samples.

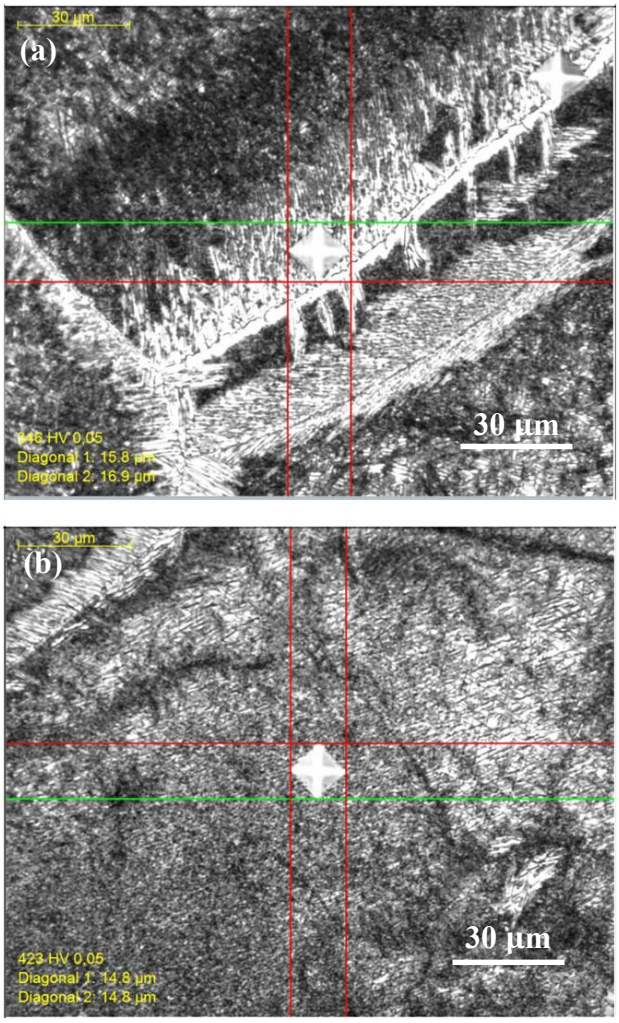

Fig. 85 OM images of hardness testing, (a) at grain boundaries area (on shell-like microstructure), (b) inside β grain (on intragranular α_s), sample was heat treated as 1000℃ 1 h, SQ, 680℃ 1h, WQ, and 640℃ 5 h, WQ.

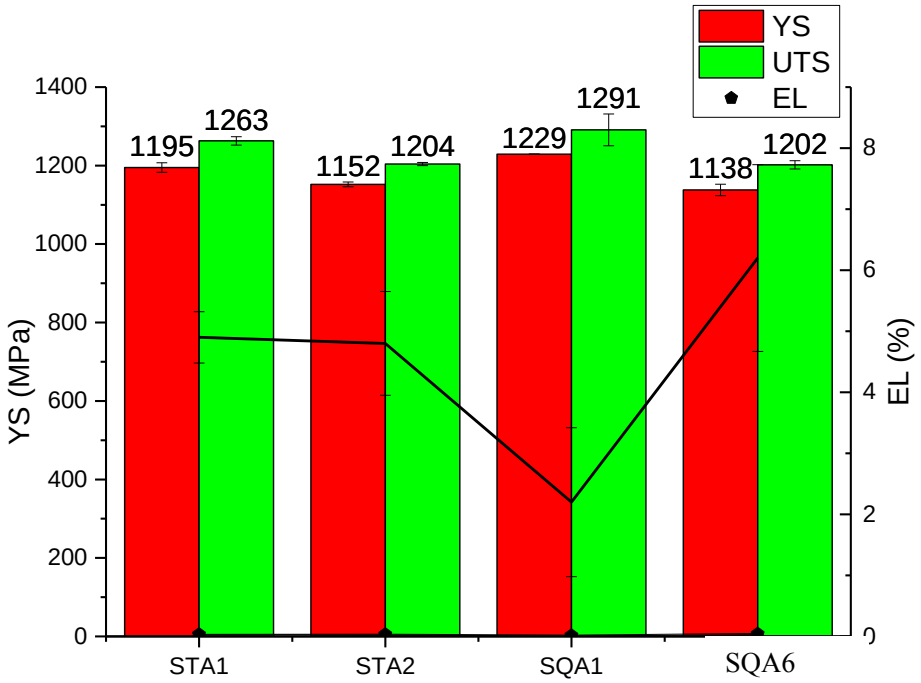

Fig. 86 Bar charts results for undoped Ti-5553 specimens through different heat treatment routes.

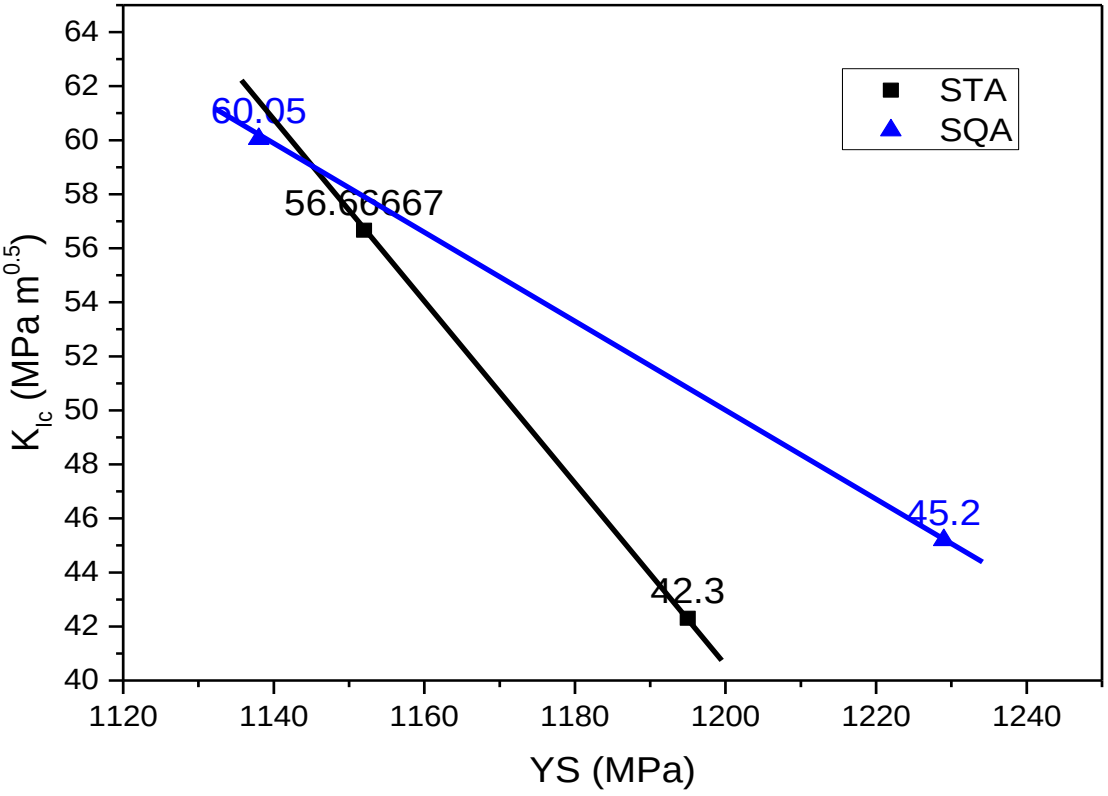

Fig. 87 K_{Ic} and YS scatter diagram from specimens (SQA and STA).

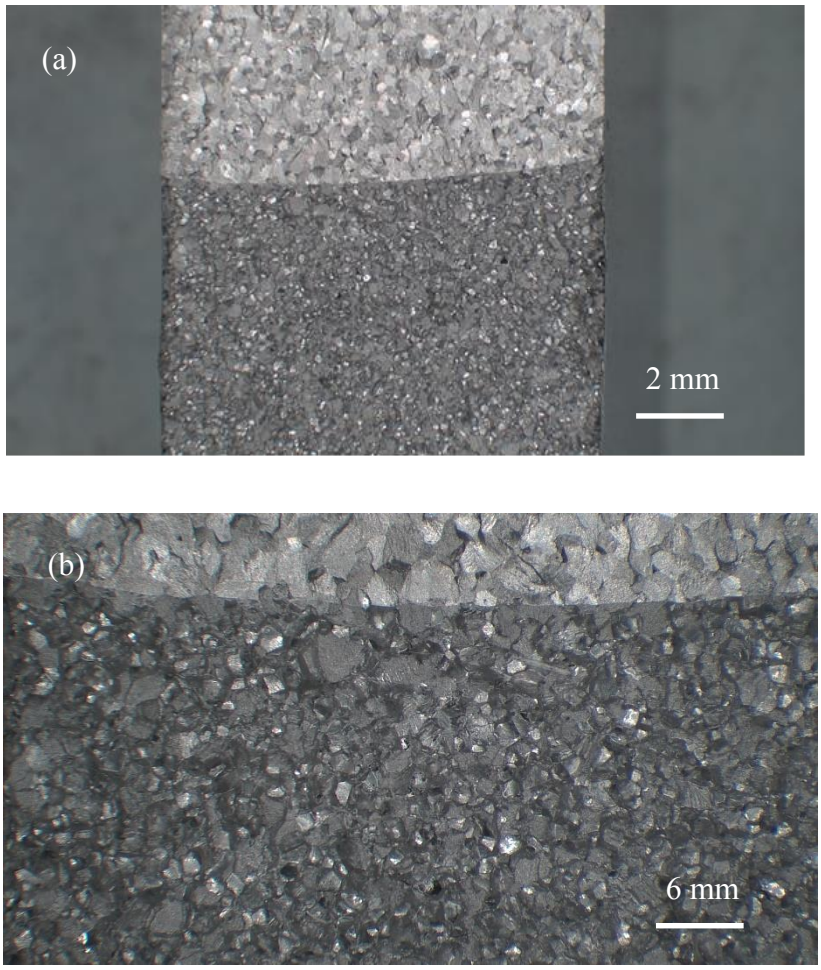

Fig. 88 Fracture surface observed under OM from STA1 specimen, (a) low magnification, (b) high magnification.

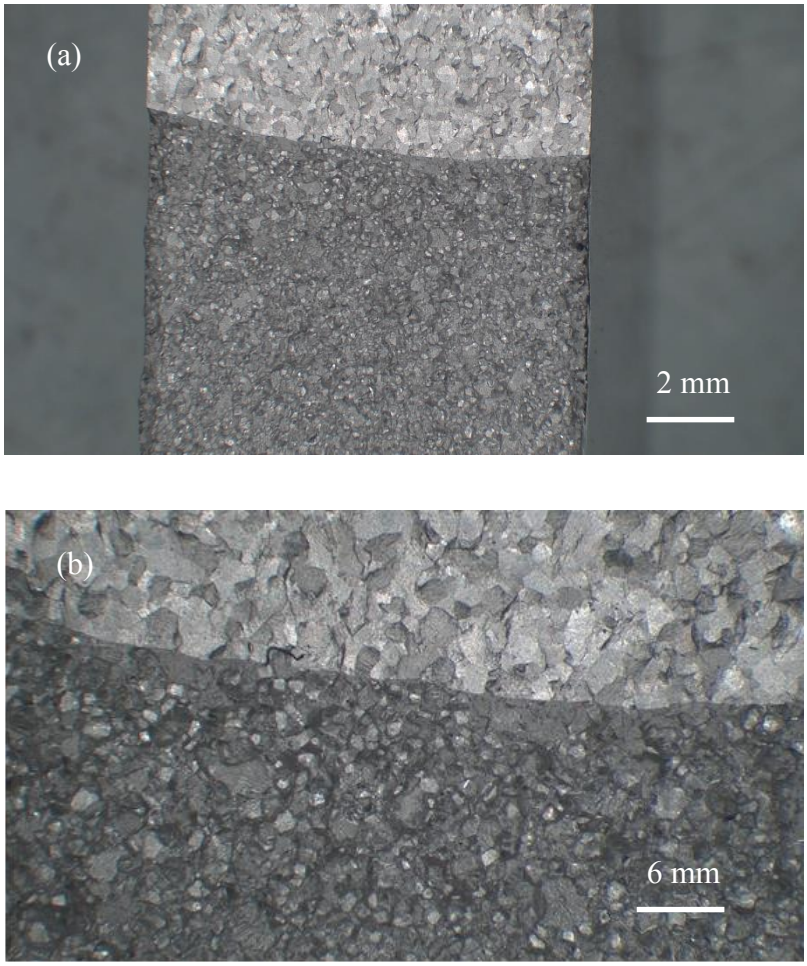

Fig. 89 Fracture surface observed under OM from SQA1 specimen, (a) low magnification, (b) high magnification.

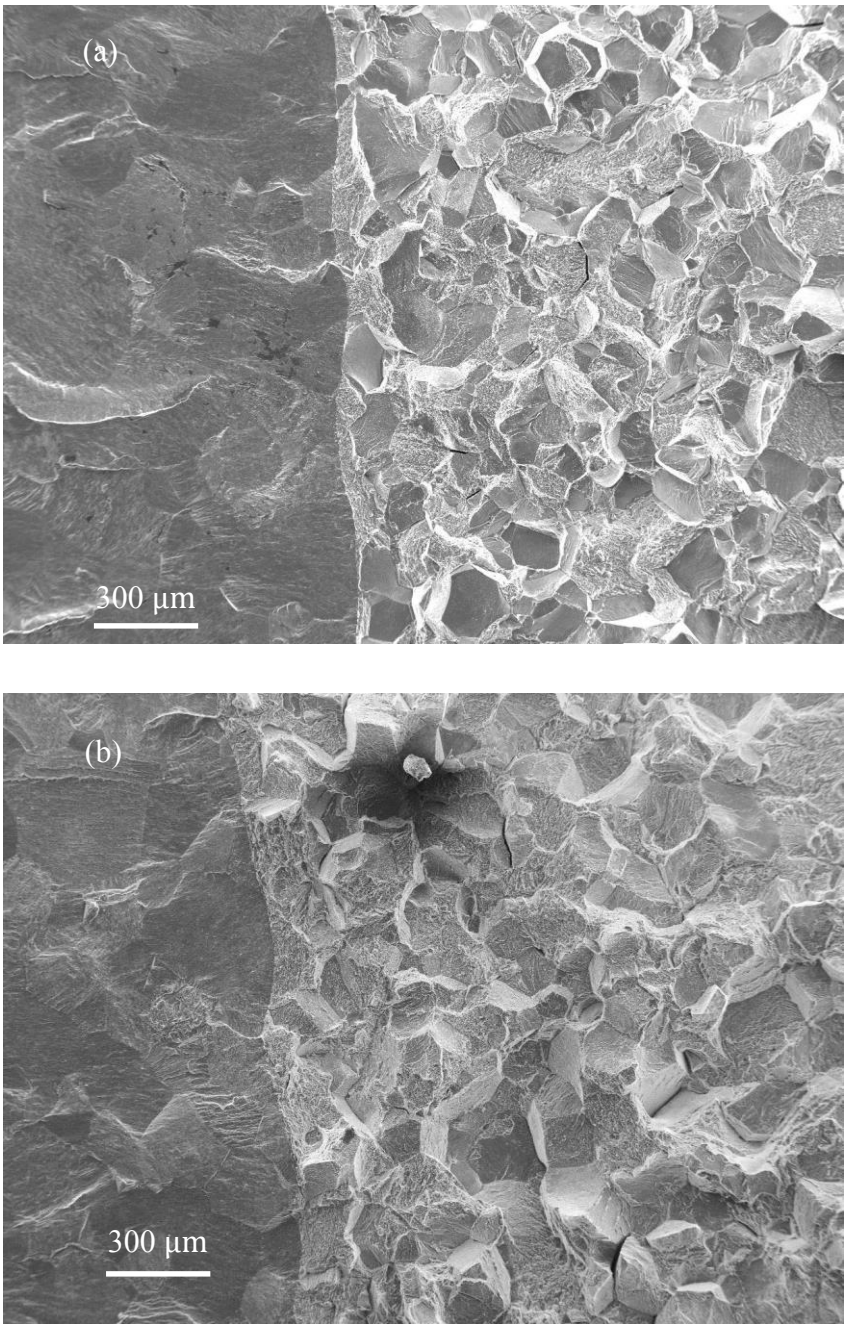

Fig. 90 Low magnification fracture surface images, (a) STA1 specimen, (b) SQA1 specimen.

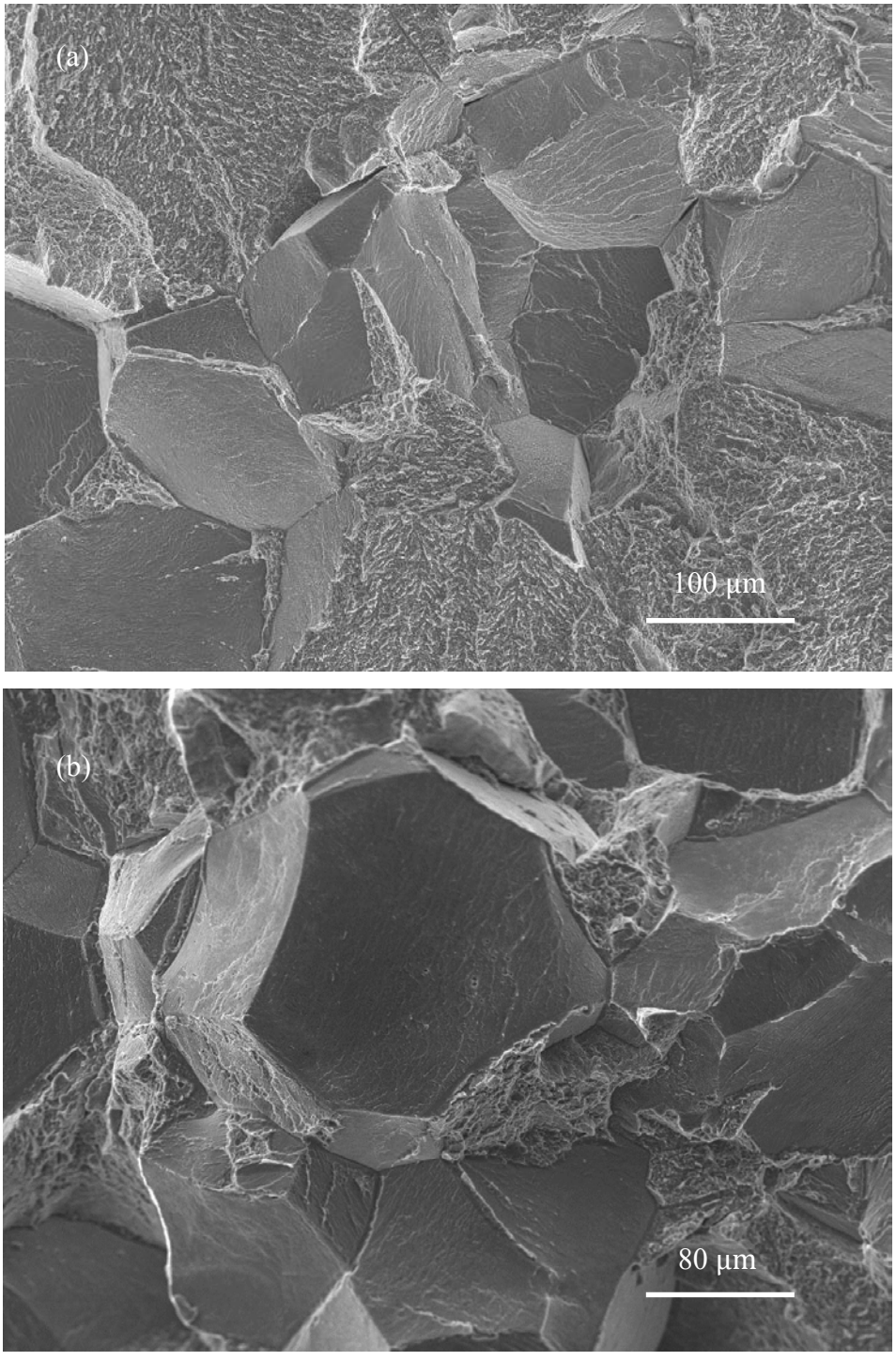

Fig. 91 SEM fracture surface image from STA1, (a) whole surface scanning, (b) intergranular area scanning.

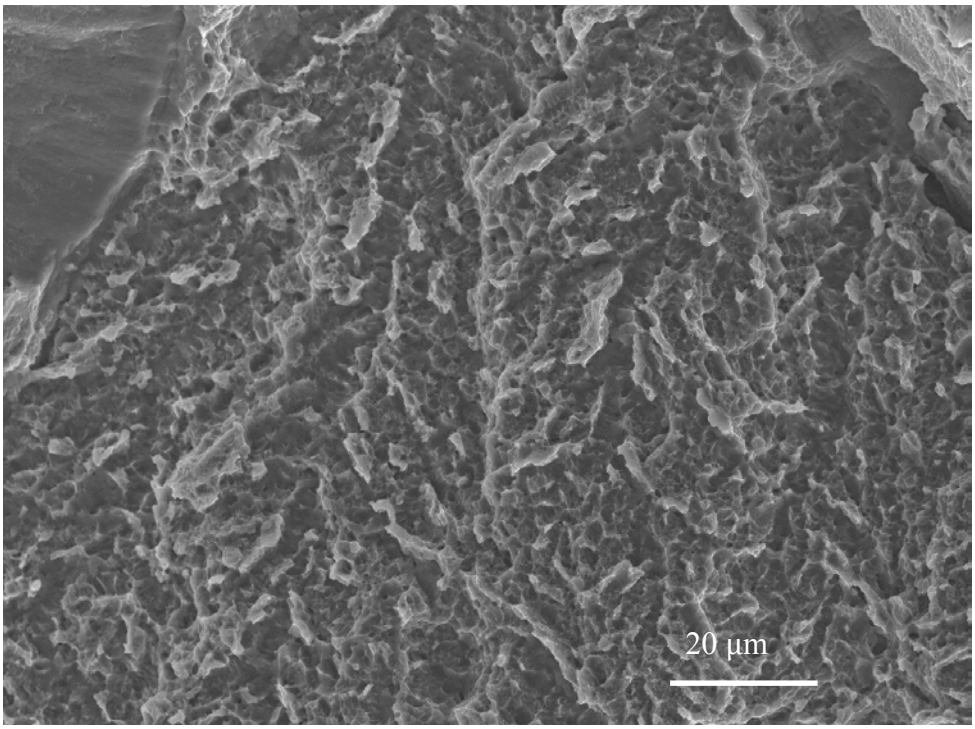

Fig. 92 High magnification SEM fracture surface image from STA1 at transgranular area.

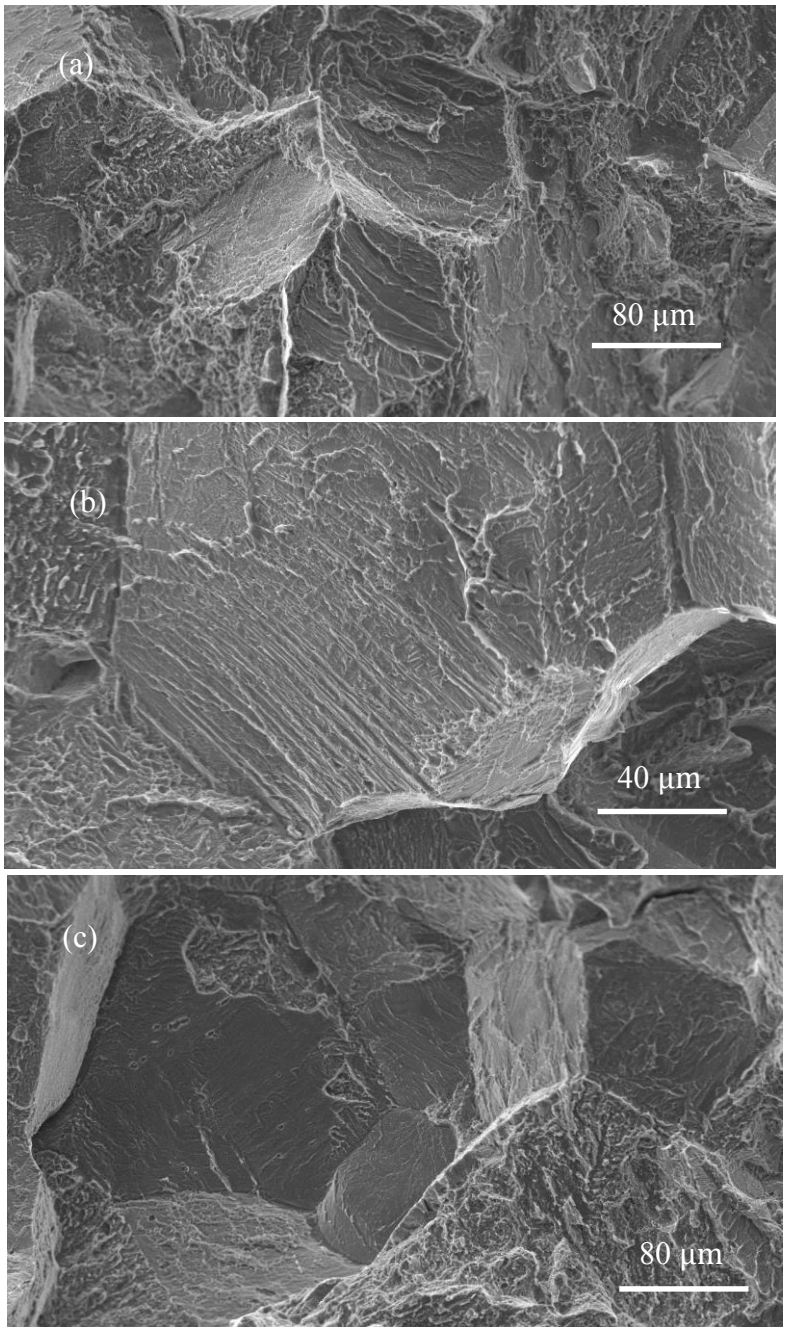

Fig. 93 High magnification SEM fracture surface image from SQA1, (a) and (b) some lath-like patterns on the intergranular facets, (c) no pattern observed on the intergranular facets.

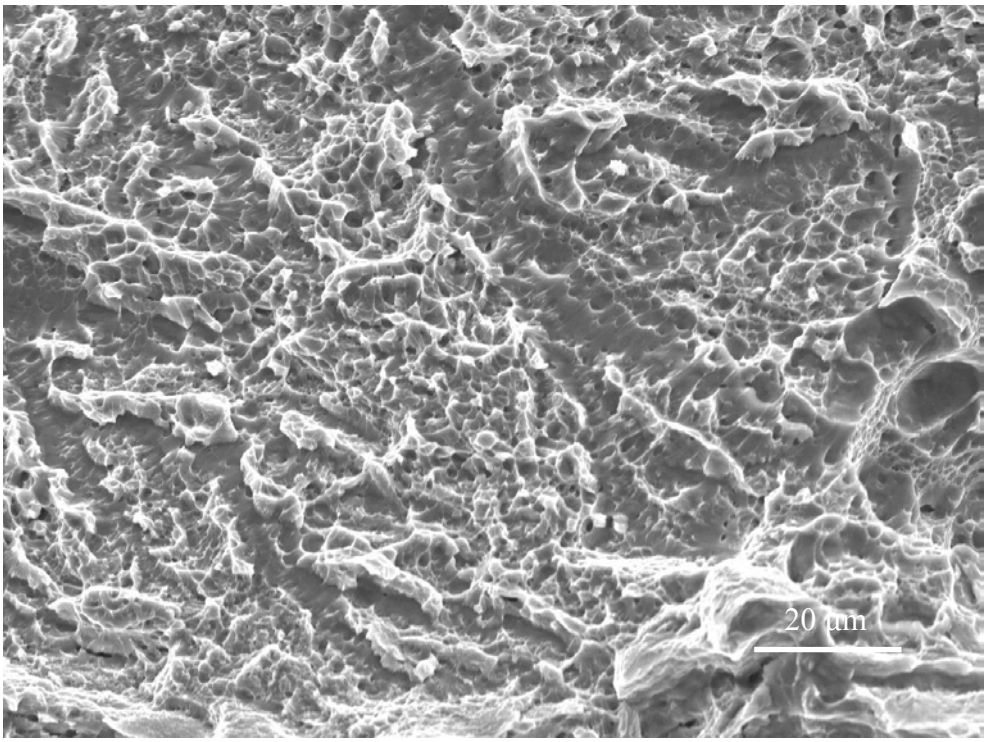

Fig. 94 High magnification SEM fracture surface image from SQA1 at transgranular area.

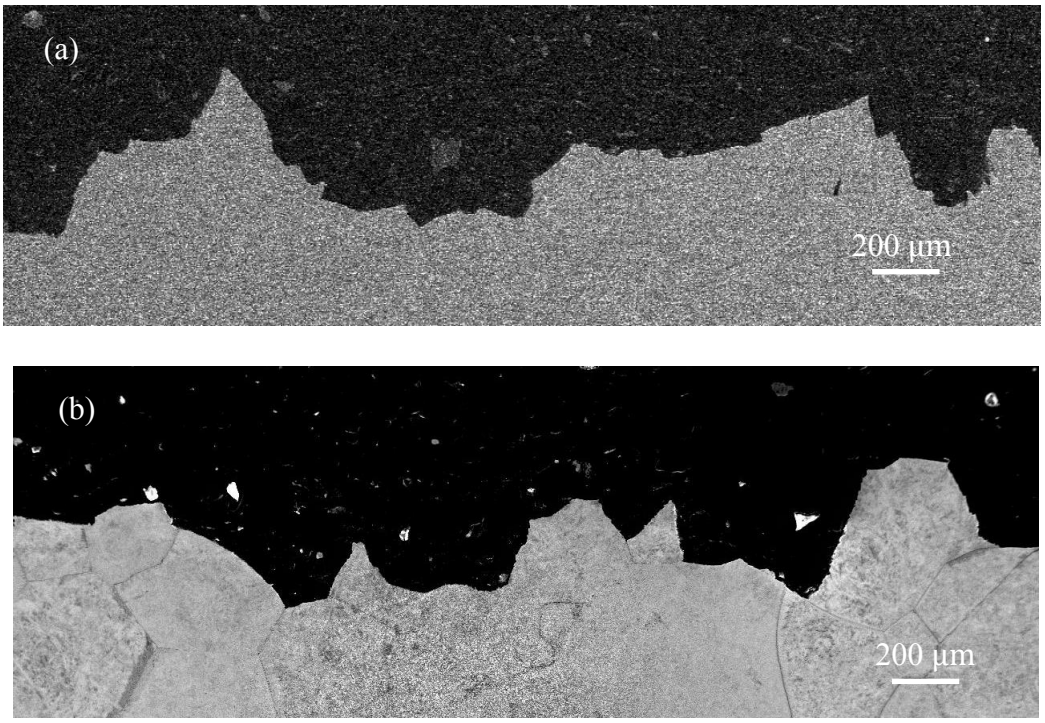

Fig. 95 Cross-sectional images of specimens via different heat treatment routes, (a) STA1, (b) SQA 1.

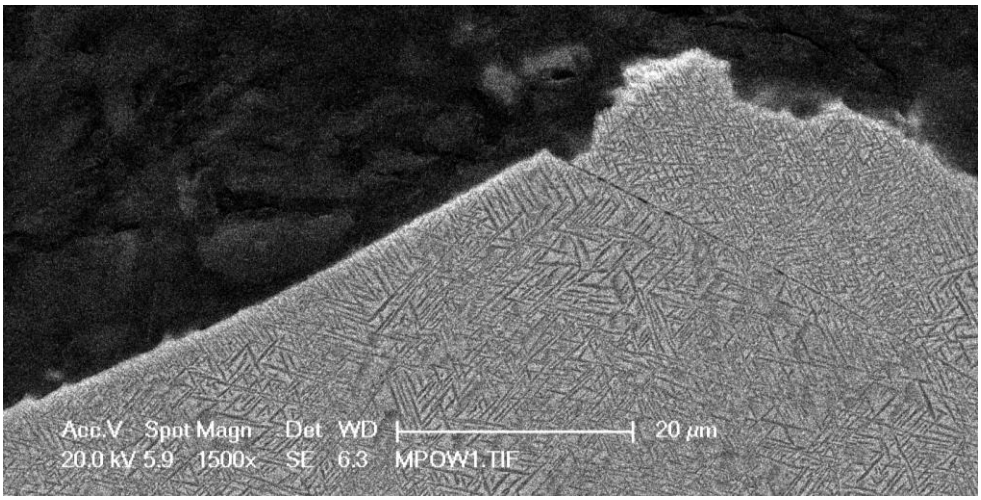

Fig. 96 High magnification SEM image from STA1 specimen, on intergranular fracture path.

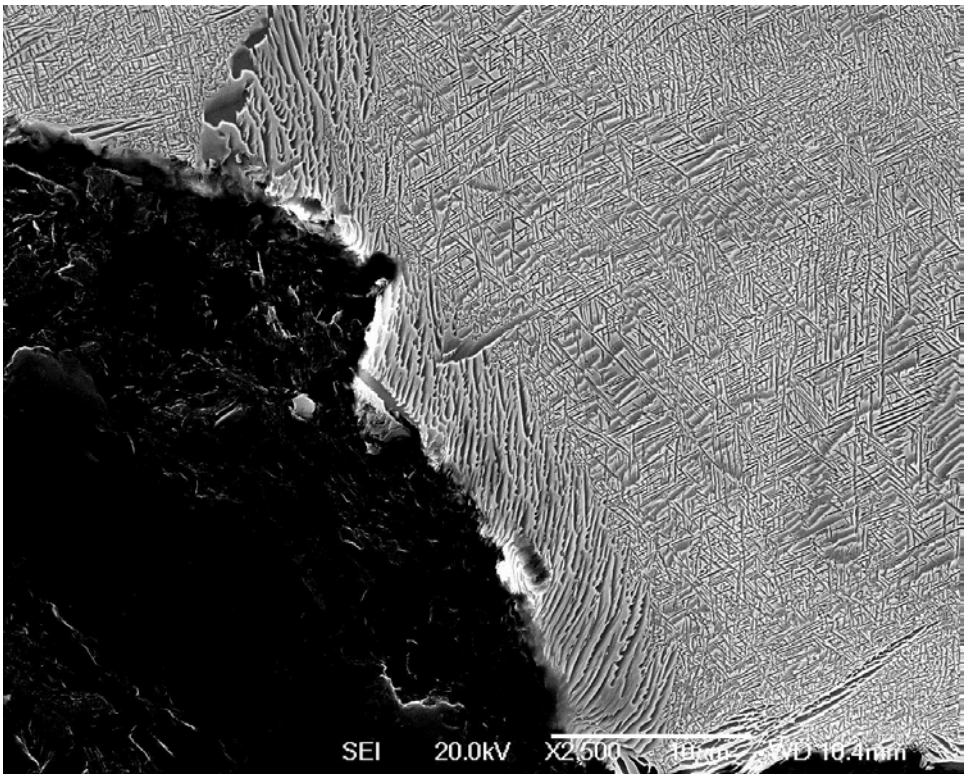

Fig. 97 High magnification SEM image from SQA1 specimen, on intergranular fracture path.

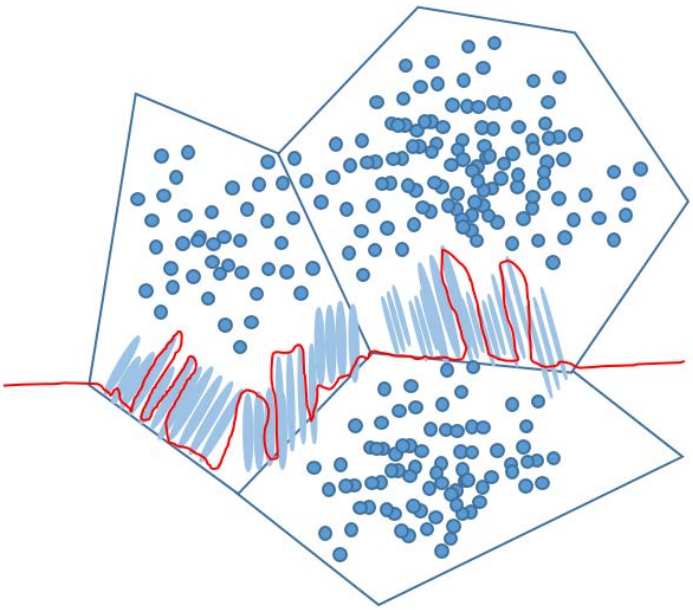

Fig. 98 The interpretation of crack propagating when it goes in SQA1 specimen.

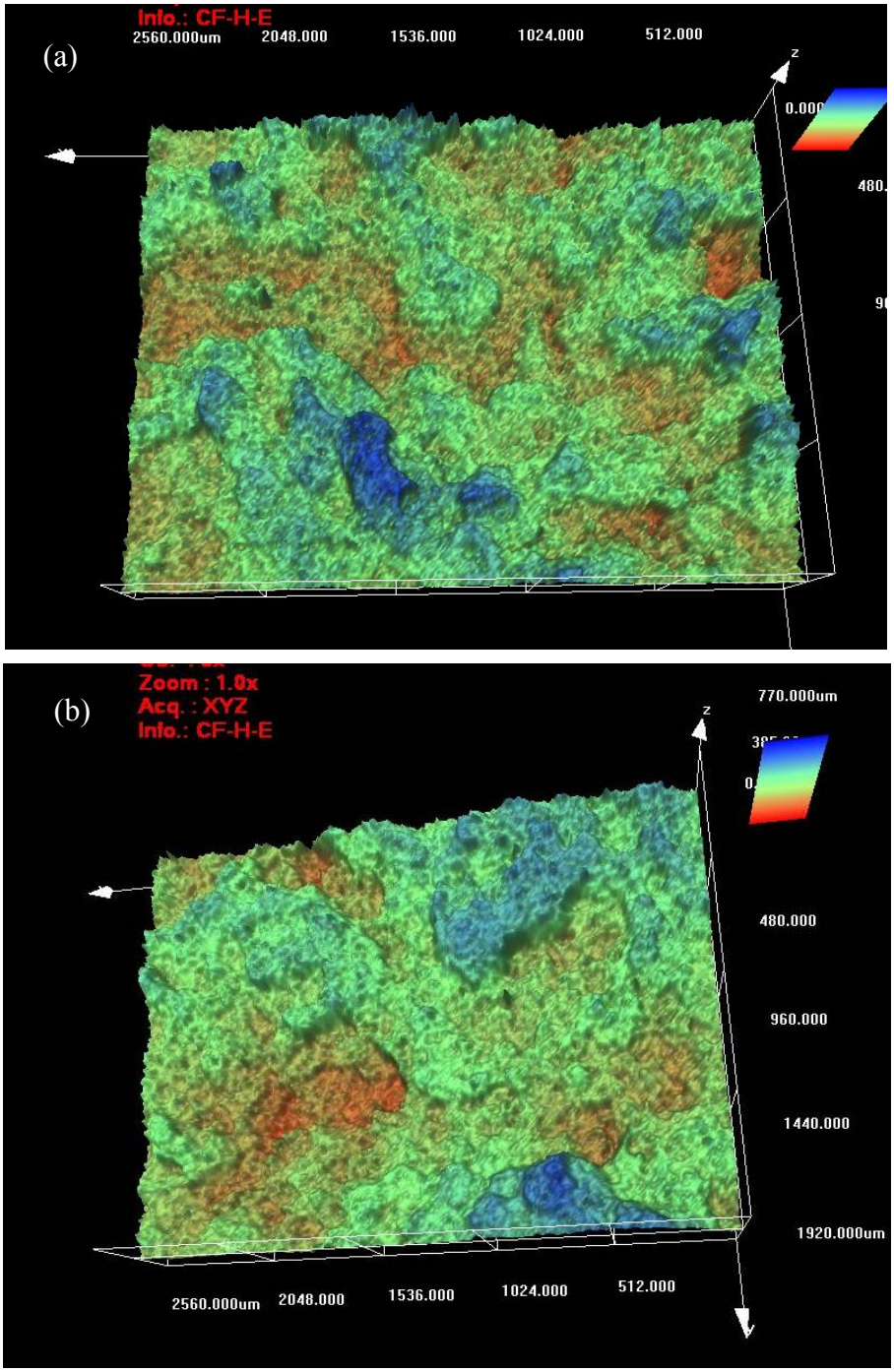

Fig. 99 Confocal images of two kinds of specimens via different heat treatment routes, (a) STA1, (b) SQA1.

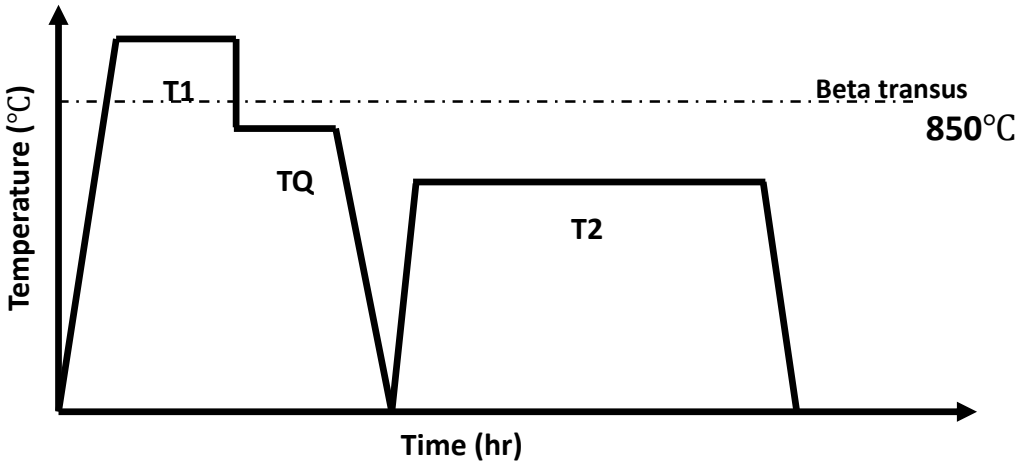

Fig. 100 Step quenching and ageing (SQA) schedule for PREP NC Ti-5553 alloy.

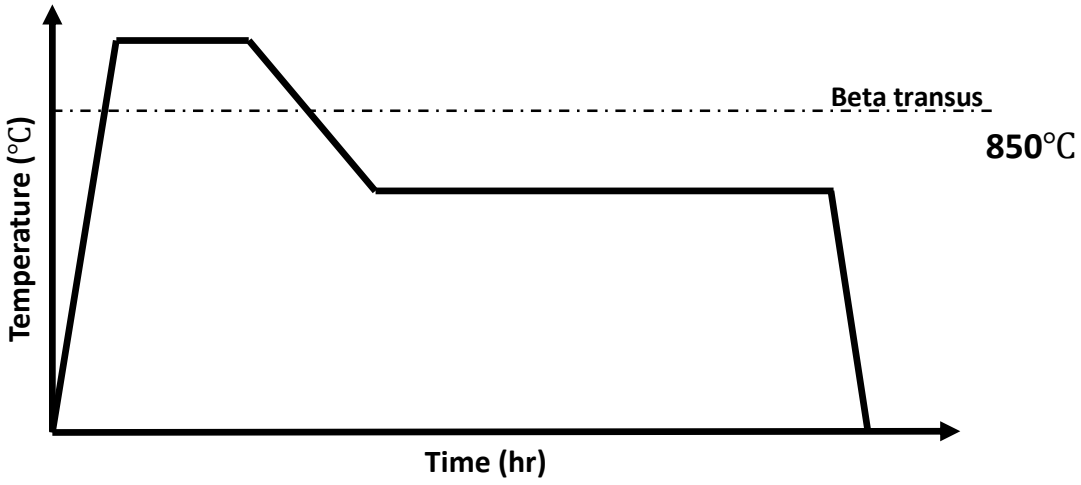

Fig. 101 Beta annealed with subsequent slow cooling and ageing (BASCA) schedule for PREP NC Ti-5553 alloy.

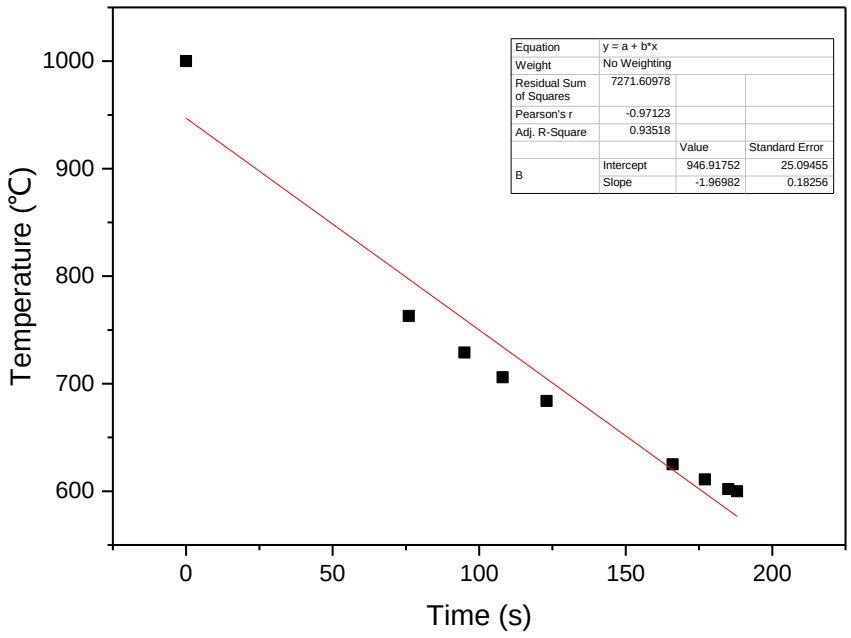

Fig. 102 Cooling rate results and linear fitting results for slow cooling process from 1000℃ to 600℃.

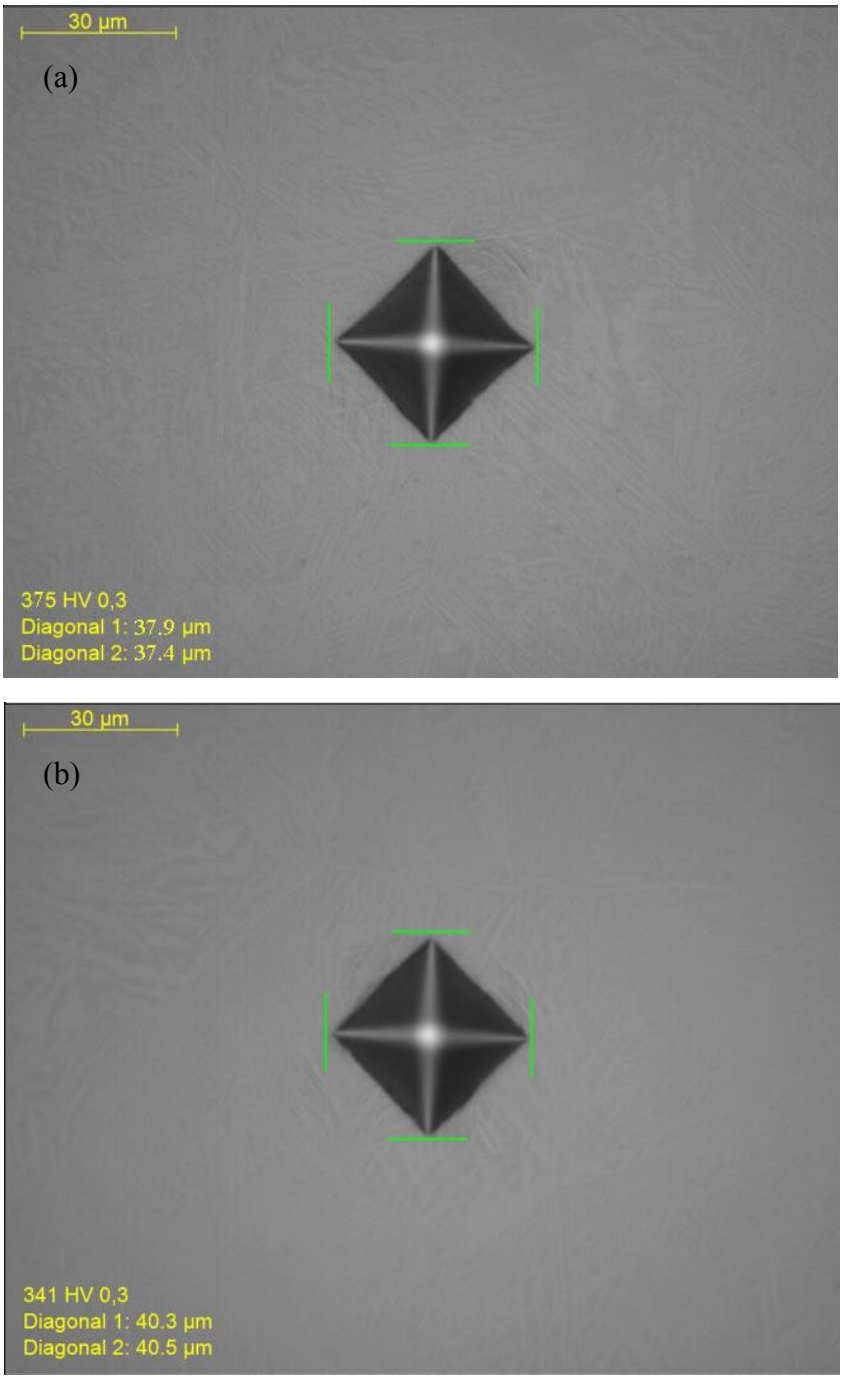

Fig. 103 OM images of indentation pattern during Vickers hardness testing, (a) BASCA3 specimen, (b) BASCA4 specimen.

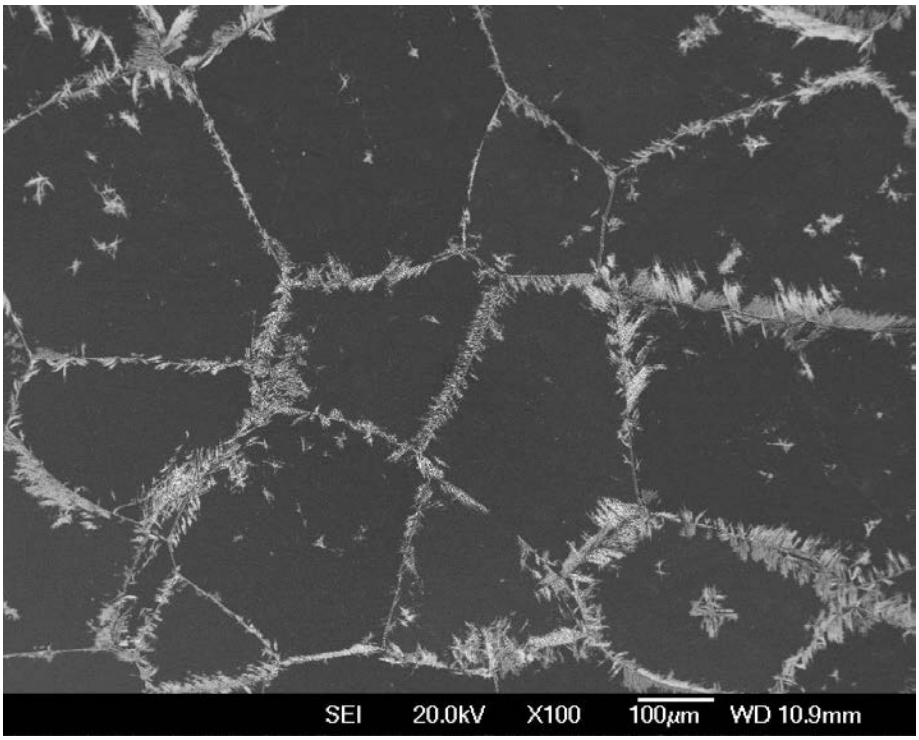

Fig. 104 SEM image from Ti-5553 alloy through the first step heat treatment, 1000℃, FC to 600℃ 4h, WQ.

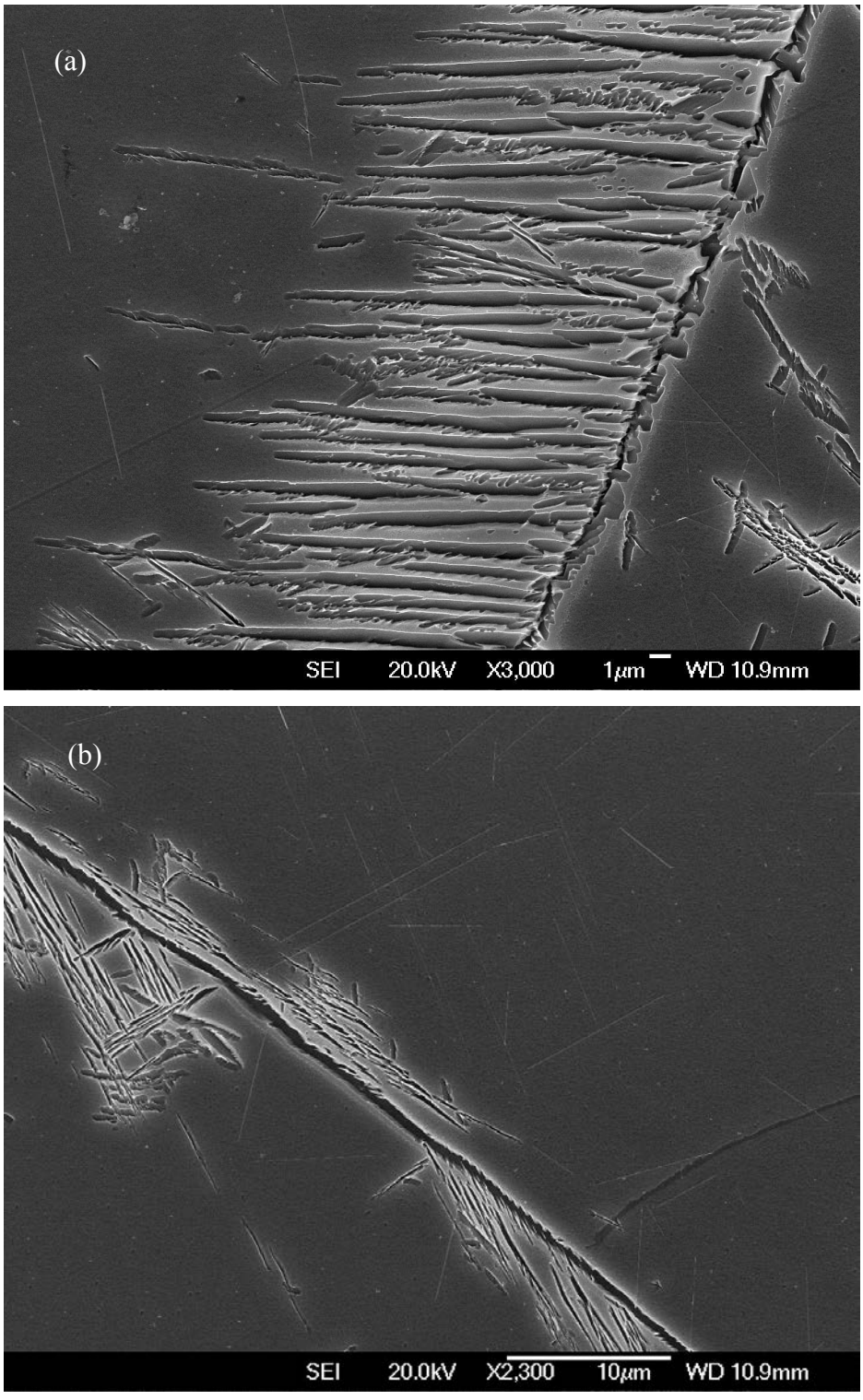

Fig. 105 Higher magnification SEM image displaying details around grain boundary in Fig. 104.

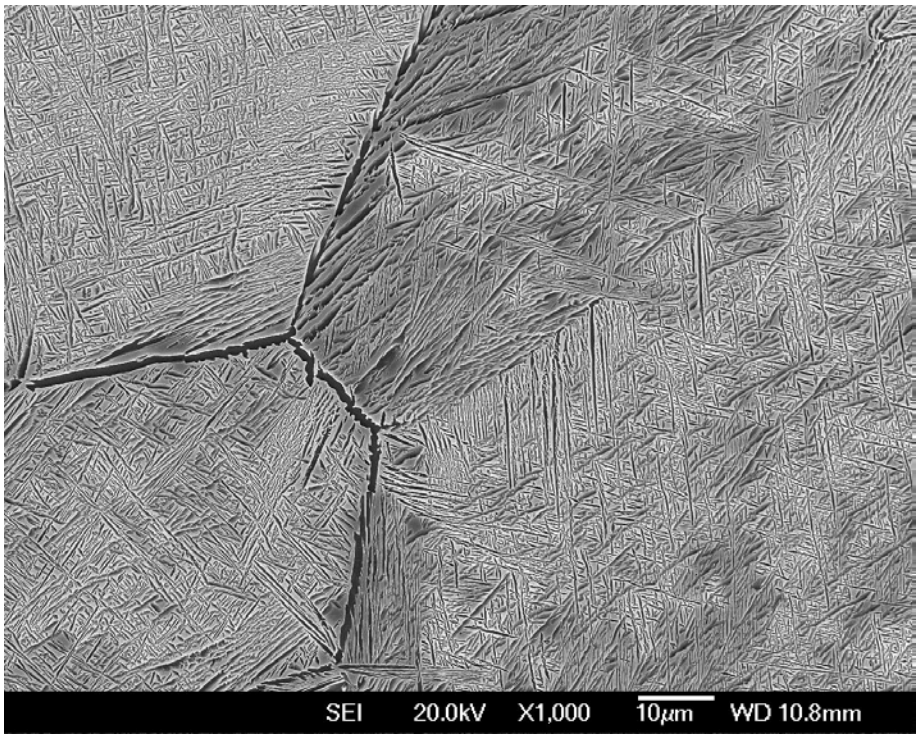

Fig. 106 SEM image from specimen heat treated using BASCA3.

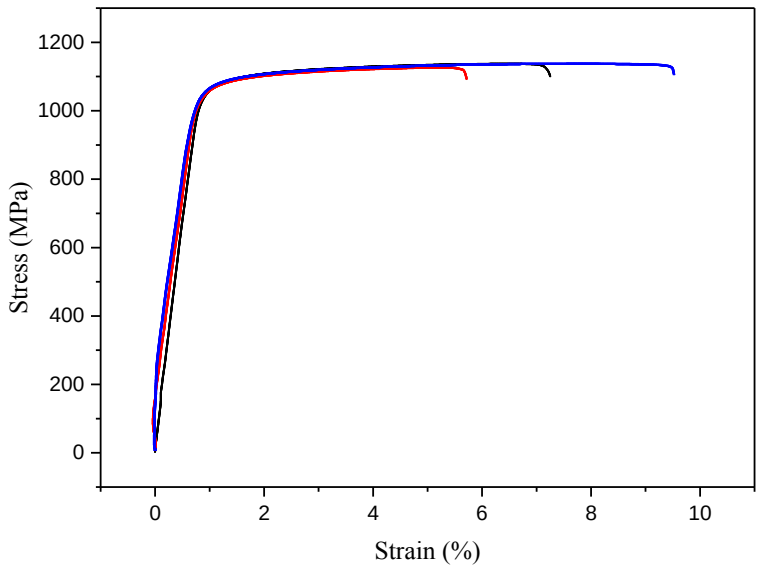

Fig. 107 Stress-strain curves of BASCA3 specimen (1000℃ 1 h, SC, 600℃ 5 h).

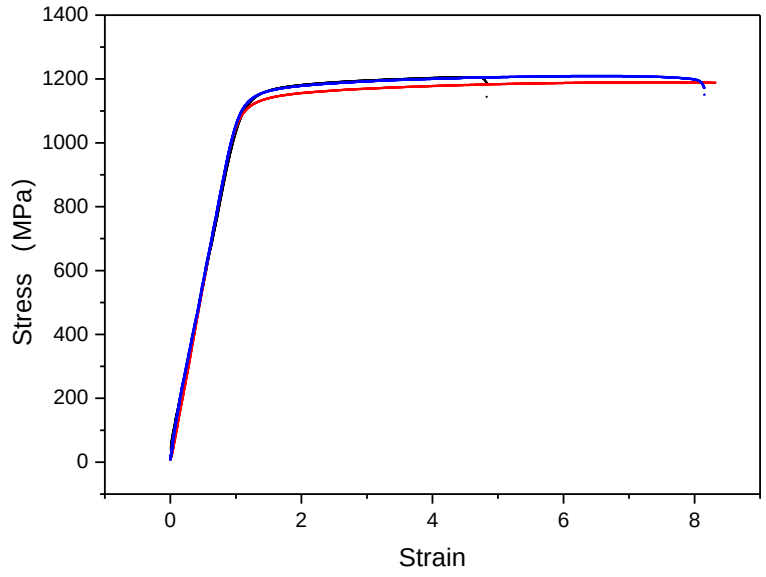

Fig. 108 Strain and force curves of SQA6 specimen (1000℃ 1 h, SC, 600℃ 5 h).

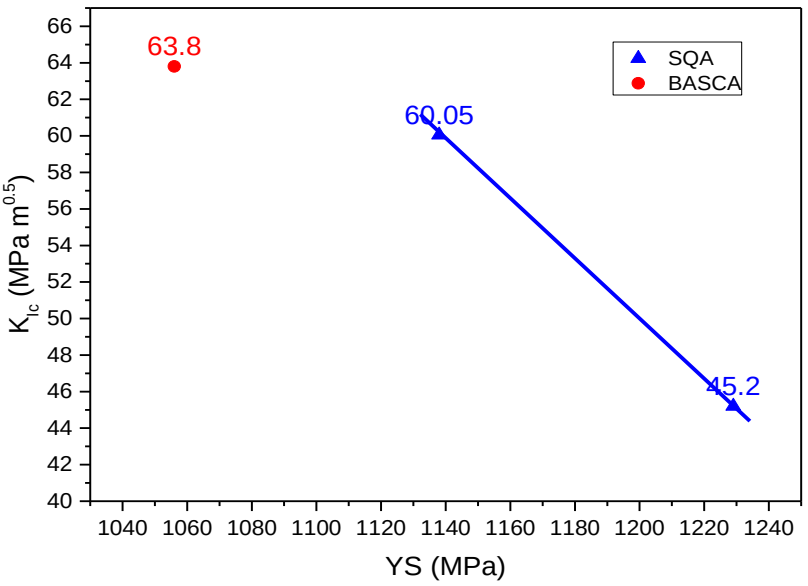

Fig. 109 K_{Ic} and YS scatter diagram from specimens (SQA and BASCA routes).

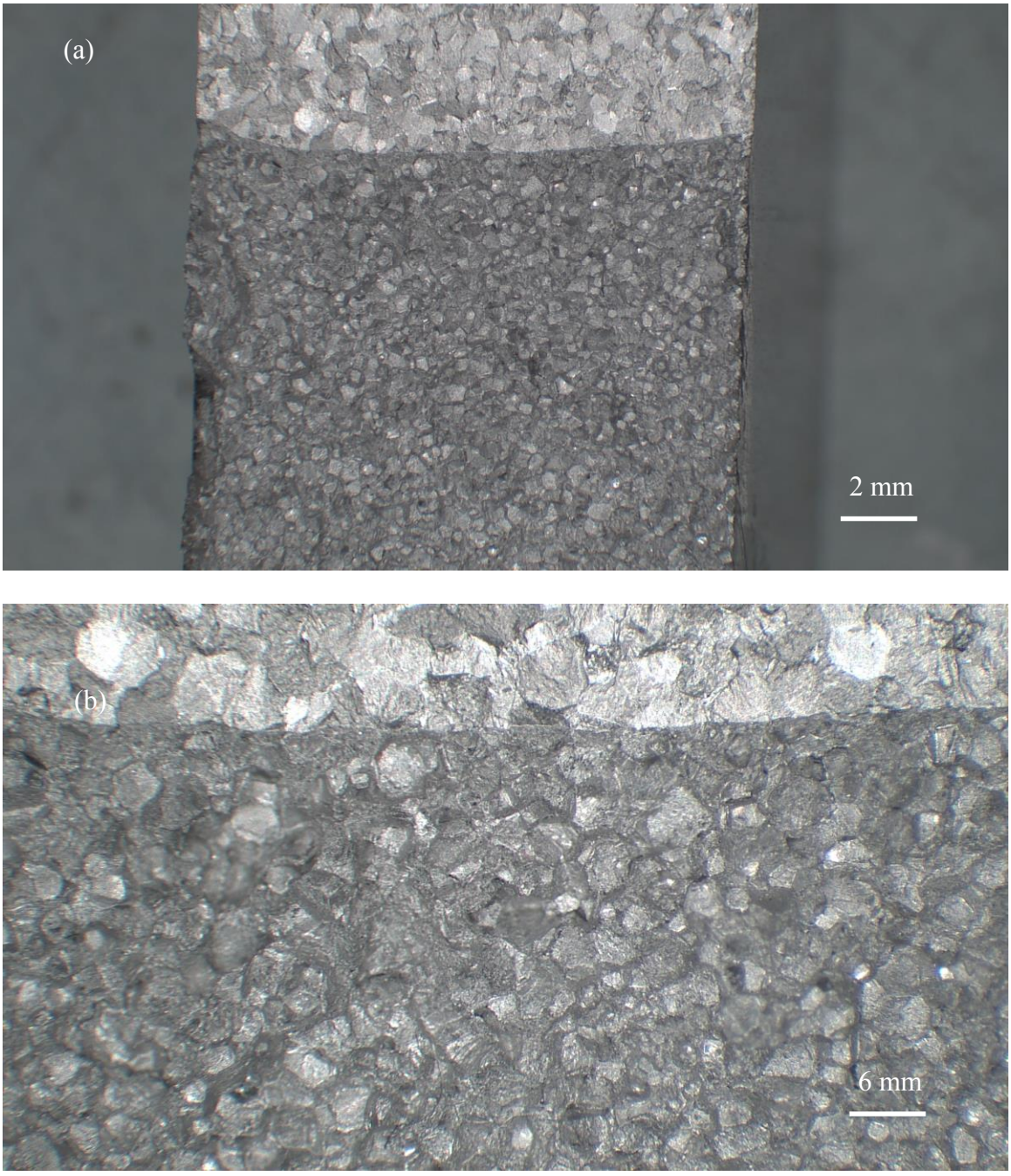

Fig. 110 Fracture surface observed under OM from BASCA3 specimen, (a) low magnification, (b) high magnification.

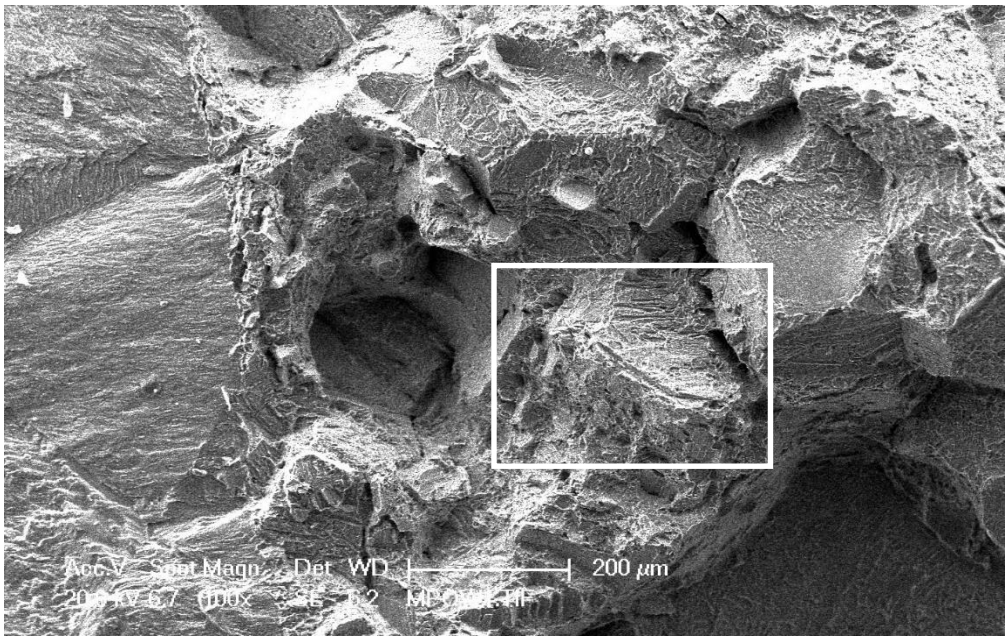

Fig. 111 Low magnification SEM fractographic image from BASCA3 specimen.

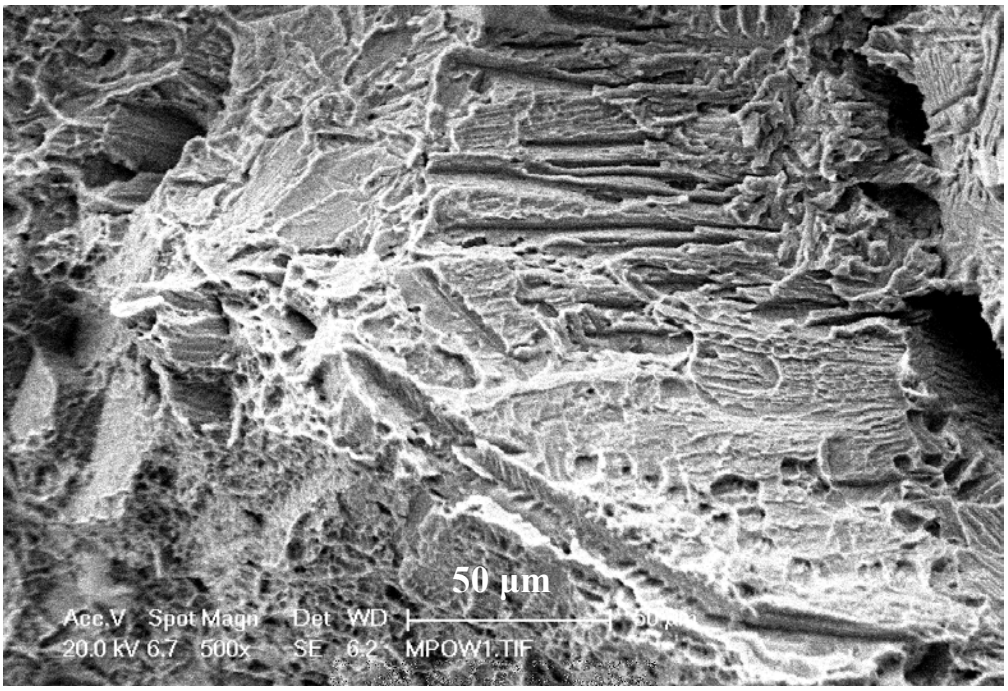

Fig. 112 High magnification image on selected area in Fig. 111.

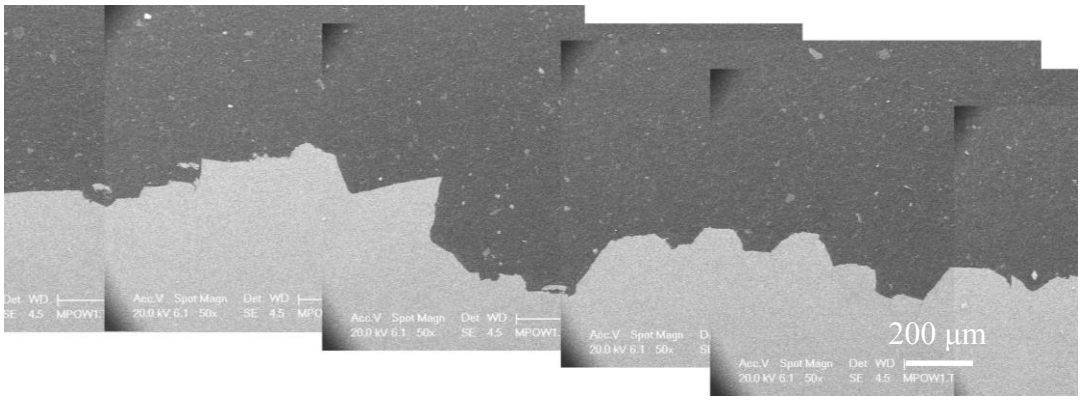

Fig. 113 Cross-sectional images of specimen via BASCA3 heat treatment routes

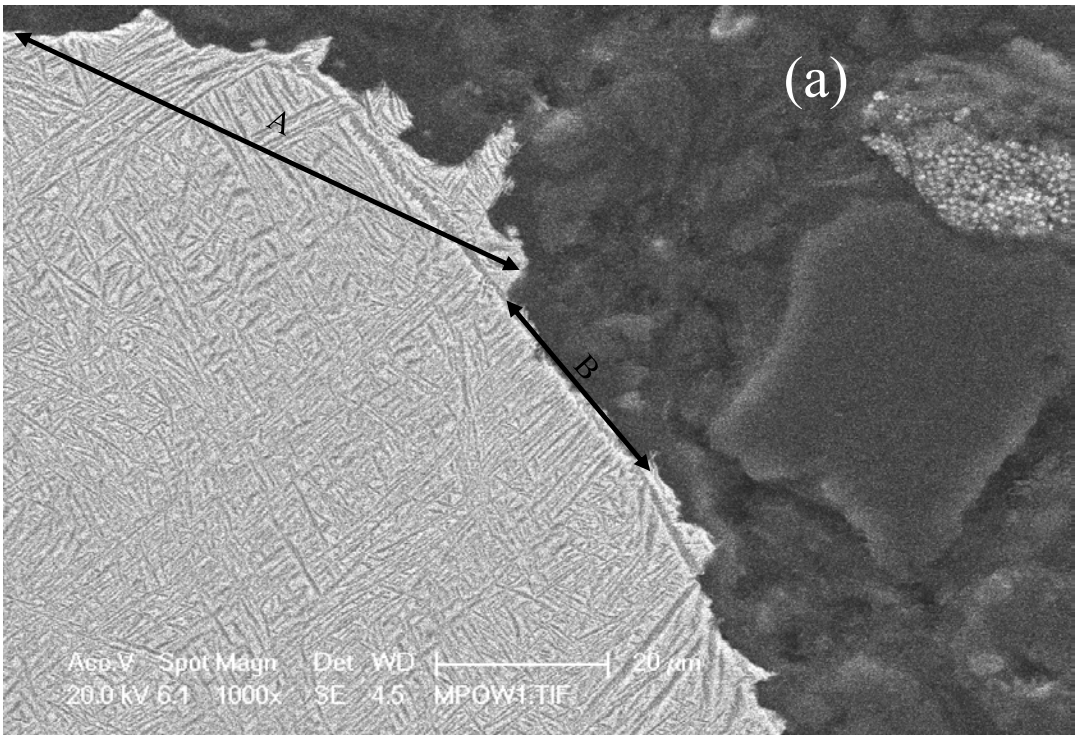
(a)
A
B
Acc.V Spot Magn Det WD 20 µm
20.0 kV 6.1 1000x SE 4.5 MPOW1.TIF

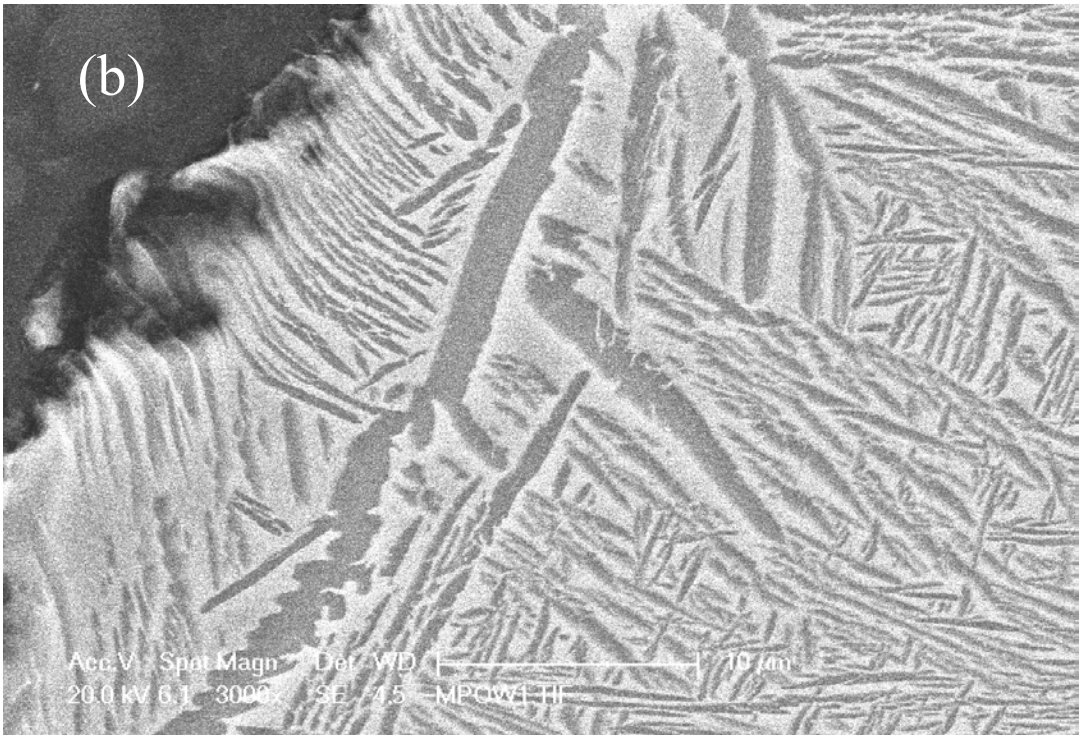
(b)
Acc.V Spot Magn Det WD 10 µm
20.0 kV 6.1 3000x SE 4.5 MPOW1.TIF

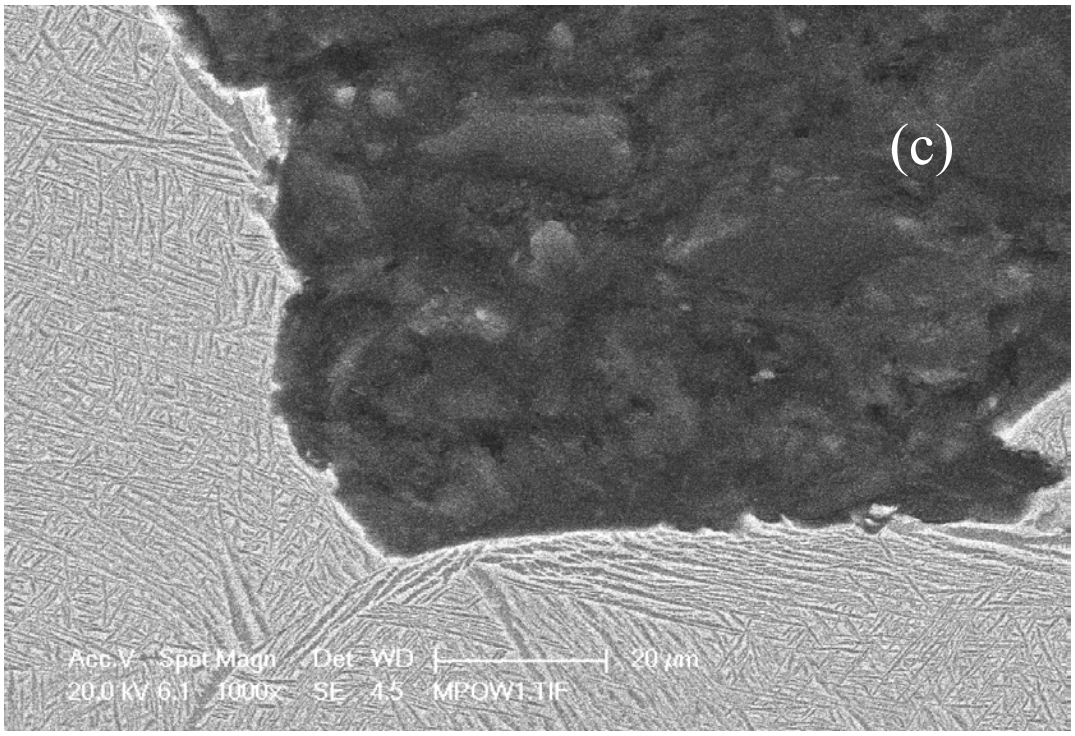

Fig. 114 High magnification SEM image from BASCA3 specimen, on intergranular fracture path.

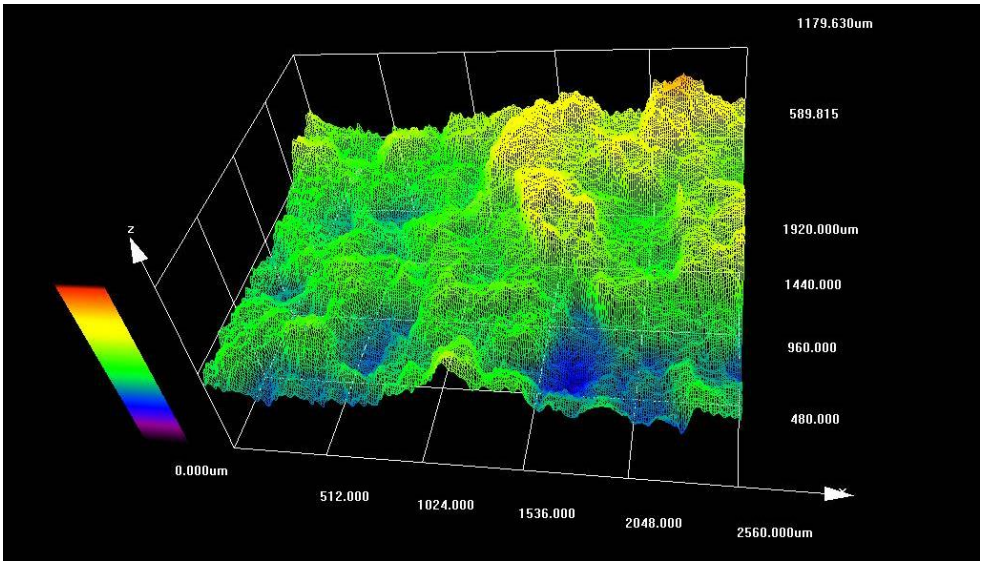

Fig. 115 Confocal images of BASCA3 specimen.